國立臺灣師範大學理學院地球科學系
博士論文

Department of Earth Sciences
College of Science
National Taiwan Normal University
Doctoral Dissertation

印尼東爪哇巴契丹地區中新世中期火山岩的年代與地球化學特徵

Age and geochemical characteristic of the Middle Miocene volcanic rocks from Pacitan, East Java, Indonesia

Student: Lediyantje Lintjewas

指導教授：賴昱銘教授
Advisor: Prof. Yu-Ming Lai

中華民國 114 年 06 月
June, 2025

ACKNOWLEDGEMENTS

Praise and gratitude to the Lord Jesus Christ for blessings and grace so that the author can complete this dissertation. This dissertation can be completed well and smoothly not because of the author's hard work but with sincere help from various parties who always support and encourage the author. For that, the author expresses deepest appreciation and gratitude:

1. To my supervisor, **Prof. Yu Ming Lai** for guidance and advice throughout the years who has helped, guided and encouraged, supporting me with funding so that I could pass all the stages well.
2. To **Prof. Sun Lin Chung** for guidance and advice during stayed in Taiwan, as well as for supporting me with funding during my time in Taiwan.
3. To **Dr. Hao Yang Lee, Dr. Kwang Nang Pang** who gave me a lot of feedback and suggestions on my dissertation.
4. To **Dr. Eng Iwan Setiawan** Thank you for your invaluable support and encouragement.
5. To thank **Wen Yu** who helped me a lot with the campus administration.
6. To thank the Academia Sinica laboratory assistants who have helped me a lot in completing my research analysis.
7. To especially thank my family: my parents, my father Mr. **Frans Lintjewas** and my mother Mrs. **Hamsiah Manda**, my husband **Kurnianto**, my daughter **Allena Bellvania Gneiss Kurnianto**, as well as my brother and sister who always provide support, understanding, enthusiasm and prayers that never break during my studies, research and thesis writing.
8. Thanks to BRIN friends who have provided a lot of support and shared experiences and input in my research process.

Finally, I hope this dissertation can be useful for science and can be used as well as possible for the advancement of geological science, especially for all those who need it.

ABSTRACT

Cenozoic volcanoes on Java, located at SE Sundaland were produced by the subduction of Indian-Australian oceanic crust beneath the Eurasian Plate. Pacitan is located on the southern coast of East Java. In addition, Pacitan is also part of the Southern Mountains range, where some volcanic rocks are exposed. The volcanic rocks are known as Old Andesite, which was formed in the Eocene. This study focuses on the volcanic rocks in this area to identify the geochemical variations from different magmatic stages. The methods used are major elements, trace elements, Sr-Nd isotopes, Zircon U-Pb ages, and zircon Lu-Hf isotopes in volcanic rocks. Based on the data obtained, the Pacitan area shows active volcanism three periods: starting from the Late Oligocene (26.7 to 26.0 Ma), followed by the Early Miocene (~20 Ma), and Middle Miocene (13.4 to 11.4 Ma). The Late Oligocene volcanic rocks are composed of medium- to low-K calc-alkaline andesite to dacite. Early Miocene volcanic rocks are composed of medium-K calc-alkaline series to low-K calc-alkaline dacite to rhyolite while, the Middle Miocene volcanic rocks are composed of high-K calc-alkaline to tholeiitic basalt to dacite. Based on the geochemical approach, in the Middle Miocene, adakite was found. Besides that, Nb/U–Nb, Ce/Pb–Ce diagrams, and the depletion of HFSEs (Nb, Ta, and Ti) show arc characteristics in these volcanic rocks. The Old Andesite, based on the data obtained, is believed to be not as old as previously thought, due to the Sunda subduction inquisition that occurred in Pacitan, and the Old Andesite is estimated to have been active since the Oligocene. The adakite process that occurred in Pacitan is associated with the beginning of the subduction ridge in the southwest of Java, where the tectonic process occurred earlier than previously thought. From this, the tectonic evolution model that occurred in Pacitan is the latest three-stage tectonomagnetic evolution model for Tertiary subduction systems.

Keywords*: Zircon U-Pb ages, Volcanic Rocks, Southern Mountain, Adakite, East Java,*

TABLE OF CONTENTS

LIST OF TABLES

LIST OF FIGURES

CHAPTER 1. INTRODUCTION

1.1 General Introduction

Southeast Asia is a continental block composed of a heterogeneous mosaic of smaller continental fragments joined by suture zones (Hall et al., 2008; Hall, 2009) and is surrounded by subduction zones. SE Asia experienced changes in the tectonic configuration at the plate boundary during the Cenozoic, resulting in consequences for the nature and volume of magma produced (Macpherson et al., 1999). Magmatism at several locations in Southeast Asia is related to subduction geochemical characteristics (Macpherson et al., 1999). Subduction is one of the causes of plate convergence, earthquakes, and volcanic eruptions, making it important to understand tectonic and magmatism processes (Hall, 2017). Some research explained that the formation of volcanic island arcs was related to subduction and became more important for explaining processes involved in the generation of island arc magmas, so it gave knowledge about Earth's evolution (Claproth, 1988). Besides, volcanic rocks along the island arc can provide an understanding of changes in the geochemistry so it contributed to the development of plate tectonic theory and the petrogenesis involved in the evolution of the island arc (Ritman, 1953; Gill, 1981; Hutchison, 1982; Wheller et al., 1987). Isotopic variations in the geochemistry of Neogene lavas can explain island arc characteristics, as published by Whitford et al. (1979) and Hutchison (1982).

Indonesia is part of SE Asia, a big country with many islands covering >18,000 islands from Sumatra Island to Papua Island (Hall et al., 2008). Located at the confluence of several plates e.g., the Eurasian Plate, Philippine Sea Plate, India-Australian Plate, and Pacific Plate (Birds, 2003). Nusa Tenggara, Sumatra, and Java lie at the confluence of the India-Australian Plate and Eurasian Plate. In contrast, North Maluku and Papua lie on the Pacific Plate (Hall, 2002) **(Fig. 1.1)**. The Indonesia is a region of complex tectonics and an important area for understanding arc processes and volcanic arc effects (Hall et al., 2008). Subduction of the India-Australian Plate beneath the Eurasian Plate has led to the development of a major magmatic arc system which is subdivided into two segments comprising the Sunda Arc in the west and the Banda Arc in the east (Dempsey, 2013). Different tectonic settings, related to the subduction of the Australian Plate in the west and the convergence of the continental Australian Plate in the east, are related to island arc geochemical variations as published by (Elburg et al., 2005).

The Sunda arc extends from the Sumatra Island to Flores Island and features a volcanic arc characteristic of subduction zone. This arc is underlain by the Australian Plates and Eurasian Plate. The crustal thickness is about 20 km, reflecting the transition between the Sunda continental shelf and the Indian Ocean (Hall and Sevastjanova, 2012). The Sunda Arc has characteristic continental archetypes and oceanic arc types. Research related to sub-terrane exposure in SE Asia and under the Sunda Arc is still unclear which parts are built on top of the continental crust and which parts are on the oceanic crust. This makes arc petrogenesis particularly problematic in terms of identifying which chemical signatures are inherited from subduction and which signatures are inherited in the earth's crust. (Edwards et al., 1993; Gasparon and Varner, 1998). Research related to magmatism in the Sunda Arc has already been conducted by previous studies with the assumption that continental crust is only located in western regions and becoming progressively oceanic towards the east. (Hamilton, 1979; Curray et al., 1977). The geochemistry of Pleistocene and Recent lava related to spatial variation from the Sunda Arc of Indonesia has been published by Whitford (1975). Within this arc, a clear association between subduction and volcanism is indicated by the geochemistry of volcanoes on Java where magma ranges from tholeiitic near the trench to calc-alkaline and alkaline farther from the trench. However, no detailed studies of the temporal variations in the geochemistry of individual volcanoes in Java have been published. Nicholas and Whitford (1980) have discussed regional geochemical variations in Java but do not include a detailed study of within volcanoes variation. The paper concluded that the primary High-K calc-alkaline magma on Java could be formed by 5% to 10% of partial melting of the peridotite mantle at a depth of 40 and 60 km. Besides that, the paper explained related to an increase in the $^{87}Sr/^{86}Sr$ ratio and K_2O at 55% SiO_2 with increase depth to the Benioff zone. Java is one of the islands in Indonesia located above the Benioff zone of the subduction plate between the India-Australian Plate and Eurasian Plate. The island extends from east to west approximately one hundred kilometers along the subduction zone. As a result, Java has the highest density of active volcanoes in the world and a large number of earthquake events (Dempsey, 2013) dominated by the Cenozoic volcanoes (Setiadji et al., 2006). Volcanoes in Java that show relatively complex geochemical variations have been reported (Whitford, 1975; Nicholls and Whitford, 1976; Nicholls et al., 1976; Whitford and Nicholls, 1976; Whitford et al., 1979; Hutchison, 1982; Wheller et al., 1987; Edwards et al., 1991; Gerbe et al., 1992; Edwards and Morris, 1993; Gasparon et al., 1994; Gasparon and Varner, 1998; Handley et al., 2007).

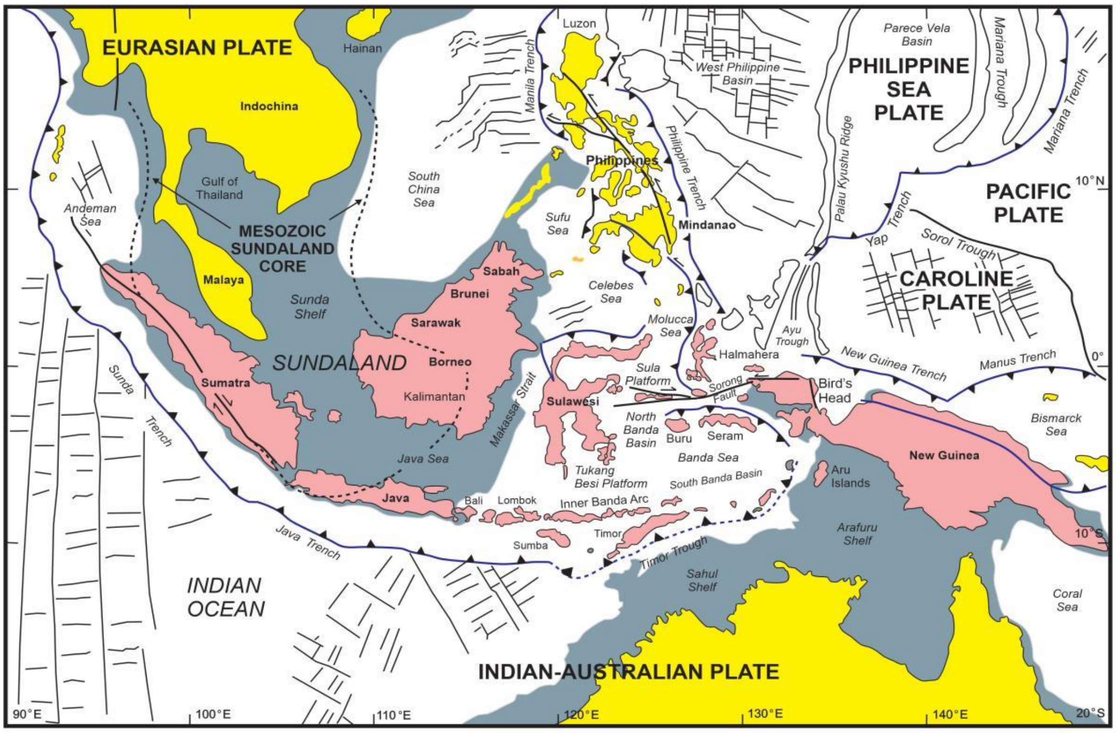

Fig. 1.1. The tectonic map of SE Asia shows the confluence of several plates in Indonesia, e.g., Eurasian Plate, Philippine Sea Plate, India-Australian Plate, and Pacific Plate (Bird, 2003). Sumatra, Java, and Nusa Tenggara lie at the confluence of the India-Australian and Eurasian Plates, while North Maluku and Papua lie on the Pacific Plate (modified from Hall (2002)). India-Australian plate beneath the Eurasian Plate has led to the development of a major magmatic arc system which is subdivided into two segments comprising the Sunda Arc in the west and the Banda Arc in the east (Hall, 2009).

1.2 Previous Studies

1.2.1 General Tectonics

Indonesia is located between the Eurasian Plate, Pacific plate, and Australian Plate (Hall, 2012; 2009; 2002). The results in the discovery of many volcanoes being discovered due to high tectonic and volcanic activity (Hall, 2012; 2009; 2002; Hamilton, 1979). Volcanoes are spread over approximately 6000 km, from the western part of Sumatra to the Maluku Islands in the east. The volcanic arc consists of 147 volcanoes (Siebert et al., 2010). Historically there have been about 78 volcanoes that have erupted and about 50 others that are solfataras or what can be known as fumaroles (Neumann van Padang, 1951; Hutchison, 1982). The volcanoes on the southern side of Java formed in the Eocene-Oligocene or around the Middle Paleogene (van Bemellen, 1949; Hamilton, 1979; Soeria-Atmadja et al.,1994). The Sunda arc has typical volcanic arc characteristics of a subduction zone (**Fig. 1.2)**. The island of Java is part of the Sunda arc which is divided into 3 parts e.g., West Java, Central Java, and East Java (Clements et al., 2009; Clement and Hall, 2007). Since the Eocene, the Sunda Arc has been active and is the result of subduction of the India-Australian plate underneath the Sundaland margin (Garwin et al., 2005; Hall, 2002; Hamilton, 1977). Sundaland comprised Indochina, Thai-Malay Peninsula, Sumatra, Java, Borneo, and the shallow sea shelf (Sunda Shelf) and was formed during the Triassic by the merging of continental blocks. Sundaland is the core of the Southeast Asian continent (Liew and McCulloch, 1985; Liew and Page, 1985). Along the southern side of Java, the volcanic arc has been forming since Eocene-Oligocene or Middle Paleogene (Soeria-Atmadja et al., 1994), while young tectonic activity is estimated from the Cretaceous to Paleogene (Hall et al., 2007). Volcanic activity intensified and produced island arc andesitic lavas (Hall, 2012; Soeria-Atmadja et al., 1994), and is thought to have occurred in the Late Oligocene and Early Miocene (Clements and Hall (2007). The composition of volcanic rocks that form Quaternary volcanics is alkaline and shows a west-east trend along the sides of Java (van Bemellen, 1949; Hamilton, 1979; Soeria-Atmadja et al., 1994).

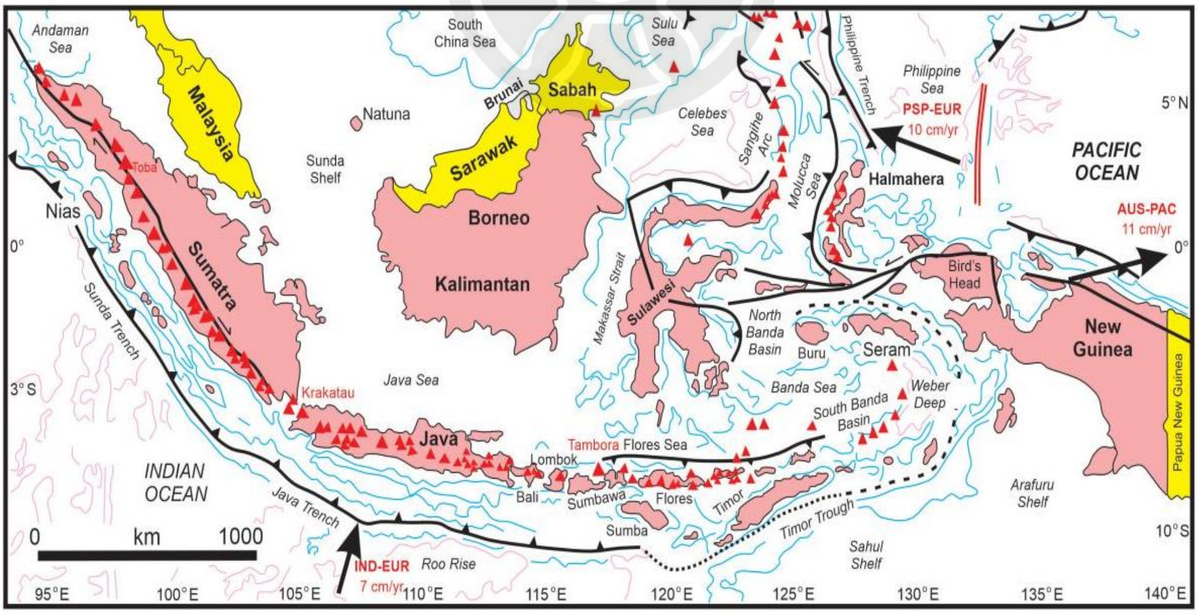

Fig. 1.2. Subduction of the India-Australian Plate under the Eurasian Plate has led to the development of major magmatic arc systems, one of which is the Sunda arc (Hall, 2009).

1.2.2 Magmatism in Java

Magmatism in the Sunda Arc extends back to the Mesozoic in Sumatra. The oldest rocks in the Lesser Sunda Islands are of Miocene age (McCourt et al., 1996). Pleistocene to Recent volcanism in the Sunda Arc has been the focus of many studies (e.g., Whitford, 1975; Whitford and Nicholls, 1976; Whitford et al., 1979; Whitford and Jezek, 1982; Nicholls and Whitford, 1976; Whitford and White, 1981; Nicholls et al., 1980; Wheller et al., 1987; Hilton and Craig, 1989; Hilton et al., 1991; Edwards et al., 1990; Gasparon et al., 1994; Alves et al., 1999; Turner and Foden, 2001; Gertisser and Keller, 2003; Handley et al., 2009). This volcanism contains the widest range of magma compositions known from any other arc or orogenic setting (Wheller et al., 1987).

The most abundant rocks are calc-alkaline basaltic-andesite and andesite, with an average silica content of 55 wt.%, characteristic of many other island arcs (Whitford, 1975; Nicholls and Whitford, 1976). However, uniformly low abundances of Mg, Ni and Cr indicate that the lavas do not represent primary mantle melts, and that most have undergone varying degrees of differentiation (Nicholls and Whitford, 1976; Nicholls et al., 1980; Wheller et al., 1987; Handley et al., 2009).

There is no evidence for the same type of crustal material in Java, and felsic rocks are notably less common. One suggestion is that the relatively basic magma compositions reflect a less mature basement, and that any contaminant has an isotopic signature similar to that of the ascending magmas, making assimilation difficult to detect (Handley, 2006; Handley et al., 2008, 2009). As a result, many studies have implicated the importance of a subducted component and source heterogeneity to explain chemical and isotopic anomalies in Java (Whitford and Jezek, 1982; Edwards et al., 1991; Turner and Foden, 2001; Alves, 1999; Handley et al., 2008, 2009; Sendjaja et al., 2009). The island of Java is located at the subduction zone. Based on the subduction configuration, it is located at a depth of 100 km in the south, extending to 400 km north of the Benioff zone. This configuration results in four magmatic arc patterns or paths, forming igneous and volcanic rock formations. According to Soeria-Atmadja et al. (1991) (**Fig. 1.3)**, the four magmatic paths in Java are as follows: (1) Eocene volcanic belt to the Middle Miocene, as the Southern Mountains Zone. (2) Upper Miocene volcanic path to Pliocene. Located to the north of the Southern Mountains, in the form of intrusion of lava and igneous rocks. (3) The Quaternary marine volcanic belt consisting of active volcanoes. (4) Quaternary back volcanic arc belt, this path is occupied by Quaternary volcanoes located back arc and became active volcanoes.

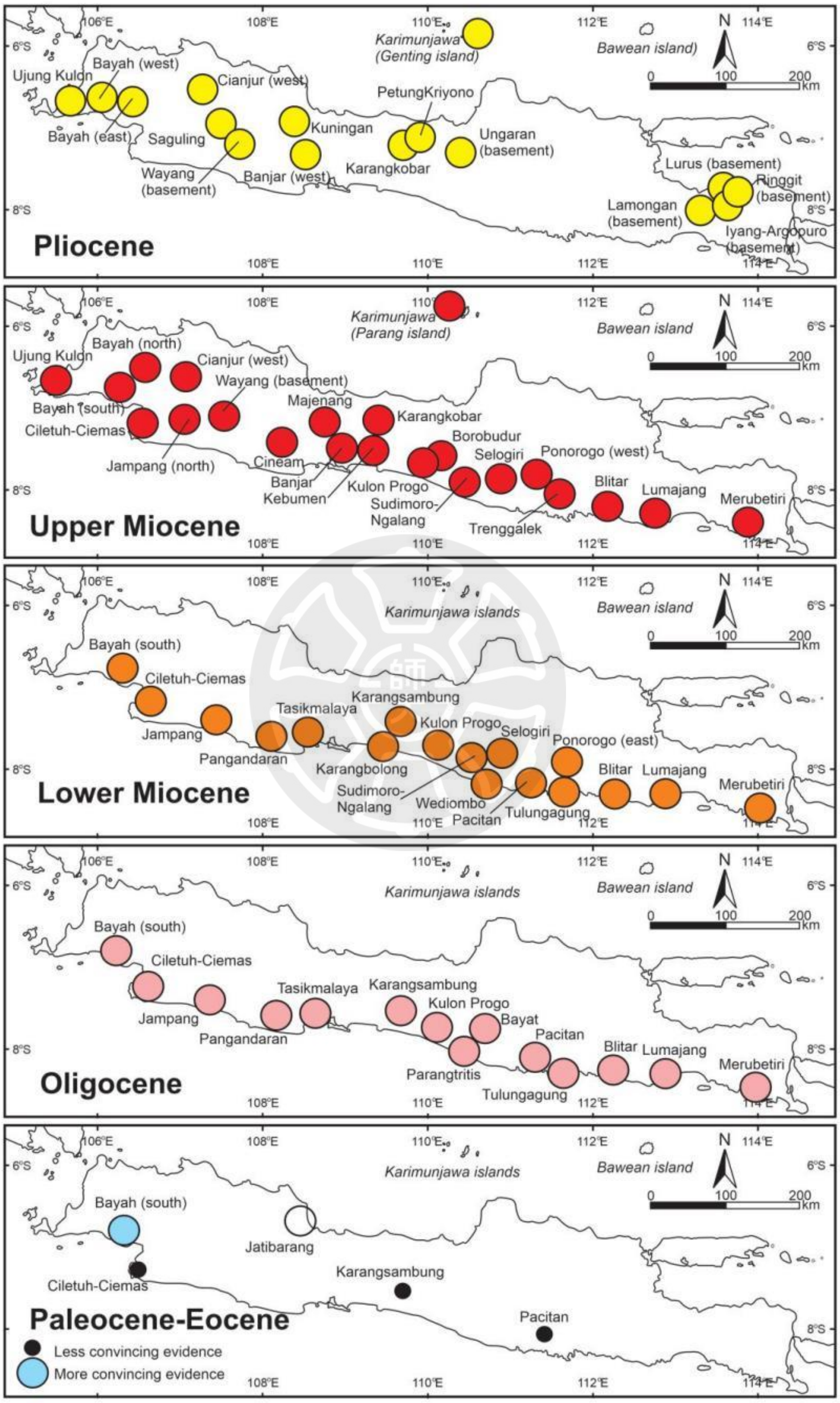

Fig. 1.3. Reconstructed Tertiary volcanic centers in Java, as modified by Setiadji et al., (2006).

1.2.3. Geochemistry and Geochronology

K- Ar ages of the magmatic rocks in Java indicate that two stages of volcanic activity can be distinguished throughout the Tertiary period (Soeria-Atmadja et al., 1994) **(Fig. 1.4)**. The earlier stage is represented by rocks from Karangsambung and Pacitan with ages of 40 Ma, and from Pacitan and Panggandaran, with ages between 19-18 Ma (Soeria-Atmadja et al., 1994). Some age data from Java include: Ciletuh, West Java (50.1 to 50.9 Ma; Pertamina-ITB, 2002); dioritic dike from Karangsambung, Central Java (37.6 Ma; Soeria-Atmadja et al., 1994); basaltic pillow lava (42.7 Ma; Soeria-Atmadja et al., 1994); and andesite intrusion (38.7 Ma; JICA-JOGMEC, 2004). In Central Java, dioritic dike from the Totogan Formation has an age of 26.5 ± 1.9 Ma (Soeria-Atmadja et al., 1994), and rocks from Kebo-Butak Formation and Kulon Progo date to 25.4-29.6 Ma (Soeria-Atmadja et al., 1994). Diorite from Bayat is dated at 33.2 ± 1.0 (Soeria-Atmadja et al., 1994), and andesite intrusive from Parangtritis Beach is dated at 26.4 to 26.55 Ma (Soeria-Atmadja et al., 1994). The Mandalika Formation dates to 33.6 Ma (Soeria-Atmadja et al., 1994), and andesite lava from Trenggalek ranges from 15.6 to 19.0 Ma (Soria-Atmadja et al, 1985). Andesite intrusive from Lumajang has an age of 23.7 ± 3.5 Ma (JICA-JOGMEC, 2004), and granodiorite from Cihara is dated at 22.4 ± 0.4 Ma (Wikarno et al., 1993). Cirotan dates to 15.3 ± 0.7 Ma (Marcoux and Milesi, 1994), while quartz andesite from Ciletuh-Ciemas and Pangandaran area is dated at 22.4 ± 1.5 Ma (Pertamina-ITB, 2002). Rocks from Kulon Progo have ages ranging from 17.0 ± 2.0 to 16.0 ± 2.2 Ma (Wikarno et al., 1993), and micro-diorite intrusion from Selogiri is dated at 21.7 ± 1.9 Ma (JICA-JOGMEC, 2004). Wonosari has and age of 19.7 ± 0.9 Ma (JICA-JOGMEC, 2004), and andesitic to basaltic intrusions from Pacitan are dated at 17.3 ± 2.0 and 19.5 ± 1.8 Ma (Saefudin, 1994), with additional dates of 18.2 ± 1.7, 20.9 ± 0.7, and 17.3 ± 1.5 Ma (JICA-JOGMEC, 2004). Ponorogo has and age of 17.1 ± 0.8 and 21.0 ± 2.6 Ma (JICA-JOGMEC, 2004), and the Karimunjawa Islands (Parang Island) are dated at 5.6 ± 0.3 and 6.5 ± 0.3 Ma (Soeria-Atmadja et al., 1985).

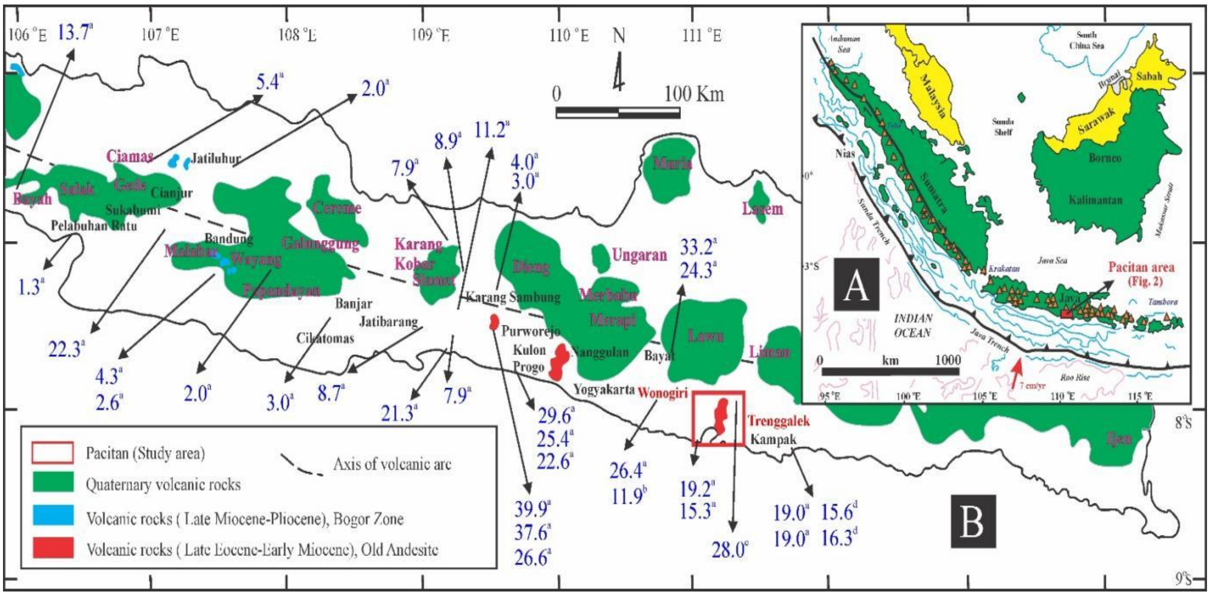

Fig. 1.4. The map of Java shows magmatic arc of Java as modified by Soeria Atmadja et al. (1994).

Table. 1.1. Ages data used K-Ar Method in Java

Location	Ages (Ma)	Method	Rocks
Karangsambung	40	K-Ar	Diorite Dike
Pacitan	19-18	K-Ar	-
Pangandaran	19-18	K-Ar	-
Kulon Progo	29.6-25.4	K-Ar	-
Bayat	33.2	K-Ar	Diorite
Parangtritis Beach	26.5	K-Ar	Andesite
Lumajang	23.7	K-Ar	Andesite
Cihara	22.4	K-Ar	Granodiorite
Cirotan	15.3	K-Ar	-
Ciletuh	22.4	K-Ar	Quartz andesite
Ciemas	22.4	K-Ar	Quartz andesite
Wonosari	19.7	K-Ar	-
Ponorogo	21.0-17.1	K-Ar	-
Karimunjawa	6.5-5.6	K-Ar	-
Kampak	19.6	K-Ar	-
Wonogiri	26.4-11.9	K-Ar	-
Banjar	3.0	K-Ar	-

1.3 Aims and Motivations

Several studies have been conducted on volcanic arcs in active volcanoes areas that have been well exposed over a long period of time, such as the Eocene to Miocene basin history and volcanic activity in East Java (Smyth, 2005), Cenozoic arc magmatism on Java (Setiadji et al., 2006), Cenozoic arc processes in Indonesia (Hall et al., 2008), Tertiary magmatic activity in southern East Java (Novianty et al., 2018), among others. One reason for the earlier research is that the products of the younger arcs included the sequences of the older arcs. In addition, many volcanic arcs in Indonesia are difficult to work with, generally not fully documented, and located in very remote locations (Hall et al., 2002). The Cenozoic stratigraphic records found in East Java provide an excellent opportunity to study the history of volcanic arc eruptions. Another important aspect to observe is the geochemical variations in volcanic arcs (Setiadji et al., 2006) and the dating of existing volcanoes. Research on the age of volcanoes in East Java has been carried out using the K-Ar method (Soeria-Atmadja et al., 1994) but it is still necessary to do research on the age of rocks in several places using different methods because in some places the complete age is not stated. Besides that, the K–Ar dating system is easily influenced by later hydrothermal alteration or weathering (Wilkinson et al. 2017). Based on the results of age determination, the volcanic arc in East Java has been active since the Eocene (Soeria-Atmadja et al., 1994; Hall et al., 2008). There is also an older southern mountain arc. The volcanic product resulting from this arc, known as "Old Andesite" (van Bemmellen, 1949), is widely recognized for its well-exposed features and prominent topography. The modern Sunda Arc began to move in its present position as far as 50 km to the north of the southern mountain arc at the end of the Middle Miocene (ca. 12-10 Ma) (Hall et al., 2008). During the Late Eocene to Early Miocene, evidence of magmatic events from pillow lava flows has been found in East Java, especially in the Pacitan area (Soeria-Atmadja et al. 1994). The geochemical composition showed an Nb anomaly and a relatively flat Rare Earth Elements (REE) pattern, and a typical Island signature. The Pacitan area is part of the Southern Mountains which is estimated to be of the Late Eocene - Early Miocene age. Hall et al. (2008) have published papers related to the stages of arc development and the sequence and timing of events within the arc, determined through field investigations, provenance analysis, and isotopic dating. However, their work is incomplete and still needs to be explained in more detailed in more detail. Besides that, the position of Pacitan, as a transition zone between the Cretaceous and Tertiary subduction pathways (Purwanto, 1997), is of particular interest, especially in relation to the geochemical processes occurring in the area. Several studies have been carried out, especially those related to geochemistry in the Pacitan area, which have produced several local papers (Sartika et al., 2009; Sutanto, 2003; Purnomo et al., 2017), but the geochemical analysis presented in several papers has not fully explained the geochemical and tectonic processes that occur in the area. Several published references explain that volcanic activity in the Pacitan area began in the Eocene, based on age dating using the K-Ar Method (Soeria-Atmadja et al., 1994; Hall et al., 2008), but some papers also state that volcanic activity of the Eocene age is only found in the Semilir, Karangsambung, and Bayat area, while in the Pacitan area volcanic activity begins from the Oligocene to Miocene (Prasetyadi et al., 2005). This situation is very confusing, so it is necessary to review the complete history of volcanic activity in the area.

To better understand the temporal and spatial succession of the Pacitan volcano, detailed petrological and geochemical studies are crucial to distinguish the key processes involved in magma evolution and to assess the significance of changes overtime and/or space (Humphreys et al., 2006; Newhall, 1979; Streck, 2008). Therefore, it is necessary to understand the petrogenesis and the processes involved in the subduction of the India-Australian oceanic crust beneath the Eurasian Plate.

Moreover, a detailed study involving zircon U-Pb dating, along with geochemical analyses including major and trace elements and isotopic measurements, of the Pacitan volcanic rocks widespread in the southern mountains needs to be conducted, as previous studies provided incomplete data. This dissertation focuses on the magmatic evolution of Pacitan, East Java, from the Late Oligocene to the Miocene, using zircon U-Pb dating. In addition, this dissertation aims to recognize the stages of arc magmatism using zircon U-Pb methods and to identify the geochemical variations associated with different stages of the Pacitan volcano, in order to better understand the magmatic and tectonic evolution of the Pacitan area in East Java. The topics discussed in this dissertation include: (1) the spatial and temporal distribution of the initial stage of volcanism in Pacitan, (2) the magma sources and petrogenesis of volcanism in Pacitan, and (3) the tectonic evolution of Pacitan, East Java.

CHAPTER 2. GEOLOGICAL BACKGROUND

2.1. Sunda Arc

Indonesia is a part of an island arc system located at the interaction zone of two or three tectonic plates (Katili 1975; Hamilton, 1979). Hamilton (1979) emphasized that the Australian Plate has moved approximately 3000 km northward relative to Asia, while the Pacific Ocean floor has shifted a similar distance westward during the Cenozoic. The Sunda Arc represents a of the convergent boundary between the Australian Plate and the Eurasian Plate, with a convergence rate of 6 to 7 cm/yr (Widiyantoro and van der Hilts, 1997). Compared to most island arcs, Java and Bali have a relatively simple tectonic setting (Hamilton, 1979). The evolution of the Indonesia archipelago has been dominated by an evolving island arc since the Late Paleozoic (Katili 1975; Hutchison, 1982). These fossil arcs are now preserved as linear volcano-plutonic complexes and associated sedimentary deposits. The age of these complexes decreases from the Late Paleozoic in Sumatra to the Late Tertiary in the Banda Arc (Barber, 2000). The current arc system became a unified structure during the Middle Tertiary (Soeria-Atmadja and Noeradi, 2005). The pre-Middle Tertiary evolution of the eastern Sunda and Banda Arcs appears linked to the adjacent Australian continent, whereas the western Sunda Arc unrelated (Soeria-Atmadja and Noeradi, 2005).

The Sunda Arc is one of four major volcanic in Indonesia, collectively containing around 80% of the country’s active volcanoes. It includes the Andaman Islands, Sumatra, Java, and the Lesser Sunda Islands, and is situated at the plate boundaries between the Eurasian Plates, the India-Australian Plate, and the Pacific Plate (Hall and Smyth, 2008). Subduction the Java trench has been continuous since the Middle Eocene (~45 Ma) due to the northward movement of the India-Australian Plate beneath the Eurasian Plate at ~6 cm/yr (Tregoning et al., 1994; Hall, 2002) **(Fig. 2.1)**. Beneath Sumatra, subduction is oblique, and the poorly constrained Benioff zones can only be traced to depths of ~ 200 km (Curray, 1989). The curvature of the margin especially near the Sunda strait, result in strong strain partitioning dextral shear Sumatra and neutral, to potentially sinistral, shear through Java and Southeast Nusa (McCaffrey, 1996). The dip of the slab remains relatively constant from the Sunda strait (~9°) to the Australian collision zone (Syracuse and Abers, 2006), although tomographic imaging suggests the presence of a slab beneath East Java. In contrast, subduction beneath Java is nearly orthogonal, and the seismic zone extends to depths exceeding 600 km. The north-dipping slab steepens to about 60° at depths greater than 100 km (Whitford, 1979; Curray, 1989). The eastern Sunda Arc has been in collision with the Australian margin since around 3 Ma. And the arc reached its current configuration by approximately 5 Ma, although active volcanic arc likely began in the Eocene (Katili, 1975; Hamilton, 1979). Quaternary volcanoes typically overlie Late Miocene to Pliocene volcanic rocks and sediments (Soeria-Atmadja and Noeradi, 2005). The magmatic arc is the most prominent feature of the island arc system. The Sunda Arc is considered a classic example of volcanic arc. The magmatic processes that produced the current subduction configuration, volcanism, and foreland basins in Java and Sumatra have been active since the Oligocene to Miocene (Katili, 1975; Hamilton, 1979). Additionally, the deformation of rocks (folding and faulting) and the distribution of volcanoes along the Sunda Arc appear closely related to major fault system (van Bemmellen, 1949).

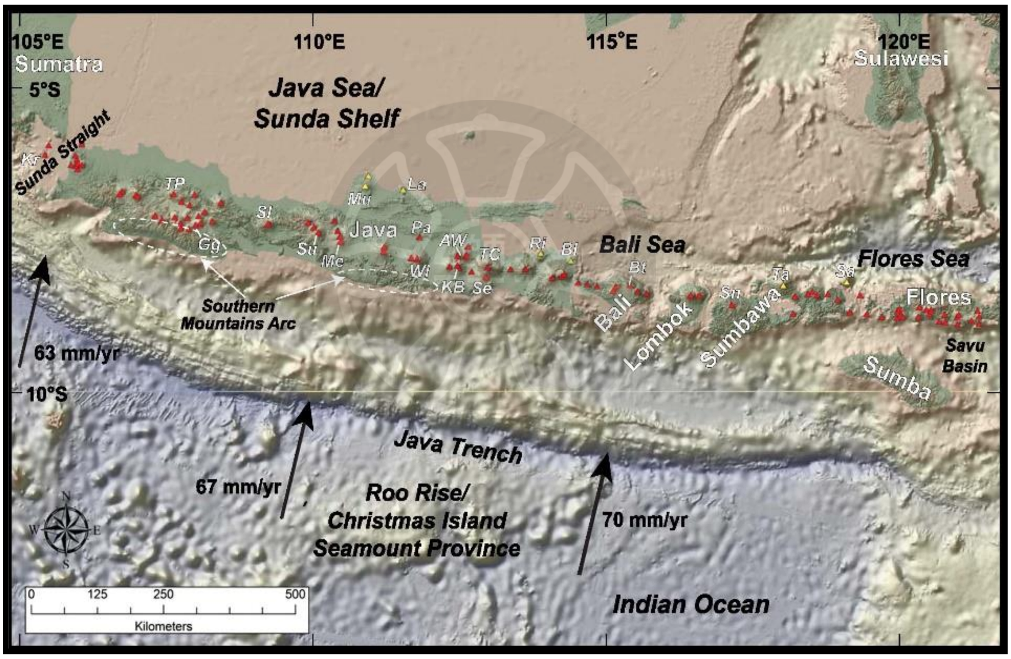

Fig. 2.1. The relief of the central Sunda Arc, derived from topographic data (Pacey et al, 2013), reflects the ongoing subduction at the Java Trench since the mid-Eocene (~45 Ma), driven by the northward propagation of the India-Australian Plate beneath the Eurasian Plate at a rate of ~6 cm/yr (Tregoning et al., 1994; Hall, 2002).

2.2. Java

Java an island of the Sunda Arc, hosts at least 50 volcanoes and is commonly divided into three provinces: West Java, Central Java, and East Java (van Bemmellen, 1949) **(Fig. 2.2)**. Most volcanic centers exhibit a calc-alkaline composition, predominantly consisting of pyroxene andesite with minor occurrences of dacite and basalt (Hutchison, 1982). The Quaternary volcanoes are constructed upon the eroded surface of Java's uplifted Miocene basement (van Bemmellen, 1949). This uplift likely fractured into an east–west-trending graben-like depression, forming an intra-arc basin bounded by fault systems between the Northern and Southern Mountain volcanic chains (van Bemmellen, 1949).

Based on topographic chronology, Cenozoic volcanic products can be subdivided into two categories: young volcanics and old volcanics (van Bemmellen, 1949). Young volcanic terrains are characterized by smooth surfaces that gently slope away from eruption centers, as erosion has yet to significantly modify them. In contrast, older volcanic surfaces are heavily dissected. Correlating topography with K-Ar dating of the lava flows, the young volcanics are assigned to the Upper Pleistocene, while the older volcanics date back to the Lower to Middle Pleistocene (van Bemmellen, 1949).

Java is included primarily for completeness in regional tectonic reconstructions and is interpreted to have undergone a ~30° counter-clockwise rotation between approximately 20 Ma and 10 Ma. This rotation represents a compromise between the estimated rotations of Sumatra and southern Borneo. While there is no significant evidence for major extension in the Java Sea during this period (e.g., Bishop, 1980; van der Weerd and Armin, 1992), a rigid rotation of Java with southern Borneo would result in excessive overlap between Java and Sumatra. The differential rotation between southern Borneo and Java suggests limited extension and likely strike-slip faulting in the East Java Sea during this time interval. Because the rotation pole lies near the Borneo, Java, and North Sumatra blocks, there is minimal change in their relative positions; however, some overlap between Java and Sumatra persists (Hall, 1996). This could be explained by arc-parallel extension, as both Java and Sumatra may have been narrower than their current outlines, consistent with the extensional evolution of Neogene sedimentary basins in Sumatra and the volume of Neogene volcanic arc. This counter-clockwise rotation constrains the likely orientation of the pre-Middle Miocene subduction zone south of Sumatra and Java, which was more NW–SE oriented compared to its present-day trend. The rotation has significant implications for the tectonic evolution of Java, including the development of oblique subduction and associated strike-slip deformation, as well as the timing of volcanic activity. The model predicts major changes in tectonic and volcanic regimes around ~20 Ma for both Java and Sumatra. Additionally, the eastern extension of the subduction boundary south of Java appears to have shifted into a tectonic linkage with the Pacific realm (Hall, 1996).

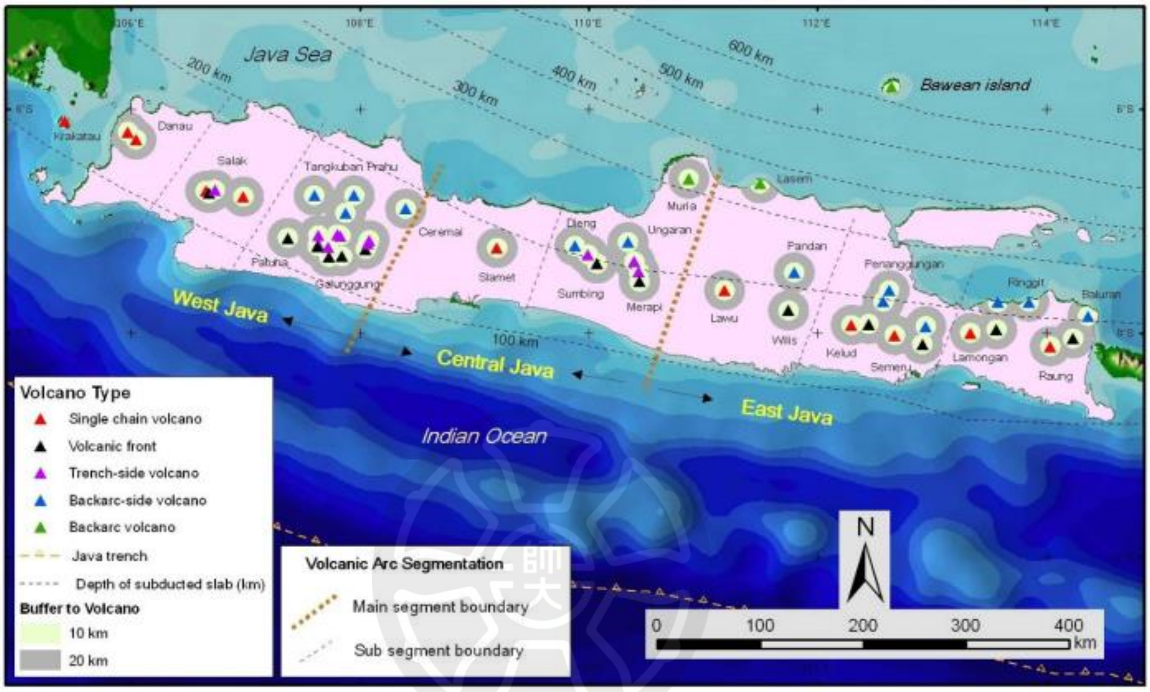

Fig. 2.2. Java hosts at least 50 volcanoes and is divided into three provinces: West Java, Central Java, and East Java. The classification of volcanoes in this study follows the framework proposed by Tatsumi and Eggins (1995).

2.2.1. Tectonic Evolution Near the Java

The tectonic processes that shaped the Sunda Arc have been active since the Eocene (Garwin et al., 2005; Hall, 2002; Hamilton, 1977). These processes are primarily driven by the subduction of the Indian-Australian oceanic crust beneath the southern margin of the Eurasian Plate, resulting in the formation of a magmatic arc that includes the Cenozoic volcanoes of Java (Setiadji et al., 2006).

- ca. 45 Ma (Middle Eocene)

Around 45 Ma, Australia began a rapid northward movement. During this time, Australia and India had already merged into a single plate, which possibly reflects the initial collision between India and Asia. Alternatively, this movement may have been triggered by changes in plate motions within the Pacific region. Significant tectonic activity occurred in the western Pacific, including arc-continent collisions in New Guinea and the formation of marginal basins such as the Celebes Sea and the Philippine Sea (Hall et al., 2009). Subduction resumed at this time (Smyth et al., 2008; Hall et al., 2009; Husein et al., 2015), giving rise to the volcanic arc in the Southern Mountains, extending along Java (Husein et al., 2015). Between the Eocene and Oligocene, the position of this volcanic arc remained relatively stable **(Fig. 2.3)**. The subduction of the Indian-Australian Plate beneath Sundaland was accompanied by significant volcanic activity (Smyth et al., 2008).

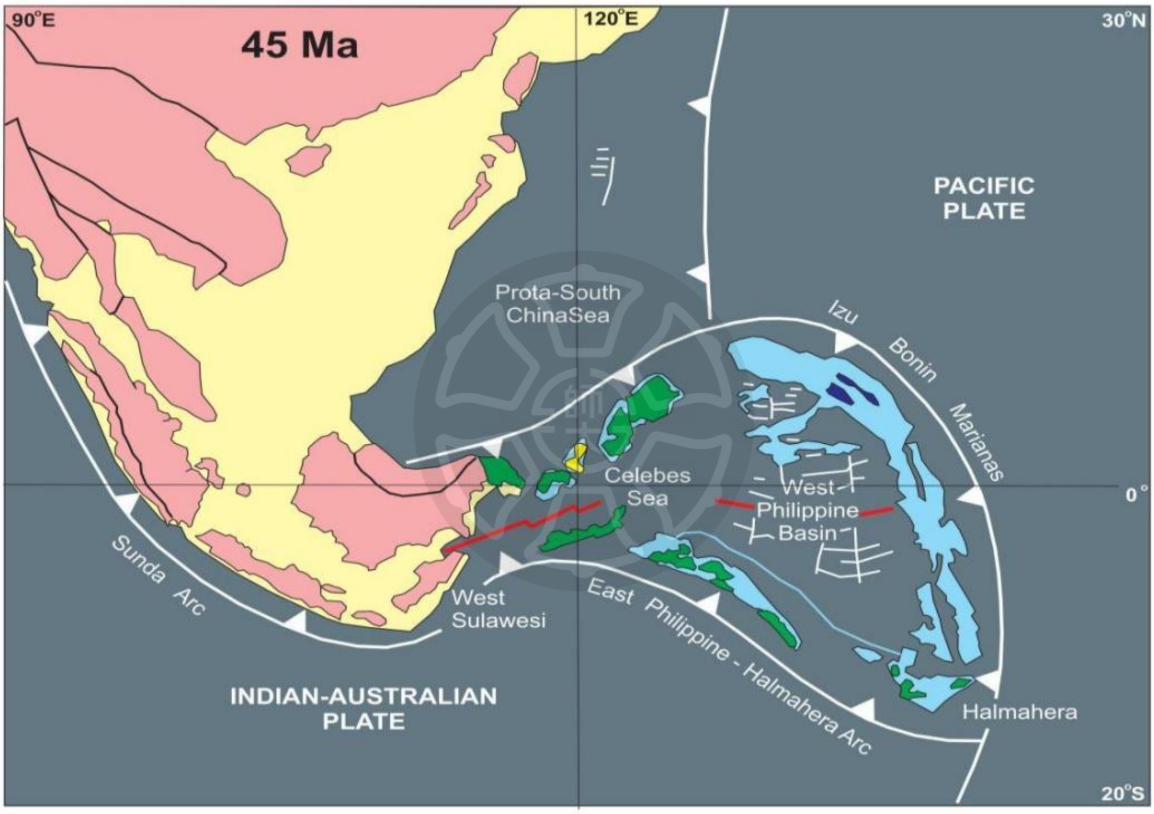

Fig. 2.3. Tectonic reconstruction at ~45 Ma showing the initiation of renewed subduction at the southern edge of Sundaland due to northward motion of the Australian Plate (modified from Hall et al., 2019; Husein et al., 2015).

- ca. 25 Ma (Late Oligocene)

By the Late Oligocene to Early Miocene (~25 Ma), the northern tip of the Australian Plate (Sula Spur) collided with the North Sulawesi Arc (Hall, 1998; Husein et al., 2015). This collision triggered a counter-clockwise rotation of the Sundaland block. Concurrently, the East Java microcontinent began rotating clockwise, closing its former subduction trench with

Sundaland and forming the Kendeng Basin above a remnant oceanic crust. This tectonic reconfiguration created a transform fault to accommodate the relative westward motion of East Java, eventually developing into the Progo-Muria Fault. Paleomagnetic data suggest that the East Java microcontinent was near its current position by this time (Mahfi, 1984; Ngkoimani et al., 2006). A reversal in subduction polarity may have occurred, initiating northward subduction along the southern margin of the East Java microcontinent **(Fig. 2.4).**

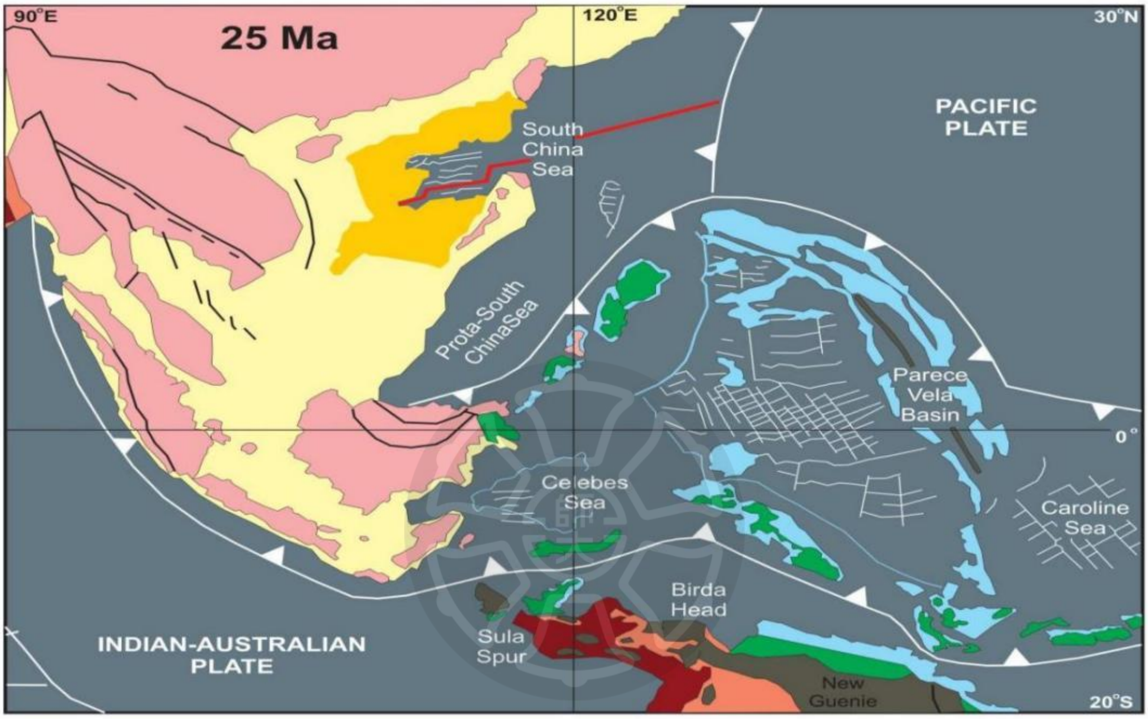

Fig. 2.4. Tectonic reconstruction at ~25 Ma showing the Sula Spur collision with the North Sulawesi Arc and onset of rotations and faulting in East Java (modified from Hall, 1998; Husein et al., 2015).

- ca. 15 Ma (Early Miocene)

By ~15 Ma, oceanic crust reached the Java Trench, and the trench began propagating eastward along the continent-ocean boundary at the northern edge of the embayment. The remaining oceanic lithosphere subducted into the mantle, and the subduction hinge rolled back into the embayment (Hall et al., 2009). This rollback led to significant extension in the Australia–Southeast Asia convergence zone, initiating in Sulawesi and propagating eastward, which contributed to the complex tectonic configuration of the modern Banda Arc. During the Early Miocene, volcanic activity decreased from Java to Sulawesi, although subduction of the Indian-Australian Plate continued. The counter-clockwise rotation of Sundaland caused northward migration of the Sunda subduction hinge, affecting the tectonics of Kalimantan to Java. Some researchers argue that this rotation halted magmatic activity due to the lack of fresh material feeding the mantle wedge (Macpherson and Hall, 1999, 2002). Others suggest that slab rollback in East Java and the onset of rollback in the Banda Arc drove continued tectono-magmatic evolution (Husein et al., 2015; Hall et al., 2009) **(Fig. 2.5)**.

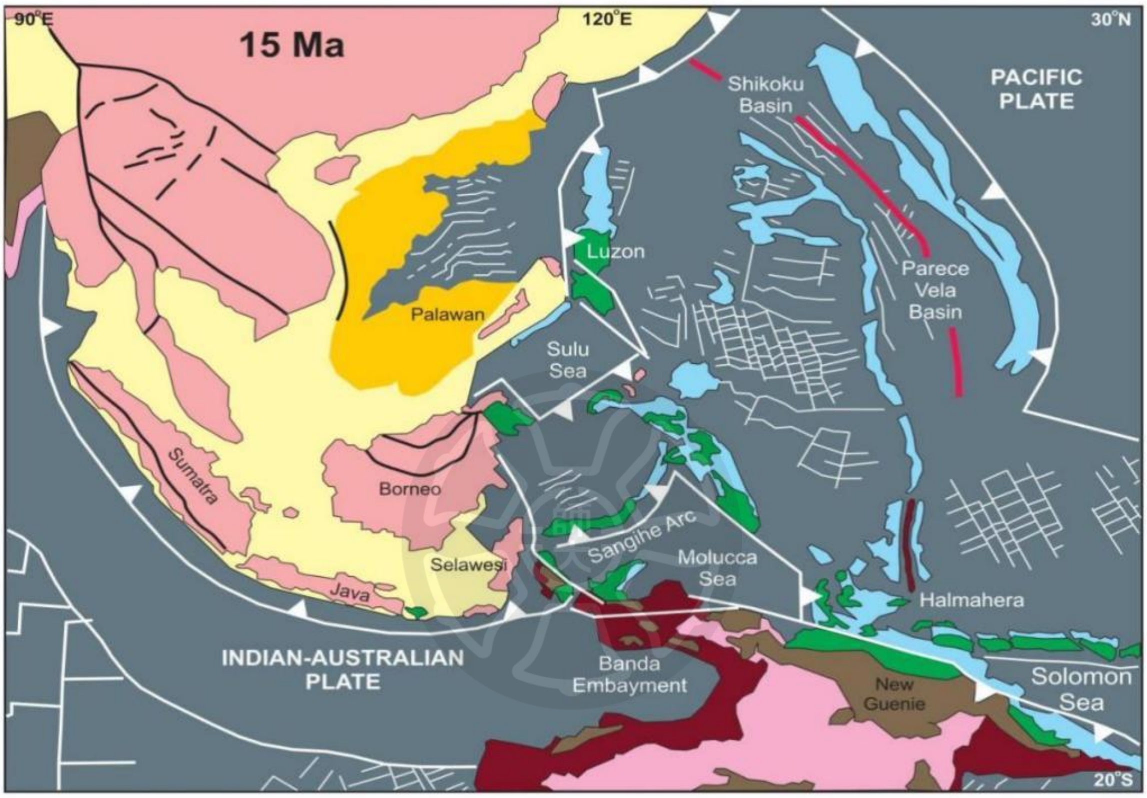

Fig. 2.5. Tectonic reconstruction at ~15 Ma illustrating slab rollback and trench propagation in the Java region (Hall et al., 2009).

During the Paleogene, magmatic activity in the northern arc of the Sunda region began to intensify, marking the onset of the modern arc system. Throughout the Cenozoic, Java evolved into a chain of volcanic islands formed in response to the subduction of the Indian-Australian oceanic plate beneath the Eurasian Plate. Most subduction zones in the region are characterized by slab rollback, a process that plays a central role in arc development and is often accompanied by significant volcanic arc (Hall, 1996, 2002; Macpherson and Hall, 1999). The Sunda Arc, particularly during the Oligocene (~25 Ma), provides a clear example of this geodynamic behavior. In East Java, volcanic activity intensified during the Paleogene, with a notable but brief explosive phase (Smyth et al., 2005), followed by a decline in surface activity, although magmatic processes continued until approximately 12–10 Ma. Volcanism in the Southern Mountains of East Java ceased in the Early Miocene after a prolonged activity period of over 20 million years. Around 12–10 Ma, a new volcanic arc emerged approximately 50 km north of the older arc, occupying a parallel trend and representing a reorganization of the magmatic system (Smyth et al., 2005).

Near the Java Trench, young accretionary complexes developed over older structural backstops, including relict accretionary complexes from earlier tectonic phases (Kopp et al., 2002, 2006; Schlüter et al., 2002). In southern Java, subduction erosion was active during the Paleocene, further shaping the margin (Kopp et al., 2006). Despite Java and Sumatra both lying along the southern margin of the Sunda Microplate and being influenced by convergence between the Indian-Australian and Eurasian Plates, their tectonic histories diverge significantly. This divergence results primarily from differences in the convergence direction: in Java, the subduction of the Indian-Australian Plate occurs at a nearly perpendicular angle to the Sunda margin, whereas in Sumatra it is oblique. The geodynamic framework of Java is influenced by several key tectonic features: (1) A Cretaceous magmatic belt located in the northern part of the island, indicating earlier subduction activity; (2) A magmatic arc, which extends across the southern portion of the island and reflects more recent volcanic activity; (3) A Tertiary subduction zone associated with an underwater ridge located south of Java; (4) A deep-sea trough south of the island, which marks the current subduction boundary where the Indian-Australian oceanic crust descends beneath Java.

2.2.2. Subduction Systems Near the Java

The Sunda Arc extends from Sumatra to Flores and exhibits typical features of a subduction-related volcanic arc. Seismic tomography studies reveal the presence of low P-wave velocity zones at depth, aligned with the subducting Australian Plate and reaching directly beneath the volcanic arc, indicating active magma generation processes (Puspito and Shimasaki, 1995; Widyantoro and van der Hilst, 1996, 1997). In the eastern part of the Sunda Arc, the interaction becomes more complex due to the incorporation of continental crust and crustal fragments carried by the Australian Plate. The entire volcanic arc spans approximately 6000 km, from northern Sumatra to the Molucca Sea, and can be subdivided (from west to east) into: (1) The Sumatra cordilleran sector, (2) The enzymatic Sunda Arc from Java to Flores, (3) The convoluted Banda Arc, and (4) The Molucca Sea collision complex. The

Indian Ocean crust is being subducted nearly perpendicularly beneath Java, while oblique subduction occurs beneath Sumatra (Hamilton, 1979). The Australian Plate moves northward toward Southeast Asia, and the subduction beneath Java is characterized by direct interaction with the oceanic lithosphere at the Wadati-Benioff zone, resulting in intense volcanic activity. Seismicity in the Java region reaches depths of up to ~600 km beneath the Java Sea **(Fig. 2.6)** (Hamilton, 1979; Ghose et al., 1990; Puspito and Shimasaki, 1995; Widyantoro and van der Hilst, 1996, 1997). The subducting Indian Ocean crust ages progressively eastward along the arc, from approximately 130–135 Ma south of Java (Widyantoro and van der Hilst, 1996). Crust beneath the Java Trench is considered to consist of cold Indian Ocean lithosphere aged between 80 and 140 Ma (Whitford, 1975; Cloetingh and Wortel, 1986; Packham, 1996). During the Early Tertiary, the oceanic floor south of Java comprised a mix of Mesozoic Indian Plate lithosphere in the west, Jurassic Australian Plate lithosphere in the east, and mid-ocean ridge basalts (MORB) formed between the Late Cretaceous and Early Tertiary. From the Cretaceous onward, divergence between the Indian-Australian Plates initiated the opening of the Indian Ocean and the closure of the Tethyan Ocean (Hall, 1996, 2002). By the Early Eocene (~50–40 Ma), the Indian and Australian Plates were still distinct, with N–S spreading centers directed northward. After ~45 Ma, the rate of motion of the Indian Plate declined, and the Australian Plate became a unified tectonic entity (Hall, 2002).

Despite being part of the same tectonic margin, the eastern Sunda subduction boundary-particularly from Central Java to Sumba Island-remains under-researched. This area still represents an active subduction zone. The Sunda margin, as a classic accretionary prism, exhibits erosional subduction characteristics along the Central Java sector, with tectonic erosion being the dominant mechanism of mass transfer. The geology of Java is complex, shaped by the interaction of basin formation, faulting, folding, and volcanism-driven by varying stress regimes (Katili, 1975) **(Fig. 2.7a)**. Three principal structural trends are observed: (1) Northeast–Southwest (NE–SW), known as the Meratus pattern; (2) North–South (N–S), referred to as the Sunda pattern; (3) East–West (E–W) directions. The key tectonic transformation occurred when the subduction direction shifted from NE–SW during the Cretaceous to a more E–W trend since the Oligocene. This shift resulted in the highly intricate Tertiary geological architecture of Java. These complexities are evident across the island: (1) In the western part, the Meratus pattern is represented by structures such as the Cimandiri Fault; (2) In the central region, it is expressed in the distribution of pre-Tertiary rock outcrops in the Karangsambung area; (3) In the eastern part, structural features such as the Pati Basin fault, the Florence fault, and the Central Deep are notable. The Tuban Basin shows structural highs like the Karimun Jawa Ridge, Bawean High, and Masalembo High, which also align with the Meratus trend. In contrast, the Sunda (N–S) pattern becomes more dominant in western Java.

The Sunda pattern generally consists of strain structures. The Meratus pattern is the oldest, based on stratigraphic and tectonic data. The faults included in this pattern date from the Cretaceous to the Paleocene and are scattered across the high Karimun of Java, from Karangsambung to the Cimandiri area in West Java. These faults were reactivated by younger tectonic activity (van Bemmellen, 1970). The Sunda pattern is younger than the Meratus pattern. Seismic data show that the Sunda pattern reactivated Meratus-patterned faults during the Late Eocene to Late Oligocene. The Java pattern represents the youngest structural trend and reactivates all existing patterns (Pulunggono, 1994). A subduction zone was formed in the Late Cretaceous in the Karangsambung region and extended to the Meratus Mountains in Borneo. This zone formed a structure with a northeast–southwest orientation (Hall, 2017). During the Tertiary, this pattern shifted, placing the subduction zone south of Java. In this phase, the structural orientation changed to an east–west direction. The collision between the Asian Plate and the Australian Plate produced a principal compressive stress-oriented north–south. This stress generated an oblique wrench fault pattern trending northwest–southeast, which roughly aligns with the final mountain trend of the Cretaceous. During the Pliocene–Pleistocene period, the principal stress direction remained north–south. Tectonic activity during this time produced a fault and fold pattern trending east–west, which is observed in the Kendeng Zone. Differences among West Java, Central Java, and East Java arise from older tectonic influences that control the bedrock structures, as well as from more recent regional tectonic developments. According to van Bemmellen (1949), the Northeast Java Basin experienced two uplifts in the Miocene and Plio-Pleistocene periods which formed the anticlinorium and associated faults. Meanwhile, Samuel and Genevraye (1972) suggested that the first uplift of the Kendeng Anticline occurred in the Late Pliocene. This uplift was accompanied by the development of faults and folds trending east–west, parallel to the axis of Java (Sitomorang, 1976) **(Fig. 2.7)**.

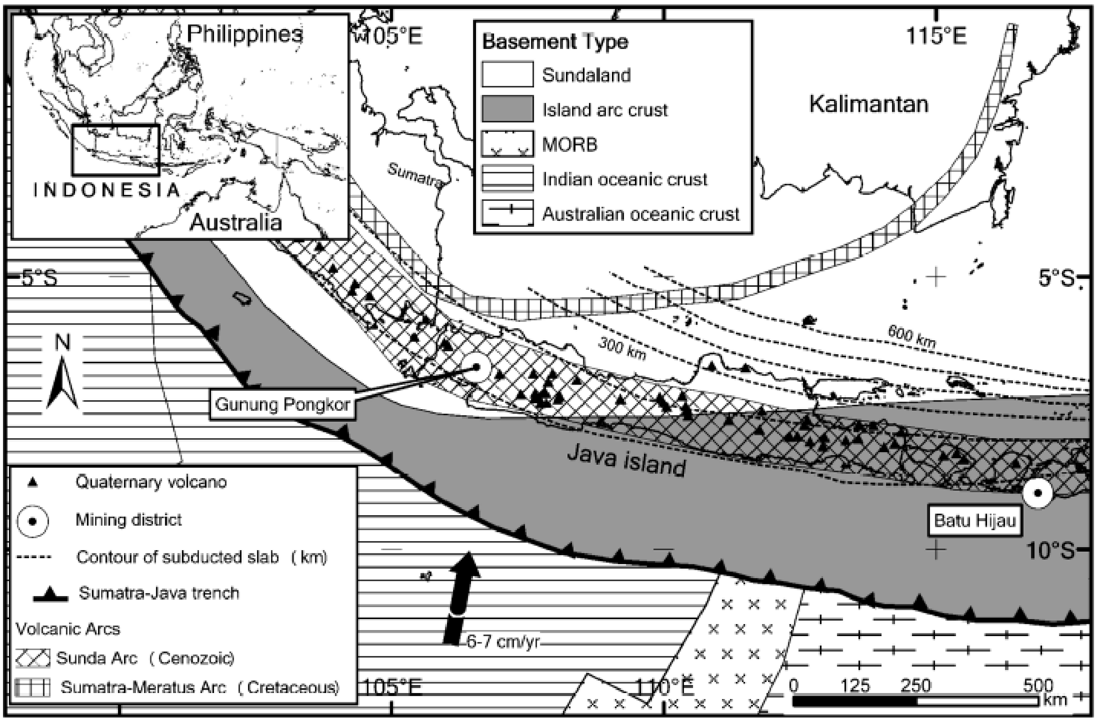

Fig. 2.6. Geologic framework of Java, shows the contour of subduction zone depth (Hamilton, 1979).

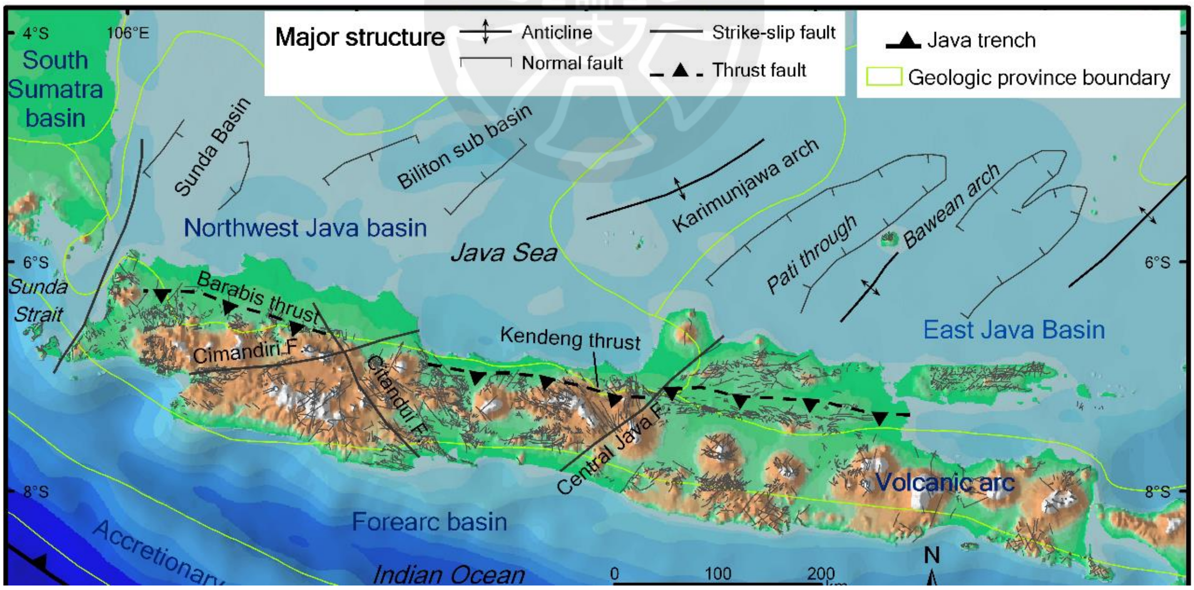

Fig. 2.7. (a) Major geologic structures of Java, compiled from Katili (1975), Hamilton (1979), and Simandjuntak and Barber (1996).

2.3. East Java

Based on structural and stratigraphic characteristics, East Java can be divided into four zones: (1) the Rembang zone, (2) the Kendeng basin, (3) the Modern Arc, and (4) the Southern Mountains Arc (after van Bemmellen, 1949; Smyth et al., 2008) **(Fig. 2.8)**.

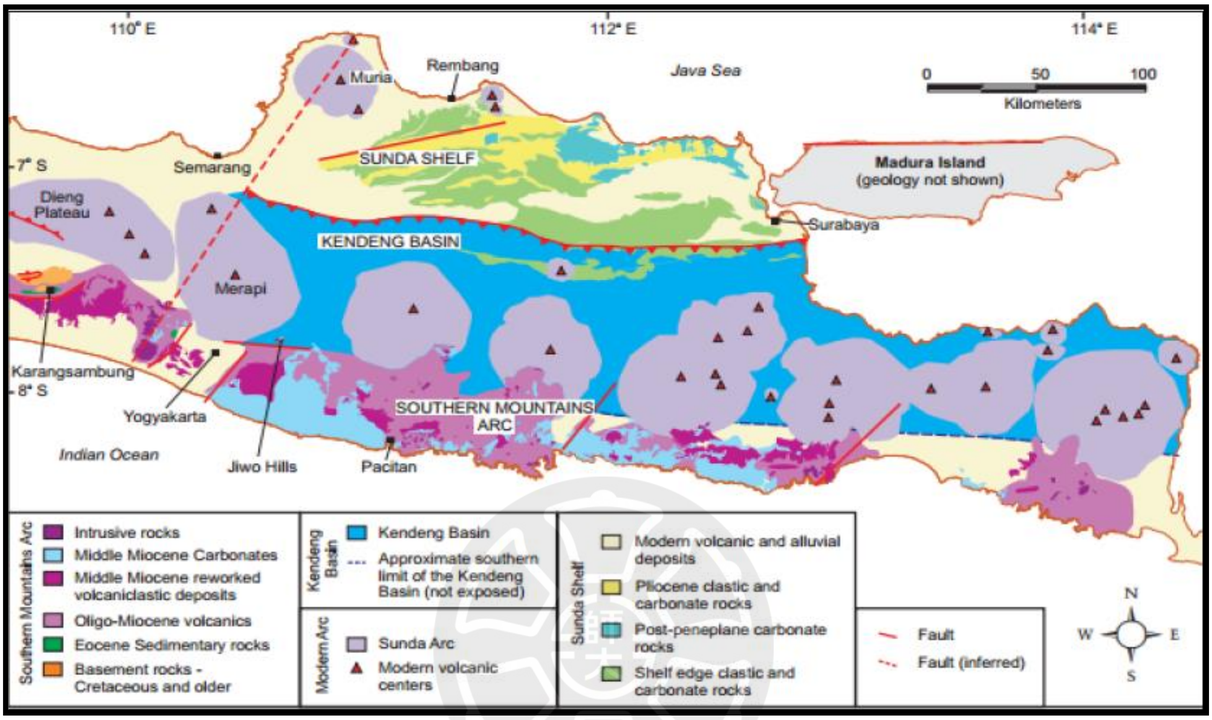

Fig. 2.8. Geological subdivisions of East Java, including the Rembang Zone, Kendeng Basin, Modern Arc, and Southern Mountains Arc (after van Bemmellen, 1949; Smyth et al., 2008).

2.3.1. Rembang Zone

The Rembang Zone is located in the northernmost part of East Java, stretching from the Muria-Progo line in the west to Madura Island in the east (Smyth, 2005). This zone consists of marine sediments and clastic carbonates, which are strongly influenced by faulting. It is estimated to be of Cenozoic age (Smyth et al., 2005, 2008). Pliocene-Pleistocene volcanoes, such as those in the Muria and Lassem areas, are present in this zone. The magma composition along the arc axis is characterized by leucite, with volcanic activity extending 150 km further east-northeast on Bawean Island (Leterrier et al., 1990). The stratigraphy of the Rembang Zone primarily follows the work of Pringgoprawiro (1983). The pre-Tertiary basement rock consists of accretionary wedges made up of gabbro, ophiolites, metamorphic rocks, metavolcanic rocks, and Cretaceous sediments, including lithified sequences of sandstone, shale, and some chert. The zone includes several formations (Smyth et al., 2008), such as the Ngimbang, Kujung, Prupuh, Tuban, Ngrayong, Bulu, Wonocolo, Ledok, Mundu, Lidah, and Paciran formations **(Fig. 2.9).**

2.3.2. Kendeng Zone

The Kendeng Zone is located south of the Rembang Zone and north of the Quaternary volcanic arc. This zone consists of basins filled with volcanic material originating from the Southern Mountains and Modern Arcs. The basin deposits are poorly exposed and consist of Eocene and Miocene sediments, up to 8000 m thick, which record the deepening of the basin over time due to the progressive loading of the volcanic arc (de Genevraye and Samuel, 1972; Smyth, 2005; Waltham et al., 2008). Tectonic deformation is more intense in the western part, becoming weaker to the east. In the central part, this anticlinorium was intruded by the Pandan Volcano during the Early Pleistocene (Lunt et al., 1998). As the fold patterns around the volcano have been symmetrically deflected, it is assumed that Kendeng deformation took place concurrently with Pandan volcanism, around the Late Pliocene to Early Pleistocene. As the rock formation is dominated by soft, fine-grained marine sediments, erosional processes are intense and have reversed the existing morphology, such as anticlinal valleys and synclinal hills. This zone consists of several formations (Smyth et al., 2008), including the Palang, Kerek, Kalibeng, Pucangan, Kabuh, and Notopuro formations.

2.3.3. The Modern Volcanic Arc

The Modern Volcanic Arc consists exclusively of Quaternary volcanoes located above the Kendeng Zone. The distance between volcanoes along the rest of East Java is approximately 25 km. Setiadji (2010) showed that the reduced volcanic activity is associated with a prominent low heat flow area, terminated by the Baribis thrust between the Kendeng and Rembang Zones. The Rembang Zone is composed of several anticlinoria aligned in an east-west direction, stretching from Purwodadi to Madura Island. It is further divided into the North Rembang Anticlinorium and South Rembang Anticlinorium, also known as the Cepu Anticlinorium (Bemmellen, 1949). These two anticlinoria are separated by the Lusi River in the west and the Kening River in the east. Anticlines are the main structural traps in hydrocarbon exploration in the region. Folds in the Rembang Zone are arranged in a left-stepping echelon pattern, controlled by several ENE-WSW sinistral basement faults with small lateral slip (Husein et al., 2015). This pattern is evident in the North Rembang

Anticlinorium, from the Dokoro fold to the Lodan fold, and in the South Rembang Anticlinorium, which stretches from the Jamprong fold to the Gabusan fold. Arc activity commenced in its present position around 10 Ma in the Late Miocene (Soeria-Atmadja et al., 1994). The volcanoes exceed 3000 m in elevation and form the central spine of the island. The average composition of present-day volcanic products is basaltic andesite (Nicholls et al., 1980), which is much more basic than the composition of the Southern Mountains Arc products. Most of the active volcanoes are situated about 100 km above the subduction slab (England et al., 2004). There are also a number of unusual K-rich back-arc volcanoes (Edwards et al., 1991), including Muria.

Fig. 2.9. Summary stratigraphy chart of East Java (Smyth et al., 2008).

2.3.4. The Southern Mountains

The Southern Mountains are the southernmost province in East Java, with a volcanic arc ranging from Eocene to Miocene in age (Smyth et al., 2008). This volcanic arc is located approximately 50 km south of the Modern Arc (Hall et al., 2007; Clements et al., 2009). During the Oligocene to Miocene, volcanoclastic deposits indicate a cessation of volcanism associated with explosive eruptions that had an intermediate and acidic magma composition. Acidic magmatism is widespread from old crustal sources (Bergman et al., 1996; Polve et al., 1997; Polve et al., 2001). Hall et al. (2009) and Hall and Sevastjanova (2012) interpret that the deep crust in East Java and West Sulawesi is part of the same continental block (the Argo block), which split from the edge of the Australian continent during the Jurassic. This model is supported by deep basement structures in Indonesia and northwest Australia (Granath et al., 2011; Hall, 2011) and zircon populations from east Java, west Sulawesi, and northwest Australia (Smyth et al., 2007; van Leeuwen et al., 2007; Southgate et al., 2011). However, there is less evidence of such continental material outside the Southern Mountains in East Java. The Southern Mountains of East Java occupy the southern part of the eastern Java, aligned in an ESE-WNW trend from Parangtritis in Yogyakarta to Ujung Purwo in Banyuwangi. It is an Eocene to Middle Miocene volcano-sedimentary basin that is conformably overlaid by Middle Miocene to Pliocene limestone. Later, it was uplifted and block-faulted, causing the formation to gently dip to the south (Husein and Srijono, 2007). The western part of the Southern Mountains was studied in detail by van Bemmellen (1949) and is divided into three geomorphic units. The southern part is characterized by karst topography, dominated by conical hills, and is known as the "region of a thousand hills," bounded directly by the Indian Ocean. To the north of the Sewu Mountains lies a circular flat terrain known as the Wonosari Plateau. The northern part consists of remnants of volcanic, known as the Batur Agung Ridge, which is bounded to the north by the Solo Zone. The stratigraphy of the Southern Mountains has been compiled by numerous researchers (van Bemmellen, 1949; Sumosusastro, 1956; Surono et al., 1992). The metamorphic rocks, as the oldest rock unit exposed in the Jiwo Hills, consist of phyllites, mica schists, calc-silicate schists, and marble. Bothé (1929) found Orbitulina in a boulder of schist, suggesting this unit formed during the Late Cretaceous to Paleocene. Epidote-glaucophane schists were also found adjacent to serpentinite. Some Eocene carbonates were metamorphosed into garnet-wollastonite skarn due to diabase intrusion. The Southern Mountains consist of several formations (Smyth et al., 2008), including the Wungkal-Gamping, Kebo-Butak, Semilir, Nglanggran, Sambipitu, Oyo, Wonosari, Kepek, and Quaternary deposits. The Quaternary deposits are composed of fluvio-volcanic sediments from the Merapi Volcano since the Pleistocene to the present. Based on this limited evidence, the basement has been interpreted to be arc and ophiolitic rocks of Cretaceous age. A volcanic arc developed on these basement rocks from the Middle Eocene to the Miocene in Southern Java (Smyth, 2005), extending from East Java into West Java (Soeria-Atmadja et al., 1994). Volcanic activity in the Southern Mountains Arc from the Late Oligocene to Early Miocene was extensive, explosive, and intermediate in composition, with acidic magma. The deposits range from andesite to rhyolite, with an average SiO_2 content of 67 wt.% (Smyth, 2005), and include thick mantling tuffs, crystal-rich tuffs, block-and-ash flows, pumice-lithic breccia, andesitic breccia, silicic lava domes, and lava flows. The Oligocene–Miocene volcanic centers can be mapped (Smyth, 2005) by the occurrence of vent-proximal facies. At least 13 centers are presently exposed, which show a similar spacing to the volcanoes of the present-day arc **(Fig. 2.10)**. The thickness of the proximal volcanic deposite ranges from 250 to over 2000 meters.

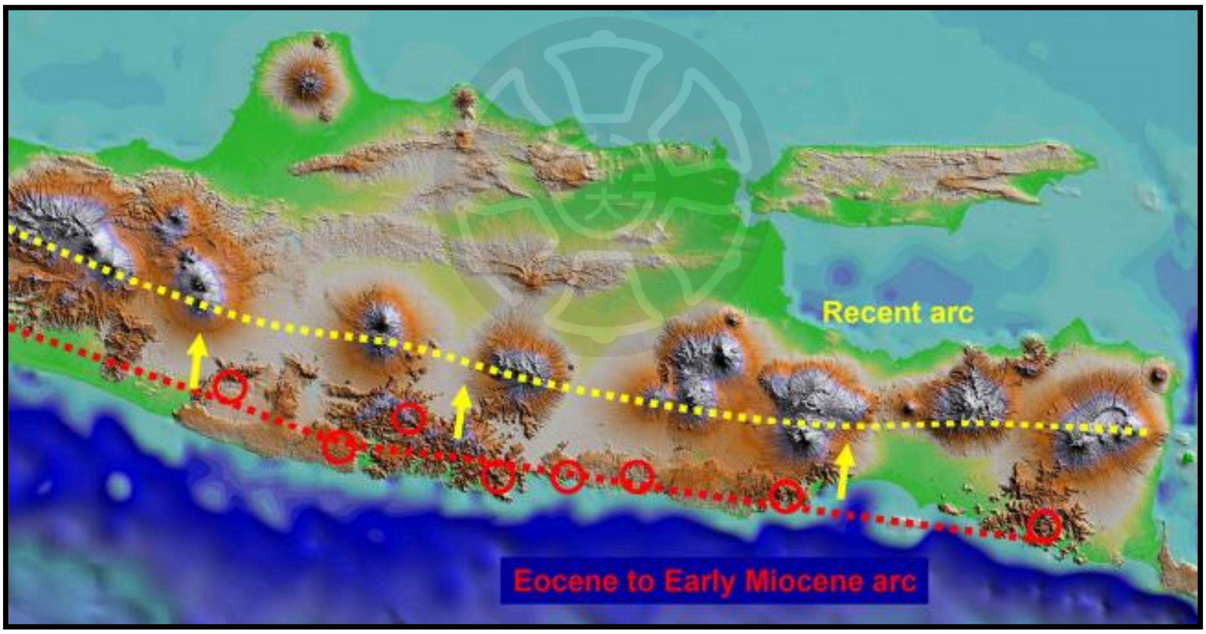

Fig. 2.10. Map of the Southern Mountains from Central Java to East Java, showing at least 13 centers that are presently exposed, which have a similar spacing to the volcanoes of the present-day arc (Smyth et al., 2008).

2.3.5. Pacitan

Pacitan is a transition zone between the Cretaceous and Tertiary subduction zones (Purwanto, 1997) and has a large number of faults compared to other areas on the island of Java. The Grindulu Fault is one of the faults that formed during the Quaternary period and is a continental plate fault line that forms the island of Java. This fault is oriented northeast-southwest and is located in the southern part of the island of Java. The Pacitan area consists of several formations, arranged from oldest to youngest, including Igneous rocks, Mandalika Formation, Watupatok Formation, Arjosari Formation, Semilir Formation, Campurdarat Formation, Jaten Formation, Wuni Formation, Nampol Formation, Oyo Formation, Wonosari Formation, Kalipucang Formation, and alluvium **(Fig. 2.11)**. These formations range in age from the Oligocene to the Quaternary (Samodra et al., 1992). The oldest volcanic rocks outcropping in the Pacitan area consist of basaltic pillow lavas with crosscutting dykes, exposed in the lower part of the Grindulu River, north of Pacitan, and represent the basal part of the Arjosari Formation (Soeria-Atmadja et al., 1994). Stratigraphically younger magmatic rocks are also exposed in the Pacitan area. Geochemical analyses of volcanic rocks such as basalt and andesite from Pacitan show SiO_2 compositions around 49.0-58.4 wt.%, and these rocks are characterized by low TiO_2 contents and high chondrite-normalized La/Nb ratios (> 5), indicative of subduction-related magmas. Light rare earth elements (LREE) and large Ion lithophile elements (LILE) are enriched with negative Nb anomalies. The concentrations of K, Rb, Sr, and Ba are lower compared to calc-alkaline andesite (Bellon et al., 1994). Chondrite-normalized incompatible element patterns show relatively flat patterns. REE patterns indicate that the depletion in alkali and alkali-earth elements is not due to alteration; instead, such features are typical of island arc tholeiitic rocks. The interpretation of K-Ar data on these rocks is relatively difficult because of their low K_2O contents and the possible mobility of alkalis during greenschist facies alteration. However, the least altered sample yielded an apparent K-Ar age of 42.7 Ma on whole rock. A dyke from the pillow lava sequence gave a K-Ar age of 28.0 Ma. These K-Ar data, along with the age obtained from Karangsambung (39.9 Ma), record the oldest known magmatic activity of the "Old Andesite" (Soeria-Atmadja et al., 1994). Porphyritic rhyolite containing no more than 15% phenocrysts (plagioclase and quartz) has a matrix consisting of very fine granular quartz, feldspar, and finely disseminated opaque particles. Chemical analysis indicates a tholeiitic affinity (Soeria-Atmadja et al., 1994).

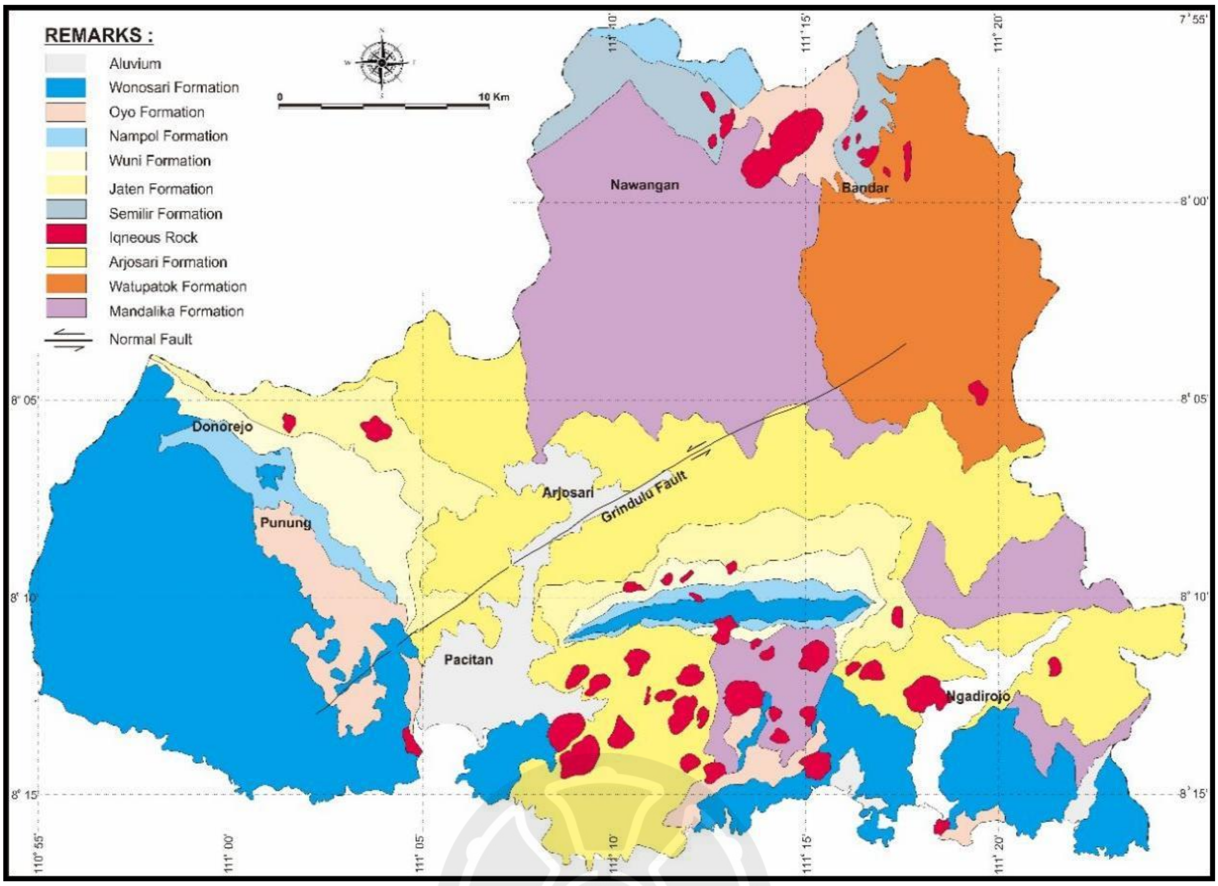

Fig. 2.11. Geological map of Pacitan, East Java (Modified from Samodra et al., 1992).

2.4. Adakite in East Java

Adakite is a type of igneous rock and related to Cenozoic arc magmatism and the subduction of young (≤ 25 Ma) oceanic lithosphere. Adakitic rocks may be derived by partial melting of thickened lower crust (e.g. Atherton & Petford, 1993; Muir et al., 1995; Petford & Atherton, 1996; Johnson et al.,1997; Arculus et al., 1999; Zhang et al., 2001; Chung et al.,2003; Xiong et al., 2003; Wang et al., 2005) or delaminated mafic lower crust (e.g. Kay & Kay, 1993; Defant et al., 2002; Xu et al., 2002; Gao et al., 2004; Wang et al., 2004a, 2004b), as well as by assimilation and fractional crystallization (AFC) processes from parental basaltic magmas (e.g. Castillo et al., 1999). The Characteristic of adakite is $SiO_2 \geq 56$ wt.%, $Al_2O_3 \geq 15$ wt.%, MgO < 3 wt.% (rarely > 6 wt.%), Sr/Y, and La/Yb ratios, and low Y and Yb concentrations (Defant and Drummond, 1990; Martin, 1999; Qu et al., 2004; Martin et al., 2005; Zhu et al., 2008). Concentrations of Y and heavy rare earth elements (HREE) are low (Y ≤ 18 ppm and Yb = 1.9 ppm), while Sr concentrations are high (typically > 400 ppm) relative to those of island arc adakites (ADRs). Consistent with most island arc ADRs, these adakites contain low concentrations of high-field strength elements and $^{87}Sr/^{86}Sr$ values typically <0.7040. Defant and Kepezhinskas (2001) suggested that adakites contain positive Eu and Sr anomalies, with Sr/Y and La/Yb ratios of 40 and 20, respectively. Adakites can be used to investigate island arc magmatism as they are products of hot slab subduction and downwelling plates in the amphibolite-eclogite transition zone (Condie, 2005; Rollinson and Martin, 2005; Castillo, 2006; Drummond and Defant, 1990). Adakites are also associated with porphyry deposits (Sun et al., 2011, 2013; Sajona and Maury, 1998), and in China, 25 of the 26 medium–large porphyry Cu deposits are associated with adakites (Leng et al., 2007). Most of the rocks on the island of Java exhibit typical island arc characteristics, but some rocks on the island are part of the adakite suite (Defant and Drummond, 1990). Garrison and Davidson (2003) characterized adakitic rocks in Java is Sr/Y > 20 ppm, Y < 19 ppm, and Sr > 400 ppm. Most adakite rocks are concentrated in the eastern part of Java. Adakitic rocks from dacitic intrusions show Sr/Y ratios of 40.4 (Upper Miocene) in the Selogiri caldera, Sr/Y = 46 (Lower Miocene) in the Wediombo volcanic center, Sr/Y = 40.3 (Miocene) in the Tulungagung volcanic center, and Sr/Y = 39.7 (Quaternary) in the Ngebel caldera lake of the Wilis volcanic complex **(Fig. 2.12)** (Defant and Drummond, 1990). These rocks have high Al_2O_3 concentrations, low K_2O/Na_2O ratios, and moderate Ni and Cr contents (Defant and Drummond, 1990; Tatsumi and Eggins, 1995; Martin, 1999; Scaillet and Proteau, 2001). The Selogiri, Pacitan, Trenggelek, and Merubetiri areas are related to porphyry mineralization, such as Cu-Au, skarn Fe, skarn Zn-Cu-Pb, and other base metals. Porphyry mineralization in East Java is related to the adakite process (Oligocene to Miocene arc) **(Fig. 2.13)** (Setijadji et al., 2006).

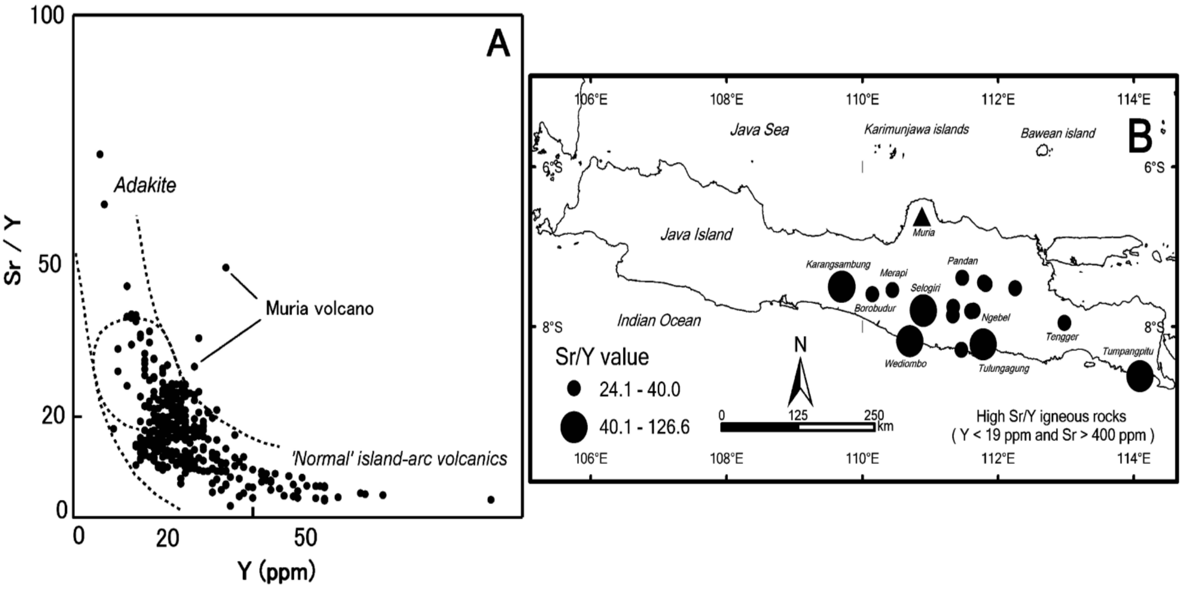

Fig. 2.12. Distribution of Java rocks within: A. The diagram of Y versus Sr/Y of Defant and Drummond (1990), and B. Spatial distributions of high Sr/Y rocks in Java, defined by Sr/Y > 20, Y < 19 ppm, and Sr > 400 ppm. Note that high Sr/Y (adakitic) rocks are consistently present only in the eastern half of Java. Backarc volcanoes such as Muria are neither adakite nor normal island-volcanic arcs.

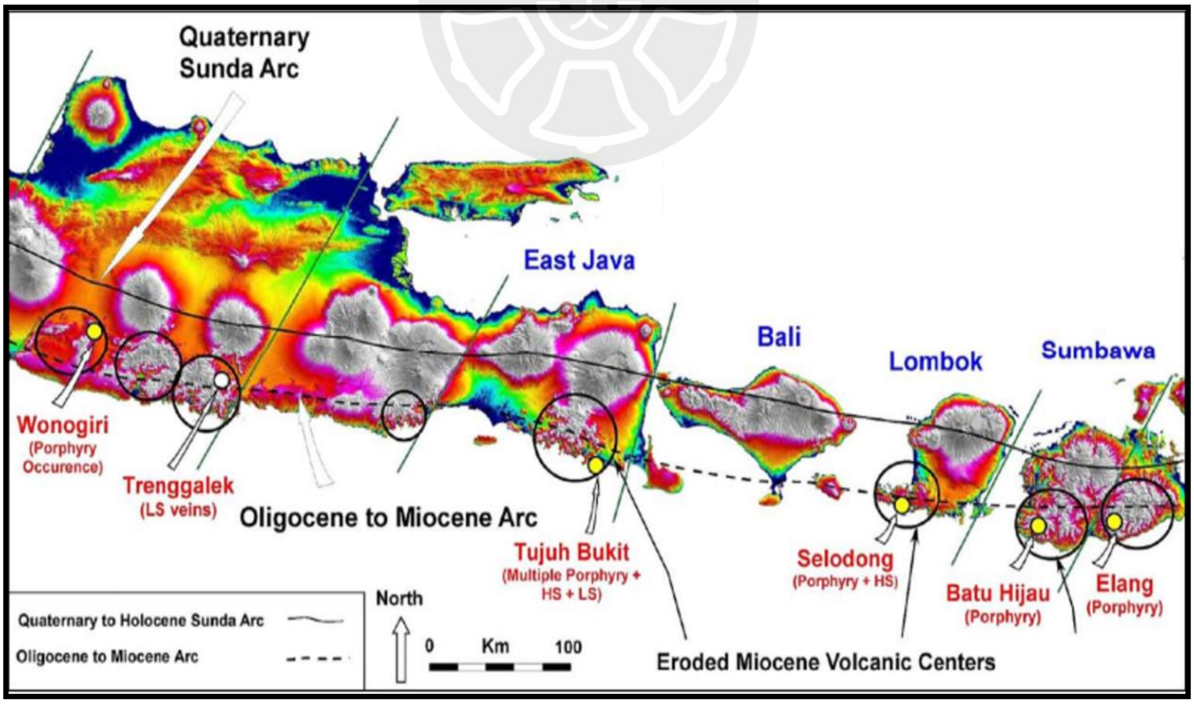

Fig. 2.13. Southern belt, Late Oligocene to Early Miocene "Old Andesite" volcanic arc (dashed line). Many of the deeply eroded Oligocene-Miocene volcanic centers in the East Sunda arc host porphyry copper-gold deposits (Roriach, 2011).

CHAPTER 3. METHODOLOGY

3.1. Petrography analysis

A total of 12 volcanic rock samples from the Pacitan area were sent to Langfang (near Beijing) for thin section preparation. All samples were examined to determine the petrographic characteristics of minerals and rock types using a polarizing microscope at the Department of Earth Sciences, National Taiwan Normal University. The petrographic analysis involved several steps:

- Thin section observation

Thin section observations were performed on all 12 volcanic rock samples. Each sample was observed in separate parts, such as phenocrysts and groundmass. The purpose of the observation was to determine the mineral compositions, structure, grain size, zoning, and mineral alteration. Observations were conducted using a polarizing microscope.

- Point counting

Point counting was conducted to determine the mineral composition in the thin sections by distinguishing minerals based on grain size. For samples with grain sizes of 0.5-0.8 mm, 300-400 points were counted, and for those with grain sizes of 1.0-2.0 mm, 300-400 points were counted. The percentage of each mineral was then calculated to estimate the relative proportions in both the phenocrysts and the groundmass.

- Photomicrograph

After completing point counting, the next step was photomicrography. This step aimed to capture images of the minerals. The photos were intended to represent all existing minerals, as well as the textures and zoning observed in the thin sections.

3.2. Zircon U-Pb dating

The analysis of zircon U-Pb dating was carried out through several steps, including sample preparation and U-Pb dating analyses. For the separation of zircon grains from ~3 kg of rock, conventional heavy liquid and magnetic separation methods were used. The process of separating zircon grains from the rock was conducted in Langfang (near Beijing).

- Sample Preparation

After the zircon separation was completed, the next step was the preparation of samples by selecting zircon grains for mounting. Approximately 60 zircon grains were mounted for magmatic zircons, and around 150 grains were mounted for inherited zircons. After mounting, the zircon grains were polished on an epoxy disc. This process was carried out at the Department of Geosciences, National Taiwan University. After mounting and polishing, the next step was cathodoluminescence (CL) imaging. This was performed at the Institute of Earth Sciences, Academia Sinica, Taiwan. CL images were used to examine the internal textures of the zircon grains and to select appropriate locations for in-situ U-Pb and Hf isotope analysis. After completing the CL imaging, U-Pb zircon analysis followed.

- U-Pb Dating Analysis

Zircon U-Pb isotopic measurements were conducted using Agilent 7500S ICP-MS in combination with PM 193, following the analytical procedure of the Institute of Earth Sciences, Academia Sinica, Taiwan (Chiu et al., 2013). GLITTER version 4.4 was used to reduce the U-Th-Pb isotopic ratios (Griffin, 2008). Lead corrections were applied following Andersen (2002). The U-Pb dating analysis was performed at the Department of Geosciences, National Taiwan University.

U-Pb system

^{232}Th, ^{235}U, and ^{238}U each initiate long decay series that involve multiple α- and β-emissions, ultimately producing various Pb isotopes.

$$^{238}U \rightarrow {}^{206}Pb + 8\alpha^{2+} + 6\beta^{-}，t_{1/2} = 4.47 \times 10^{9} yr，\lambda = 1.551 \times 10^{-10} yr^{-1} \text{ (Jaffey at al., 1971)}$$

$$^{235}U \rightarrow {}^{206}Pb + 7\alpha^{2+} + 4\beta^{-}，t_{1/2} = 7.04 \times 10^{8} yr，\lambda = 9.849 \times 10^{-10} yr^{-1} \text{ (Jaffey at al., 1971)}$$

Natural Pb consists of four isotopes: ^{204}Pb, ^{206}Pb, ^{207}Pb and ^{208}Pb. The ingrowth equations for the three radiogenic Pb isotopes are as follows:

$$^{206}Pb_t = {}^{206}Pb_0 + {}^{238}U(e^{\lambda_{238}t} - 1)$$
$$^{207}Pb_t = {}^{207}Pb_0 + {}^{235}U(e^{\lambda_{235}t} - 1)$$
$$^{206}Pb_t{}^{*} = {}^{206}Pb_t - {}^{206}Pb_0 + {}^{238}U(e^{\lambda_{238}t} - 1)$$
$$^{207}Pb_t{}^{*} = {}^{207}Pb_t - {}^{207}Pb_0 + {}^{235}U(e^{\lambda_{235}t} - 1)$$
$$\rightarrow \frac{^{206}Pb_t{}^{*}}{^{238}U} = (e^{\lambda_{238}t} - 1)$$
$$\rightarrow \frac{^{207}Pb_t{}^{*}}{^{235}U} = (e^{\lambda_{235}t} - 1)$$

Concordia curve (Wetherill, 1956)

$$\frac{^{206}Pb}{^{238}U} = \frac{^{207}Pb(e^{\lambda_{238}t} - 1)}{^{235}U(e^{\lambda_{235}t} - 1)}$$

$^{235}U/^{238}U$ = 1/137.82 (present-day) (Hiess et al., 2012)

$$\frac{^{207}Pb}{^{206}Pb} = \frac{1}{137.82} \times \frac{e^{\lambda_{235}t} - 1}{e^{\lambda_{238}t} - 1}$$

Common Pb correction (Andersen, 2002)

The presence of common lead contamination in zircons used for U-Pb geochronology is a potentially serious source of error. Traditionally, common lead is measured by analyzing ^{204}Pb, and the isotopic composition is corrected accordingly.

Th/U calculation

^{232}Th: [[Th]/232 $_{\text{atomic weight}}$ (mole)] × 100% $_{\text{isotope abundance}}$

^{238}Th: [[Th]/238.02891 $_{\text{atomic weight}}$ (mole)] × 99.2745% $_{\text{isotope abundance}}$

$$\frac{^{238}U}{^{232}Th} = \frac{\left(^{[\boldsymbol{U}]}/_{238.02891}\right) \times 99.2745\%}{\left(^{[\boldsymbol{Th}]}/_{232}\right) \times 100\%}$$

$$\frac{^{238}U}{^{232}Th} \times \frac{100\%}{99.2745\%} = \frac{^{[\boldsymbol{U}]}/_{238}}{^{[\boldsymbol{Th}]}/_{232}}$$

$$\frac{^{238}U}{^{232}Th} \times \frac{100\%}{99.2745\%} \times \frac{238}{232} = \frac{[U]}{[Th]}$$

$$\rightarrow \frac{[Th]}{[U]} = \frac{^{232}Th}{^{238}U} \times 99.2745\% \times \frac{232}{238}$$

Discordance %

$$= \left[\left(^{206}Pb/^{238}U\ age\right) \Big/ \left(^{207}Pb/^{206}Pb\ age\right) \right] \times 100\%$$

$$= \left[\left(^{207}Pb/^{235}U\ age\right) \Big/ \left(^{206}Pb/^{238}U\ age\right) \right] \times 100\%$$

Boundary of $^{206}Pb/^{207}Pb$ age or $^{206}Pb/^{238}U$ age

1. 1000 Ma: For samples that contain a cluster of analyses with concordant to slightly discordant $^{206}Pb/^{238}U$ ages of ~500 Ma, we use $^{206}Pb/^{238}U$ ages up to 1000 Ma, and $^{206}Pb/^{207}Pb$ ages if the $^{206}Pb/^{238}U$ ages are >1000 Ma (Gehrels et al., 2006; DeCelles et al., 2007).

2. 800Ma: For zircons that are <800 Ma or reversely discordant, $^{206}Pb^{*}/^{238}U$ apparent ages are used. For zircons >800 Ma with normal discordance, $^{207}Pb^{*}/^{206}Pb^{*}$ apparent ages are used (Kapp et al., 2003).
3. ~541 Ma: Due to various factors, $^{207}Pb^{*}/^{206}Pb^{*}$ is generally more useful for Precambrian samples, while $^{206}Pb^{*}/^{238}U$ is more informative for Phanerozoic samples (Corfu, 2013).

Sample Standards

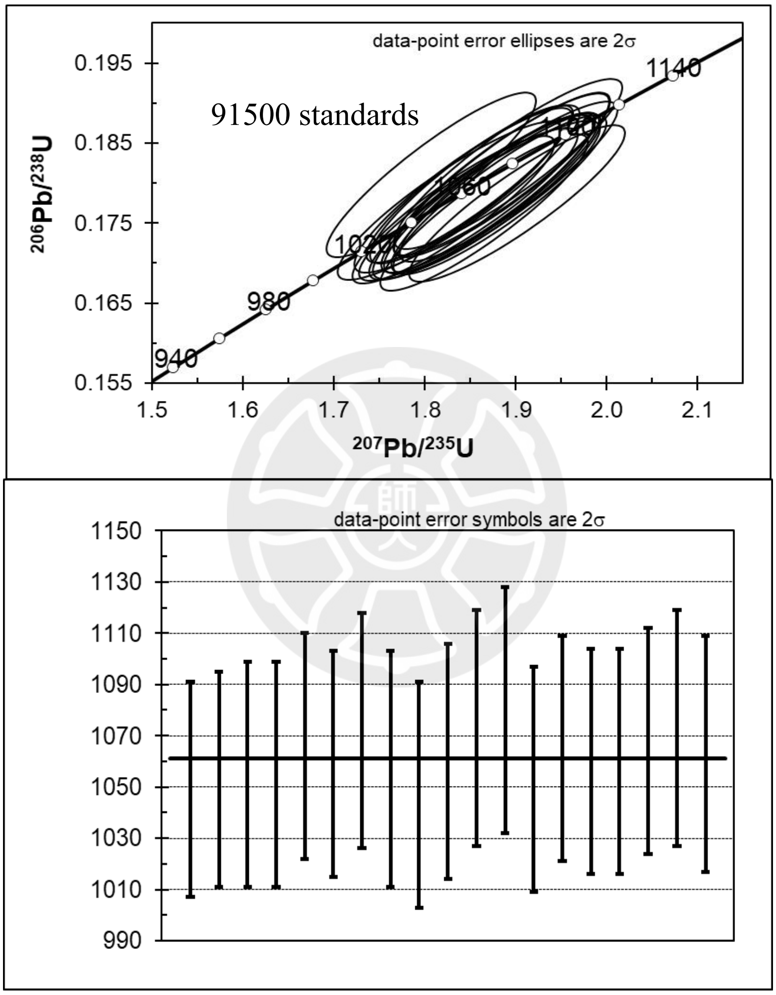

Fig. 3.1. Results from National Taiwan University 91500 standard, measured from 16 to 20 September 2019. Concordia diagram showed mean age = 1061 ± 10 Ma [0.94%], 95% confidence, n = 19, MSWD = 0.16, probability = 1.000 (error bars are 2σ) (Standard from Wiedenbeck et al., 1995).

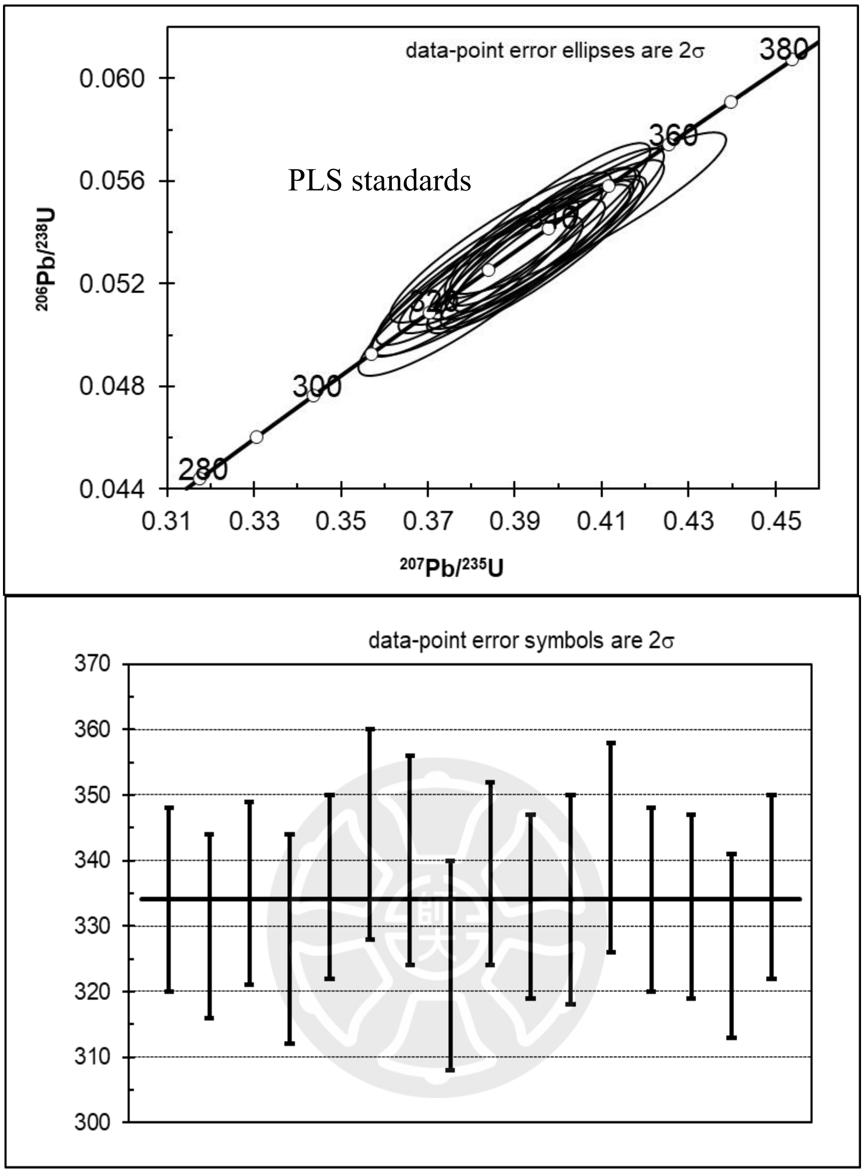

Fig. 3.2. Results from National Taiwan University PLS standard, measured from 16 to 20 September 2019. Concordia diagram showed mean age = 334.1 ± 3.6 Ma [1.1%], 95% confidence, n = 16, MSWD = 0.47, probability = 0.95 (error bars are 2σ) (Standard from Slàma et al., 2008).

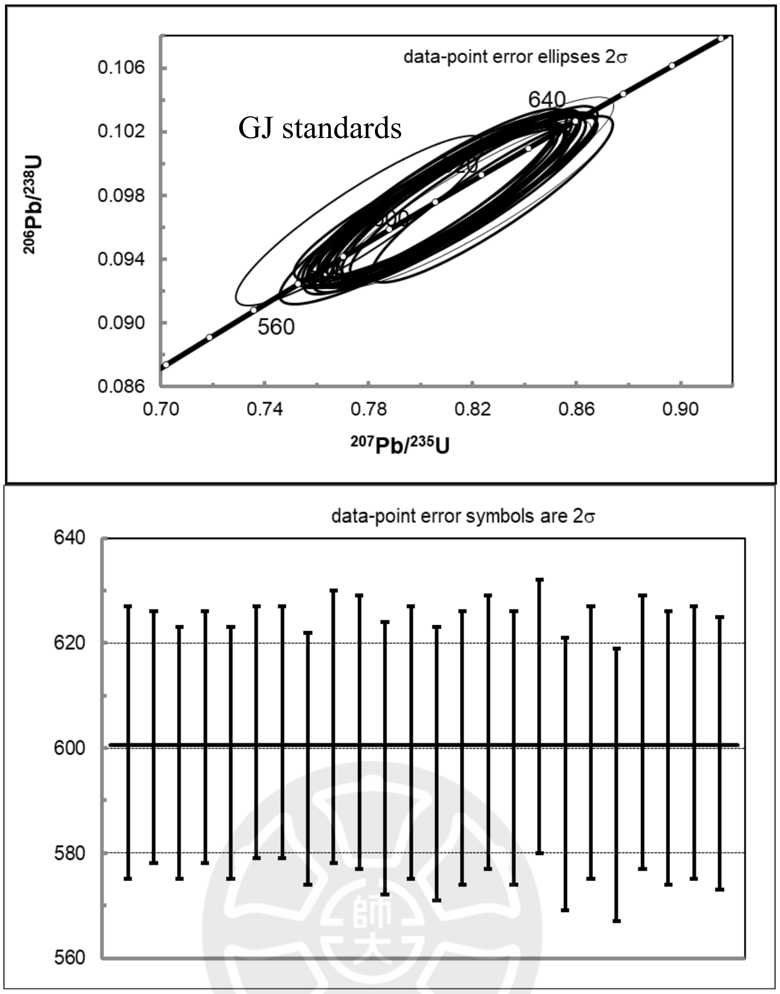

Fig. 3.3. Results from National Taiwan University GJ standard, measured from 16 to 20 September 2019. Concordia diagram showed Mean age = 600.5 ± 5.1 Ma [1.1%], 95% confidence, n = 16, MSWD = 0.5, probability = 0.95 (error bars are 2σ) (Standard from Jackson et al., 2004).

3.3. Zircon Hf isotopic analysis

In-situ zircon Hf isotopic measurements were performed on the dated zircon spots using a Nu Plasma II MC-ICP-MS (Multicollector Inductively Coupled Plasma Mass Spectrometer) coupled with a Photon Machines Analyte G2 laser-ablation system at the Institute of Earth Sciences, Academia Sinica, Taiwan. A spot size of 50 μm was used to analyze the preexisting pits made by U-Pb isotopic analyses, with an energy level of approximately 4 to 5 J/cm². The two standards used were 91500 and Mud Tank, with a repetition rate of 5–6 Hz and an energy fluence of ~4–5 J/cm². The time required for each analysis was about 2 minutes, including 30 seconds for background measurement and approximately 85 seconds for measuring sample intensity after laser ablation. Mud Tank zircon was employed as the primary external reference material to monitor instrument conditions, while Plešovice, 91500, and TEMORA zircons were used as secondary external reference materials for data quality control. These exhibited long-term average $^{176}Hf/^{177}Hf$ values of 0.282498 ± 20 (2σ, n = 720), 0.282483 ± 17 (2σ, n = 192), 0.282311 ± 22 (2σ, n = 45), and 0.282692 ± 20 (2σ, n = 61), respectively, consistent with the values reported by Woodhead and Hergt (2005), Wu et al. (2006), and Sláma et al. (2008): 0.282504 ± 44, 0.282482 ± 13, 0.282307 ± 31, and 0.282680 ± 31. All calculated data were evaluated for isobaric interferences and normalized to $^{179}Hf/^{177}Hf$ = 0.7325 using an exponential correction for mass bias. Additionally, the results for the Mud Tank standard acquired during the experimental period yielded a mean value of $^{176}Hf/^{177}Hf$ = 0.282494 ± 09. The detailed analytical procedure is described in Bikramaditya et al. (2018). Calculations for Hf model ages were made using the constants and equations listed in **Table 3.1**.

Table. 3.1 The calculation for Hf model ages

Reservoir	$^{176}Lu/^{177}Hf$	$^{176}Hf/^{177}Hf$	Reference
CHUR 0	0.0332	0.282772	Blichert-Toft and Albarède (1997)
DM 0	0.0384	0.28325	Griffin et al. (2000)
Mean crust 0	0.015		Griffin et al. (2002)
$T_{DM} = 1/\lambda \times \ln\{1+[(^{176}Hf/^{177}Hf)_{sample}-(^{176}Hf/^{177}Hf)_{DM}]/[(^{176}Lu/^{177}Hf)_{sample}-(^{176}Lu/^{177}Hf)_{DM}]\}$			
$T_{DMC} = T_{DM} - (T_{DM} - T) \times [(f_{CC} - f_{sample})/(f_{CC} - f_{DM})]$			
$f_{Lu/Hf} = [(^{176}Lu/^{177}Hf)_{Source} / (^{176}Lu/^{177}Hf)_{CHUR0}] - 1$			
$f_{CC} = (0.015/0.0332)-1 = -0.5482$			
$f_{DM} = (0.0384/0.0332)-1 = 0.1566$			

3.4. Whole rock analysis

3.4.1. Major Elements analysis

The major element compositions of 45 representative volcanic rock samples were determined using X-ray fluorescence (XRF) at National Taiwan University. Each rock sample was crushed into chips and then ground to <200 mesh for analysis. Samples were first dried at 110°C for 24 hours to remove water and then ignited at 1000°C for 1 hour to remove volatile components. Loss on ignition (L.O.I.) was calculated based on the weight difference. Powdered samples were mixed with a lithium tetraborate flux at a 1:5 ratio, fused at 1000°C in a platinum crucible to form glass beads, and analyzed using a Rigaku RIX 2000 wavelength-dispersive X-ray fluorescence spectrometer. Data quality was monitored using USGS rock standards (e.g., BCR-2, AGV-2, and BHVO-2). The analytical uncertainties for major elements are typically less than 2%. All data are normalized to an anhydrous basis.

Formula for LOI:
L.O.I. (weight %) = 100 x ((n2-n3) / (n2-n1))

Remark:

n1 = Ceramic weight

n2 = Sample weight + Ceramic weight

n3 = Total weight

All elements have an analytical uncertainty below 5%. The L.O.I analysis process is carried out in the Department of Geosciences, National Taiwan University.

3.4.2. Trace elements measurements

- Sample preparation

The first step involves weighing the 45 samples and USGS reference standards (AGV-2, BHVO-2, BCR-2, and DNC-1) to be used **(Table 3.2)**. Both sample and standard weights were approximately 40 ± 5 mg. Each sample was handled using tweezers and placed into labeled Teflon beakers. A 1:1 mixture of HNO_3 was added, followed by 25 drops of super-pure HF. The beakers were sealed and heated at 140°C for 2 days to dissolve the samples. After dissolution, the solutions were dried at 160°C for 1.5 hours with the beakers open until a solid “cake” formed. Then, 1.5 ml of HNO_3 (in a 1:2 ratio) was added, and the samples were reheated at 140°C overnight with the beakers sealed to ensure complete dissolution. The resulting solutions were diluted with 2% HNO_3 in 50 ml bottles. A second dilution was performed by adding 10 ppb of Rh and Bi internal standards and 2% HNO_3, adjusting the sample-to-solution weight ratio to 1:4000 in 12 ml tubes. The prepared samples were then ready for analysis using Inductively Coupled Plasma–Mass Spectrometry (ICP-MS).

- Analysis trace elements.

Trace element analyses were conducted using an Agilent 7500cx quadrupole ICP-MS at the Institute of Earth Sciences, Academia Sinica, Taiwan. Calibration was performed using USGS rock standards (AGV-2, BHVO-2, BCR-2, and DNC-1). Analytical precision was better than 3% **(Fig. 3.4).**

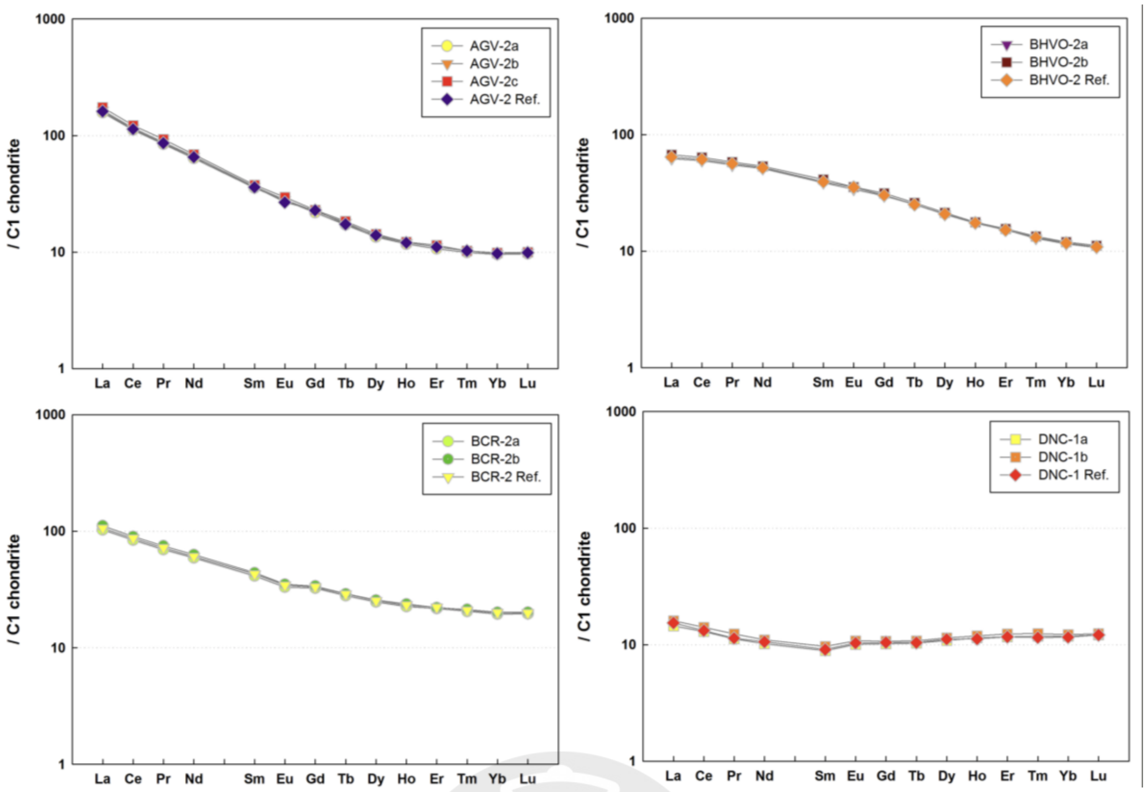

Fig. 3.4. Results from the Institute of Earth Sciences, Academia Sinica, Taiwan. The AGV, BCR, BHVO, and DNC standards were measured from May 4 to 7, 2021. Trace element standards follow the USGS reference values and recommended concentrations reported by Jochum et al. (2005; 2011; 2016).

Table. 3.2. Trace element standards (AGV, BCR, BHVO, and DNC) follow the USGS reference values and recommended concentrations reported by Jochum et al (2005; 2011; 2016).

		AGV-2a	AGV-2b	AGV-2c	Recommended Values	2s	BCR-2a	BCR-2b	Recommended Values	2s	BHVO-2a	BHVO-2b	Recommended Values	2s	DNC-1a	DNC-1b	Recommended Values
P	ppm	2028	2081	2136	2100		1548	1597	1500		1193	1216	1200		326	358	371
Sc	ppm	20.6	20.6	21.9	13.1	0.31	31.3	31.3	33.5	0.40	33.4	32.5	31.8	0.34	29.2	29.1	31.0
Ti	ppm	6314	6353	6509	6300		13320	13590	13500		16240	16480	16300		2839	2877	2878
V	ppm	118	119	120	119	1.20	415	415	418	4.50	325	324	318	2.30	144	146	148-157
Cr	ppm	19.0	18.8	18.8	16.2	0.72	12.4	12.3	15.9	0.38	291	290	287	3.10	281	283	270-285
Mn	ppm	756	764	776	770		1489	1502	1520		1298	1310	1290		1159	1174	1139
Co	ppm	15.7	15.6	15.8	15.5	0.50	36.2	36.2	37.3	0.37	43.7	43.8	44.9	0.32	56.3	56.7	54.7-57
Ni	ppm	18.7	19.0	18.8	18.9	0.41	14.6	14.5	12.6	0.30	114	115	120	1.20	249	251	247-256
Cu	ppm	51.8	51.8	51.7	51.5	0.65	20.1	20.2	19.7	0.72	129	131	129	1.40	94.8	95.3	96-100
Zn	ppm	82.9	84.6	84.2	86.7	1.20	132	134	130	1.80	106	108	104	1.00	58.5	58.7	66-70
Ga	ppm	20.3	20.6	21.0	20.4	0.17	22.1	22.3	22.1	0.20	21.5	21.8	21.4	0.20	14.4	14.6	13.7-15
Rb	ppm	66.9	68.2	69.4	67.8	0.66	46.2	47.0	46.0	0.56	9.37	9.53	9.26	0.10	3.86	3.94	3.9-4.5
Sr	ppm	652	657	670	660	5.70	341	346	337	6.70	398	404	394	1.70	140	142	145
Y	ppm	19.3	19.7	19.9	19.1	0.84	35.4	35.9	36.1	0.37	26.1	26.4	25.9	0.28	17.8	18.1	17.7-18
Zr	ppm	232	233	236	232	2.00	184	187	187	1.50	172	174	171	1.30	38.7	39.0	38-41
Nb	ppm	13.9	14.0	14.2	14.1	0.22	12.3	12.4	12.4	0.20	18.3	18.4	18.1	0.20	1.81	1.86	2-3
Cs	ppm	1.19	1.20	1.23	1.17	0.02	1.15	1.16	1.16	0.02	0.12	0.13	0.10	0.00	0.24	0.24	0.21-0.34
Ba	ppm	1115	1176	1128	1134	8.00	669	666	684	4.70	132	132	131	1.00	106	106	103-118
La	ppm	37.2	38.9	41.2	38.2	0.38	24.3	26.3	25.1	0.16	14.7	15.9	15.2	0.08	3.44	3.80	3.53-3.8
Ce	ppm	68.1	70.7	74.7	69.4	0.57	51.3	55.0	53.1	0.33	36.6	39.0	37.5	0.19	7.91	8.63	8.11-10.6
Pr	ppm	7.99	8.31	8.79	8.17	0.08	6.58	7.10	6.83	0.04	5.21	5.53	5.34	0.03	1.07	1.17	1.1-1.3
Nd	ppm	29.7	30.8	32.1	30.5	0.47	27.5	29.4	28.3	0.37	23.9	25.0	24.3	0.25	4.76	5.15	4.86-5.2
Sm	ppm	5.40	5.55	5.76	5.51	0.08	6.30	6.72	6.55	0.05	5.92	6.30	6.02	0.06	1.36	1.48	1.38-1.43
Eu	ppm	1.60	1.62	1.72	1.55	0.02	1.92	2.04	1.99	0.02	1.97	2.06	2.04	0.01	0.58	0.62	0.57-0.6
Gd	ppm	4.47	4.61	4.71	4.68	0.06	6.66	6.95	6.81	0.08	6.13	6.45	6.21	0.04	2.09	2.21	2-2.11
Tb	ppm	0.64	0.67	0.69	0.65	0.01	1.04	1.08	1.08	0.03	0.94	0.97	0.94	0.01	0.39	0.40	0.39-0.41
Dy	ppm	3.43	3.48	3.61	3.55	0.03	6.28	6.52	6.42	0.06	5.25	5.44	5.28	0.03	2.76	2.91	2.7-3
Ho	ppm	0.66	0.68	0.69	0.68	0.01	1.28	1.35	1.31	0.01	0.98	1.00	0.99	0.01	0.65	0.68	0.62-0.65
Er	ppm	1.77	1.83	1.89	1.83	0.01	3.58	3.65	3.67	0.04	2.52	2.58	2.51	0.01	1.94	2.05	1.87-2
Tm	ppm	0.25	0.26	0.26	0.26	0.00	0.52	0.54	0.53	0.01	0.33	0.34	0.33	0.00	0.30	0.32	0.33
Yb	ppm	1.62	1.64	1.68	1.65	0.01	3.30	3.42	3.39	0.04	1.96	2.04	1.99	0.03	2.01	2.08	1.97-2.01
Lu	ppm	0.25	0.25	0.25	0.25	0.00	0.50	0.51	0.50	0.01	0.27	0.28	0.28	0.00	0.31	0.32	0.31
Hf	ppm	5.16	5.23	5.30	5.14	0.06	4.88	4.93	4.97	0.03	4.44	4.56	4.47	0.03	1.05	1.05	1.01-1.05
Ta	ppm	0.85	0.86	0.86	0.87	0.02	0.78	0.79	0.79	0.02	1.16	1.17	1.15	0.02	0.09	0.09	0.10
W	ppm	2.41	1.36	1.21	0.55	0.09	1.97	1.22	0.47	0.05	0.27	(0.27)	0.25	0.04	(1.23)	(1.70)	0.20
Tl	ppm	0.28	0.28	0.28	0.28	0.01	0.26	0.26	0.27	0.02	0.02	0.02	0.02	0.00	0.03	0.03	0.03
Pb	ppm	13.3	13.3	13.3	13.1	0.15	10.4	10.3	10.6	0.17	1.65	1.69	1.65	0.04	6.38	6.39	6.2-6.3
Th	ppm	6.18	6.15	6.05	6.17	0.06	5.91	5.79	5.83	0.05	1.23	1.22	1.22	0.02	0.25	0.24	0.2-0.24
U	ppm	1.92	1.87	1.83	1.89	0.02	1.70	1.65	1.68	0.02	0.43	0.41	0.41	0.04	0.06	0.05	0.05-0.1

3.4.3. Sr-Nd-Hf Isotopes

The whole-rock analysis was conducted using powdered rock samples decomposed in a 1:1 mixture of HF and HNO_3 for more than 5 days at 145°C. This process was repeated 2 to 3 times until complete digestion. After digestion, the solution was evaporated to dryness, then redissolved in 2 ml of 4N HCl, followed by 1N HCl. After centrifugation, the samples were finally dissolved in 1 ml of 2N HCl. Column chemistry for Sr–Nd employed 4 ml of 6N HCl, while Hf column chemistry used 1 ml of 0.2N HF. The procedures for Sr–Nd and Hf isotopic analyses followed Lee et al. (2012) and Shinjo et al. (2010). Seven samples were selected for Sr–Nd–Hf isotopic analyses using a Nu Plasma II multicollector ICP-MS at the Institute of Earth Sciences, Academia Sinica, Taiwan. International standards SRM987 ($^{87}Sr/^{86}Sr$ = 0.710250; Cunningham et al., 2009), JNdi-1 ($^{143}Nd/^{144}Nd$ = 0.512115; Tanaka et al., 2000), and AmesHf ($^{176}Hf/^{177}Hf$ = 0.282160) were used for normalization. The long-term mean values for the Sr and Nd standards in the laboratory during the measurement period were $^{87}Sr/^{86}Sr$ = 0.710253 ± 21 (2σ, n = 1101) and $^{143}Nd/^{144}Nd$ = 0.512103 ± 23 (2σ, n = 341). Sr–Nd–Hf isotopic compositions were age-corrected using the calculations show in **Table**. **3.3** Trace element contents of Rb, Sr, Sm, Nd, Lu, and Hf were measured by an Agilent 7500cx ICP-MS.

Table 3.3. The calculation Sr-Nd-Hf isotopic composition

Item	Value	Source
^{147}Sm	0.1499	Böhlke et al., 2005, J Phys Chem Ref Data
^{144}Nd	0.238	Böhlke et al., 2005, J Phys Chem Ref Data
MSm	150.36	Wieser, 2006, Pure Appl Chem
MNd	144.242	Wieser, 2006, Pure Appl Chem
λSm	6.54E-12	Lugmair and Marti, 1978, EPSL
$(^{143}Nd/^{144}Nd)\ CHUR_0$	0.512638	Goldstein et al., 1984, EPSL
$(^{147}Sm/^{144}Nd)\ CHUR_0$	0.1967	Jacobsen and Wasserburg, 1980, EPSL
$(^{143}Nd/^{144}Nd)DM_0$	0.513151	Liew and Hofmann, 1988, CMP
$(^{147}Sm/^{144}Nd)\ DM_0$	0.2136	Liew and Hofmann, 1988, CMP
^{87}Rb	0.2783	Böhlke et al., 2005, J Phys Chem Ref Data
^{86}Sr	0.0986	Böhlke et al., 2005, J Phys Chem Ref Data
MRb	85.4678	Wieser, 2006, Pure Appl Chem
MSr	87.62	Wieser, 2006, Pure Appl Chem
λRb	1.42E-11	Steiger and Jäger, 1977, EPSL

1. Steiger and Jäger. (1977)

$$\left(\frac{^{87}Sr}{^{86}Sr}\right)_i = \frac{^{87}Sr}{^{86}Sr} - \frac{^{87}Rb}{^{86}Sr} \times (e^{\lambda T} - 1)$$

$\lambda_{Rb\text{-}Sr} = 1.42 \times 10^{-11}\ yr^{-1}$ and $^{87}Rb/^{86}Sr = (Rb/Sr) \times 2.8956$

2. Lugmair and Marti. (1978)

$$\left(\frac{^{143}Nd}{^{144}Nd}\right)_i = \frac{^{143}Nd}{^{144}Nd} - \frac{^{143}Sm}{^{144}Nd} \times (e^{\lambda T} - 1)$$

$\lambda_{Sm\text{-}Nd} = 6.54 \times 10^{-12}\ yr^{-1}$ and $^{147}Sm/^{144}Nd = (Sm/Nd) \times 0.60456$

3. Pettingill and Patchett. (1981)

$$\left(\frac{^{176}Hf}{^{177}Hf}\right)_i = \frac{^{176}Hf}{^{177}Hf} - \frac{^{176}Lu}{^{177}Hf} \times (e^{\lambda T} - 1)$$

$\lambda_{Lu\text{-}Hf} = 1.867 \times 10^{-11}\ yr^{-1}$ and $^{176}Lu/^{177}Hf = (Lu/Hf) \times 0.142$

4. Jacobsen and Wassenberg. (1980); Hamilton et al., (1983)

$$\varepsilon_{Nd}(T) = \left[\frac{\left(\frac{^{143}Nd}{^{144}Nd}\right)_{Sample}^{(T)}}{\left(\frac{^{143}Nd}{^{144}Nd}\right)_{CHUR}^{(T)}} - 1\right] \times 10^4 \ ; \ \left(\frac{^{143}Nd}{^{144}Nd}\right)_{CHUR}(T) = 0.512638 - 0.1966 \times \left(e^{\lambda T} - 1\right)$$

5. Blichert-Toft and Albarède. (1997)

$$\varepsilon_{Hf}(T) = \left[\frac{\left(\frac{^{176}Hf}{^{177}Hf}\right)_{Sample}^{(T)}}{\left(\frac{^{176}Hf}{^{177}Hf}\right)_{CHUR}^{(T)}} - 1\right] \times 10^4 \ ; \ \left(\frac{^{176}Hf}{^{177}Hf}\right)_{CHUR}(T) = 0.282772 - 0.332 \times \left(e^{\lambda T} - 1\right)$$

3.5. Methods diagram

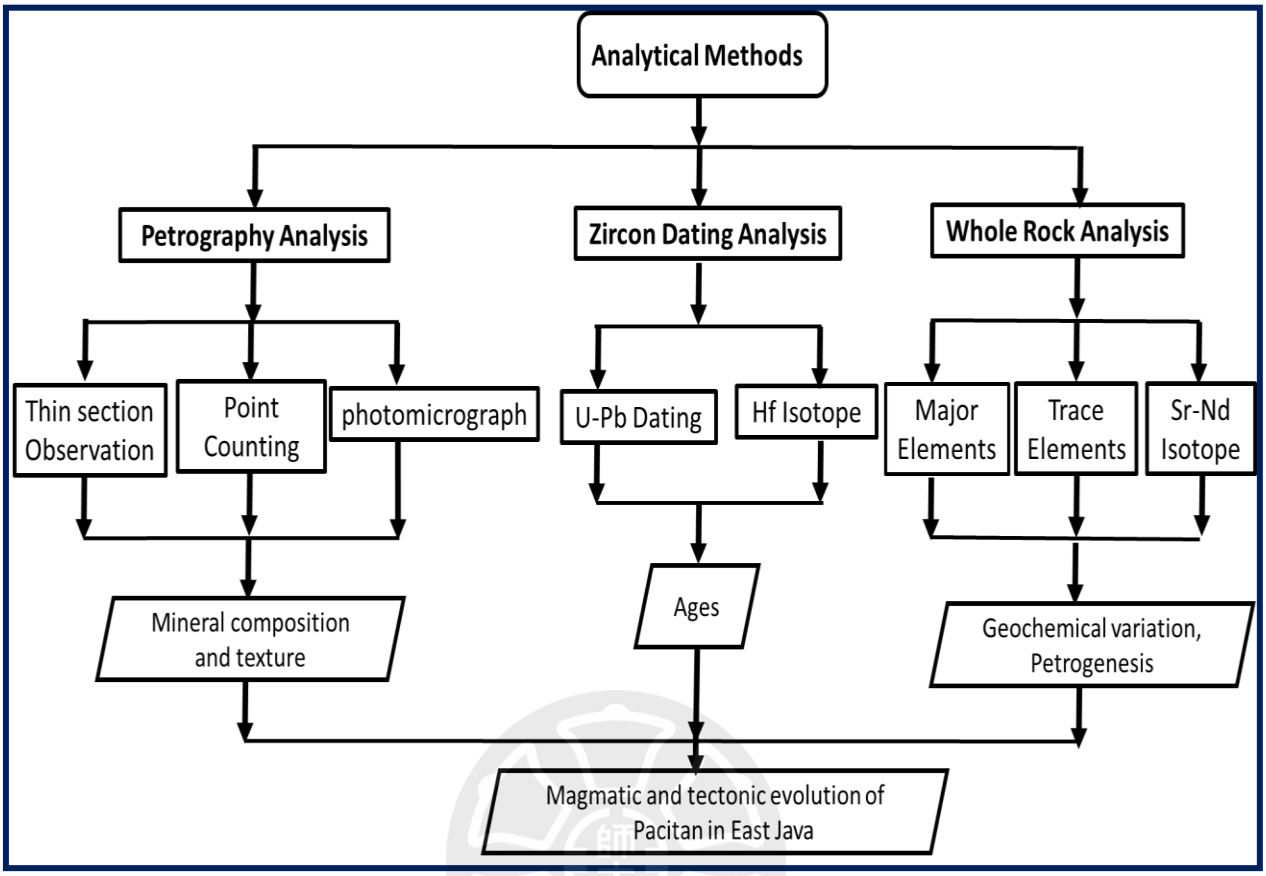

This diagram describes the research methods that have been carried out. The methods include petrography analysis conducted to determine mineral composition and texture; age analysis consisting of zircon U-Pb ages and zircon Hf isotope analysis, aiming to determine the age of volcanic rocks in the Pacitan area; and geochemical analysis consisting of major elements, trace elements, and Sr-Nd isotope analysis, aiming to identify geochemical variations and petrogenesis. The purpose of the study is to determine the magmatic and tectonic evolution of the Pacitan area.

CHAPTER 4. SAMPLE AND ANALYTICAL RESULTS

This chapter discusses the samples and the results of the analyses that have been carried out, including age analysis, petrography analysis, and geochemical analysis. Based on these results, several samples were found to have the same age, while others have different ages. Similarly, the geochemical analysis shows that some samples share the same geochemical trends, while others exhibit different trends. The similarities and differences in age and geochemical characteristics allow the samples to be grouped into three categories: Group A, Group B, and Group C. Group C is further divided into two subgroups, C1 and C2, because although they share the same age, they have different geochemical trends. Group A consists of 4 samples: 19JA20-01, 19JA20-02, 19JA20-03, and 19JA43-01. Group B consists of 5 samples: 19JA21-02, 19JA23-01, 19JA23-02, 19JA44-02, and 19JA51-02. Group C consists of 31 samples, subdivided into: C1, which includes 10 samples: 19JA19-01, 19JA19-02, 19JA25-01, 19JA25-02, 19JA29-01, 19JA30-01, 19JA31-01, 19JA34-01, 19JA39-01, and 19JA40-01. C2, which includes 21 samples: 19JA17-01, 19JA18-02, 19JA18-03, 19JA18-04, 19JA18-05, 19JA26-01, 19JA26-02, 19JA26-03, 19JA27-01, 19JA28-01, 19JA32-01, 19JA32-02, 19JA32-03, 19JA33-01, 19JA34-01, 19JA35-01, 19JA36-01, 19JA37-01, 19JA42-01, 19JA46-01, and 19JA47-01.

4.1. Samples

The Pacitan area, various types of volcanic rock samples were collected from S 08°03'27.87" to S 08°42'52.4" and E 110°01'16.3" to E 110°21'20.01" **(Fig. 4.1 and Fig. 4.2)**. All samples collected during the fieldwork are listed in Table 4. For analysis, a total of 10 samples were selected for petrographic analysis, 38 samples for geochemical analysis included whole-rock major and trace elements. 14 samples for zircon U-Pb dating, 8 samples for zircon Hf isotopic analysis, and 7 samples for whole rock Sr–Nd isotopic analysis.

Tabel. 4.1. List of volcanic rocks collected in Pacitan, East Java and analysis methods.

Sample	Location	Latitude	Longitude	Rock Type	Analysis					
					Petrography	zircon U-Pb	Major Element	Trace Element	zircon Hf- Isotope	Sr-Nd Isotope
19JA17-01	Northeast of Pantai Pidakan	S 8°14'52.41"	E 111°14'59.06"	Andesite			x	x		x
19JA18-02	Near Musholla Sibon Darusalam	S 8°14'14.88"	E 111°10'45.25"	Dacite	x	x	x	x		
19JA18-03	Near Musholla Sibon Darusalam	S 8°14'14.88"	E 111°10'45.25"	Andesite	x	x	x	x	x	
19JA18-04	Near Musholla Sibon Darusalam	S 8°14'14.88"	E 111°10'45.25"	Andesite	x	x	x	x	x	x
19JA18-05	Near Musholla Sibon Darusalam	S 8°14'14.88"	E 111°10'45.25"	Dacite	x	x	x	x		
19JA19-01	West of Masjid Al-Fallah	S 8°13'48.93"	E 111°10'0.24"	Andesite		x	x	x	x	x
19JA19-02	West of Masjid Al-Fallah	S 8°13'48.93"	E 111°10'0.24"	Andesite	x	x	x	x		x
19JA20-01	West of Masjid Al-Fallah	S 8°7'17.36"	E 111°21'20.01"	Dacite	x	x	x	x	x	x
19JA20-02	West of Masjid Al-Fallah	S 8°7'17.36"	E 111°21'20.01"	Andesite		x	x	x		x
19JA20-03	West of Masjid Al-Fallah	S 8°7'17.36"	E 111°21'20.01"	Dacite	x	x	x	x	x	
19JA21-02	West of Masjid At Taqwa	S 8°4'49.32"	E 111°15'8.27"	Dacite	x		x	x		
19JA23-01	South of Masjid Nurul Iman	S 8°3'27.87"	E 111°19'52.44"	Ryolite	x		x	x		
19JA23-02	South of Masjid Nurul Iman	S 8°3'27.87"	E 111°19'52.44"	Ryolite	x		x	x		x
19JA25-01	Waru (Kebonagung),	S 8°12'10.3"	E 111°07'36.7"	Basaltic Andesite			x	x		
19JA25-02	Waru (Kebonagung),	S 8°12'10.3"	E 111°07'36.7"	Basaltic Andesite			x	x		
19JA26-01	River Valley (G. Ngampel)	S 8°12'37.3"	E 111°12'04.5"	Andesite			x	x		
19JA26-02	River Valley (G. Ngampel)	S 8°12'37.3"	E 111°12'04.5"	Dacite			x	x		
19JA26-03	River Valley (G. Ngampel)	S 8°12'37.3"	E 111°12'04.5"	Dacite			x	x		
19JA27-01	River Valley (G.Gundang Legi)	S 8°12'37.8"	E 111°12'01.9"	Dacite		x	x	x		
19JA28-01	Roadside (G. puyang)	S 8°12'39.3"	E 111°11'39.9"	Dacite			x	x		
19JA29-01	Gowang, Ketro (Kebonagung)	S 8°11'58.1"	E 111°06'12,7"	Andesite			x	x		
19JA30-01	Gowang	S 8°10'26.3"	E 111°17'29.2"	Andesite			x	x		
19JA31-01	Panggerejo	S 8°13'04.2"	E 111°18'13.4"	Trachybasalt			x	x		
19JA32-02	G. Tenon	S 8°12'05.0"	E 111°17'15.9"	Andesite		x	x	x	x	
19JA33-01	G. Karangnongko	S 8°13'25.3"	E 111°08'32.3"	Andesite			x	x		
19JA34-01	Karangnongko (Roadside)	S 8°13'39.8"	E 111°08'38.3"	Andesite			x	x		
19JA35-01	Karangnongko (Roadside)	S 8°14'02.9"	E 111°08'41.7"	Andesite			x	x		
19JA36-01	Mantren (River)	S 8°13'37.1"	E 111°12'03.1"	Dacite		x	x	x		
19JA37-01	G. Masong	S 8°11'47.2"	E 111°12'28.1"	Basaltic Andesite			x	x		
19JA39-01	G. Punir	S 8°14'18.3"	E 111°14'58.1"	Basaltic Andesite			x	x		
19JA40-01	Sambirejo (Roadside)	S 8°12'18.5"	E 111°08'41.1"	Andesite			x	x		
19JA42- 01	Kebonagung (Roadside)	S 8°13'45.7"	E 111°09'51.0"	Andesite			x	x		
19JA43- 01	Wonojoyo	S 8°09'26.0"	E 111°11'43.2"	Andesite			x	x		
19JA44-02	Bandulan (River Valley)	S 8°05'13.1"	E 111°01'15.1"	Dacite			x	x		
19JA45-01	Bandulan (Roadside)	S 8°05'47.2"	E 111°03'16.3"	Tuff		x	x	x	x	
19JA46-01	G. Sepang	S 8°11'15.9"	E 111°15'32.2"	Basaltic Andesite		x	x	x	x	
19JA47-01	Beach (Near Sea)	S 8°13'58.3"	E 111°04'38.9"	Andesite			x	x		
19JA51-02	Grindulu River	S 8°03'18.5"	E 111°20'07.6"	Dacite			x	x		

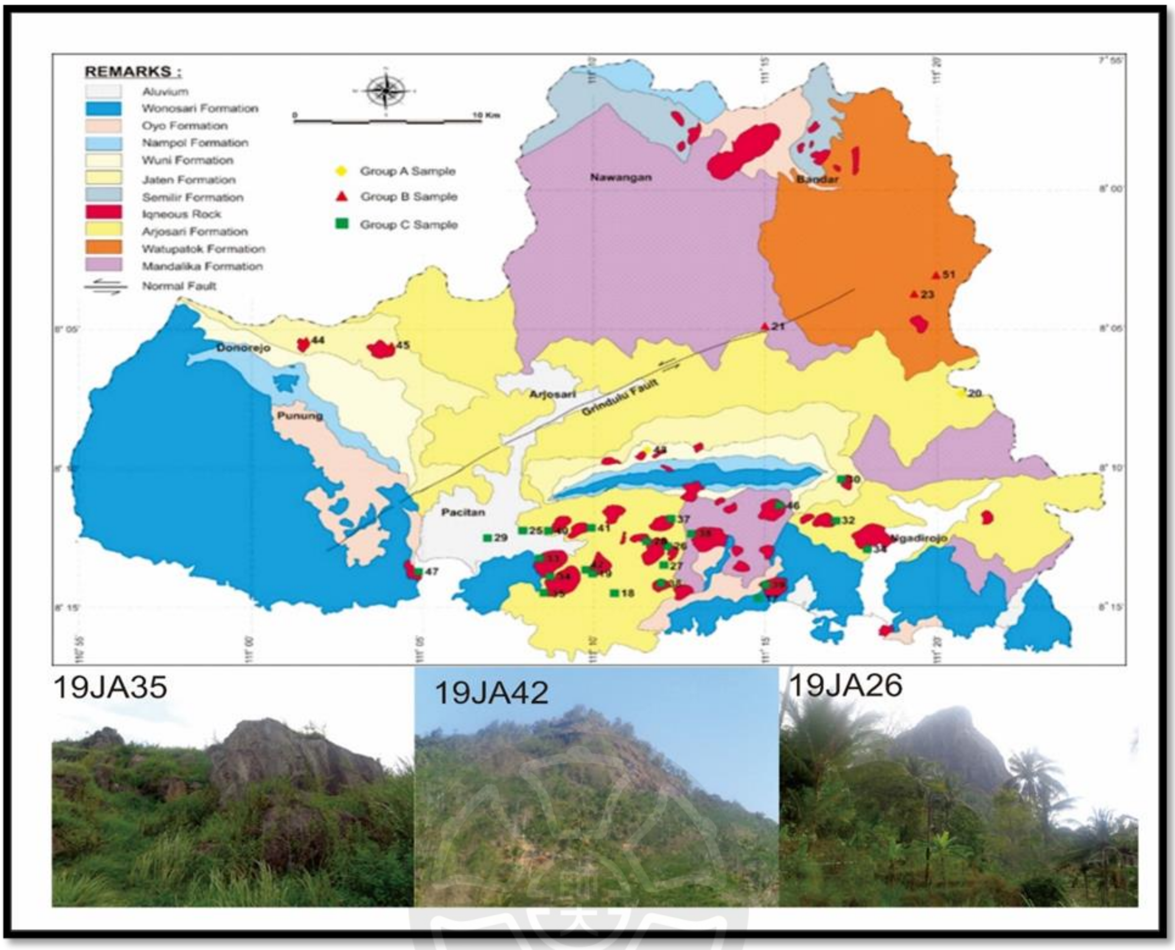

Fig. 4.1. Simplified geological map (modified from Samodra et al., 1992) showing sample locations and major volcanic suites in the Pacitan area. The collected samples are divided into three groups based on their geochemical characteristics and spatial distribution.

Fig. 4.2. Collected volcanic rock samples in Pacitan, East Java.

4.2. Geochronology

Zircon grains from the Pacitan area exhibit variable morphologies. Some samples contain elongate zircons with length-to-width ratios of approximately 2:1, while others contain isometric zircons with length-to-width ratios close to 1:1. The zircons are mostly colorless to light brown, subhedral, and display oscillatory zoning-features consistent with a magmatic origin (Hoskin and Schaltegger, 2003).

A total of 14 samples from the Pacitan magmatic rocks were dated using the LA-ICP-MS method. The zircon grains show a wide range of U concentrations (26 to 1935 ppm) and Th/U ratios (0.30 to 2.20). The U-Pb dating results are plotted on Concordia diagrams and summarized in **Table. 4.2**, along with the sample coordinates and rock types. All reported ages are based on $^{206}Pb/^{238}U$ ratios, presented at a 95% confidence level (2σ analytical uncertainties), and are accompanied by mean square weighted deviations (MSWD). The magmatic ages obtained in this study range from 26.0 ± 0.3 to 26.7 ± 0.4 Ma (Late Oligocene; **Fig. 4.3**), 19.9 ± 0.4 Ma (Early Miocene; **Fig. 4.4**), and 11.4 ± 0.2 to 13.4 ± 0.3 Ma (Middle Miocene; **Fig. 4.5**). While Cenozoic volcanic successions in this region are known to have begun in the Eocene, our results highlight a significant number of zircon ages from the Late Oligocene, Early Miocene, and Middle Miocene periods **(Fig. 4.6).**

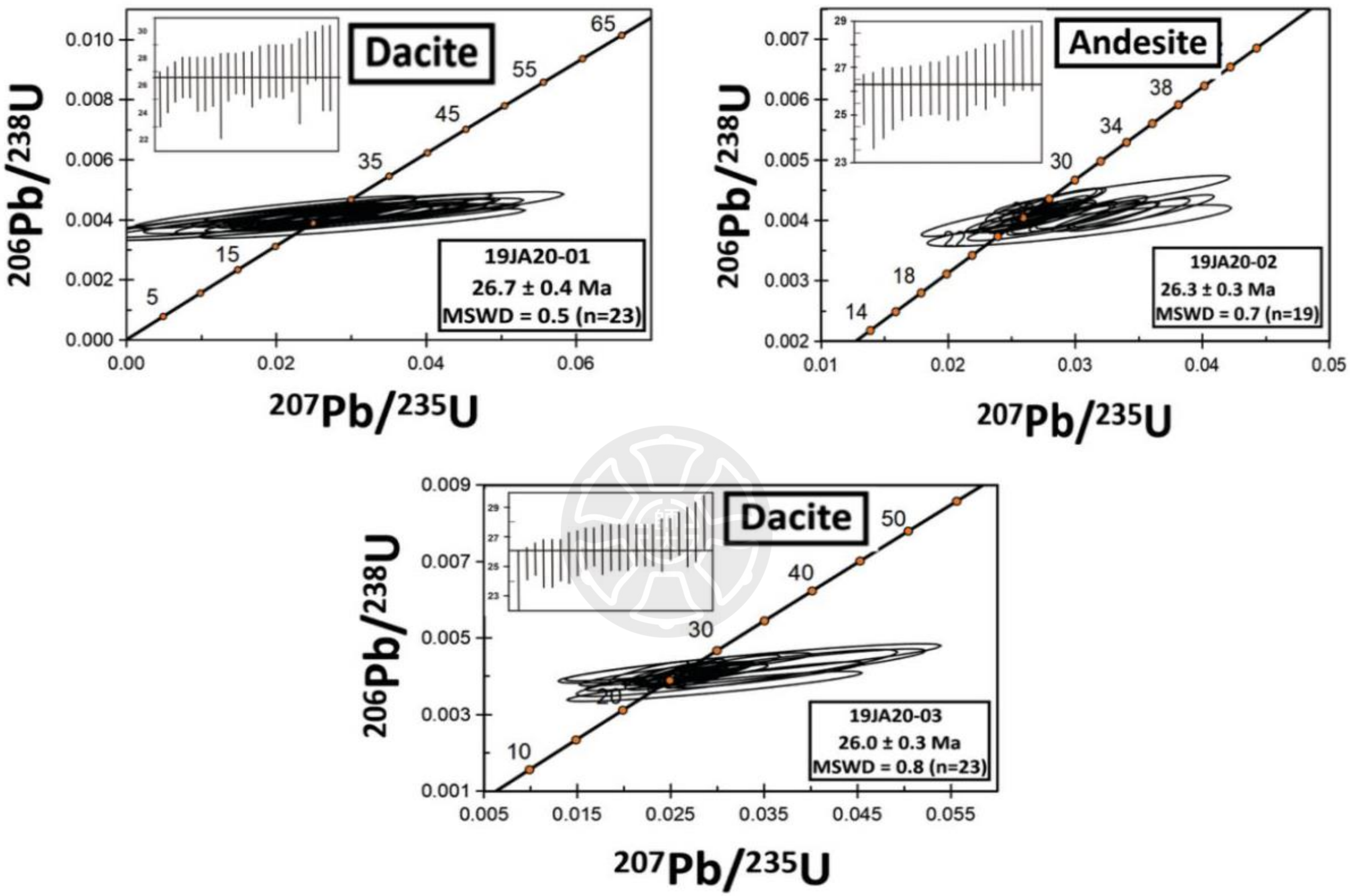

Fig. 4.3. Concordia plot of Pacitan samples showing Late Oligocene ages (26.0 ± 0.3 Ma – 26.7 ± 0.4 Ma), dated by LA-ICP-MS.

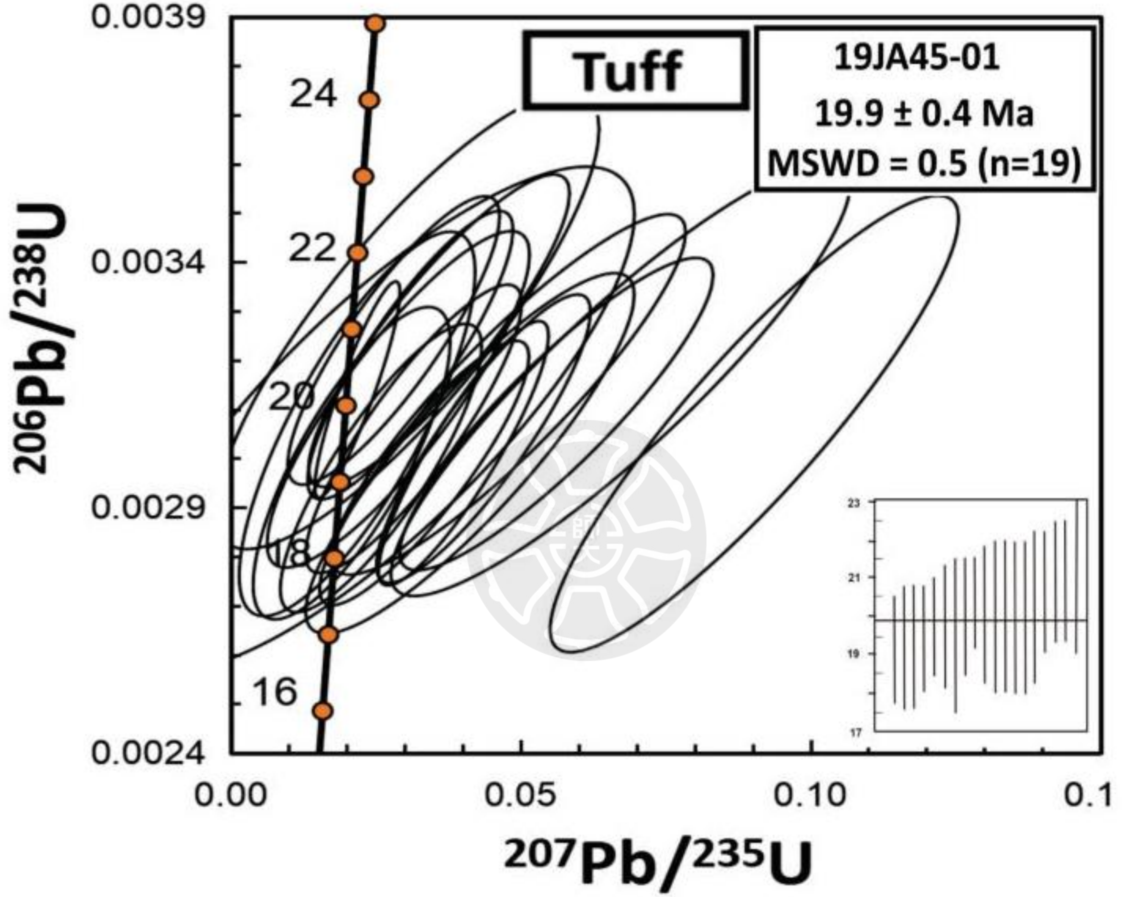

Fig. 4.4. Concordia plot of Pacitan samples showing Early Miocene age (19.9 ± 0.4 Ma), dated by LA-ICP-MS.

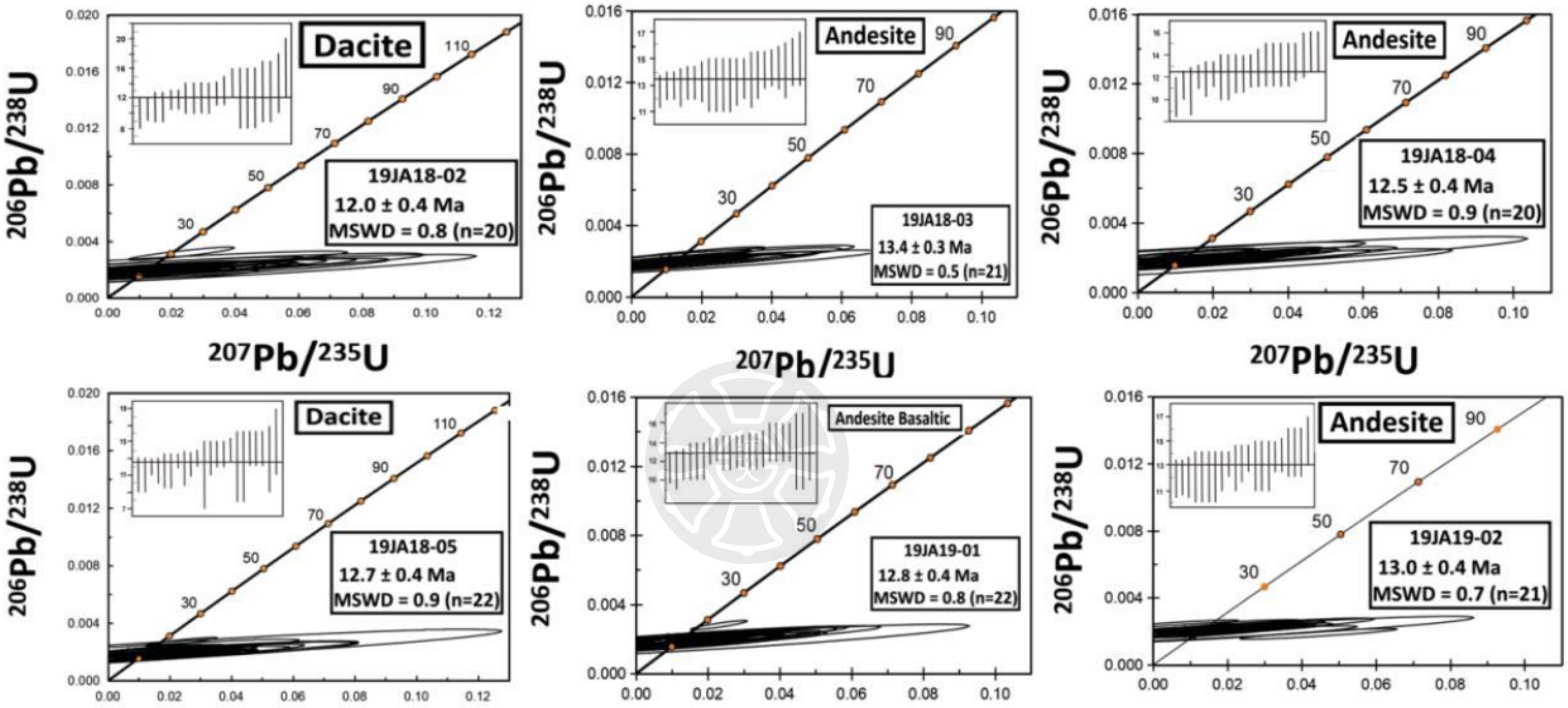

Fig. 4.5. Concordia plot of Pacitan samples showing Middle Miocene ages (13.4 ± 0.3 Ma – 11.4 ± 0.2 Ma), dated by LA-ICP-MS.

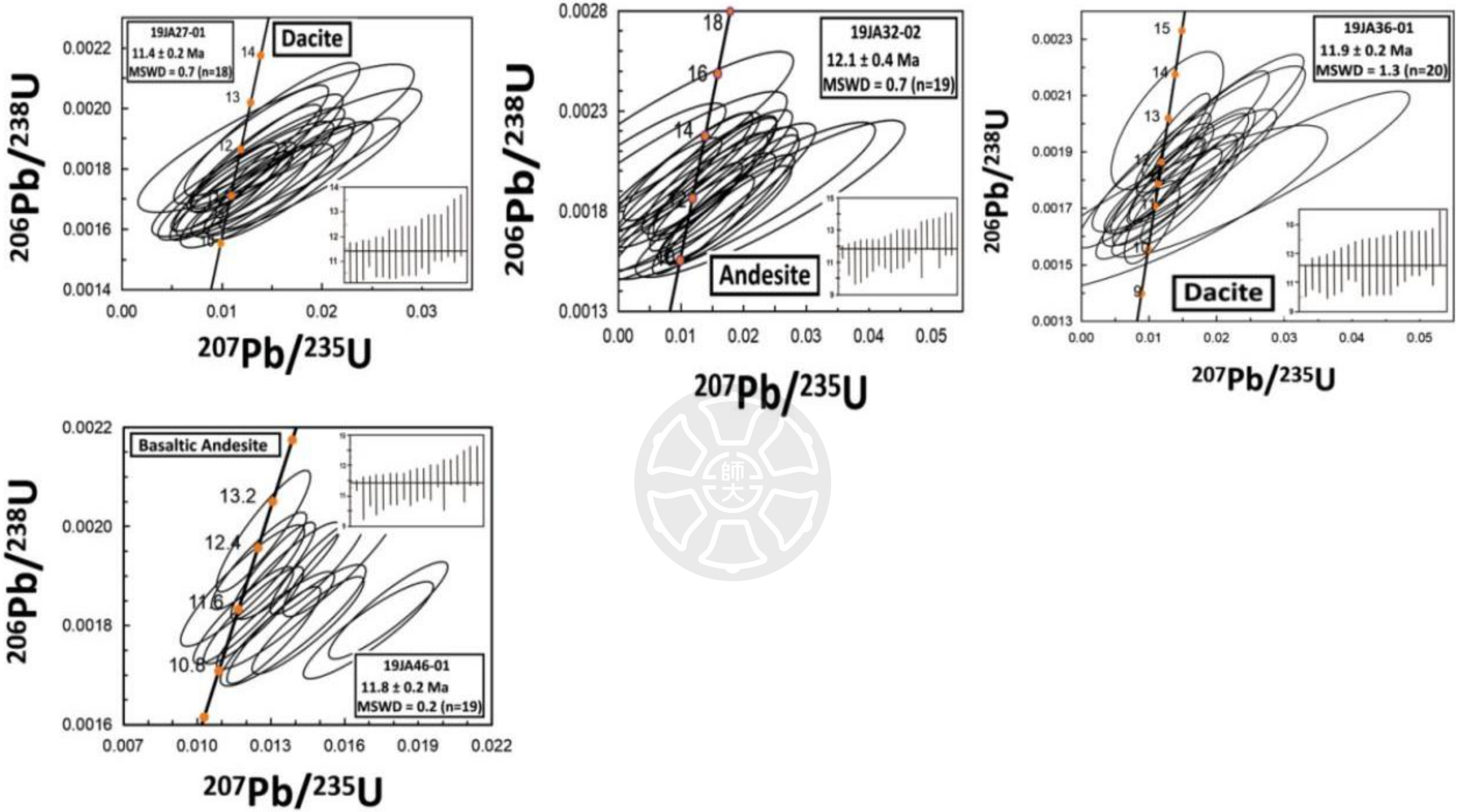

Fig. 4.5. continued 2. Concordia plot of Pacitan samples showing Middle Miocene ages (13.4 ± 0.3 Ma – 11.4 ± 0.2 Ma), dated by LA-ICP-MS.

Table. 4.2. Summary of the sample localities and zircon U-Pb ages of the Pacitan.

Sample	Longitude	Latitude	Rock Type	Ages ±2σ (Ma)	MSWD	Number of used for mean ages calculation
Late Oligocene						
19JA20-01	111°21'20.01"	8°7'17.36"	Dacite	26.7 ± 0.4	0.5	19
19JA20-02	111°21'20.01"	8°7'17.36"	Andesite	26.3 ± 0.3	0.7	19
19JA20-03	111°21'20.01"	8°7'17.36"	Dacite	26.0 ± 0.3	0.8	23
Early Miocene						
19JA45-01	111°01'15.1"	8°05'13.1"	Tuff	19.9 ± 0.4	0.5	20
Middle Miocene						
19JA18-02	111°10'45.25"	8°14'14.88"	Dacite	12.0 ± 0.4	0.8	20
19JA18-03	111°10'45.25"	8°14'14.88"	Andesite	13.4 ± 0.3	0.5	21
19JA18-04	111°10'45.25"	8°14'14.88"	Andesite	12.5 ± 0.4	0.9	20
19JA18-05	111°10'45.25"	8°14'14.88"	Dacite	12.7 ± 0.4	0.9	22
19JA19-01	111°10'0.24"	8°13'48.93"	Andesite	12.8 ± 0.4	0.8	22
19JA19-02	111°10'0.24"	8°13'48.93"	Basaltic andesite	13.0 ± 0.4	0.7	21
19JA27-01	111°12'01.9"	8°12'37.8"	Dacite	11.4 ± 0.2	0.7	18
19JA32-02	111°17'15.9"	8°12'05.0"	Andesite	12.1 ± 0.4	0.7	19
19JA36-01	111°12'03.1"	8°13'37.1"	Dacite	11.9 ± 0.2	1.3	20
19JA46-01	111°15'32.2"	8°11'15.9"	Basaltic andesite	11.8 ± 0.2	0.2	19

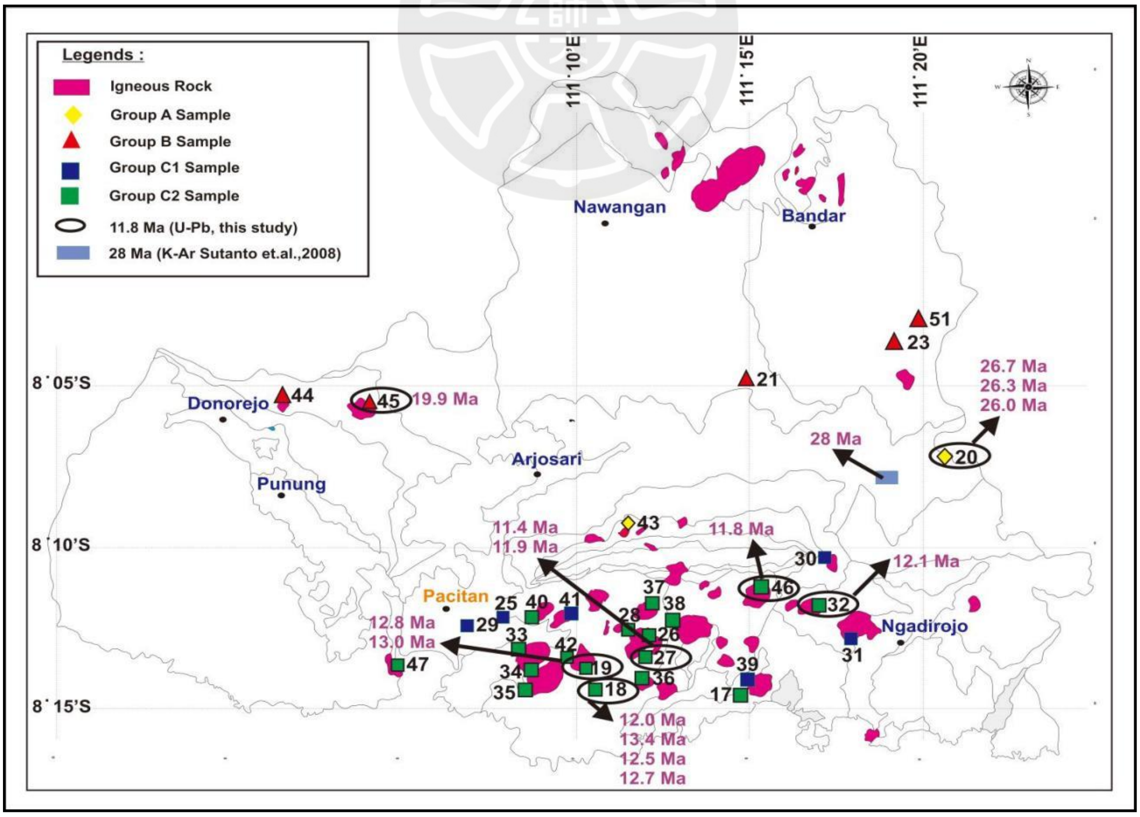

Fig. 4.6. Pacitan map showing the age of volcanic rocks based on the results of zircon U-Pb analysis (this study), combined with data from previous researchers using K-Ar analysis.

4.2.1 Group A

The samples collected from Group A (sample codes 19JA20-01, 19JA20-02, 19JA20-03) with rock types dacite and andesite showed magmatic ages ranging from 26.0 ± 0.3 to 26.7 ± 0.4 Ma (Late Oligocene). The mean ages are $^{206}Pb/^{238}U$ ages reported at the 95% confidence level (i.e., 2σ analytical uncertainties), along with mean square weighted deviations (MSWD). These ages are younger than those reported in previous studies, which were around 28 Ma (Sutanto et al., 2008). All zircon grains are magmatic in origin, with U concentrations ranging from 43 to 1395 ppm, Th concentrations from 40 to 2958 ppm, and U/Th ratios from 0.36 to 2.20.

4.2.2 Group B

The sample collected from Group B, with rock type tuff and sample code 19JA45-01, showed a magmatic age of 19.9 ± 0.4 Ma (Early Miocene). The mean age is a $^{206}Pb/^{238}U$ age at the 95% confidence level (i.e., 2σ analytical uncertainties), coupled with MSWD. This age is younger than those of Group A. All zircon grains are magmatic in origin, with U concentrations ranging from 55 to 491 ppm, Th concentrations from 20 to 610 ppm, and U/Th ratios from 0.49 to 1.17.

4.2.3 Group C

The samples collected from Group C (sample codes 19JA18-02, 19JA18-03, 19JA18-04, 19JA18-05, 19JA19-01, 19JA19-02, 19JA27-01, 19JA36-01, 19JA32-02, 19JA46-01) with rock types ranging from trachy-basalt to dacite, showed magmatic ages ranging from 11.4 ± 0.2 to 13.4 ± 0.3 Ma (Middle Miocene). The mean ages are $^{206}Pb/^{238}U$ ages at the 95% confidence level (i.e., 2σ analytical uncertainties), coupled with MSWD. These ages are younger than those from previous studies, which range from 15 Ma to 19 Ma (Soeria-Atmadja et al., 1994). All zircon grains are magmatic, with U concentrations from 37 to 1935 ppm, Th concentrations from 13 to 3924 ppm, and U/Th ratios from 0.33 to 1.90 **(Fig. 4.7).**

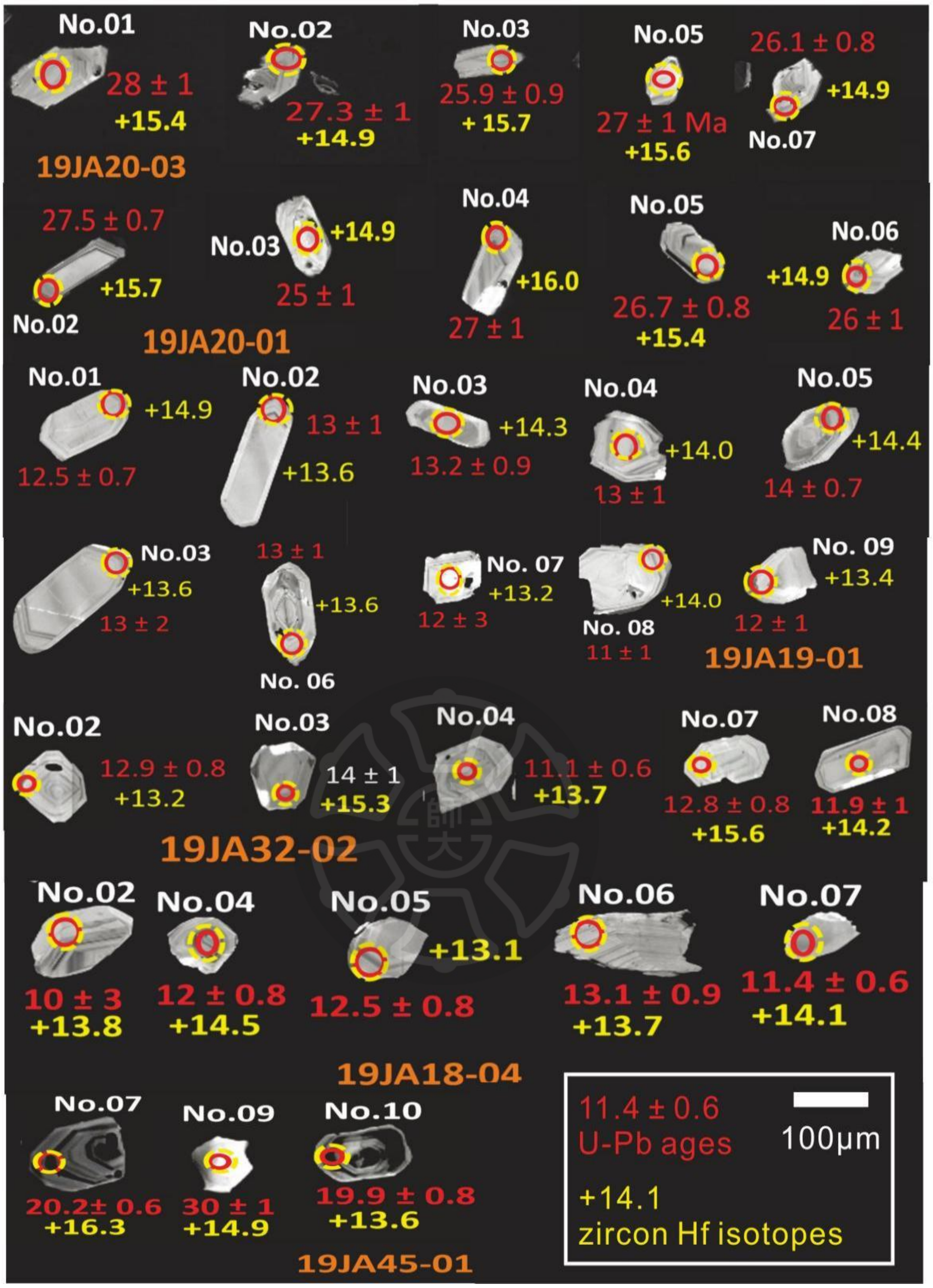

Fig. 4.7. Zircon U-Pb and Hf isotope age results of magmatic rocks from Pacitan.

4.3. Petrography

A total of three types of volcanic rocks were identified: rhyolite, dacite, and andesite. All specimens are fresh, light grey to brown, with porphyritic, subhedral textures and medium to coarse grains. The rocks are grouped into three categories:

- Group A consists of samples 19JA20-01 and 19JA20-03, both classified as dacite.
- Group B consists of samples 19JA21-02, 19JA23-01, and 19JA23-02, which include dacite and rhyolite.
- Group C includes samples 19JA17-01, 19JA18-02, 19JA18-03, 19JA18-04, 19JA18-05, 19JA19-02, and 19JA19-03, comprised andesite and dacite.

Table 4.3. Petrographic analysis results of volcanic rocks in Pacitan.

Thin Section No.	Rock Type	Mineral Portion (%)						Phenocrysts (%)	Groundmass (%)	Total Counts	Group
		Plagioclase	Quartz	Hornblende	Biotite	Pyroxene	Sanidine				
19JA23-01	Rhyolite	34	16	-	1	-	2	52	48	380	B
19JA23-02	Rhyolite	42	14	-	2	-	2	60	40	350	B
19JA20-01	Dacite porphyry	50	14	2	2	-	-	68	32	370	A
19JA20-03	Dacite porphyry	50	9	1	2	-	-	62	38	330	A
19JA21-02	Dacite porphyry	55	6	-	2	-	-	63	37	378	B
19JA18-02	Dacite porphyry	58	16	4	2	-	-	80	20	350	C2
19JA18-05	Dacite porphyry	50	4	-	2	-	-	56	44	380	C2
19JA19-02	Andesite	46	2	10	-	6	-	64	36	376	C1
19JA18-03	Andesite	30	1	2	-	6	-	40	60	280	C2
19JA18-04	Andesite	46	3	11	-	7	-	67	33	250	C2

4.3.1. Group A

4.3.1.1. Dacite Porphyry

Two dacite rock samples were selected for petrographic analysis: 19JA20-01 and 19JA20-03. The hand specimens are grey to brown and is a fresh rock sample. All rocks exhibit porphyritic textures, subhedral crystal forms, and coarse grains. The mineral composition includes phenocrysts (62–68%) and groundmass (32–40%), with plagioclase (50%), quartz (9–14%), biotite (2%), and hornblende (1–2%) **(Fig. 4.8a, 4.8b)**.

Plagioclase is the most abundant phenocryst phase, occurring as subhedral to euhedral grains ranging from 0.8 to 2.0 mm in length, though most grains are between 0.3 and 0.5 mm long. Carlsbad-albite twinning is observed in the plagioclase crystals. Some phenocryst grains exhibit ragged edges due to resorption. Fresh phenocrysts show well-developed cleavage.

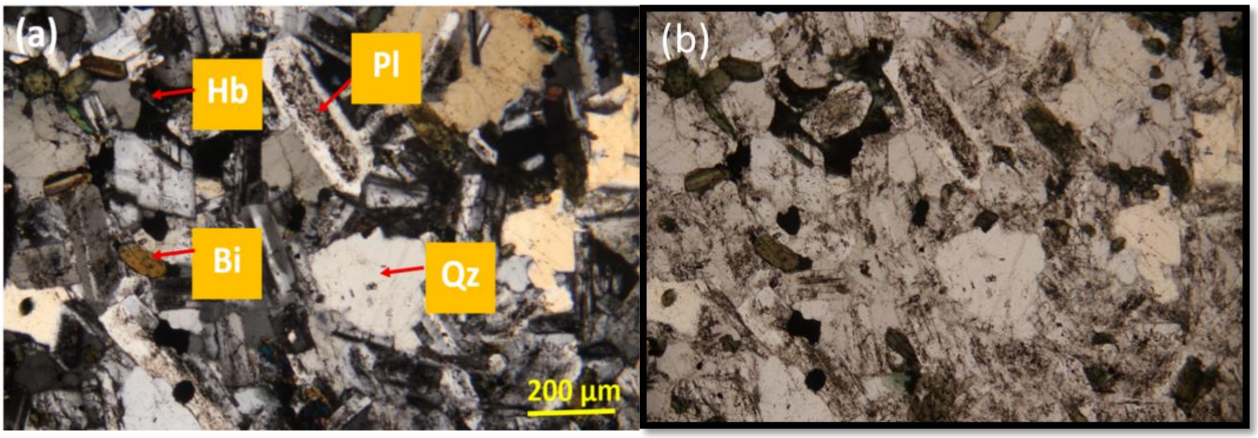

Fig. 4.8. Photomicrographs showing mineral assemblages and textures from dacite porphyry (Group A): (a) under cross-polarized light; (b) under plane-polarized light, from samples collected in Pacitan.

4.3.2 Group B

4.3.2.1 Dacite Porphyry

The dacite rock sample selected for petrographic analysis consists of one sample with the code 19JA21-02. The dacite is grey to brown in color and is a fresh rock sample. The rock is porphyritic, with subhedral textures and coarse grains. The composition includes phenocrysts (63%) and groundmass (37%), with mineral constituents comprised plagioclase (55%), quartz (6%), and biotite (2%) **(Fig. 4.9a, 4.9b).**

The most abundant phenocryst phase is plagioclase, which occurs as subhedral to euhedral grains ranging from 1.0 to 4.0 mm in length, though most grains are between 0.3 and 0.6 mm long. Carlsbad-albite twinning is present in the plagioclase. Some phenocryst grains show ragged edges resulting from resorption. Fresh phenocrysts display well-developed cleavage.

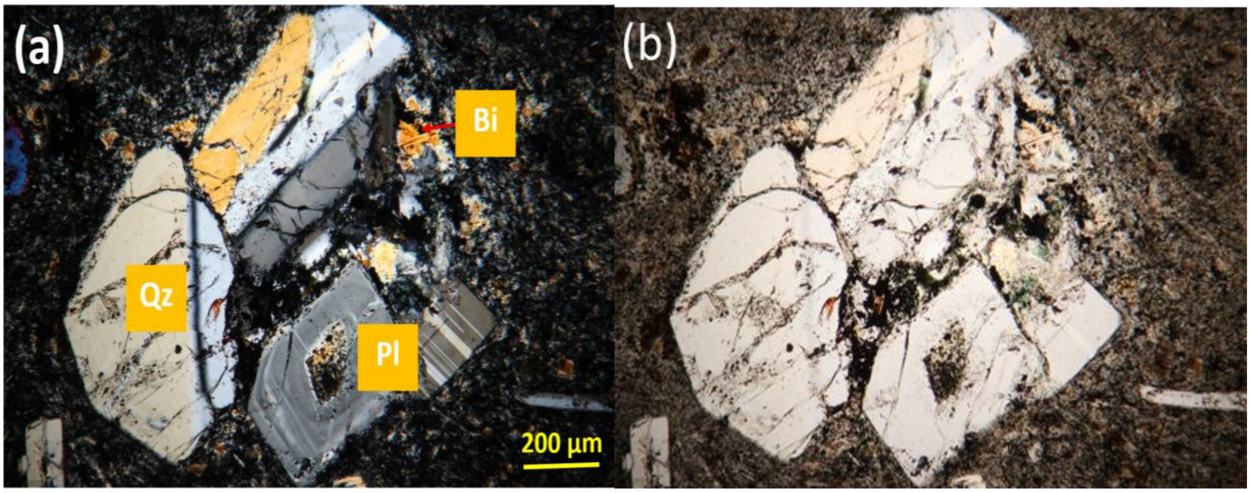

Fig. 4.9. Photomicrographs showing mineral assemblages and textures from dacite porphyry (Group B): (a) under cross-polarized light; (b) under plane-polarized light, from samples collected in Pacitan.

4.3.2.2 Rhyolite

The rhyolite rock samples selected for petrographic analysis consist of two samples with the codes 19JA23-01 and 19JA23-02. The rhyolite is light grey in color and is a fresh rock sample. The rocks are porphyritic, with subhedral textures and medium to coarse grains. The composition includes phenocrysts (52–60%) and groundmass (40–48%), with mineral constituents including plagioclase (34–42%), quartz (14–16%), biotite (1–2%), and sanidine (2%) **(Fig. 4.10a, 4.10b).**

The most abundant phenocryst phase is plagioclase, occurring as subhedral to euhedral grains ranging from 0.8 to 2.0 mm in length, though most are between 0.1 and 0.4mm. Plagioclase exhibits Carlsbad-albite twinning. Quartz phenocrysts are subhedral to euhedral, ranging from 0.5 to 1.5 mm, with most between 0.1 and 0.3 mm. Some phenocryst grains show ragged edges due to resorption. Fresh phenocrysts display well-developed cleavage.

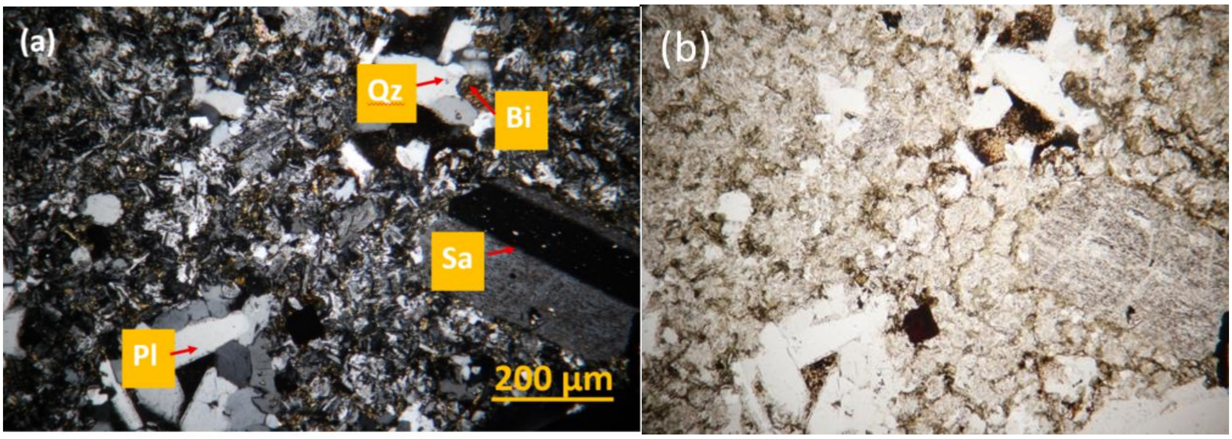

Fig. 4.10. Photomicrographs showing mineral assemblages and textures from Rhyolite (Group B): (a) under cross-polarized light; (b) under plane-polarized light, from samples collected in Pacitan.

4.3.3 Group C

4.3.3.1 Andesite

Three andesite rock samples were selected for petrographic analysis, with the codes 19JA18-03, 19JA18-04, and 19JA19-02. Group C is subdivided into two subgroups: C1 and C2.

- Group C1 consists of one sample (19JA19-02). The andesite is dark grey to black in color and is a fresh rock sample. It exhibits subhedral intergranular texture and coarse grains. The composition includes phenocrysts (64%) and groundmass (36%), with plagioclase (46%), hornblende (10%), pyroxene (6%), quartz (2%), and biotite (2%) **(Fig. 4.11a, 4.11b).**
- Group C2 consists of two samples (19JA18-03 and 19JA18-04). The andesite is also dark grey to black in color and is a fresh rock sample. It shows subhedral intergranular texture and coarse grains. The composition includes phenocrysts (40–67%) and groundmass (33–60%), with plagioclase (30–46%), pyroxene (6–7%), hornblende (2–11%), and quartz (1–3%), Plagioclase is the most abundant phenocryst, occurring as subhedral to euhedral grains ranging from 0.1 to 3.0 mm in length, with most grains between 0.4 and 0.6mm. Carlsbad-albite twinning is observed in plagioclase. Some phenocryst grains show ragged edges due to resorption. Hornblende appears as subhedral to euhedral grains. Fresh phenocrysts display well-developed cleavage.

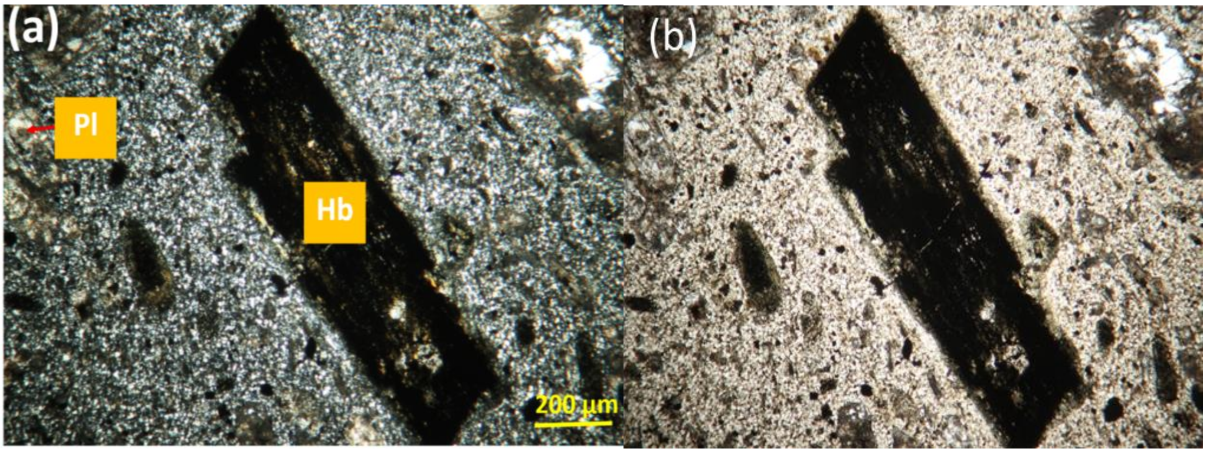

Fig. 4.11. Photomicrographs showing mineral assemblages and textures from Andesite (Group C): (a) under cross-polarized light; (b) under plane-polarized light, from samples collected in Pacitan.

4.3.3.2 Dacite Porphyry

Two dacite rock samples were selected for petrographic analysis, with the codes 19JA18-02 and 19JA18-05. The dacite is grey to brown in color and is a fresh. The rocks are porphyritic, with subhedral textures and coarse grains. The composition includes phenocrysts (56–80%) and groundmass (20–44%), with plagioclase (55–58%), quartz (4–16%), biotite (2%), and hornblende (4%) **(Fig. 4.12a, 4.12b).**

Plagioclase is the most abundant phenocryst phase, appearing as subhedral to euhedral grains ranging from 1.5 to 5.0 mm in length, though most are between 1.0 and 2.0mm. Carlsbad-albite twinning is present. Some phenocryst grains show ragged edges due to resorption. Fresh phenocrysts display well-developed cleavage and strong pleochroism. Zoning in plagioclase includes oscillatory, reverse, and normal zoning. This zoning indicates the failure of the mineral to attain equilibrium with the surrounding melt and is usually attributed to changes in temperature and pressure either within the magma chamber or during magma ascent (McBirney, 1979). The coexistence of normal, reverse, and oscillatory zoning is commonly interpreted as evidence of magma mixing (Lung et al., 1982).

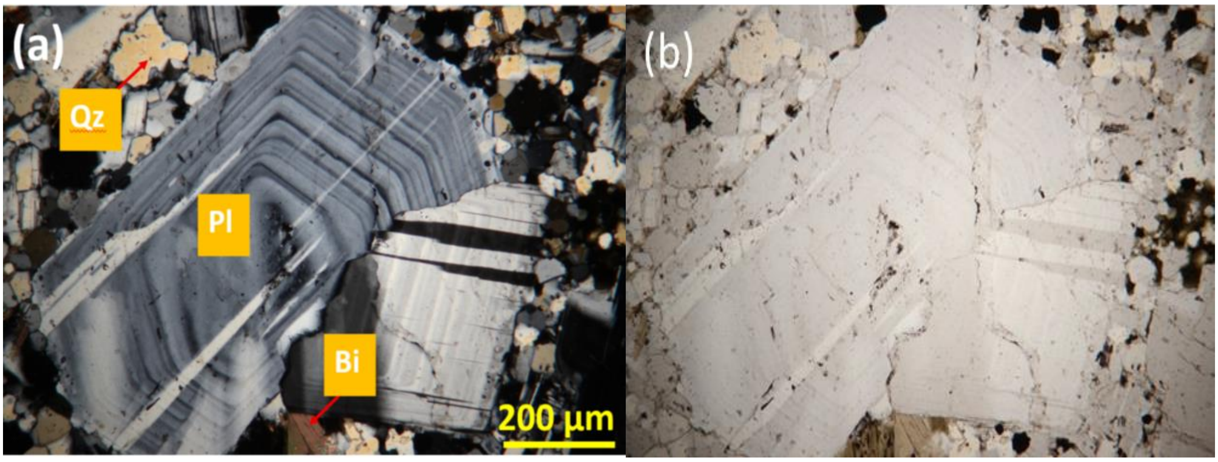

Fig. 4.12. Photomicrographs showing mineral assemblages and textures from dacite porphyry (Group C): (a) under cross-polarized light; (b) under plane-polarized light, from samples collected in Pacitan.

4.4. Geochemistry

Whole-rock major and trace element compositions of volcanic rocks from the Pacitan area were divided into three groups (Group A, Group B, and Group C) based on compositional differences and geochemical variations.

4.4.1. Major Elements – Group A

Samples collected from Group A in the Pacitan area for major element compositions are shown in **Table 4.4**. The Group A samples exhibit variable L.O.I. (loss on ignition, 0.9–2.1 wt.%), likely reflecting different degrees of alteration. Four samples were collected, comprising sub-alkaline andesite to dacite, with SiO_2 contents ranging from 59 to 68 wt.% **(Fig. 4.13a).** These samples generally exhibit medium-K to low-K characteristics within the calc-alkaline series **(Fig. 4.13b)**. In the Harker diagram, these rocks show negative correlations with TiO_2 (0.36–0.84 wt.%), Fe_2O_3 (2.90–7.17 wt.%), MgO (1.07–2.83 wt.%), MnO (0.09–0.15 wt.%), and CaO (4.21–5.61 wt.%) (Fig. 35). Variation diagrams show La concentrations from 7.5 to 9.70 ppm, Ba from 134 to 150 ppm, Ni from 16.7 to 43.1 ppm, Th from 1.08 to 2.32 ppm, Yb from 0.26 to 0.88 ppm, Zr from 105 to 145 ppm, Sr from 242 to 278 ppm, and La/Yb from 1.46 to 5.52 ppm **(Fig.4.14)**. La/Yb, Ni, La, and Zr show positive correlations with SiO_2, while Yb and Th show negative correlations with SiO_2

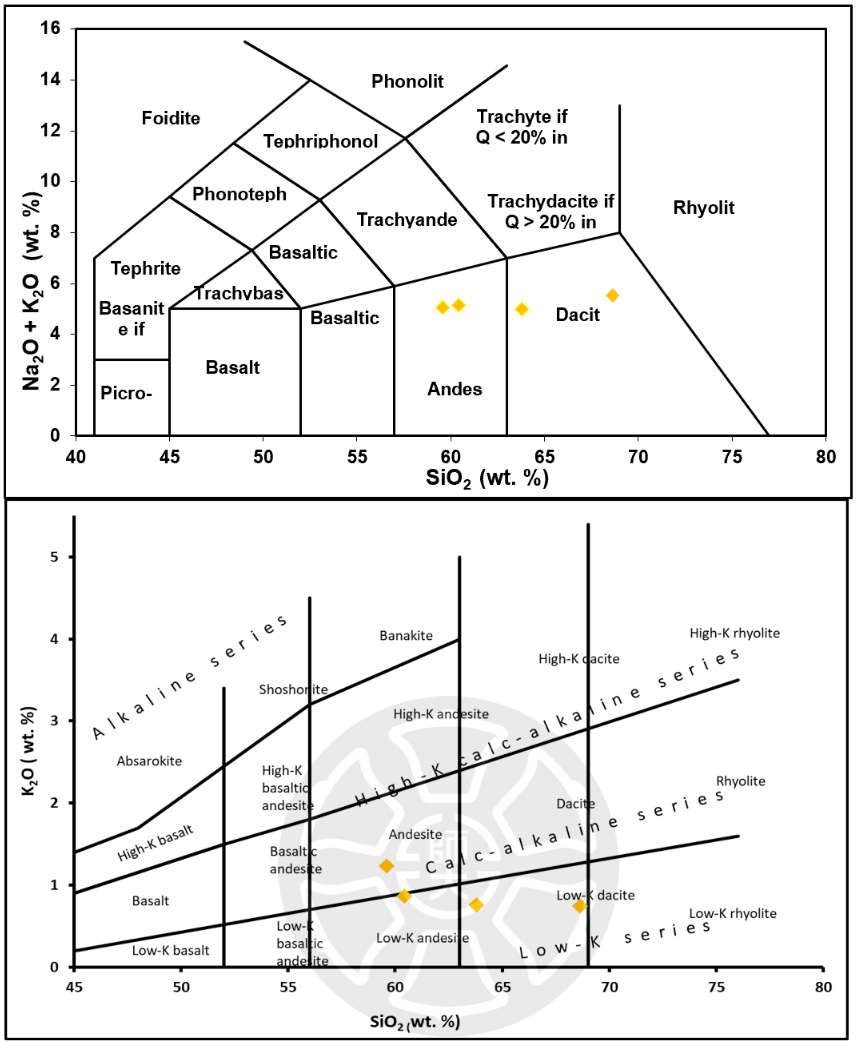

Fig. 4.13. **(a).** Total alkalis vs. SiO_2 diagram (after Le Bas et al., 1986; Le Maître, 2002) from Group A. The line separating the sub-alkaline and alkaline regions was after Irvine and Baragar (1971). **(b).** Variation of K_2O vs. SiO_2 from Group A. The classification for K_2O-SiO_2 contents was after Gill (1981), Ewart 1982 and Peccerillo and Taylor (1976), respectively.

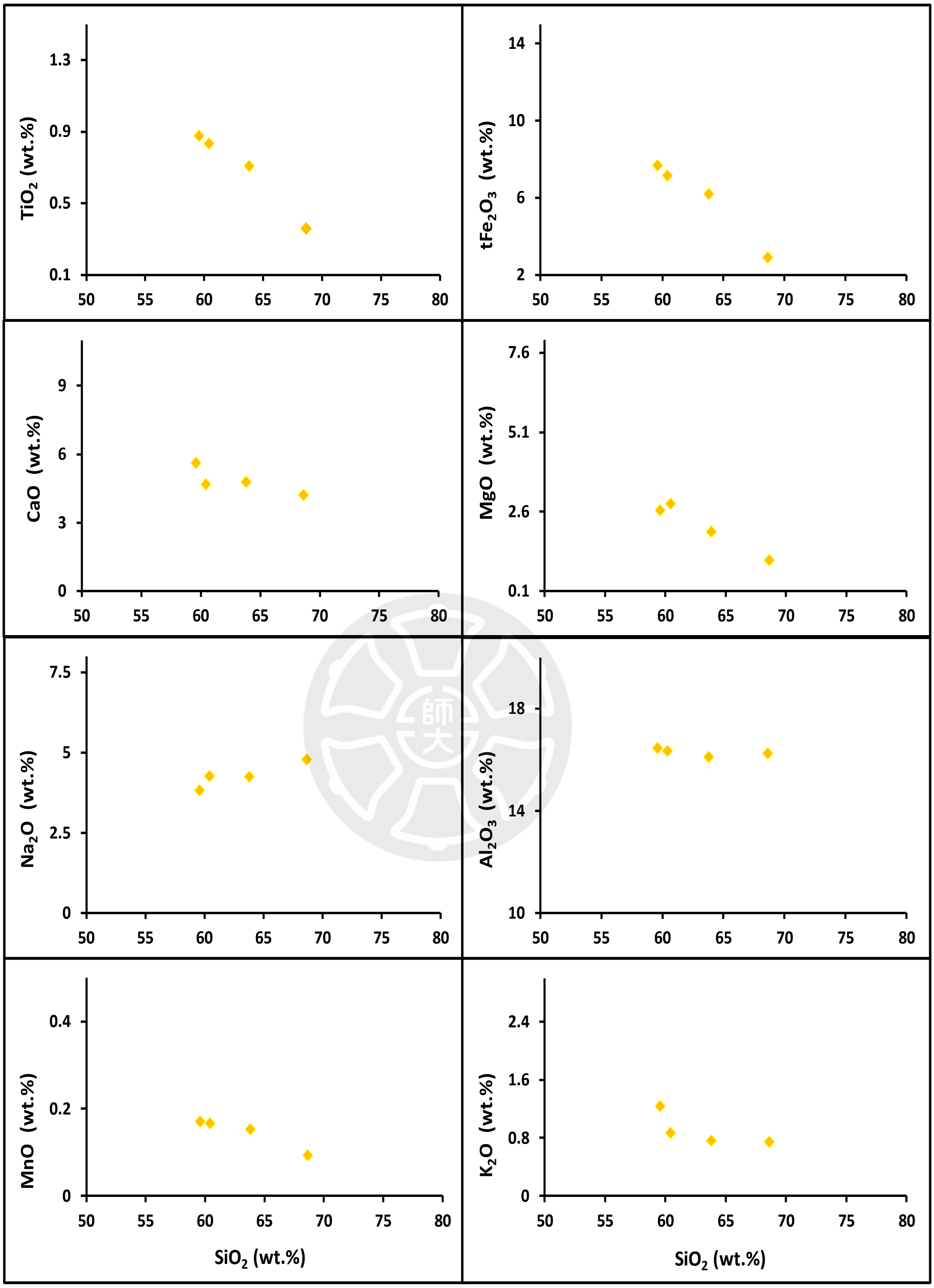

Fig. 4.14. Plot of major elements vs SiO_2 for the studied sample from Pacitan group A

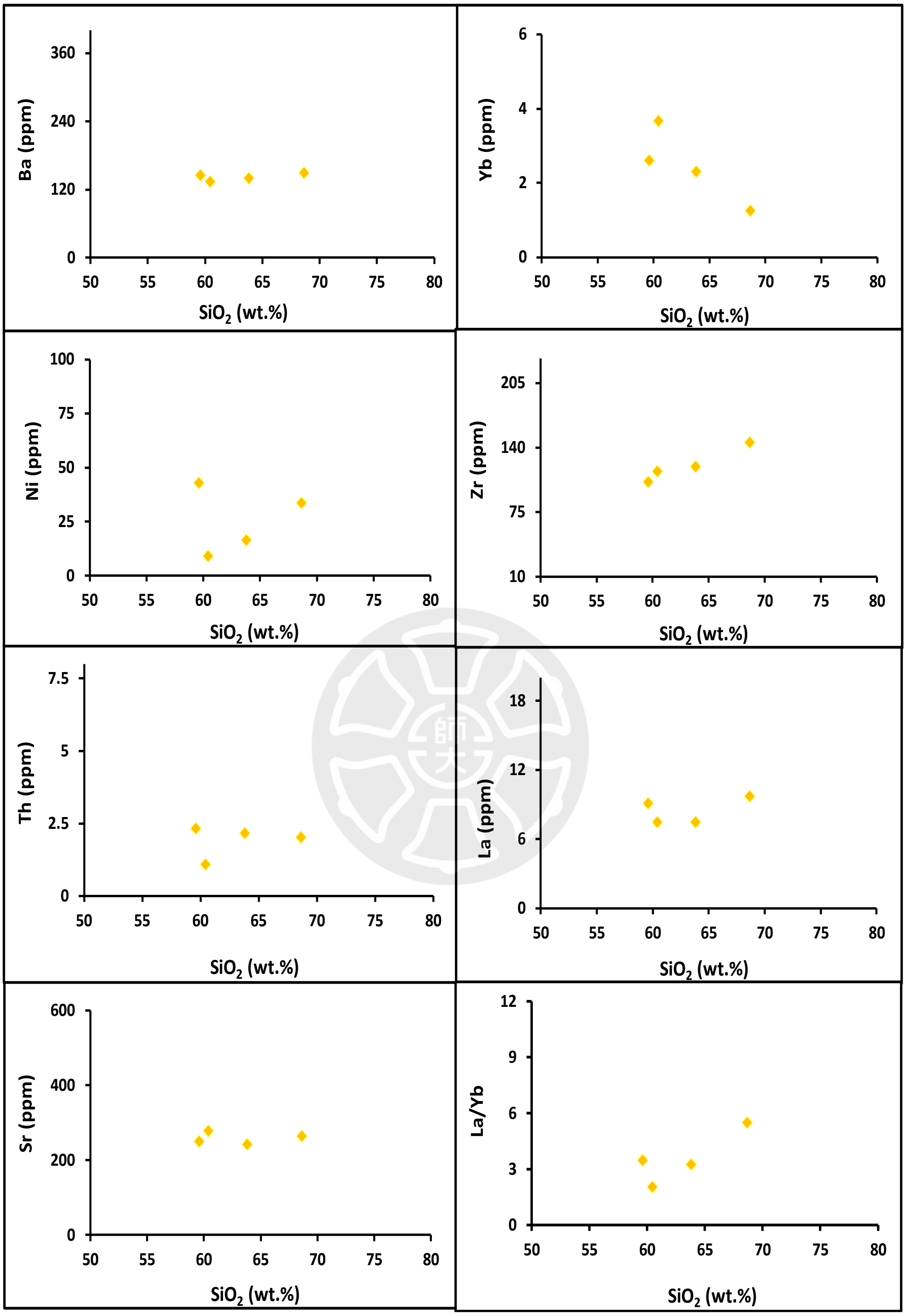

Fig. 4.15. Plot of variation elements vs SiO_2 for the studied sample from Pacitan (group A).

Table 4.4. Whole-rock major and trace-element composition for volcanic rocks in Pacitan (Group A)

Sample	19JA20-01	19JA20-02	19JA20-03	19JA43- 01
Latitude	S 8°7'17.36"	S 8°7'17.36"	S 8°7'17.36"	S 8°09'26.0"
Longitude	E 111°21'20.01"	E 111°21'20.01"	E 111°21'20.01"	E 111°11'43.2"
Unit	528	528	528	562
Locality	West of Masjid Al-Fallah	West of Masjid Al-Fallah	West of Masjid Al-Fallah	Wonojoyo
Group	A	A	A	A
Major Element				
SiO_2	68.6	59.6	63.8	60.4
TiO_2	0.36	0.87	0.70	0.84
Al_2O_3	16.2	16.4	16.1	16.3
tFe_2O_3	2.90	7.68	6.19	7.17
MnO	0.09	0.17	0.15	0.17
MgO	1.07	2.64	1.95	2.83
CaO	4.21	5.61	4.78	4.68
Na_2O	4.78	3.83	4.24	4.27
K_2O	0.74	1.23	0.76	0.87
P_2O_5	0.09	0.16	0.15	0.18
LOI	0.99	1.36	2.02	2.05
TOTAL	100	97	100	100
Trace element				
P	301	659	617	808
Sc	15.1	20.3	13.4	19.0
Ti	2023	5239	4120	4889
V	42.0	109	97.0	112
Cr	88.9	78.4	42.3	14.5
Mn	699	1295	1136	1213
Co	6.80	13.1	10.4	14.1
Ni	33.7	43.1	16.7	9.30
Cu	5.60	16.2	5.40	11.2
Zn	19.0	86.0	130	66.9
Ga	15.0	17.1	16.3	16.8
Rb	10.1	16.6	9.40	13.4
Sr	265	250	242	278
Y	10.4	23.8	21.3	34.0
Zr	145	105	121	116
Nb	1.90	2.30	2.90	2.00
Cs	0.15	0.22	0.14	0.27
Ba	150	145	140	134
La	9.70	9.10	7.50	7.48
Ce	17.1	19.3	16.6	19.6
Pr	1.96	2.59	2.30	3.05
Nd	7.40	11.3	10.3	14.6
Sm	1.57	3.01	2.73	4.22
Eu	0.80	1.03	0.94	1.35
Gd	1.67	3.63	3.24	5.21
Tb	0.26	0.61	0.54	0.88
Dy	1.68	3.97	3.55	5.68
Ho	0.37	0.86	0.77	1.27
Er	1.12	2.53	2.27	3.69
Tm	0.17	0.40	0.35	0.57
Yb	1.26	2.61	2.30	3.67
Lu	0.20	0.41	0.37	0.57
Hf	3.33	2.75	3.06	3.24
Ta	0.15	0.19	0.19	0.12
Pb	6.63	1.68	1.34	3.59
Th	2.02	2.32	2.16	1.08
U	0.53	0.67	0.60	0.30
Mg#	40	38	36	41

4.4.2. Major Elements – Group B

Samples collected from Group B in the Pacitan area for major element compositions are shown in **Table 4.5**. Group B samples exhibit variable L.O.I. (0.8–3.6 wt.%), likely reflecting different degrees of alteration. Six samples were collected, comprising sub-alkaline dacite to rhyolite, with SiO_2 contents ranging from 54 to 75 wt.% **(Fig. 4.16a)**. These samples generally exhibit medium-K to low-K characteristics within the calc-alkaline series **(Fig. 4.16b)**. In the Harker diagram, these rocks show negative correlations with TiO_2 (0.24–0.83 wt.%), Fe_2O_3 (2.74–5.26 wt.%), MgO (0.26–5.26 wt.%), MnO (0.07–0.27 wt.%), and CaO (0.36–5.27 wt.%) **(Fig. 4.17)**. Variation diagrams show La concentrations from 5.10 to 12.0 ppm, Ba from 26.0 to 208 ppm, Ni from 6.30 to 111 ppm, Th from 1.79 to 3.54 ppm, Yb from 2.69 to 5.35 ppm, Zr from 122 to 221 ppm, Sr from 38.2 to 237 ppm, and La/Yb from 0.68 to 2.59 ppm **(Fig. 4.18)**. La/Yb, Th, Sr, and Ba show negative correlations with SiO_2, while Yb, Zr, and La show positive correlations with SiO_2.

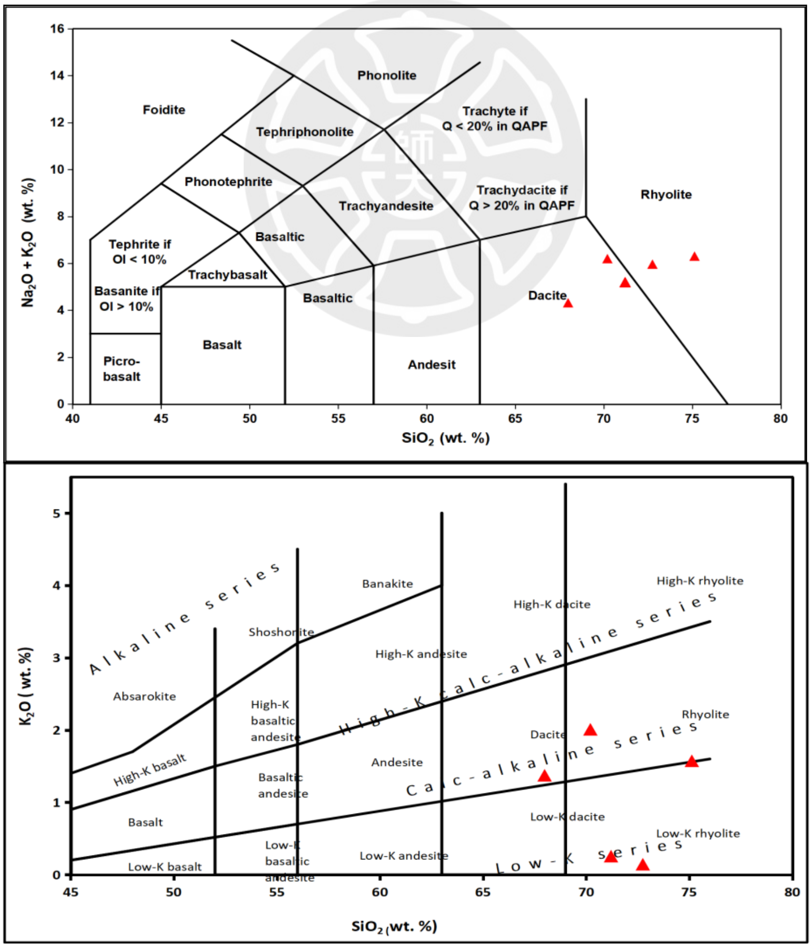

Fig. 4.16. **(a).** Total alkalis vs. SiO_2 diagram (after Le Bas et al., 1986; Le Maître, 2002) from Group A. The line separating the sub-alkaline and alkaline regions was after Irvine

and Baragar (1971). **(b).** Variation of K_2O vs. SiO_2 from Group A. The classification for K_2O-SiO_2 contents was after Gill (1981), Ewart 1982 and Peccerillo and Taylor (1976), respectively.

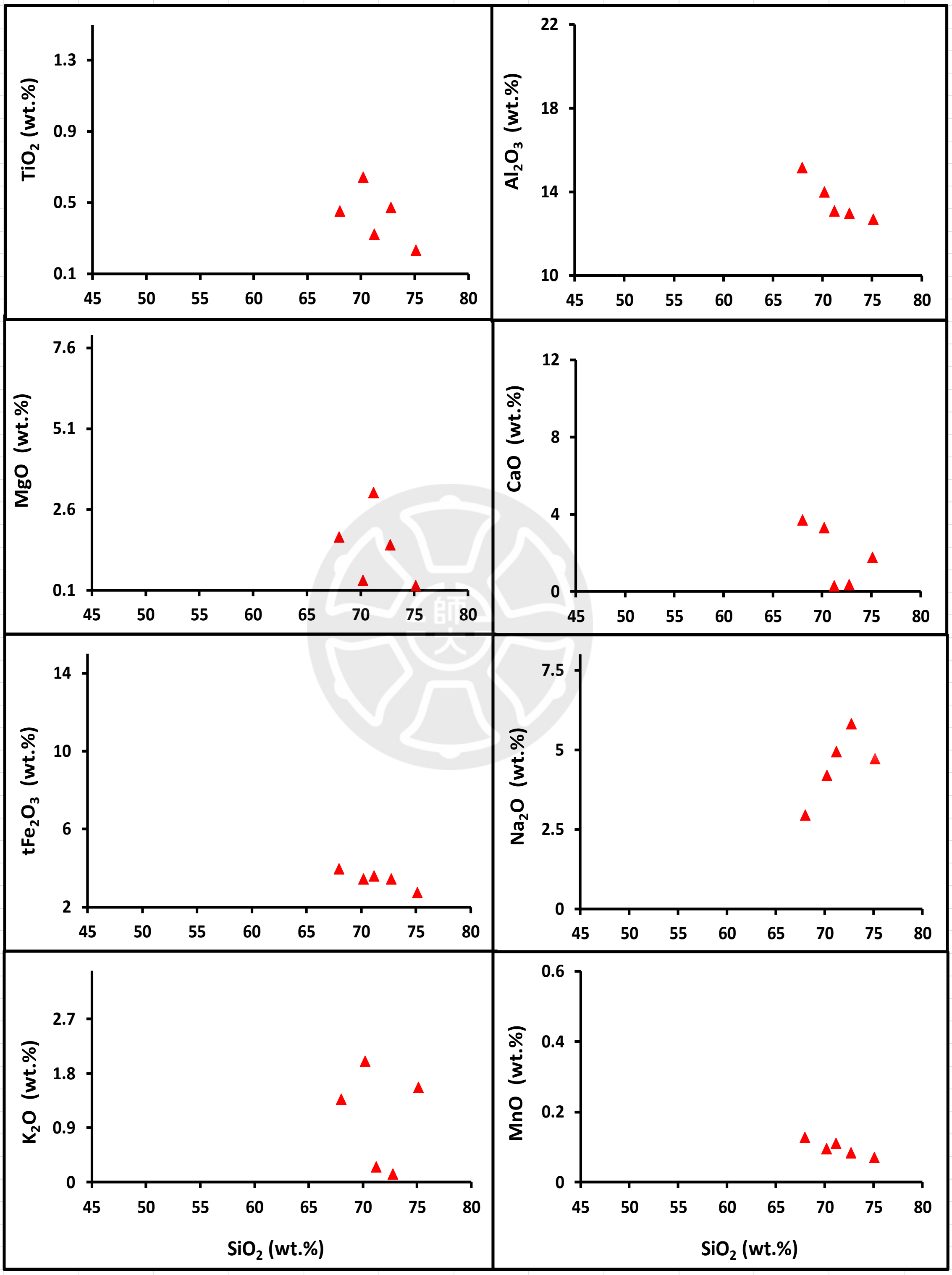

Fig.4.17. Plot of major elements vs SiO_2 for the studied sample from Pacitan (Group B).

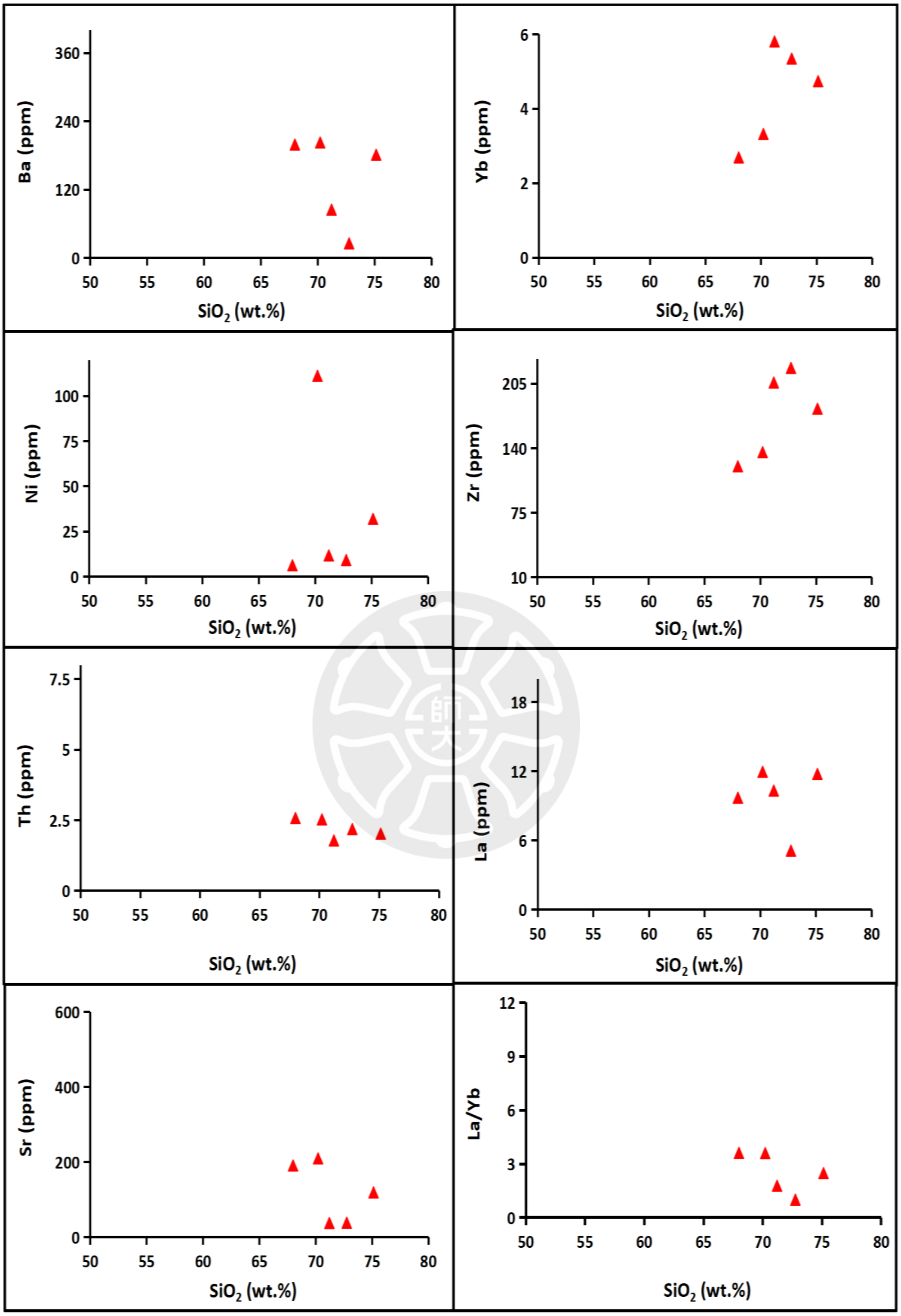

Fig. 4.18. Plot of variation elements vs SiO_2 for the studied sample from Pacitan (Group B).

Table 4.5. Whole-rock major and trace-element composition for volcanic rocks in Pacitan (Group B).

Sample	19JA21-01	19JA21-02	19JA23-02	19JA44-02	19JA51-02
Latitude	S 8°4'49.32"	S 8°4'49.32"	S 8°3'27.87"	S 8°05'13.1"	S 8°03'18.5"
Longitude	E 111°15'8.27"	E 111°15'8.27"	E 111°19'52.44"	E 111°01'15.1"	E 111°20'07.6"
Unit	49.3	49.3	259	246	386
Locality	West of Masjid At Taqwa	West of Masjid At Taqwa	South of Masjid Nurul Iman	Bandulan (River Valley)	Grindulu River
Group	B	B	B	B	B
Major Element					
SiO_2	54.1	70.2	72.8	68.0	71.2
TiO_2	0.8	0.64	0.47	0.45	0.32
Al_2O_3	14.7	14.0	13.0	15.2	13.1
tFe_2O_3	5.3	3.45	3.46	3.96	3.61
MnO	0.3	0.09	0.08	0.13	0.11
MgO	5.6	0.41	1.51	1.76	3.12
CaO	5.3	3.29	0.36	3.70	0.28
Na_2O	5.3	4.19	5.82	2.94	4.93
K_2O	0.0	2.01	0.15	1.38	0.26
P_2O_5	0.1	0.22	0.12	0.12	0.09
LOI	4.7	0.88	2.04	3.64	4.56
TOTAL	100.0	99	98	101	101
Trace Element					
P	417	920	436	632	581
Sc	23.3	17.6	31.0	23.2	16.1
Ti	4836	3774	2574	2449	1737
V	281	35.0	18.0	40.7	3.40
Cr	51.1	32.1	17.6	14	22.3
Mn	1958	743	618	950	799
Co	30.6	4.40	3.00	6.40	2.80
Ni	49.5	111	9.20	6.30	11.8
Cu	64.7	7.60	1.70	4.60	43.4
Zn	170	65	101	36.8	409
Ga	14.2	15.2	14.7	14.1	15.7
Rb	0.78	41.9	3.70	30.7	6.30
Sr	80	210	39.0	191	38.2
Y	20.5	31.3	49.8	24.6	52.1
Zr	47	136	221	122	206
Nb	0.91	3.20	3.60	2.00	3.50
Cs	0.14	0.63	0.14	1.24	0.13
Ba	14	203	26.0	199	23.5
La	3.0	12.0	5.10	9.70	10.3
Ce	7.6	27.2	12.9	21.5	26.8
Pr	1.28	3.93	1.97	2.86	4.02
Nd	6.5	17.2	9.20	12.1	19.1
Sm	2.16	4.38	3.22	3.03	5.72
Eu	0.77	1.3	1.02	0.99	1.62
Gd	3.03	5.01	5.83	3.48	7.40
Tb	0.52	0.81	1.11	0.58	1.28
Dy	3.44	5.19	7.77	3.78	8.71
Ho	0.76	1.13	1.73	0.82	1.91
Er	2.17	3.29	5.18	2.48	5.67
Tm	0.33	0.5	0.82	0.4	0.89
Yb	2.12	3.32	5.35	2.69	5.81
Lu	0.32	0.51	0.83	0.44	0.87
Hf	1.38	3.64	5.53	3.26	5.26
Ta	0.06	0.24	0.26	0.17	0.25
Pb	2.50	2.58	2.06	5.71	0.41
Th	0.40	2.53	2.19	2.58	1.79
U	0.14	1.95	0.61	0.81	0.64
Mg#	65	18	44	44	61

4.4.3. Major Elements – Group C

Samples collected from Group C in the Pacitan area are divided into two subgroups (C1 and C2). Major element compositions are shown in **Tables 4.6 – 4.7**.

Group C1:

Group C1 consists of 10 samples with variable L.O.I. (0.6–6.0 wt.%), likely reflecting different degrees of alteration. The samples are composed of sub-alkaline basalt to dacite with SiO_2 contents ranging from 50.99 to 61.26 wt.% **(Fig. 4.19a)**. These samples generally exhibit high-K to low-K characteristics within the calc-alkaline series **(Fig. 4.19b)**. In the Harker diagram, these rocks show negative correlations with TiO_2 (0.50–1.28 wt.%), total Fe_2O_3 (5.87–11.90 wt.%), MgO (2.14–3.94 wt.%), MnO (0.13–0.18 wt.%), and CaO (6.07–9.02 wt.%) **(Fig. 4.20).** Variation diagrams show La concentrations from 4.01 to 21.8 ppm, Ba from 64.0 to 387 ppm, Ni from 7.90 to 25.7 ppm, Th from 0.47 to 7.49 ppm, Yb from 1.71 to 3.11 ppm, and Zr from 67.5 to 113 ppm **(Fig. 4.21)**. La/Yb, Th, Sr, La, and Ba show positive correlations with SiO_2, while Yb and Zr show negative correlations with SiO_2.

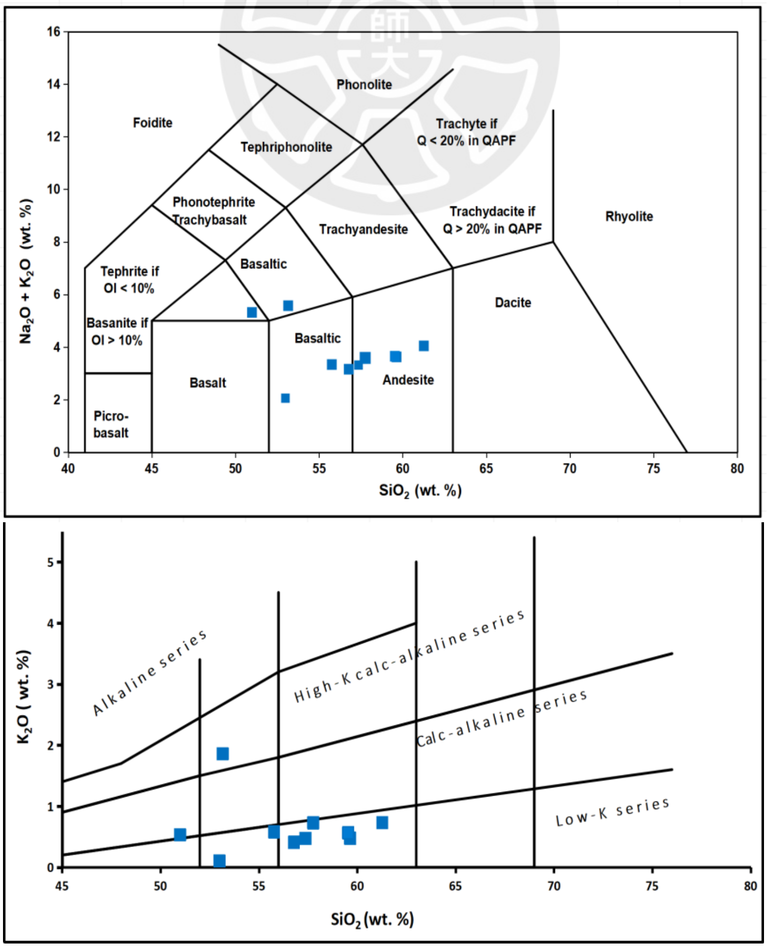

Fig. 4.19. (a) Total alkalis vs. SiO_2 diagram (after Le Bas et al., 1986; Le Maître, 2002) for the samples in Pacitan from Group C1. The line separating the sub-alkaline and alkaline regions was after Irvine and Baragar (1971). (b). Variation of K_2O vs. SiO_2 for the Pacitan volcanic rocks from Group C1. The classification for K_2O-SiO_2 contents was after Gill (1981), Ewart 1982 and Peccerillo and Taylor (1976), respectively.

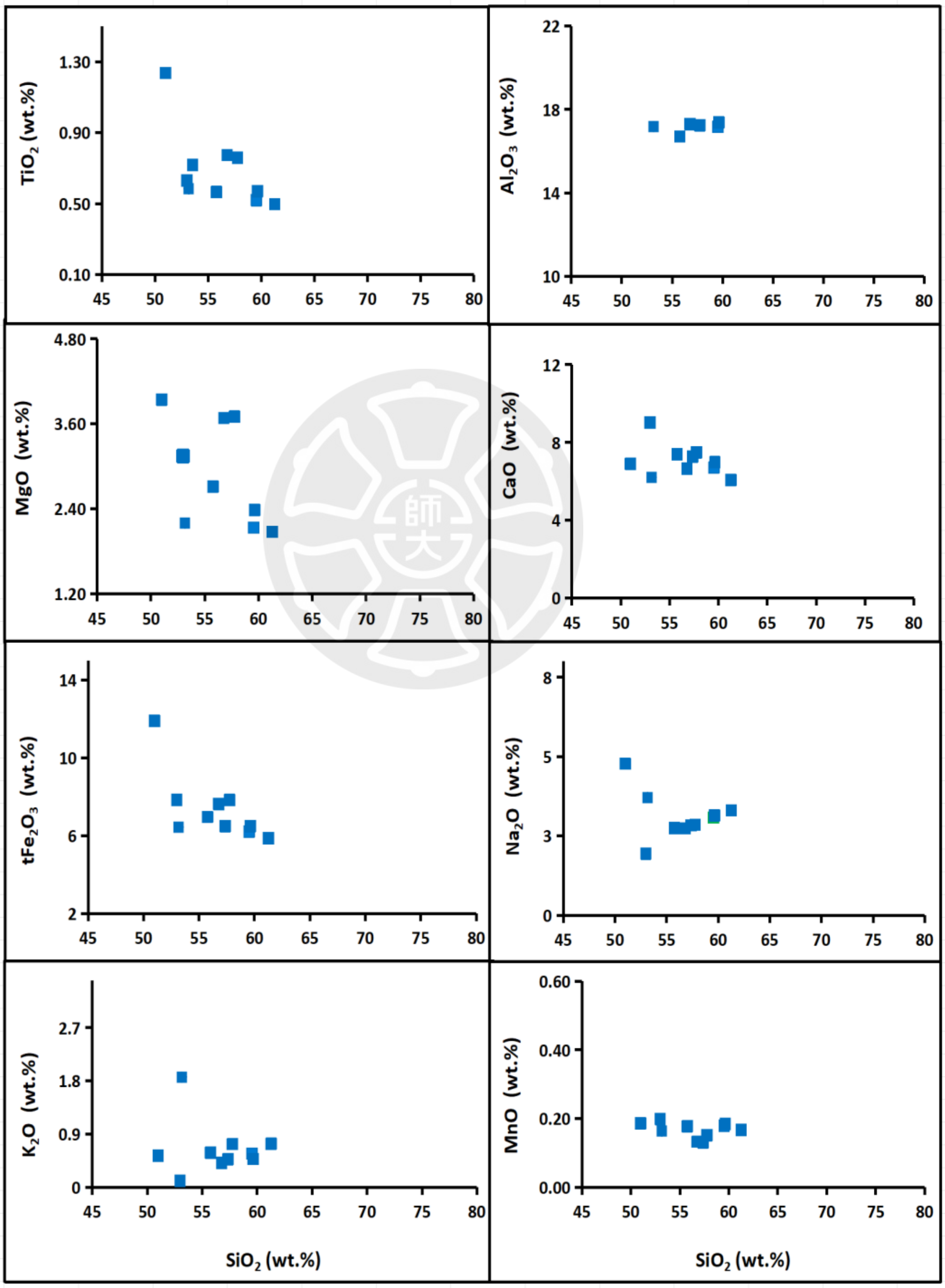

Fig. 4.20. Plot of major elements vs SiO_2 for the studied sample from Pacitan (Group C1).

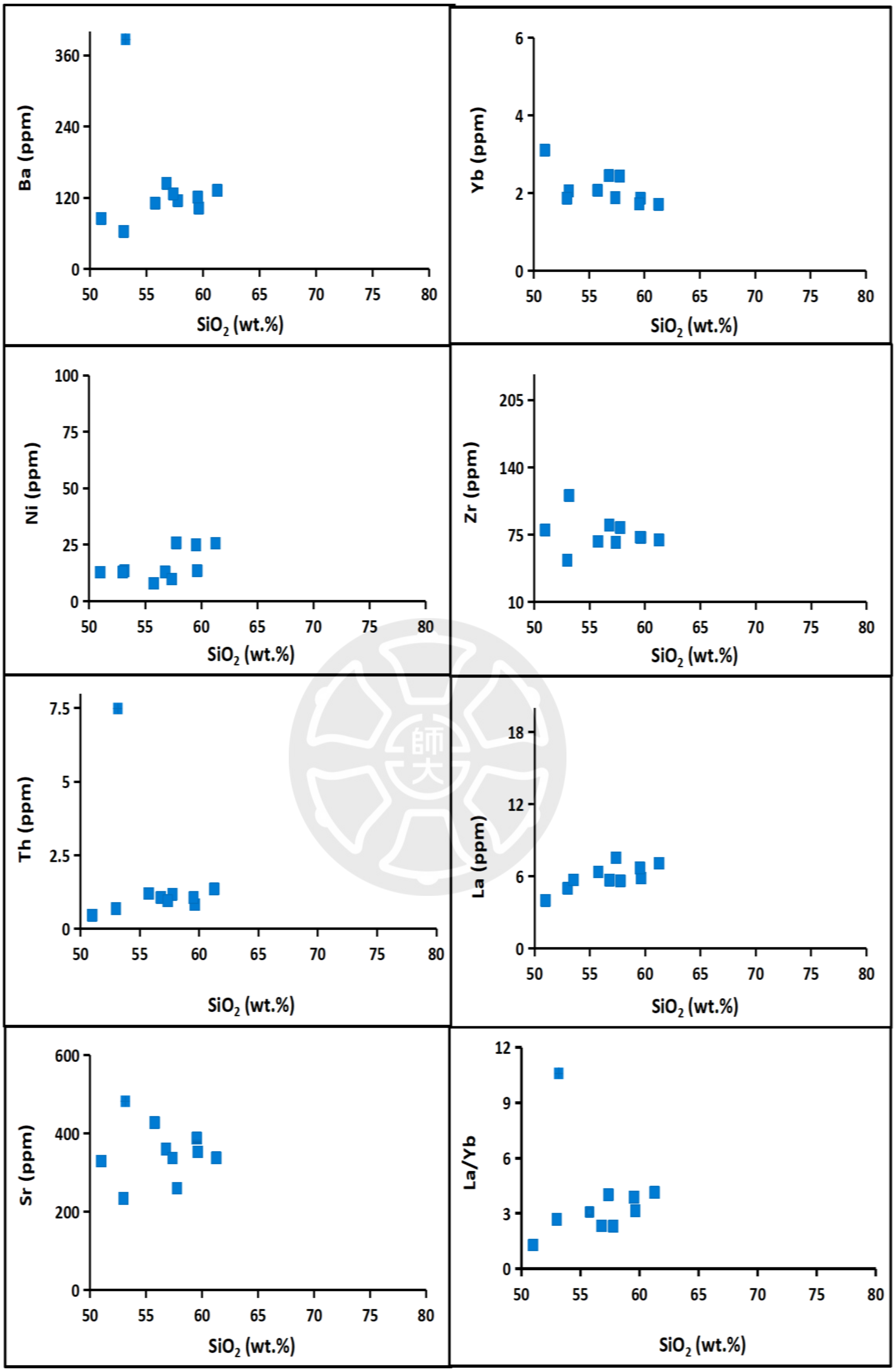

Fig. 4.21. Plot of variation elements vs SiO_2 for the studied sample from Pacitan (Group C1).

Table. 4.6. Whole-rock major and trace-element composition for volcanics rocks in Pacitan (Group C1).

Sample	19JA19-01	19JA19-02	19JA25-01	19JA25-02
Latitude	S 8°13'48.93"	S 8°13'48.93"	S 8°12'10.3"	S 8°12'10.3"
Longitude	E 111°10'0.24"	E 111°10'0.24"	E 111°07'36.7"	E 111°07'36.7"
Unit	36.3	36.3	26	26
Locality	West of Masjid Al-Fallah	West of Masjid Al-Fallah	Waru (Kebonagung)	Waru (Kebonagung)
Group	C1	C1	C1	C1
Major Element				
SiO_2	55.8	53.1	56.8	57.8
TiO_2	0.57	0.58	0.77	0.76
Al_2O_3	16.7	17.2	17.3	17.2
tFe_2O_3	6.97	6.44	7.63	7.84
MnO	0.18	0.16	0.13	0.15
MgO	2.72	2.20	3.68	3.70
CaO	7.39	6.21	6.66	7.49
Na_2O	2.75	3.71	2.74	2.85
K_2O	0.59	1.86	0.41	0.73
P_2O_5	0.16	0.23	0.13	0.12
LOI	5.93	7.80	4.50	1.06
TOTAL	100	99	100	100
Trace Element				
P	630	1100	529	494
Sc	9.80	24.6	27.3	20.9
Ti	3151	3950	4752	4440
V	99.0	117	166	166
Cr	6.20	26.6	19.9	46.8
Mn	1344	1374	1046	1119
Co	13.3	12.9	18.8	17.9
Ni	7.90	13.5	12.9	25.9
Cu	24.3	17.3	40.9	47.1
Zn	83.0	83.3	65.4	55.5
Ga	16.6	19.0	17.2	15.8
Rb	14.4	47.9	3.90	15.9
Sr	428	483	361	260
Y	18.6	20.1	26.2	24.4
Zr	68.0	113	84.4	82.0
Nb	1.60	6.30	1.40	1.30
Cs	0.58	1.11	0.22	0.81
Ba	111	387	145	116
La	6.40	21.8	5.70	5.64
Ce	15.3	42.1	14.5	14.4
Pr	2.21	4.83	2.27	2.20
Nd	10.0	19.0	11.14	10.67
Sm	2.63	4.03	3.25	3.14
Eu	0.85	1.19	0.92	0.89
Gd	2.96	3.73	4.06	3.76
Tb	0.48	0.57	0.67	0.62
Dy	3.06	3.41	4.22	4.08
Ho	0.67	0.71	0.90	0.87
Er	1.96	2.01	2.60	2.54
Tm	0.31	0.30	0.38	0.38
Yb	2.07	2.05	2.45	2.44
Lu	0.32	0.32	0.38	0.37
Hf	1.94	2.85	2.54	2.47
Ta	0.10	0.42	0.08	0.08
Pb	4.70	11.0	6.42	5.99
Th	1.20	7.49	1.07	1.18
U	0.31	1.58	0.13	0.33
Mg#	41	38	47	46

Table 4.6-2 (continued)

Sample	19JA29-01	19JA30-01	19JA31-01	19JA39-01	19JA40-01	19JA34-01
Latitude	S 8°11'58.1"	S 8°10'26.3"	S 8°13'04.2"	S 8°14'18.3"	S 8°12'18.5"	S 8°13'39.8"
Longitude	E 111°06'12,7"	E 111°17'29.2"	E 111°18'13.4"	E 111°14'58.1"	E 111°08'41.1"	E 111°08'38.3"
Unit	500	454	138	149	111	196
Locality	Gowang, Ketro (Kebonagung)	Gowang	Panggerejo	G. Punir	Sambirejo (Roadside)	Karangnongko (Roadside)
Group	C1	C1	C1	C1	C1	C1
Major Element						
SiO_2	61.3	59.7	50.99	52.9	59.5	57.4
TiO_2	0.50	0.57	1.24	0.63	0.52	0.56
Al_2O_3	16.9	17.4	17.66	17.6	17.2	17.2
tFe_2O_3	5.87	6.49	11.90	7.84	6.22	6.50
MnO	0.17	0.19	0.19	0.20	0.18	0.13
MgO	2.08	2.38	3.94	3.15	2.14	2.40
CaO	6.07	6.98	6.90	9.02	6.71	7.28
Na_2O	3.31	3.15	4.78	1.95	3.08	2.84
K_2O	0.74	0.48	0.54	0.11	0.57	0.48
P_2O_5	0.15	0.19	0.15	0.20	0.17	0.17
LOI	1.39	2.66	2.86	3.95	2.92	2.15
TOTAL	98	100	100	98	99	97
Trace Element						
P	497	868	608	854	733	746
Sc	13.5	15.4	33.3	15.6	9.90	8.00
Ti	2642	3385	6887	3884	2957	3143
V	56.8	72.5	296	118	77.1	92.5
Cr	14.5	13.1	13.6	14.4	37.3	14.9
Mn	1219	1424	1323	1524	1343	1005
Co	9.20	10.6	27.6	15.9	10.6	11.9
Ni	25.7	13.5	12.9	12.9	25.1	9.90
Cu	8.60	9.40	80.8	19.7	11.2	16.7
Zn	53.2	79.2	89.5	69.7	68.2	68.8
Ga	15.6	16.7	17.4	17.7	18.1	18.1
Rb	16.0	12.4	10.4	2.40	14.8	13.7
Sr	338	353	330	235	389	338
Y	16.4	17.4	29.5	17.2	16.0	20.5
Zr	70.0	72.4	79.6	50.3	72.8	67.5
Nb	1.70	1.80	1.5	1.50	2.00	1.80
Cs	0.64	0.63	2.98	0.20	0.41	0.83
Ba	133	103	85	64.0	121	127
La	7.09	5.86	4.01	5.02	6.71	7.54
Ce	17.0	14.4	11.0	12.7	16.5	15.3
Pr	2.40	2.13	1.83	1.94	2.40	2.60
Nd	10.59	9.94	9.58	9.27	10.98	11.83
Sm	2.62	2.60	3.16	2.54	2.74	3.02
Eu	0.92	0.96	1.08	0.92	0.93	1.05
Gd	2.75	2.88	4.27	2.87	2.79	3.28
Tb	0.45	0.46	0.75	0.46	0.44	0.53
Dy	2.72	2.91	4.97	2.97	2.71	3.25
Ho	0.58	0.63	1.10	0.63	0.57	0.71
Er	1.67	1.78	3.18	1.83	1.65	2.03
Tm	0.26	0.28	0.48	0.29	0.26	0.31
Yb	1.71	1.87	3.11	1.87	1.73	1.88
Lu	0.27	0.30	0.46	0.28	0.27	0.30
Hf	2.01	1.96	2.28	1.46	2.10	1.96
Ta	0.11	0.11	0.09	0.07	0.11	0.10
Pb	9.71	3.85	1.15	3.50	5.08	6.33
Th	1.36	0.83	0.47	0.69	1.06	0.96
U	0.30	0.24	0.14	0.17	0.28	0.26
Mg#	37	40	46	42	38	40

Group C2:

Group C2 consists of 19 samples with variable L.O.I. (0.6–6.0 wt.%), likely reflecting different degrees of alteration. The samples are composed of sub-alkaline basalt to dacite with SiO_2 contents ranging from 56.86 to 66.58 wt.% **(Fig. 4.22a)**. These samples generally exhibit high-K to low-K characteristics within the calc-alkaline series **(Fig. 4.22b)**. In the Harker diagram, these rocks show negative correlations with TiO_2 (0.49–0.80 wt.%), total Fe_2O_3 (3.51–7.77 wt.%), MgO (0.90–3.74 wt.%), MnO (0.03–0.18 wt.%), and CaO (4.25–7.56 wt.%) **(Fig. 4.23)**. Variation diagrams show La concentrations from 5.95 to 8.80 ppm, Ba from 102 to 1112 ppm, Ni from 4.60 to 26.0 ppm, Th from 0.93 to 1.90 ppm, Yb from 0.65 to 1.58 ppm, and Zr from 56.3 to 78.8 ppm **(Fig.4.24)**. La/Yb, Th, Sr, La, and Ba show positive correlations with SiO_2, while Yb and Zr show negative correlations with SiO_2.

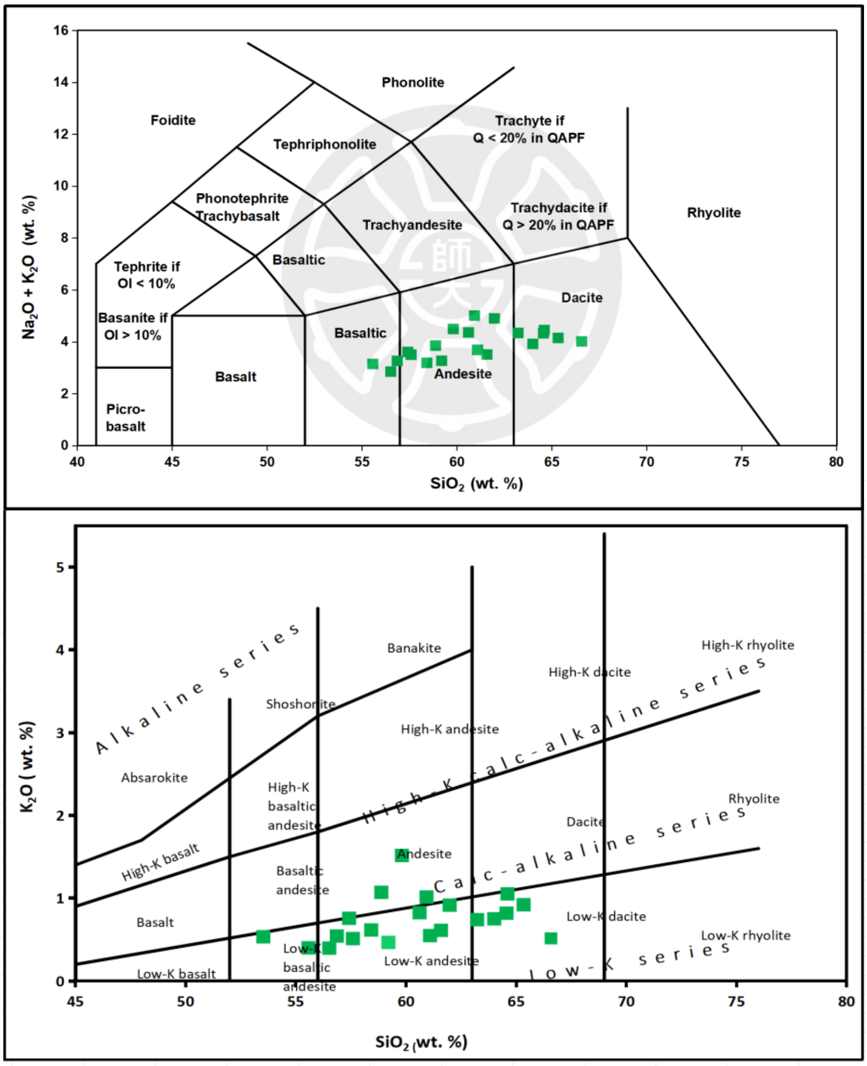

Fig. 4.22. **(a)** Total alkalis vs. SiO_2 diagram (after Le Bas et al., 1986; Le Maître, 2002) for the samples in the Pacitan area from Group C2. The line separating the sub-alkaline

and alkaline regions is after Irvine and Baragar (1971). **(b)** Variation of K_2O vs. SiO_2 for the Pacitan volcanic rocks from Group C2. The classification for K_2O-SiO_2 contents is after Gill (1981), Ewart (1982), and Peccerillo and Taylor (1976), respectively.

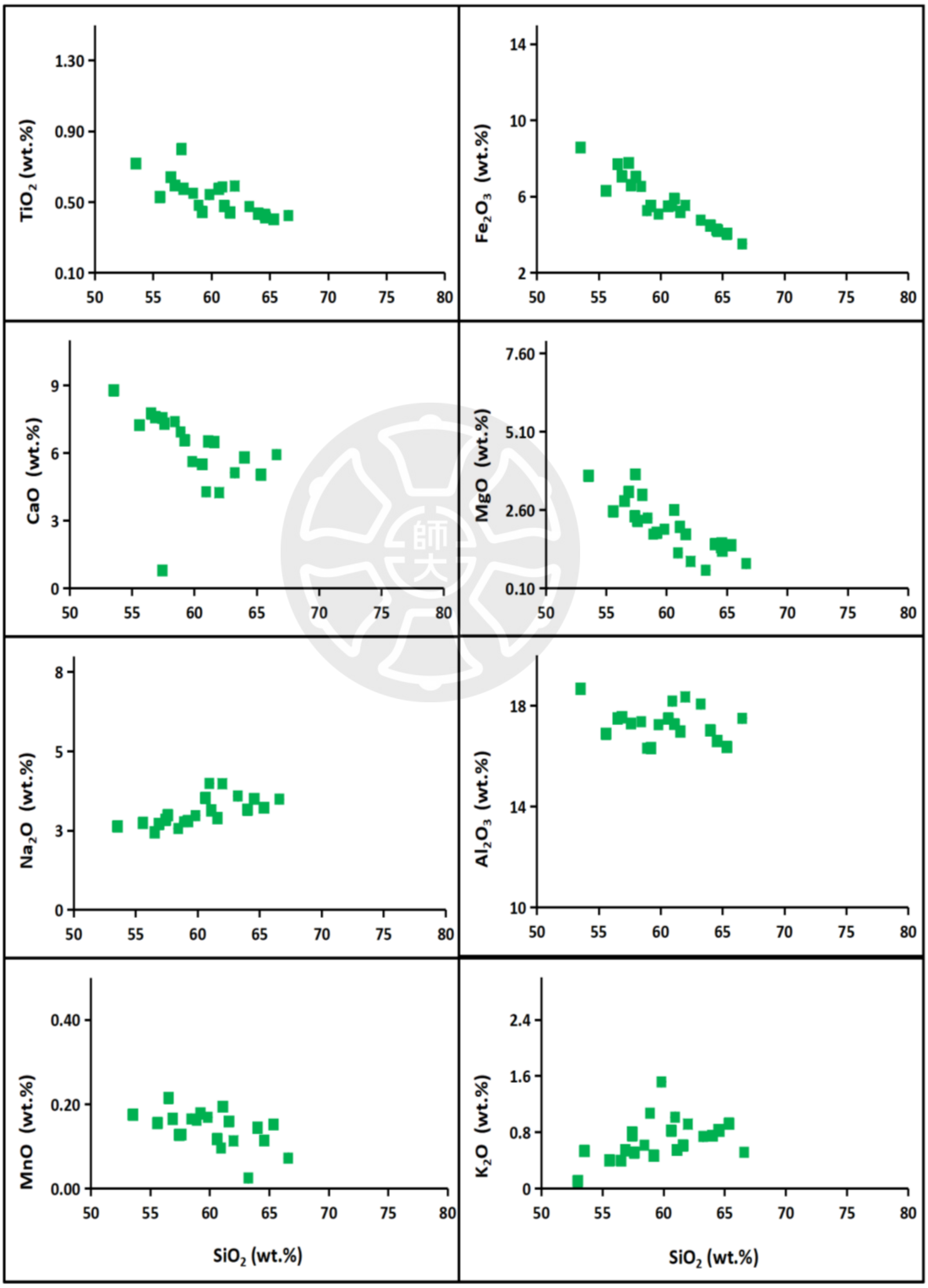

Fig. 4.23. Plot of major elements vs. SiO_2 for the studied samples from Pacitan (Group C2).

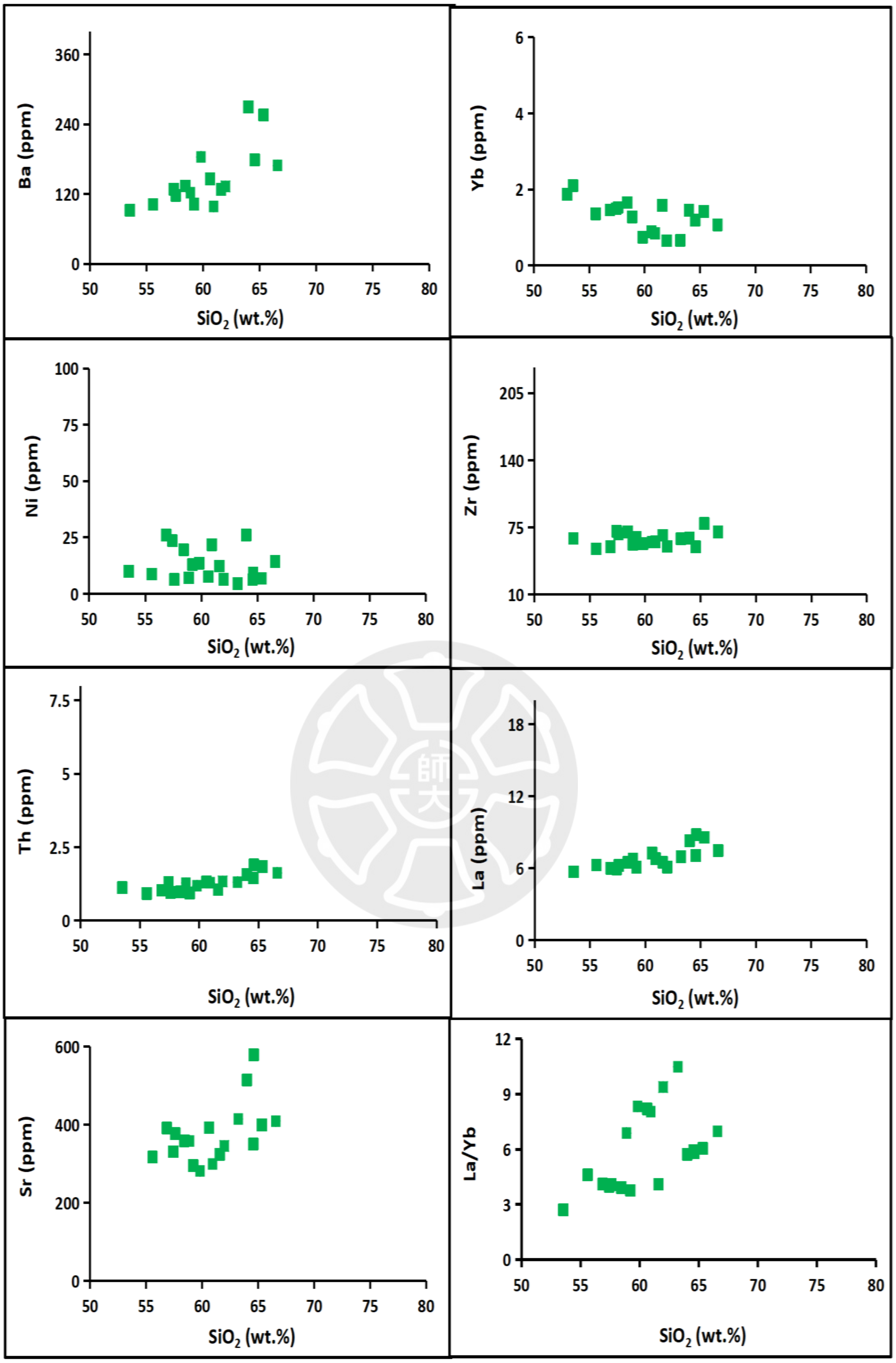

Fig. 4.24. Plot of variation elements vs. SiO_2 for the studied samples from Pacitan (Group C2).

Table. 4.7. Whole-rock major and trace-element composition for volcanics rocks in Pacitan (Group C2).

Sample	19JA17-01	19JA18-02	19JA18-03	19JA18-04	19JA18-05
Latitude	S 8°14'52.41"	S 8°14'14.88"	S 8°14'14.88"	S 8°14'14.88"	S 8°14'14.88"
Longitude	E 111°14'59.06"	E 111°10'45.25"	E 111°10'45.25"	E 111°10'45.25"	E 111°10'45.25"
Unit	31.6	123	123	123	123
Locality	Northeast of Pantai Pidakan	Near Musholla Sibon Darusalam	Near Musholla Sibon Darusalam	Near Musholla Sibon Darusalam	Near Musholla Sibon Darusalam
Group	C2	C2	C2	C2	C2
Major Element					
SiO_2	61.9	66.6	59.8	58.8	63.2
TiO_2	0.59	0.42	0.54	0.48	0.48
Al_2O_3	18.3	17.5	17.3	16.3	18.1
Fe_2O_3	5.54	3.51	5.08	5.27	4.76
MnO	0.11	0.07	0.17	0.16	0.03
MgO	0.96	0.90	1.99	1.83	0.68
CaO	4.25	5.94	5.63	6.95	5.13
Na_2O	3.98	3.50	2.97	2.78	3.60
K_2O	0.92	0.52	1.52	1.07	0.74
P_2O_5	0.16	0.17	0.16	0.15	0.14
LOI	3.33	0.63	4.00	6.00	1.62
TOTAL	100	100	99	100	98
Trace Element					
P	624	652	612	550	560
Sc	3.40	3.20	16.3	0.50	4.50
Ti	3291	2317	3098	2646	2687
V	105	37.0	88.0	70.0	59.0
Cr	5.10	24.1	19.0	5.30	1.50
Mn	825	573	1269	1205	204
Co	9.90	4.50	11.4	10.4	5.80
Ni	6.40	14.4	13.6	7.10	4.60
Cu	11.0	3.20	9.00	12.6	6.10
Zn	65.0	61.0	80.0	122	70.0
Ga	18.6	17.5	17.9	16.5	18.8
Rb	25.6	13.2	37.9	31.4	9.50
Sr	346	409	282	359	415
Y	7.40	11.4	7.60	10.6	7.70
Zr	57.0	71.0	59.0	59.0	64.0
Nb	1.80	2.20	1.70	1.90	1.70
Cs	1.69	1.26	2.32	5.05	2.45
Ba	133	169	184	122	1112
La	6.10	7.50	6.20	6.80	7.00
Ce	14.5	17.6	14.4	16.0	17.6
Pr	2.04	2.44	1.98	2.25	2.29
Nd	8.80	10.5	8.50	9.90	9.90
Sm	1.98	2.37	1.85	2.35	2.28
Eu	0.71	0.86	0.64	0.78	0.93
Gd	1.87	2.28	1.71	2.26	1.98
Tb	0.27	0.34	0.25	0.33	0.28
Dy	1.46	1.95	1.38	1.88	1.49
Ho	0.28	0.39	0.27	0.37	0.29
Er	0.73	1.08	0.73	0.99	0.73
Tm	0.11	0.16	0.11	0.15	0.10
Yb	0.65	1.07	0.74	0.99	0.66
Lu	0.10	0.17	0.11	0.16	0.10
Hf	1.74	2.12	1.75	1.75	2.00
Ta	0.13	0.17	0.12	0.14	0.15
Pb	6.56	5.52	5.13	6.26	8.80
Th	1.34	1.63	1.19	1.28	1.31
U	0.34	0.40	0.37	0.37	0.23
Mg#	24	31	41	38	20

Table. 4.7-2 (continued)

Sample	19JA26-01	19JA26-02	19JA26-03	19JA27-01	19JA28-01
Latitude	S 8°12'37.3"	S 8°12'37.3"	S 8°12'37.3"	S 8°12'37.8"	S 8°12'39.3"
Longitude	E 111°12'04.5"	E 111°12'04.5"	E 111°12'04.5"	E 111°12'01.9"	E 111°11'39.9"
Unit	439	439	439	447	415
Locality	River Valley (G. Ngampel)	River Valley (G. Ngampel)	River Valley (G. Ngampel)	River Valley (G.Gundang Legi)	Roadside (G. puyang)
Group	C2	C2	C2	C2	C2
Major Element					
SiO_2	57.9	64.5	64.6	64.6	65.3
TiO_2	0.59	0.42	0.42	0.43	0.40
Al_2O_3	17.6	16.8	16.5	16.6	16.4
Fe_2O_3	7.04	4.28	4.20	4.23	4.05
MnO	0.15	0.15	0.16	0.11	0.15
MgO	3.09	1.42	1.30	1.54	1.48
CaO	7.54	5.57	5.33	5.51	5.04
Na_2O	2.59	3.53	3.40	3.50	3.22
K_2O	0.61	0.84	1.05	0.82	0.92
P_2O_5	0.16	0.15	0.15	0.15	0.15
LOI	3.73	1.32	2.89	1.40	1.76
TOTAL	101	99	100	99	99
Trace Element					
P	678	622	675	468	632
Sc	11.4	32.2	3.90	0.80	10.2
Ti	3544	2388	2361	1990	2277
V	123	54.0	46.1	45.9	46.3
Cr	65.2	12.5	10.7	10.7	9.00
Mn	1113	1138	1195	726	1137
Co	15.0	6.90	6.50	6.00	6.20
Ni	45.4	9.10	9.30	6.30	6.80
Cu	14.5	6.80	5.80	8.70	7.50
Zn	65.2	47.9	49.7	36.0	49.5
Ga	17.2	16.5	16.5	14.3	16.4
Rb	16.4	23.8	39.0	20.5	29.3
Sr	338	359	579	351	400
Y	14.8	12.9	14.5	11.9	14.4
Zr	63.8	60.4	66.0	56.3	78.8
Nb	1.70	2.10	2.20	1.80	2.10
Cs	0.32	1.94	2.13	0.95	1.97
Ba	122	198	229	179	256
La	6.38	8.05	8.80	7.06	8.57
Ce	15.2	18.4	19.5	15.7	18.8
Pr	2.16	2.45	2.67	2.11	2.55
Nd	9.60	10.17	11.16	8.90	10.6
Sm	2.37	2.24	2.51	2.02	2.27
Eu	0.81	0.80	0.86	0.69	0.84
Gd	2.44	2.15	2.48	1.94	2.28
Tb	0.40	0.35	0.39	0.31	0.36
Dy	2.52	2.11	2.32	1.86	2.15
Ho	0.53	0.44	0.50	0.39	0.46
Er	1.53	1.26	1.43	1.11	1.30
Tm	0.24	0.20	0.23	0.18	0.21
Yb	1.51	1.37	1.51	1.19	1.42
Lu	0.24	0.22	0.25	0.20	0.23
Hf	1.82	1.84	2.01	1.68	2.31
Ta	0.10	0.14	0.15	0.12	0.15
Pb	3.53	7.39	8.27	5.59	8.88
Th	1.16	1.78	1.90	1.46	1.85
U	0.29	0.46	0.49	0.37	0.48
Mg#	44	37	36	40	40

Table. 4.7-3 (continued).

Sample	19JA32-01	19JA32-02	19JA32-03	19JA33-01	19JA34-01
Latitude	S 8°12'05.0"	S 8°12'05.0"	S 8°12'05.0"	S 8°13'25.3"	S 8°13'39.8"
Longitude	E 111°17'15.9"	E 111°17'15.9"	E 111°17'15.9"	E 111°08'32.3"	E 111°08'38.3"
Unit	463	463	463	125	196
Locality	G. Tenon	G. Tenon	G. Tenon	G.Karangnongko	Karangnongko (Roadside)
Group	C2	C2	C2	C2	C2
Major Element					
SiO_2	59.2	61.6	61.1	58.4	57.4
TiO_2	0.44	0.44	0.48	0.55	0.56
Al_2O_3	16.3	16.9	17.3	17.4	17.2
Fe_2O_3	5.52	5.19	5.89	6.53	6.50
MnO	0.18	0.16	0.19	0.17	0.13
MgO	1.88	1.83	2.06	2.34	2.40
CaO	6.57	6.50	6.52	7.40	7.28
Na_2O	2.80	2.89	3.14	2.57	2.84
K_2O	0.47	0.61	0.55	0.62	0.48
P_2O_5	0.19	0.17	0.20	0.17	0.17
LOI	2.86	4.46	2.69	4.03	2.15
TOTAL	96	100	100	100	97
Trace Element					
P	608	832	722	657	746
Sc	33.3	5.10	6.30	12.0	8.00
Ti	6887	2490	2476	3197	3143
V	296	51.3	58.6	92.6	92.5
Cr	13.6	11.8	20.0	35.4	14.9
Mn	1323	1326	1215	1280	1005
Co	27.6	8.20	8.60	12.3	11.9
Ni	12.9	13.0	12.3	19.5	9.90
Cu	80.8	7.60	4.70	25.7	16.7
Zn	89.5	58.8	45.1	75.1	68.8
Ga	17.4	14.8	15.7	18.1	18.1
Rb	10.4	12.8	16.7	18.3	13.7
Sr	330	296	325	359	338
Y	29.5	14.9	14.1	16.0	20.5
Zr	79.6	65.4	67.3	70.0	67.5
Nb	1.50	1.60	1.70	1.90	1.80
Cs	2.98	0.63	0.65	0.76	0.83
Ba	85.0	102	128	134	127
La	4.01	6.10	6.49	6.49	7.54
Ce	11.0	14.5	15.1	16.1	15.3
Pr	1.83	2.08	2.10	2.38	2.60
Nd	9.58	9.34	9.26	10.89	11.83
Sm	3.16	2.31	2.23	2.68	3.02
Eu	1.08	0.84	0.83	0.94	1.05
Gd	4.27	2.48	2.31	2.82	3.28
Tb	0.75	0.40	0.38	0.45	0.53
Dy	4.97	2.45	2.35	2.74	3.25
Ho	1.10	0.54	0.50	0.57	0.71
Er	3.18	1.53	1.46	1.64	2.03
Tm	0.48	0.25	0.24	0.25	0.31
Yb	3.11	1.62	1.58	1.65	1.88
Lu	0.46	0.26	0.26	0.26	0.30
Hf	2.28	1.83	1.89	2.03	1.96
Ta	0.09	0.09	0.09	0.10	0.10
Pb	1.15	4.84	3.91	7.99	6.33
Th	0.47	0.94	1.06	0.97	0.96
U	0.14	0.25	0.30	0.26	0.26
Mg#	38	39	39	39	40

Table. 4.7-4 (continued).

Sample	19JA35-01	19JA36-01	19JA37-01	19JA42- 01	19JA46-01	19JA47-01
Latitude	S 8°14'02.9"	S 8°13'37.1"	S 8°11'47.2"	S 8°13'45.7"	S 8°11'15.9"	S 8°13'58.3"
Longitude	E 111°08'41.7"	E 111°12'03.1"	E 111°12'28.1"	E 111°09'51.0"	E 111°15'32.2"	E 111°04'38.9"
Unit	391	445	512	91	420	9
Locality	Karangnongko (Roadside)	Mantren (River)	G. Masong	Kebonagung (Roadside)	G. Sepang	Beach (Near Sea)
Group	C2	C2	C2	C2	C2	C2
Major Element						
SiO_2	57.6	64	56.7	60.6	55.6	57.4
TiO_2	0.58	0.43	0.59	0.58	0.53	0.80
Al_2O_3	17.3	17	17.6	17.5	16.9	17.7
Fe_2O_3	6.61	4.49	7.06	5.49	6.30	7.77
MnO	0.13	0.14	0.17	0.12	0.16	0.13
MgO	2.26	1.51	3.18	2.60	2.56	3.74
CaO	7.31	5.81	7.60	5.51	7.25	7.56
Na_2O	2.99	3.16	2.72	3.53	2.74	2.85
K_2O	0.51	0.75	0.54	0.83	0.40	0.76
P_2O_5	0.17	0.14	0.16	0.15	0.16	0.14
LOI	2.73	2.55	3.75	2.98	2.91	1.17
TOTAL	98	100	100	100	96	100
Trace Element						
P	741	566	601	670	929	708
Sc	8.80	4.30	9.20	6.40	13.8	19.1
Ti	3469	2358	3558	3335	3123	4954
V	99.2	61.2	119	95.9	102	173
Cr	6.70	20.4	35.0	11.0	10.9	38.0
Mn	995	1108	1248	903	1153	985
Co	12.0	7.80	15.4	11.5	13.4	20.4
Ni	6.30	10.7	26.1	7.7	8.8	23.5
Cu	16.8	9.30	18.6	13.0	17.2	31.6
Zn	68.4	54.5	75.2	61.2	64.7	63.2
Ga	18.1	17.1	17.1	18.7	16.9	17.9
Rb	14.1	22.3	15.3	24.6	8.10	20.4
Sr	378	515	391	393	317	332
Y	14.9	15.7	15.2	10.1	12.7	15.7
Zr	68.7	64.7	56.4	60.8	54.3	71.4
Nb	1.90	1.90	1.50	1.90	1.60	1.50
Cs	0.53	1.34	0.59	0.82	0.74	0.77
Ba	118	270	119	146	102	128
La	6.24	8.30	6.00	7.26	6.30	5.95
Ce	15.4	16.7	13.8	16.8	14.7	14.2
Pr	2.28	2.49	1.98	2.34	2.06	2.12
Nd	10.5	10.6	8.80	10.29	9.00	9.81
Sm	2.65	2.38	2.19	2.40	2.16	2.77
Eu	0.90	0.87	0.79	0.84	0.78	0.91
Gd	2.73	2.50	2.38	2.22	2.24	3.02
Tb	0.42	0.38	0.38	0.34	0.35	0.47
Dy	2.59	2.34	2.36	1.86	2.21	2.87
Ho	0.55	0.50	0.51	0.35	0.46	0.60
Er	1.53	1.46	1.47	0.97	1.32	1.60
Tm	0.24	0.22	0.22	0.14	0.20	0.24
Yb	1.53	1.45	1.46	0.89	1.36	1.49
Lu	0.25	0.24	0.24	0.14	0.21	0.23
Hf	1.97	1.93	1.68	1.80	1.57	2.12
Ta	0.10	0.14	0.10	0.12	0.09	0.08
Pb	5.45	6.87	6.69	6.52	4.16	5.26
Th	0.97	1.57	1.04	1.32	0.93	1.31
U	0.28	0.40	0.28	0.34	0.22	0.36
Mg#	38	38	45	46	42	46

4.4.4. Trace Elements

Based on the age results in the Pacitan area, three different ages are observed: Late Oligocene, Early Miocene, and Middle Miocene. Group A corresponds to the Late Oligocene, Group B to the Early Miocene, and Group C to the Middle Miocene. The rare earth element (REE) diagram shows that samples from Pacitan are plotted separately. Based on the rock types, the samples are divided into two ages: Late Oligocene and Middle Miocene. The Early Miocene samples, with tuff rock type, do not have trace element data. The Late Oligocene samples with dacite rock type have SiO_2 ranging from 63.8 to 68.6 wt.% and show negative anomalies for high field strength elements (HFSEs) such as Nb, Ta, and Ti, with relative depletion, while large ion lithophile elements (LILEs) are relatively enriched. Chondrite-normalized REE patterns show a gentle slope with highly LREE and relatively HREE. The Late Oligocene samples with andesite rock type have SiO_2 around 59.6 wt.% and show similar trends with negative anomalies for HFSEs such as Nb, Ta, and Ti, while LILEs are relatively enriched. Chondrite-normalized patterns show a steep REE pattern with highly LREE and lower HREE, along with positive Eu anomalies (Eu/Eu* = 1.35) **(Fig. 4.25).**

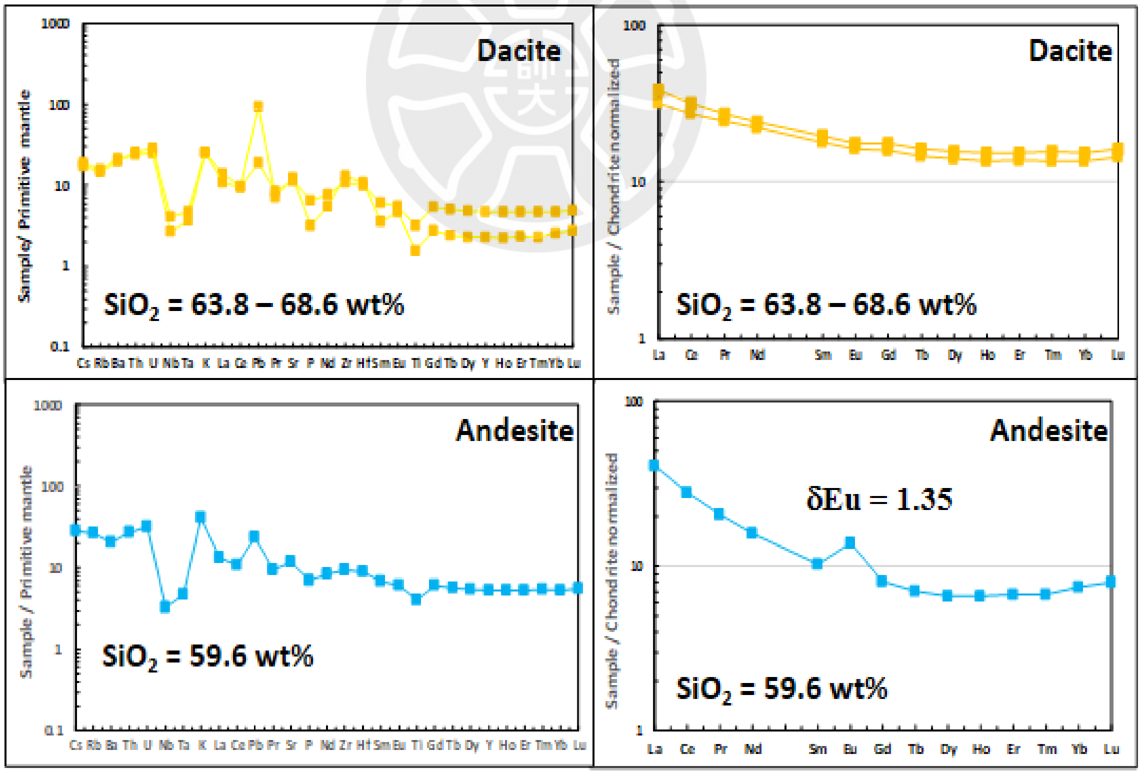

Fig. 4.25 Primitive mantle-normalized trace-element diagrams for the samples in Pacitan. Chondrite-normalized pattern with highly LREE and lower HREE, with positive Eu anomalies.

The Middle Miocene samples with dacite rock type have SiO_2 ranging from 63.3 to 66.6 wt.% and show negative anomalies for HFSEs such as Nb, Ta, and Ti, with relative depletion, while LILEs are relatively enriched. Chondrite-normalized REE patterns show a gentle slope with highly LREE and lower HREE. The Middle Miocene samples with andesite rock type have SiO_2 ranging from 55.8 to 61.1 wt.% and show similar trends. Chondrite-normalized patterns show a gentle REE pattern with highly LREE and highly HREE. The Middle Miocene basaltic andesite rock type has SiO_2 ranging from 53.1 to 55.5 wt.% and shows negative anomalies for HFSEs with relative depletion, while LILEs are relatively enriched. Chondrite-normalized patterns show a steep REE pattern with highly LREE and highly HREE, as well as a gentle REE pattern with highly LREE and lower HREE **(Fig. 4.26)**.

4.4.4.1. Group A

Samples from Group A on the primitive mantle diagram show negative anomalies for HFSEs such as Nb, Ta, and Ti, with relative depletion, while LILEs such as Rb, Ba, Th, U, and K are relatively enriched. Chondrite-normalized REE patterns show both steep and gentle slopes, with highly LREE and highly HREE, or highly LREE and lower HREE (LREE/HREE = 2.3-5.5). Most samples show slight or obvious positive Eu anomalies (Eu/Eu* = 1.35) **(Fig. 4.27)**.

The diagrams of Nb/U-Nb and Ce/Pb-Ce for Group A are plotted within the volcanic arc domain. Nb is one of the HFSEs, showing depletion due to fluid effects in the magma region associated with dehydration of the subduction slab. Nb/U values reflect all volcanic, calc-alkaline rocks, exhibiting an arc-like signature with HFSE depletion. Ce/Pb values indicate that the volcanic rocks from Group A are related to volcanic arc **(Fig. 4.28)**.

Trace element concentrations related to $(La/Yb)_N$ and $(Dy/Yb)_N$ in Group A volcanic rocks have values of $(La/Yb)_N$ = 1.46-5.52 and $(Dy/Yb)_N$ = 0.89-1.04, with rock types andesite and dacite **(Fig. 4.29).**

Trace element concentrations related to $(La/Yb)_N$ and $(Yb)_N$ in Group A volcanic rocks have values of $(La/Yb)_N$ = 1.46-5.52 and $(Yb)_N$ = 7.42-21.5, with rock types andesite and dacite. The Sr/Y value ranges from 8.17 to 25.5, and the Y value ranges from 10.4 to 34 **(Fig. 4.30).**

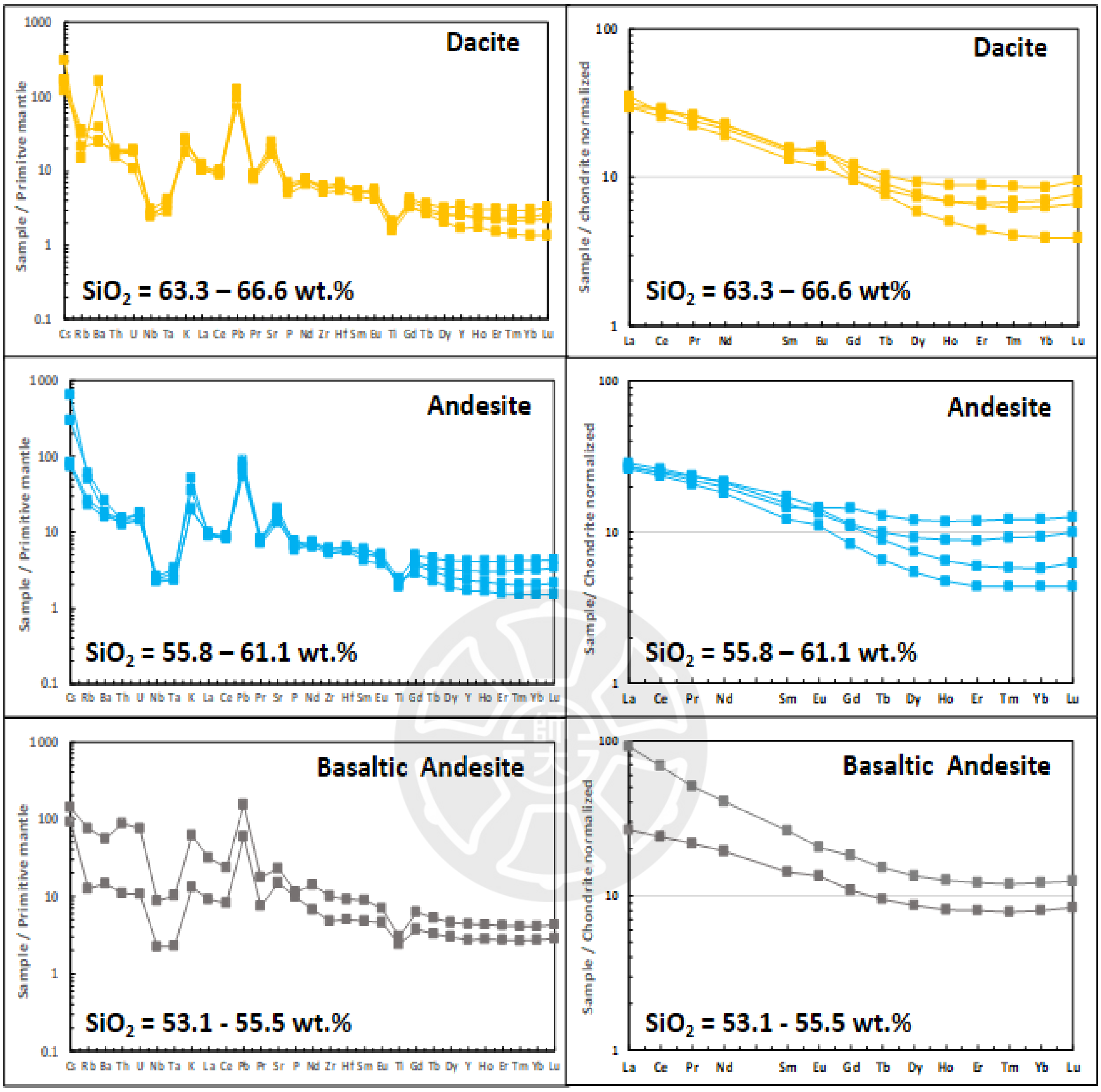

Fig. 4.26 Primitive mantle-normalized trace-element diagrams for the samples in Pacitan. Primitive mantle values for normalization and Chondrite-normalized REE diagrams are from Sun and McDonough (1989). The Middle Miocene samples with dacite, andesite, and basaltic andesite rock types show negative anomalies for HFSEs such as Nb, Ta, and Ti, with relative depletion, while LILEs are relatively enriched. Chondrite-normalized REE patterns show gentle and steep slopes.

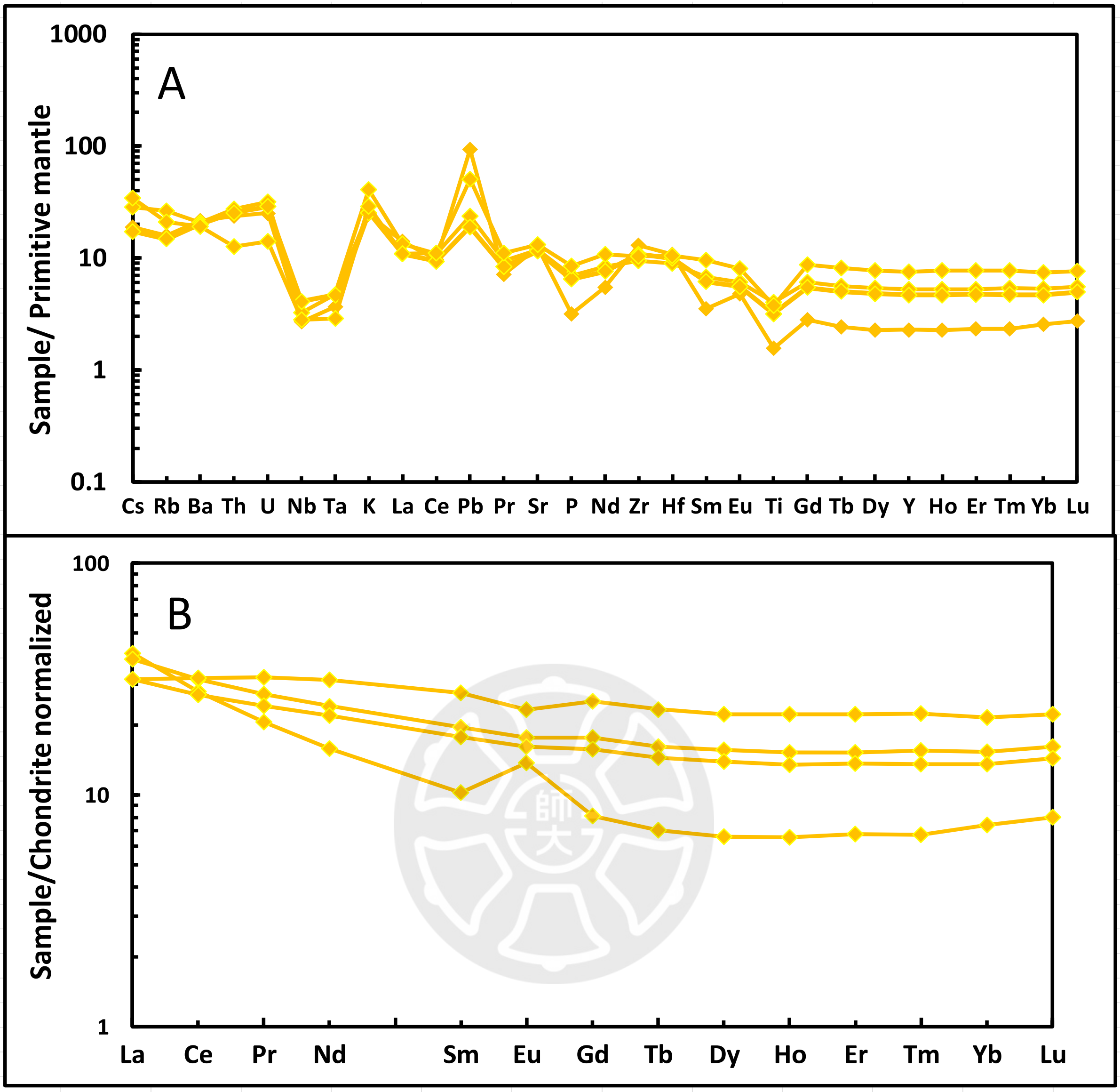

Fig. 4.27. (A). Primitive mantle-normalized trace-element diagrams for samples from Group A. Primitive mantle values for normalization and Chondrite-normalized REE diagrams are from Sun and McDonough (1989). The primitive mantle diagram shows negative anomalies for HFSEs such as Nb, Ta, and Ti, with normalized variation, while LILEs are relatively enriched. (B). The Chondrite-normalized REE patterns show gentle and steep slopes.

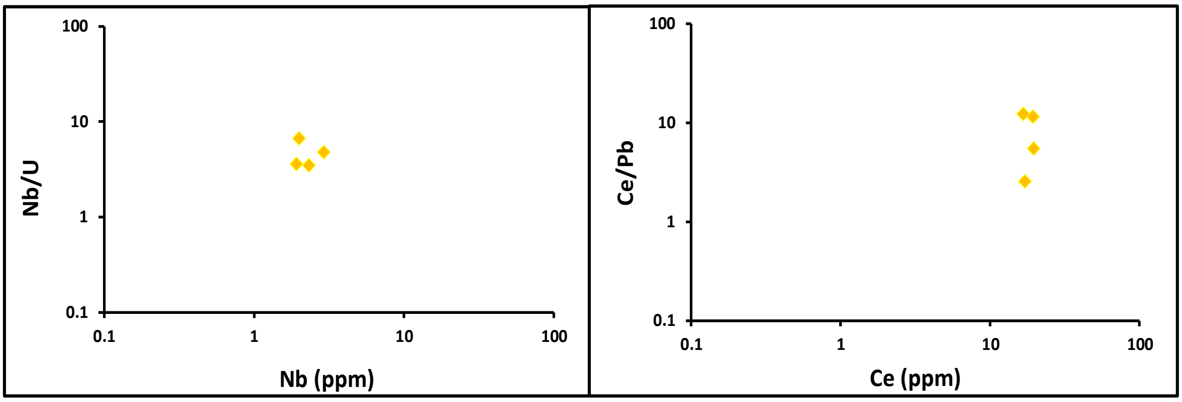

Fig. 4.28. Plots of the samples in the Nb/U vs. Nb diagram and Ce/Pb vs. Ce diagram for Group A. Average values for MORB and upper crust, and data for volcanic arc are from Edwards et al. (1994), Hart and Reid (1991), Hofmann et al. (1986), Kersting and Arculus (1995), McDonough et al. (1992), Miller et al. (1994), and Pearce and Peate (1995).

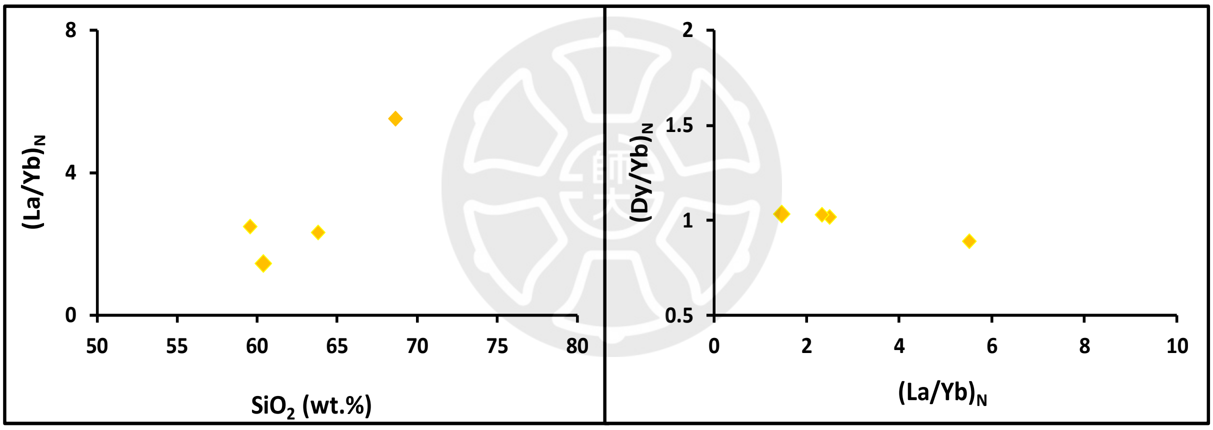

Fig.4.29. Plot of chondrite-normalized $(La/Yb)_N$ vs. SiO_2 diagram and $(Dy/Yb)_N$ vs. $(La/Yb)_N$ for the studied samples from Group A.

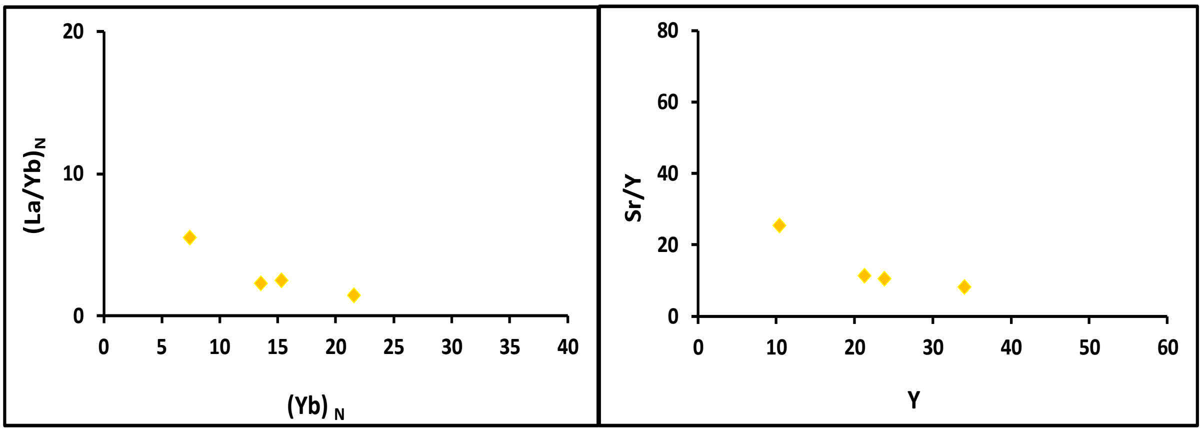

Fig. 4.30. Plot of chondrite-normalized $(La/Yb)_N$ vs. $(Yb)_N$ diagram and major elements Sr/Y and Y for the studied samples from Group A.

4.4.4.2. Group B

Samples from Group B, in the primitive mantle diagram, show negative anomalies for HFSEs such as Nb, Ta, and Ti, normalized variation, while LILEs such as Rb, Ba, Th, U, and K are relatively enriched. The chondrite-normalized REE diagram shows that Group B has gentle REE patterns with high LREE and relatively lower HREE (LREE/HREE = 0.6-2.5). The REE patterns are flat, with LREE and HREE being almost equal, and most are accompanied by obvious or slightly negative Eu anomalies (Eu/Eu* = 0.71–0.92) **(Fig. 4.31).**

The diagrams of Nb/U-Nb and Ce/Pb-Ce show that the geochemical characteristics of Group B plot within the domain of volcanic arc rocks. Nb, being one of the HFSEs, shows a depletion due to fluid effects in the magma region associated with dehydration of the subduction slab. Nb/U values reflect a volcanic, calc-alkaline signature with obvious HFSE depletions. Ce/Pb values show that the volcanic rocks from Group B are related to volcanic arc rocks **(Fig. 4.32).**

Trace element concentrations related to $(La/Yb)_N$ and $(Dy/Yb)_N$ in Group B volcanic rocks show that the values of $(La/Yb)_N$ = 0.68-2.59 and $(Dy/Yb)_N$ = 0.87-1.08, with rock types being dacite and rhyolite **(Fig. 4.33).**

Trace element concentrations related to $(La/Yb)_N$ and $(Yb)_N$ in Group A volcanic rocks show values of (La/Yb)n = 0.68-2.59 and (Yb)n = 15.8-34.5, with rock types being andesite and dacite. The Sr/Y value is 0.87-7.80, and the Y value is 12.7-49.8 **(Fig. 4.34).**

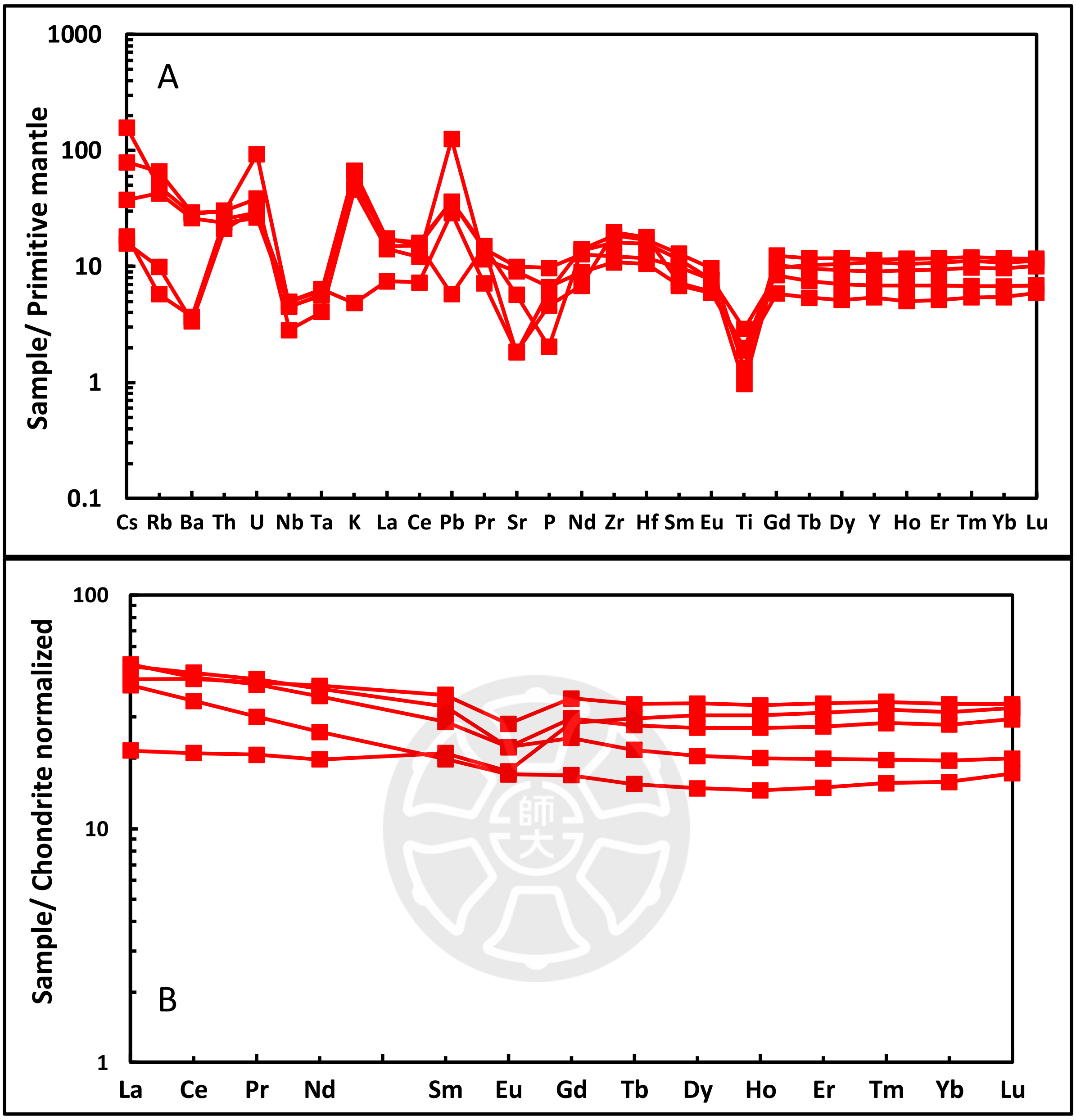

Fig. 4.31. (A). Primitive mantle-normalized trace-element diagrams of the samples from Group B. Primitive mantle values for normalization and chondrite-normalized REE diagrams are from Sun and McDonough (1989). The primitive mantle diagram shows negative anomalies for HFSEs such as Nb, Ta, and Ti normalized variation, while LILEs are relatively enriched. (B). The chondrite-normalized diagram shows a gentle REE pattern and a flat REE pattern.

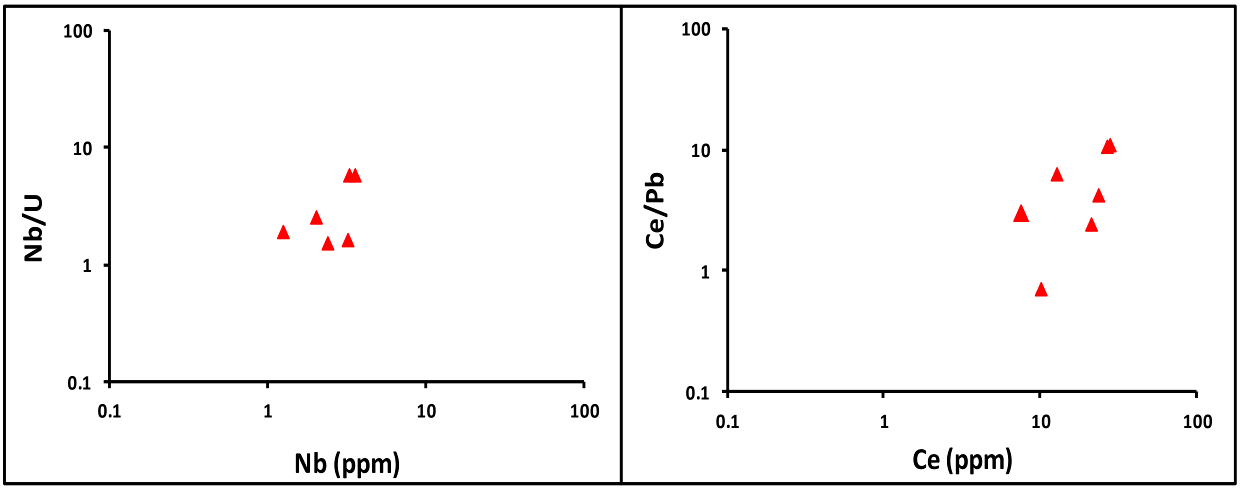

Fig. 4.32. Plots of the samples in the Nb/U vs. Nb diagram and Ce/Pb vs. Ce diagram for Group B. Average values for MORB and upper crust, and data for volcanic arc rocks are from Edwards et al. (1994), Hart and Reid (1991), Hofmann et al. (1986), Kersting and Arculus (1995), McDonough et al. (1992), Miller et al. (1994), and Pearce and Peate (1995).

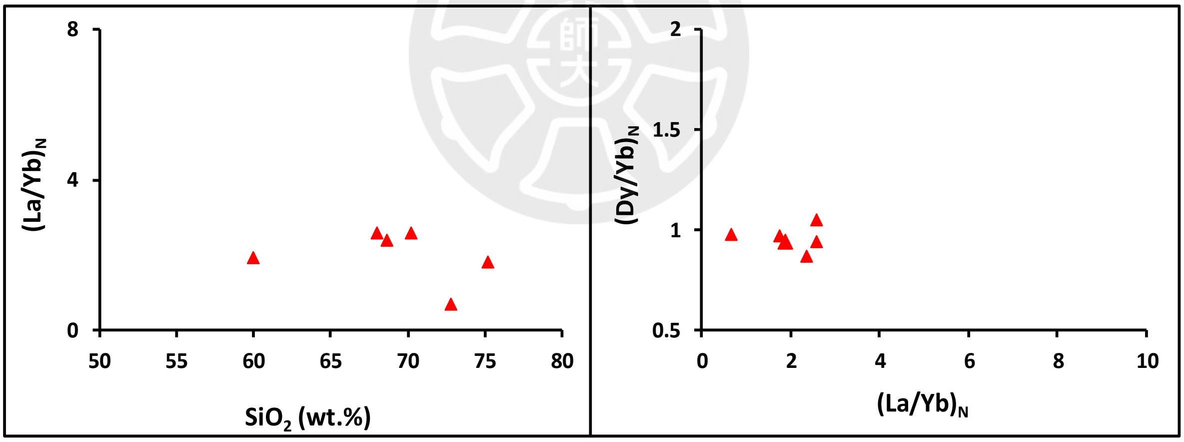

Fig. 4.33. Plot of chondrite-normalized $(La/Yb)_N$ diagram vs. major elements and $(Dy/Yb)_N$ vs. $(La/Yb)_N$ for the studied samples from Group B.

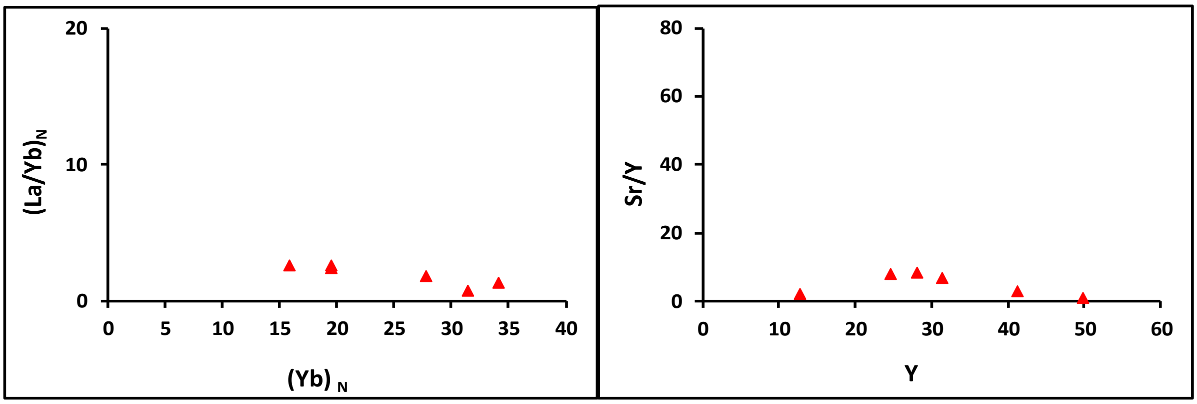

Fig. 4.34. Plot of chondrite-normalized $(La/Yb)_N$ vs. $(Yb)_N$ diagram and major elements Sr/Y and Y for the studied samples from Group B.

4.4.4.3. Group C

Samples from Group C1 and C2, in the primitive mantle diagram, show negative anomalies for HFSEs such as Nb, Ta, and Ti, with relative depletion, while LILEs such as Rb, Ba, Th, U, and K are relatively enriched. These characteristics are similar to those of arc magmas from subduction zones, representing a typical subduction-related feature (Pearce and Peate, 1995; Shinjo et al., 1999; Tatsumi and Eggins, 1995; Tatsumi et al., 1986). This is related to the Tertiary subduction zones in the Pacitan area (Purwanto, 1997). The chondrite-normalized REE diagram shows that Group C exhibits steep REE patterns with high LREE and relatively low HREE (LREE/HREE = 2.2-7.5) **(Fig. 4.35,** and **Fig. 4.36)**.

The diagrams of Nb/U-Nb and Ce/Pb-Ce show that the geochemical characteristics of Group C1 plot within the domain of volcanic arc rocks. Nb, being one of the HFSEs, shows a depletion due to fluid effects in the magma region associated with dehydration of the subduction slab. Nb/U values reflect a volcanic, calc-alkaline signature with obvious HFSE depletions. Ce/Pb values show that the volcanic rocks from Group C are related to volcanic arc rocks **(Fig. 4.37).**

Trace element concentrations related to $(La/Yb)_N$ and $(Dy/Yb)_N$ in Group C1 and C2 volcanic rocks are higher than the values in Group A and Group B volcanic rocks. In addition to the $(La/Yb)_N$ value, the $(Dy/Yb)_N$ value in Group C1 and C2 volcanic rocks is also higher than those in Group A and Group B volcanic rocks. The values are $(La/Yb)_N$ = 0.93-7.52 and $(Dy/Yb)_N$ = 0.87-1.50, with rock types being trachyte basalt, basaltic trachyte andesite, basaltic andesite, andesite, and dacite **(Fig. 4.38).**

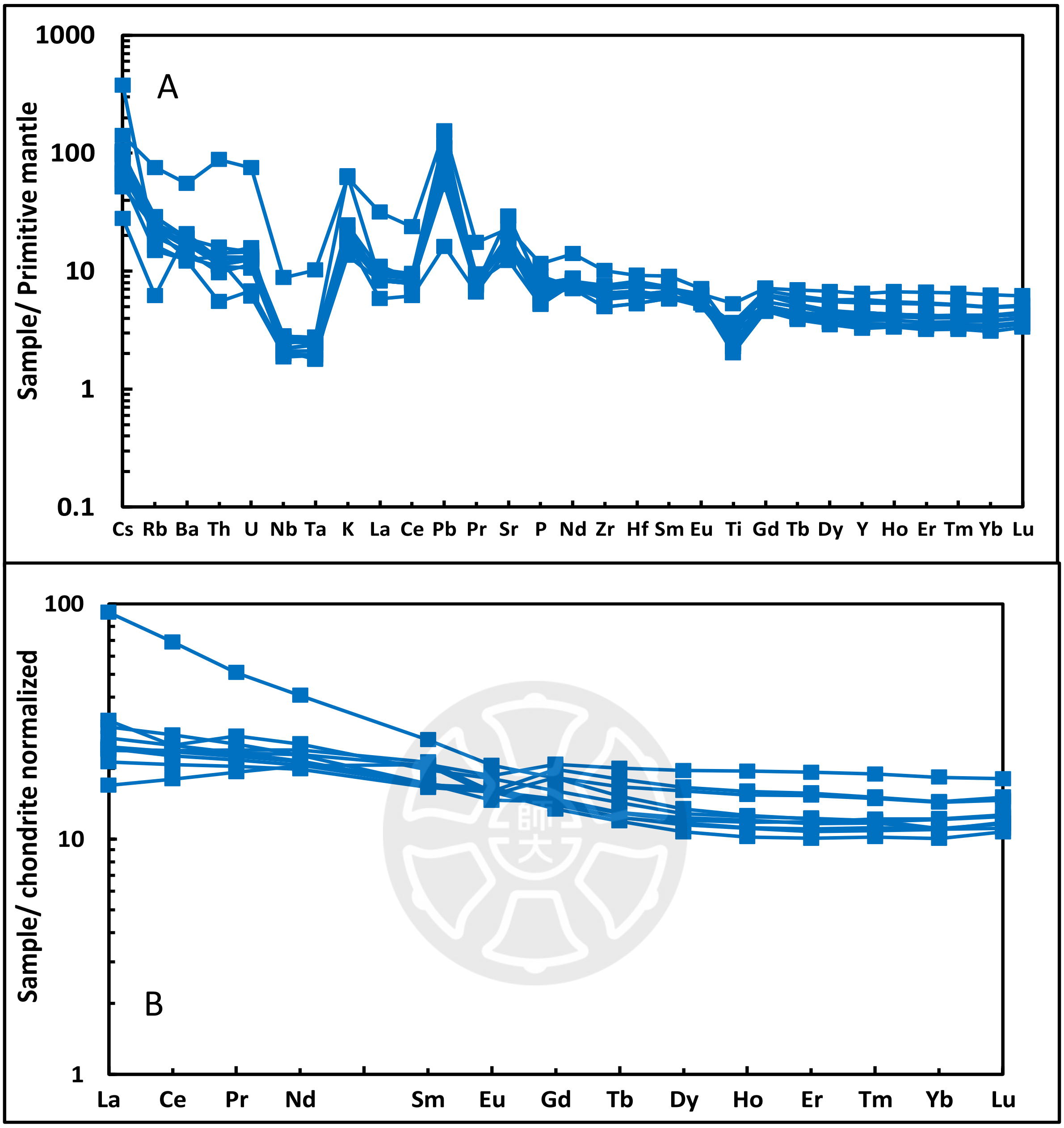

Fig. 4.35. (A). Primitive mantle-normalized trace-element diagrams of the samples from Group C1. Primitive mantle values for normalization and chondrite-normalized REE diagrams are from Sun and McDonough (1989). The primitive mantle diagram shows negative anomalies for HFSEs such as Nb, Ta, and Ti normalized variation, while LILEs are relatively enriched. (B). The chondrite-normalized diagram shows gentle and steep REE patterns.

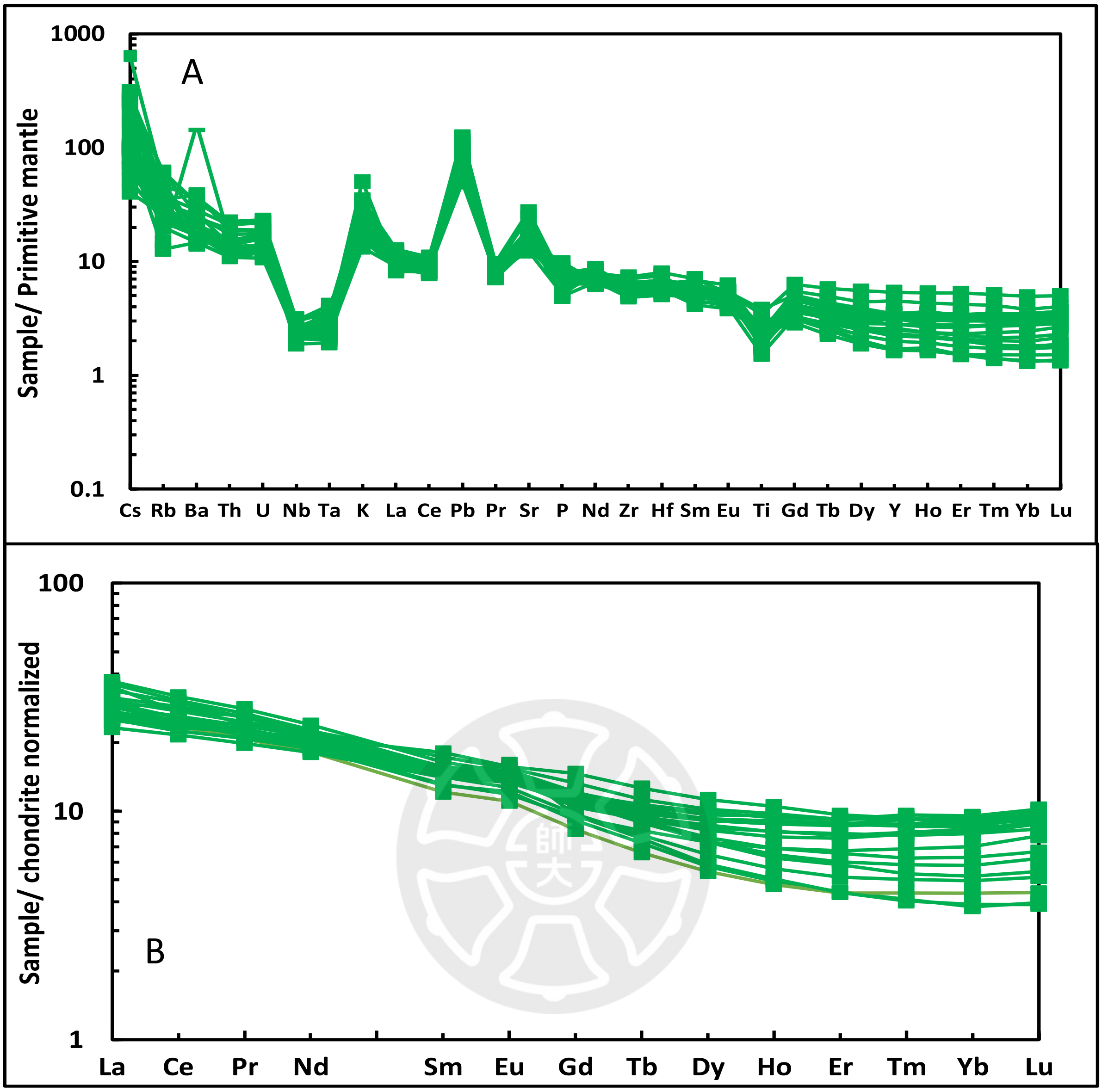

Fig. 4.36. (A). Primitive mantle-normalized trace-element diagrams of the samples from Group C2. Primitive mantle values for normalization and chondrite-normalized REE diagrams are from Sun and McDonough (1989). The primitive mantle diagram shows negative anomalies for HFSEs such as Nb, Ta, and Ti normalized variation, while LILEs are relatively enriched. (B). The chondrite-normalized diagram shows gentle and steep REE patterns.

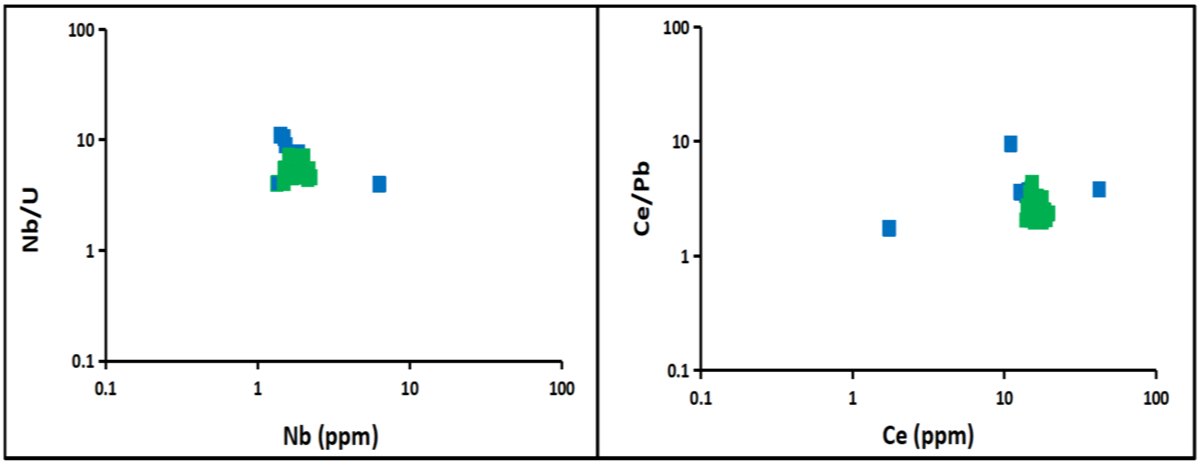

Fig. 4.37. Plots of the samples in the Nb/U vs. Nb diagram and Ce/Pb vs. Ce diagram for Group C1 (blue color) and C2 (green color). Average values for MORB and upper crust, and data for volcanic arc rocks are from Edwards et al. (1994), Hart and Reid (1991), Hofmann et al. (1986), Kersting and Arculus (1995), McDonough et al. (1992), Miller et al. (1994), and Pearce and Peate (1995).

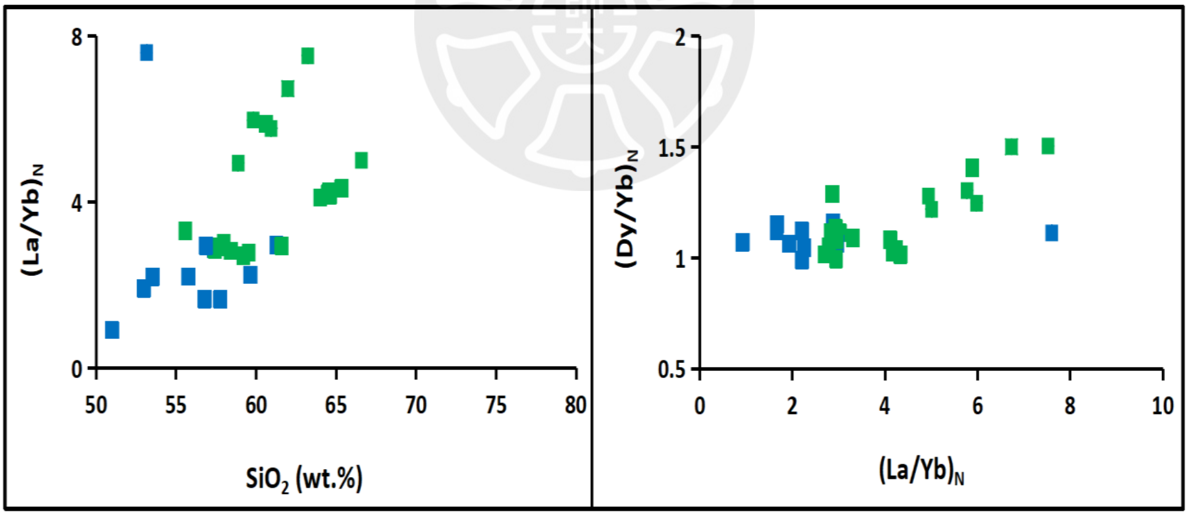

Fig. 4.38. Plot of chondrite-normalized $(La/Yb)_N$ diagram vs. major elements and $(Dy/Yb)_N$ vs. $(La/Yb)_N$ for the studied samples from Pacitan. Blue colour C1 and green color C2.

4.4.5. Sr-Nd Isotope

Table 4.8. Sr-Nd isotope composition of the selected samples from Pacitan.

No.	Group	Rock Type	SiO_2 (%)	Age (Ma)	$^{87}Rb/^{86}Sr$	$^{87}Sr/^{86}Sr$ (± 2σ)	$^{143}Sm/^{144}Nd$	$^{143}Nd/^{144}Nd$ (± 2σ)	εNd[a]
19JA20-01	A	Dacite	68.64	26.7 ± 0.4	0.110	0.703923 ± 07	0.128	0.512947 ± 05	6.0
19JA20-02	A	Andesite	59.59	26.3 ± 0.3	0.193	0.704076 ± 07	0.161	0.512965 ± 07	6.4
19JA21-01	B	Pillow Basalt	54.09	19.9 ± 0.4[b]	0.028	0.705501 ± 07	0.200	0.513007 ± 10	7.2
19JA23-02	B	Rhyolite	72.75	19.9 ± 0.4	0.658	0.705161 ± 08	0.166	0.512997 ± 09	7.0
19JA19-01	C1	Andesite	55.76	12.8 ± 0.4	0.098	0.705132 ± 08	0.158	0.512855 ± 07	4.2
19JA19-02	C1	Basaltic Andesite	53.15	13.0 ± 0.4	0.287	0.704798 ± 08	0.128	0.512909 ± 07	5.3
19JA18-04	C2	Andesite	58.88	12.5 ± 0.4	0.253	0.704821 ± 09	0.144	0.512897 ± 06	5.1

[a] $\varepsilon Nd = [(^{143}Nd/^{144}Nd)_{measured}/(^{143}Nd/^{144}Nd)_{CHUR}-1] \times 10^4$,CHUR (Chondritic uniform reservoir) = 0.512638 (Goldstein et al., 1984).

[b] ages are suggested ages according to samples from the same group.

Analysis was carried out on seven samples. Based on the data obtained, Group A consists of 19JA20-01 ($^{87}Sr/^{86}Sr$ = 0.703923 ± 0.07, $^{143}Nd/^{144}Nd$ = 0.512947 ± 0.05, εNd = 6.0) and 19JA20-02 ($^{87}Sr/^{86}Sr$ = 0.704076 ± 0.07, $^{143}Nd/^{144}Nd$ = 0.512965 ± 0.07, εNd = 6.4). Group B consists of 19JA21-01 ($^{87}Sr/^{86}$6Sr = 0.7055013 ± 0.07, $^{143}Nd/^{144}Nd$ = 0.513007 ± 0.10, εNd = 7.2) and 19JA23-02 ($^{87}Sr/^{86}Sr$ = 0.705161 ± 0.08, $^{143}Nd/^{144}Nd$ = 0.512997 ± 0.09, εNd = 7.0). Group C is divided into two parts: Group C1 consists of 19JA19-01 ($^{87}Sr/^{86}Sr$ = 0.705132 ± 0.08, $^{143}Nd/^{144}Nd$ = 0.512855 ± 0.07, εNd = 4.2) and 19JA19-02 ($^{87}Sr/^{86}Sr$ = 0.704798 ± 0.07, $^{143}Nd/^{144}Nd$ = 0.512909 ± 0.07, εNd = 5.3). Group C2 consists of 19JA19-02 ($^{87}Sr/^{86}Sr$ = 0.704821 ± 0.09, $^{143}Nd/^{144}Nd$ = 0.512897 ± 0.06, εNd = 5.1). Based on the Sr-Nd analysis, the εNd values in Group A and Group B range from +6.0 to +6.4 and +7.0 to +7.2, respectively, indicating the same magma source composition. In contrast, Group C displays εNd values between +4.2 and +5.3, suggesting an enrichment process relative to Groups A and B **(Figs. 4.39** and **4.40)**.

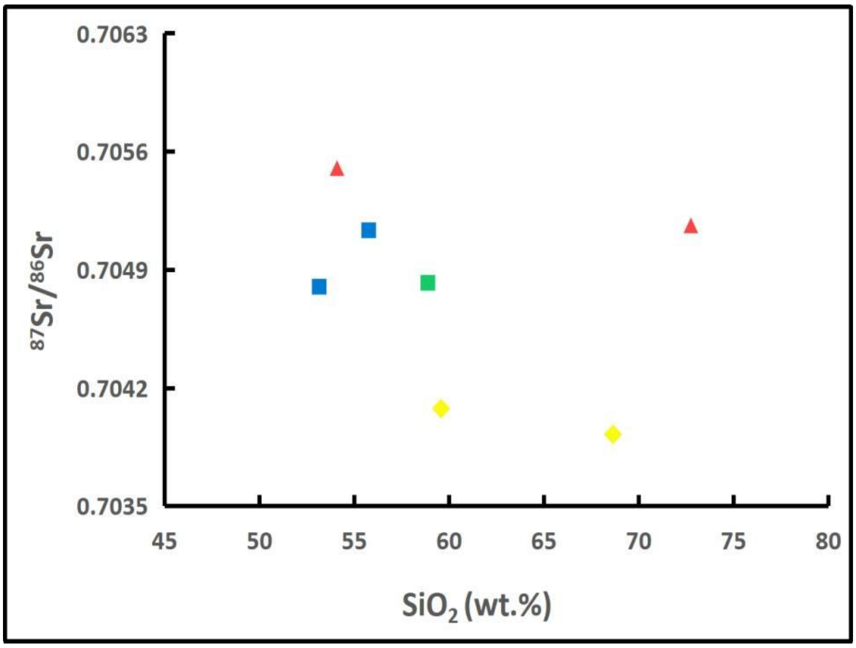

Fig. 4.39. $^{87}Sr/^{86}Sr$ vs SiO_2 diagram for samples from Pacitan.

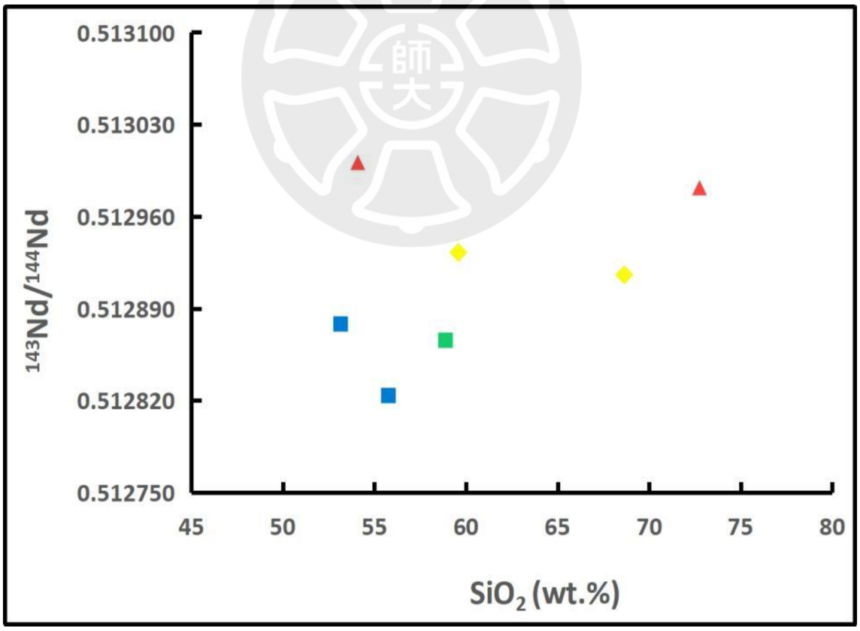

Fig. 4.40. $^{87}Sr/^{86}Sr$ vs SiO_2 diagram for samples from Pacitan.

4.5. Lu-Hf Isotope

The study analyzed eight samples, consisting of Group A (19JA20–01 and 19JA20–03) with εHf values ranging from +13.8 to +17.5, one sample from Group B (19JA45–01) with εHf values from +13.6 to +16.3, one sample from Group C1 (19JA19–01) with εHf values from +12.4 to +15.4, and four samples from Group C2 (19JA18–03, 19JA18–04, 19JA32–02, and 19JA46–01) with εHf values from +11.9 to +15.6. The data suggest that zircon grains in Groups A, B, and C have very similar εHf values, ranging from +11.9 to +17.5 **(Fig. 4.41).** When compared with the Hf isotope values of zircons from West Java, the results are consistent (Lai et al., 2022), as well as with the Hf isotope values of zircons from the island of Sumatra (Lai et al., 2023), showing the characteristics of the Sunda Arc.

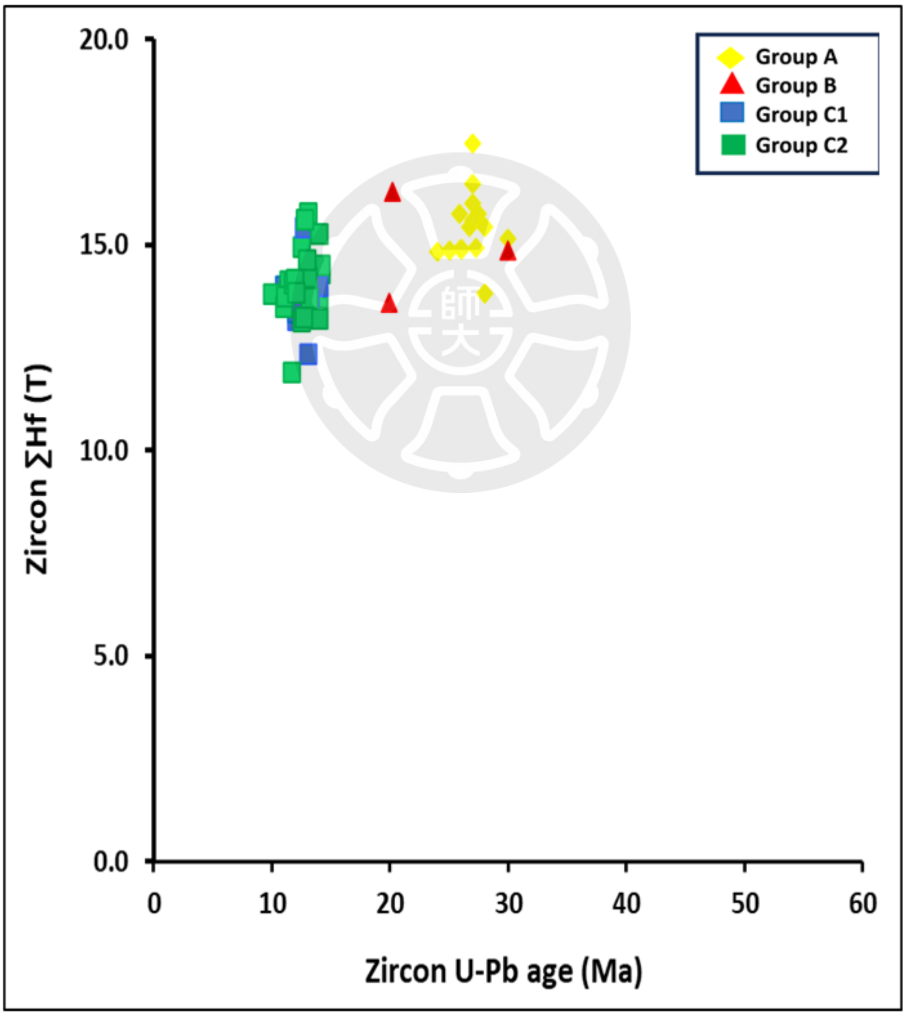

Fig. 4.41. Zircon ε_{Hf} versus U-Pb age diagram showing relatively similar values, indicating the characteristics of the Sunda Arc.

Table 4.9. Zircon Hf isotopes used in this study.

Spot	U (ppm)	Th/U	Inferred age (Ma)	±1 s	Hf isotopes										
					$^{176}Hf/^{177}Hf$	±2 s	$^{176}Lu/^{177}Hf$	±2 s	$^{176}Yb/^{177}Hf$	±2 s	$^{176}Hf/^{177}Hf$ (T)	$^{176}Hf/^{177}Hf$ CHUR (T)	$\varepsilon Hf_{(0)}$	$\varepsilon Hf_{(T)}$	±2 s
19JA20-01A-01	111	0.4	28	1	0.283159	0.000014	0.001736	0.000019	0.062670	0.000740	0.283158	0.282767	13.2	13.8	0.5
19JA20-01A-02	1064	2.2	27.5	0.7	0.283216	0.000034	0.005435	0.000094	0.218451	0.003800	0.283213	0.282768	15.2	15.7	1.2
19JA20-01A-03	107	0.5	25	1	0.283191	0.000015	0.001998	0.000026	0.069939	0.001060	0.283189	0.282769	14.4	14.9	0.5
19JA20-01A-04	208	0.4	27	1	0.283222	0.000016	0.002213	0.000015	0.080186	0.000440	0.283221	0.282768	15.4	16.0	0.6
19JA20-01A-05	229	0.6	26.7	0.8	0.283206	0.000016	0.002394	0.000024	0.087316	0.000680	0.283196	0.282768	14.9	15.4	0.6
19JA20-01A-06	97	0.5	26	1	0.283191	0.000015	0.002272	0.000005	0.079830	0.000138	0.283189	0.282769	14.4	14.9	0.5
19JA20-01A-07	100	0.4	27	2	0.283263	0.000028	0.002370	0.000084	0.078375	0.001540	0.283262	0.282768	16.9	17.5	1.0
19JA20-01A-08	263	0.6	27	1	0.283235	0.000018	0.002893	0.000032	0.104771	0.001000	0.283234	0.282768	15.9	16.5	0.6
19JA20-01A-09	296	0.6	30	4	0.283195	0.000017	0.001059	0.000046	0.036579	0.001500	0.283195	0.282766	14.5	15.2	0.6
19JA20-03A-01	101	0.4	28	1	0.283205	0.000017	0.002217	0.000028	0.077267	0.000980	0.283211	0.282767	14.8	15.4	0.6
19JA20-03A-02	535	0.7	27.3	1	0.283191	0.000017	0.001846	0.000028	0.065498	0.000800	0.283191	0.282768	14.4	14.9	0.6
19JA20-03A-03	153	0.6	25.9	0.9	0.283215	0.000024	0.001703	0.000030	0.063015	0.001420	0.283214	0.282769	15.2	15.7	0.8
19JA20-03A-05	222	0.8	27	1	0.283210	0.000024	0.001860	0.000044	0.066861	0.001360	0.283209	0.282768	15.0	15.6	0.8
19JA20-03A-07	129	0.5	26.1	0.8	0.283191	0.000020	0.002231	0.000038	0.072689	0.000540	0.283191	0.282769	14.4	14.9	0.7
19JA20-03A-09	96	0.4	24	1	0.283190	0.000016	0.002282	0.000028	0.081252	0.000960	0.283189	0.282769	14.3	14.8	0.6
19JA18-03A-01	222	0.7	12.5	0.7	0.283200	0.000019	0.001703	0.000034	0.057951	0.001120	0.283191	0.282777	14.7	14.9	0.7
19JA18-03A-02	56	0.3	13	1	0.283161	0.000019	0.001401	0.000030	0.048297	0.001040	0.283161	0.282777	13.3	13.6	0.7
19JA18-03A-03	122	0.5	13.2	0.9	0.283181	0.000019	0.001330	0.000022	0.045019	0.000720	0.283181	0.282777	14.0	14.3	0.7
19JA18-03A-04	75	0.4	13	1	0.283174	0.000020	0.001580	0.000011	0.051819	0.000460	0.283174	0.282777	13.8	14.0	0.7
19JA18-03A-05	185	0.5	14	0.7	0.283182	0.000015	0.001419	0.000010	0.048268	0.000440	0.283182	0.282776	14.1	14.4	0.5
19JA18-03A-06	46	0.4	14	1	0.283164	0.000017	0.001200	0.000004	0.040648	0.000182	0.283164	0.282776	13.4	13.7	0.6
19JA18-03A-07	154	0.6	13.3	0.6	0.283179	0.000022	0.000859	0.000019	0.027905	0.000520	0.283179	0.282777	13.9	14.2	0.8
19JA18-03A-08	161	0.5	14.2	0.7	0.283181	0.000017	0.001583	0.000022	0.055753	0.001040	0.283181	0.282776	14.0	14.3	0.6
19JA18-03A-09	153	0.7	13.1	0.9	0.283187	0.000016	0.001900	0.000024	0.064094	0.000700	0.283186	0.282777	14.2	14.5	0.6
19JA19-01A-01	95	0.3	14	1	0.283173	0.000022	0.000675	0.000005	0.020899	0.000186	0.283173	0.282776	13.7	14.0	0.8
19JA19-01A-02	272	0.8	13.2	0.6	0.283163	0.000022	0.000458	0.000013	0.015414	0.000560	0.283162	0.282777	13.3	13.6	0.8
19JA19-01A-03	40	0.4	13	2	0.283127	0.000020	0.000946	0.000018	0.030855	0.000720	0.283126	0.282777	12.1	12.4	0.7
19JA19-01A-04	142	0.6	12.7	0.9	0.283214	0.000020	0.001859	0.000048	0.063091	0.001580	0.283213	0.282777	15.2	15.4	0.7
19JA19-01A-05	76	0.3	13	1	0.283166	0.000020	0.001186	0.000038	0.039275	0.001220	0.283166	0.282777	13.5	13.8	0.7
19JA19-01A-06	152	0.4	13	1	0.283161	0.000020	0.001376	0.000018	0.046727	0.000380	0.283161	0.282777	13.3	13.6	0.7
19JA19-01A-07	37	0.4	12	3	0.283151	0.000020	0.000763	0.000004	0.024536	0.000220	0.283151	0.282777	12.9	13.2	0.7
19JA19-01A-08	93	0.4	11	1	0.283174	0.000018	0.001528	0.000013	0.051428	0.000440	0.283174	0.282778	13.8	14.0	0.6
19JA19-01A-09	116	0.6	12	1	0.283156	0.000022	0.001064	0.000004	0.034349	0.000162	0.283155	0.282777	13.1	13.4	0.8
19JA18-04A-01	120	0.5	14.2	0.9	0.283187	0.000020	0.002236	0.000034	0.073770	0.001280	0.283186	0.282776	14.2	14.5	0.7
19JA18-04A-02	33	0.4	10	3	0.283169	0.000020	0.001353	0.000022	0.043177	0.000760	0.283169	0.282779	13.6	13.8	0.7
19JA18-04A-03	92	0.5	11	1	0.283160	0.000020	0.000994	0.000013	0.032217	0.000440	0.283160	0.282778	13.3	13.5	0.7
19JA18-04A-04	196	0.5	12	0.8	0.283188	0.000026	0.001480	0.000022	0.049291	0.000900	0.283187	0.282777	14.2	14.5	0.9
19JA18-04A-05	171	0.4	12.5	0.8	0.283149	0.000018	0.001575	0.000015	0.052219	0.000420	0.283149	0.282777	12.9	13.1	0.6
19JA18-04A-06	97	0.4	13.1	0.9	0.283165	0.000017	0.001207	0.000004	0.039126	0.000154	0.283165	0.282777	13.4	13.7	0.6
19JA18-04A-07	189	0.6	11.4	0.6	0.283178	0.000018	0.001662	0.000007	0.054998	0.000320	0.283177	0.282778	13.9	14.1	0.6
19JA18-04A-08	120	0.5	13	1	0.283180	0.000019	0.001360	0.000024	0.044290	0.000740	0.283179	0.282777	14.0	14.2	0.7
19JA18-04A-09	35	0.4	14	2	0.283150	0.000022	0.000795	0.000014	0.025049	0.000360	0.283150	0.282776	12.9	13.2	0.8
19JA32-02A-01	51	0.4	12.7	1	0.283152	0.000020	0.001500	0.000011	0.047857	0.000400	0.283151	0.282777	13.0	13.2	0.7
19JA32-02A-02	73	0.4	12.9	0.8	0.283192	0.000022	0.001936	0.000007	0.062978	0.000440	0.283191	0.282777	14.4	14.7	0.8
19JA32-02A-03	34	0.3	14	1	0.283209	0.000024	0.001381	0.000028	0.043213	0.000760	0.283208	0.282776	15.0	15.3	0.8
19JA32-02A-04	113	0.6	11.1	0.6	0.283167	0.000022	0.002494	0.000024	0.084172	0.000900	0.283166	0.282778	13.5	13.7	0.8
19JA32-02A-05	82	0.5	13	0.7	0.283224	0.000020	0.002508	0.000032	0.080193	0.000360	0.283223	0.282777	15.5	15.8	0.7
19JA32-02A-06	62	0.4	11.7	0.7	0.283176	0.000028	0.001516	0.000020	0.045797	0.000300	0.283176	0.282778	13.8	14.1	1.0
19JA32-02A-07	77	0.5	12.8	0.8	0.283219	0.000020	0.002254	0.000010	0.072351	0.000700	0.283219	0.282777	15.4	15.6	0.7
19JA32-02A-08	45	0.6	11.9	1	0.283178	0.000024	0.001994	0.000052	0.068484	0.001980	0.283178	0.282778	13.9	14.2	0.8
19JA32-02A-09	31	0.4	12	1	0.283170	0.000024	0.001674	0.000012	0.054561	0.000560	0.283169	0.282777	13.6	13.9	0.8
19JA45-01-07	193	0.6	20.2	0.6	0.283234	0.000032	0.002056	0.000052	0.068283	0.000440	0.282772	0.283233	15.9	16.3	1.1
19JA45-01-09	248	0.7	30	1	0.283189	0.000054	0.004498	0.000100	0.142778	0.004200	0.282766	0.283187	14.3	14.9	1.9
19JA45-01-10	229	0.7	19.9	0.8	0.283158	0.000056	0.003462	0.000008	0.100921	0.000240	0.282773	0.283157	13.2	13.6	2.0
19JA46-01A-02	1581	2.5	11.6	0.3	0.283115	0.000020	0.001750	0.000038	0.059012	0.000620	0.282778	0.283115	11.7	11.9	0.7

CHAPTER 5. DISCUSSION

5.1. Age of magmatism in Pacitan

Based on previous publications using the K-Ar method, age data indicate that the magmatic process in the southern mountains generally began in the Late Eocene, around 40 Ma (Soeria-Atmadja et al., 1994). Specifically, in the Pacitan area, most of the samples were found to be from the Late Oligocene, around 28 Ma (Sutanto, 2003), with the youngest dated at the Middle Miocene, around 15 Ma (Soeria-Atmadja et al., 1994). The oldest dated magmatic activity in Pacitan took place in the Late Eocene, but the main period was during the Oligocene–Miocene (Soeria-Atmadja et al., 1994). In our latest data using the U-Pb zircon method on several volcanic rock samples, three different age ranges were obtained. These ages show that the most recent data are younger than previously reported. Magmatic ages obtained in this study range from 26.7 ± 0.4 to 26.0 ± 0.3 Ma (Late Oligocene), from samples collected from Group A with rock types of dacite and andesite; 19.9 ± 0.4 Ma (Early Miocene), from a sample collected from Group B with tuff; and 11.4 ± 0.2 to 13.4 ± 0.3 to 1.4 ± 0.2 Ma (Middle Miocene), from samples collected from Group C **(Fig. 5.1),** with rock types including andesite, dacite, and basaltic andesite. Based on the data obtained, three eruption periods can be identified in the Pacitan area. The first eruption period was from 28 to 26.0 Ma, followed by the second from 20 to 19 Ma, and the final from 16.3 to 11.8 Ma. The volcanism began in the Oligocene, as indicated by the U-Pb zircon data, with an estimated time distribution from around 30 to 25 Ma. This was followed by a magmatic pause of approximately 5 Ma, then a minor eruption from 20 to 19 Ma, and a second magmatic pause lasting 3 to 4 Ma. The final phase of magmatism occurred around 16 Ma.

The Old Andesite is thought to represent older volcanic rocks along the southern coast of Java, estimated to be Eocene in age. In the Pacitan area, Group A is considered part of the Old Andesite unit in southern Java (Setijadji et al., 2006). According to previous K-Ar research by Soeria-Atmadja et al. (1994), the age of the Old Andesite is approximately 28 to 26.0 Ma in the Pacitan area, 39.9 to 26.6 Ma in the Karangsambung area, and 29.6 to 22.6 Ma around Purworejo. U-Pb zircon dating results show that the Old Andesite is associated with early arc magmatism resulting from the subduction of the India-Australian Plate beneath southern Java, with volcanic activity estimated to have occurred during the Oligocene, around 30 Ma.

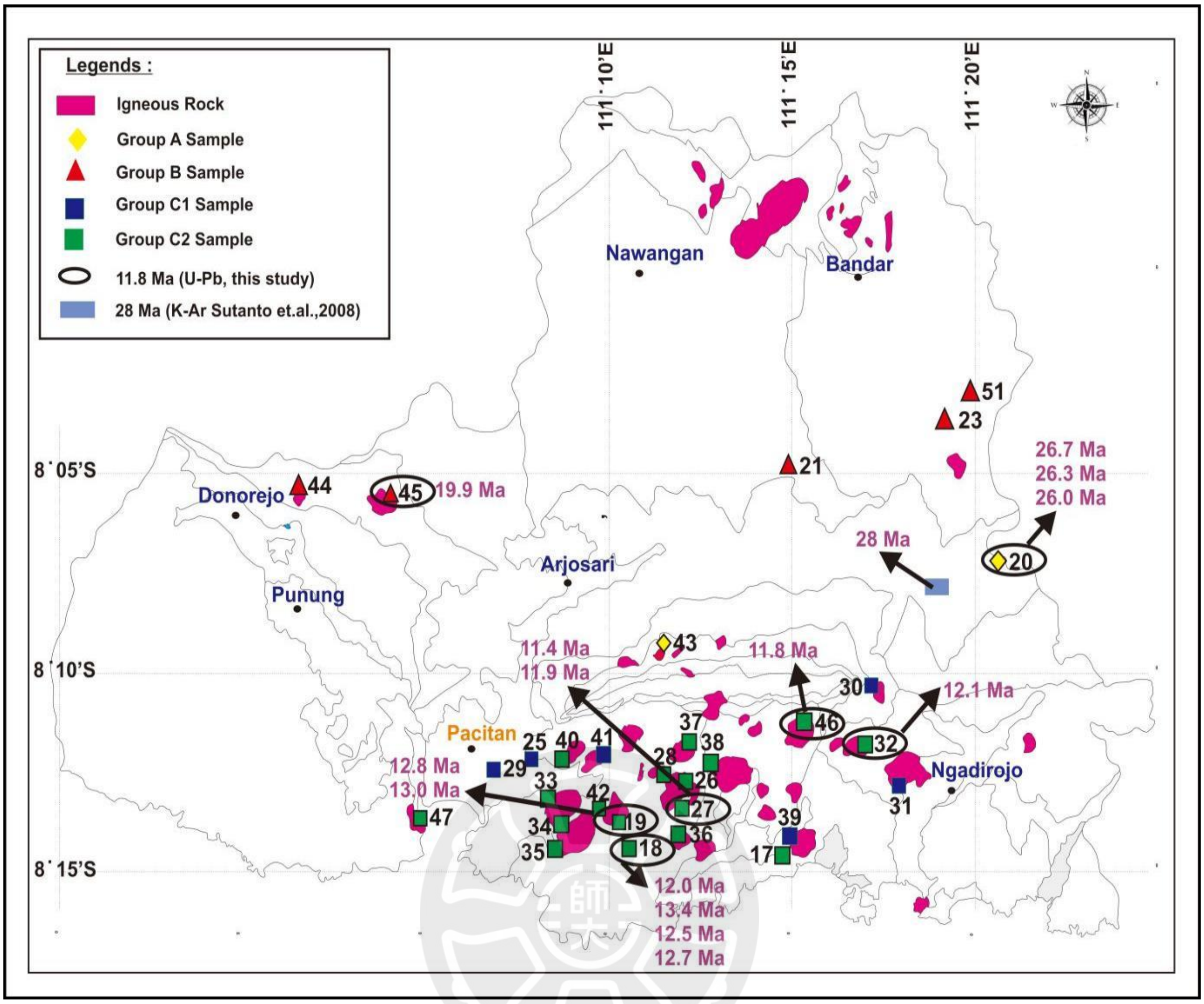

Fig. 5.1. Distribution of igneous rocks in Pacitan (modified by Samodra et al., 1992)

5.2. Temporal and spatial geochemical variations in the Pacitan area

Based on the geochemical results of the volcanic rocks from Pacitan, the primitive mantle-normalized trace element diagram shows that all samples exhibit depletions in Ta, Nb, and Ti, which are typical of island arc magmatism. The rare earth element (REE) diagrams of the volcanic rocks (**Fig. 5.2**) show that Groups A and B display negative Eu anomalies, whereas Group C does not. Group C can be subdivided into Group C1, which shows a flat trend in heavy rare earth elements (HREEs), and Group C2, which is characterized by HREE depletion in certain samples. Although some samples from Group B show less consistent trends, most samples are highly enriched in large ion lithophile elements (LILEs), such as Cs, Rb, Ba, K, and Sr, as well as in Pb. These patterns suggest that the magmatic processes were influenced by island arc magmatism, caused by the subduction of the Indian-Australian Plate beneath the Eurasian Plate during the Cenozoic, which led to the formation of the Sunda Arc.

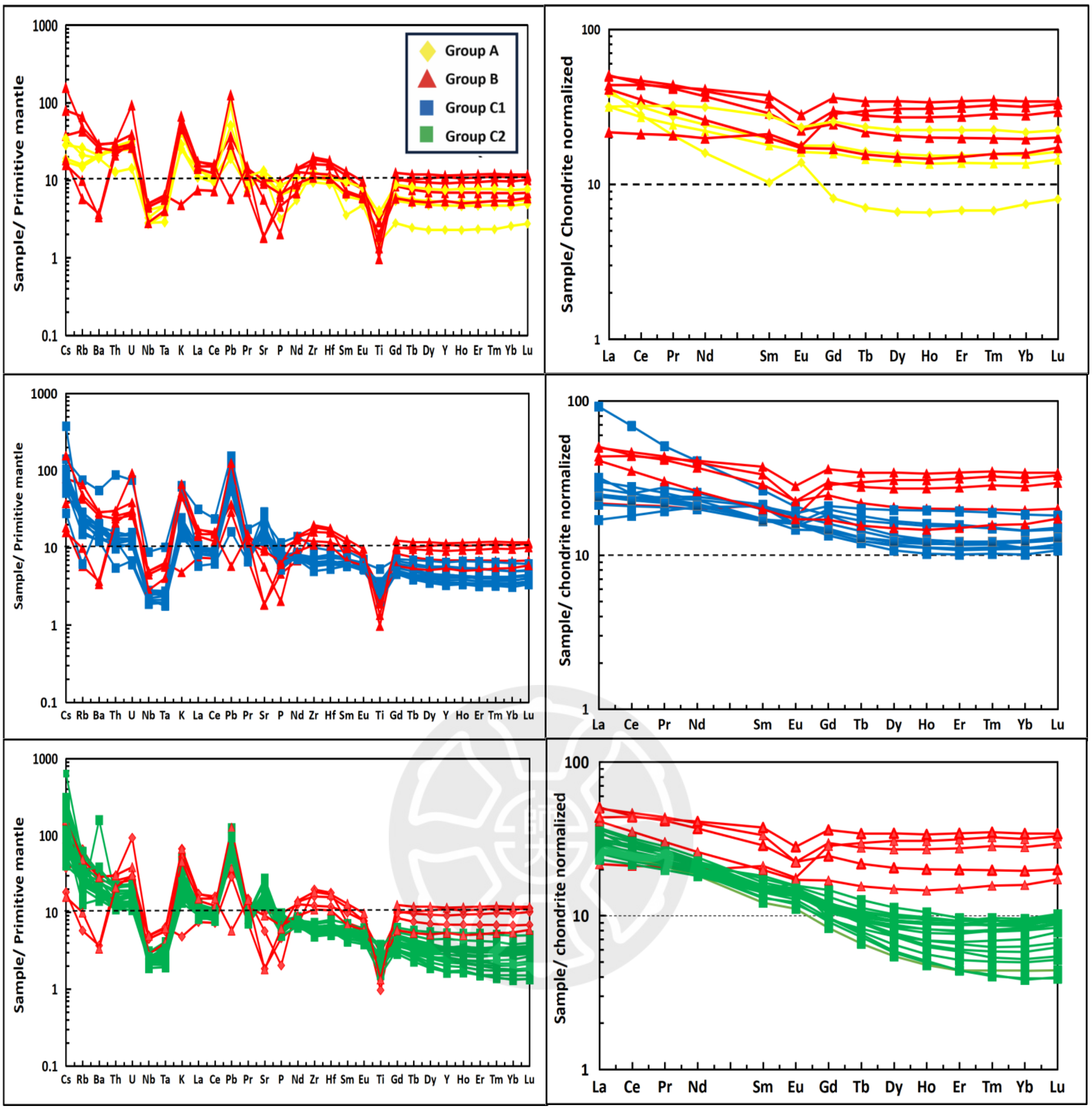

Fig. 5.2. Chondrite-normalized rare earth elements (REE) and Primitive mantle normalized multi-element spider diagram from Pacitan. Value were source from Sun and McDonough (1989).

Group A based on isotopic results is known to have values ($^{87}Sr/^{86}Sr$ = 0.703 to 0.704, ε_{Nd} value = +6.0 to +6.4, ε_{Hf} zircon value = +13.8 to +17.5) and Group B ($^{87}Sr/^{86}Sr$ = 0.705, ε_{Nd} value = +7.0 to +7.2, zircon ε_{Hf} value = +13.6 to +16.3) on the other hand, Group C is contaminated with crustal material where the values obtained decrease to +4.2 to +5.3 and the zircon ε_{Hf} value decreases slightly to +11.9 to +15.6.

Samples with $^{87}Sr/^{86}Sr$ ratios ranging from 0.704 to 0.706 found in the Sunda–Banda Arc are interpreted as being derived from melting of a depleted mantle source, subsequently contaminated by limited crustal material (Wheeler et al., 1987). According to Turner and Foden (2001), magmas originating from the Sunda Arc result from partial melting of a thinned mantle, followed by source contamination, as evidenced by Nd isotope data from volcanic rocks in the Sunda Arc. Additionally, the ε_{Nd} values typically range from +10 to 0. Compared to data from Sumatra (Lai et al., 2023), magma from the Sunda Arc generally exhibits ε_{Hf} values between +17 and +10. These observations clearly indicate that the magmatism in Pacitan represents typical Sunda Arc magmatism, formed through partial melting of a depleted mantle, followed by source contamination (Whitford, 1981; Wheeler et al., 1987; Edwards, 1993; Turner and Foden, 2001; Handley et al., 2007, 2014). In the final stage, a greater degree of crustal involvement occurred compared to the earlier magmatic periods.

In addition to the partial melting process, the composition of the plate also plays a very important role in the petrogenesis of magma that occurs in the Pacitan area. Based on geochemical data, it shows that the magma from the three periods is influenced by the process of enrichment of plate fluids accompanied by partial melting with a composition of SiO_2 = 51 wt.% of group C1 where the initial magma undergoes differentiation from the mantle. The petrogenesis process that occurs is controlled by the presence of a fractional crystallization **(Fig. 5.3).** The La/Yb diagrams plotted against La clearly show the influence of the fractional crystallization. Groups A and B are also related to fractional crystallization processes.

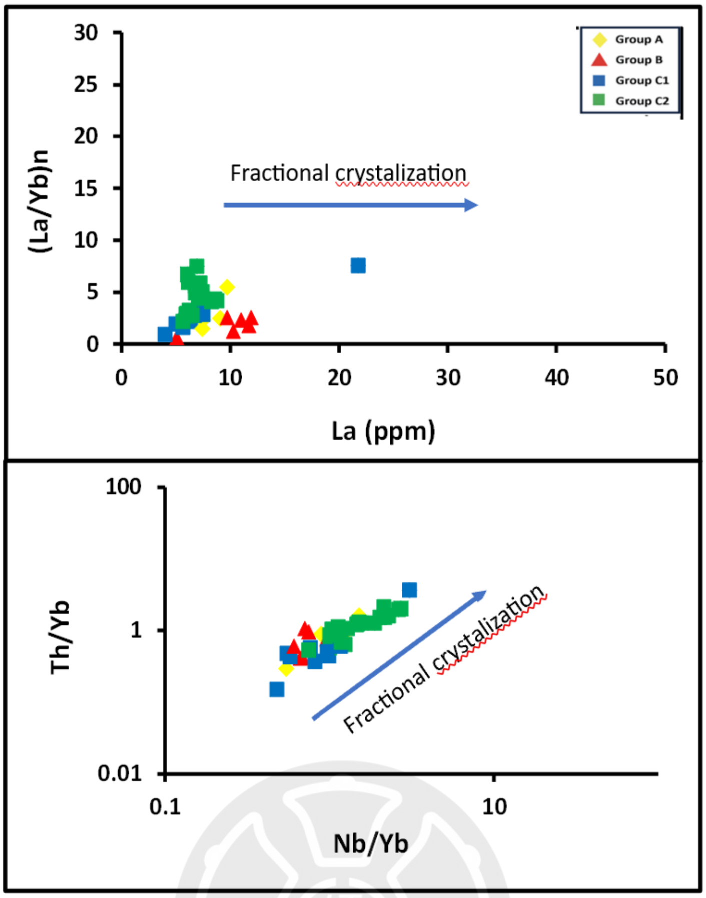

Fig. 5.3. La/Yb versus La and Th/Yb versus Nb/Yb diagram show petrogenesis process control by fractional crystallization.

Based on magma composition, Group B has SiO_2 > 67 wt.%, with low Pb, P, and K contents, high HREE concentrations, and an age ranging from 19.9 to 19.0 Ma. This suggests that the magmatism was driven by a brief thermal event. Available data indicate that Group B magma was generated in the inner part of the subduction zone (see **Fig. 5.8**) Around 5 Ma, Group A and Group B experienced tectonic changes that ceased subduction, resulting in a short-lived thermal intrusion within the subduction zone. This thermal intrusion was caused by continued subduction of the leading edge of the slab even after the cessation of slab pull. This process could have led to slab tearing, allowing heat from the asthenosphere to rise and warm the lower crust, forming magma with high SiO_2 and HREE contents, and low concentrations of elements such as Pb and P. These elements are stable in the lower crust and have limited mobility during partial melting.

Group C is located closer to the trench than the other groups, which may account for its distinct magmatic characteristics, likely influenced by a steeper subduction angle (see **Fig.**

5.2, and Fig. 5.6). Group C1 displays a flat REE pattern and has a normal arc composition, based on the Sr/Y versus Y plot. Group C2, according to the Sr/Y versus Y plot, belongs to the adakite field, showing depletion in HREE. Both magmatic processes appear to have occurred simultaneously **(Fig. 5.4)**. A comparison of Groups C1 and C2 indicates that C2 was more strongly influenced by slab melt enrichment, consistent with the formation of adakites.

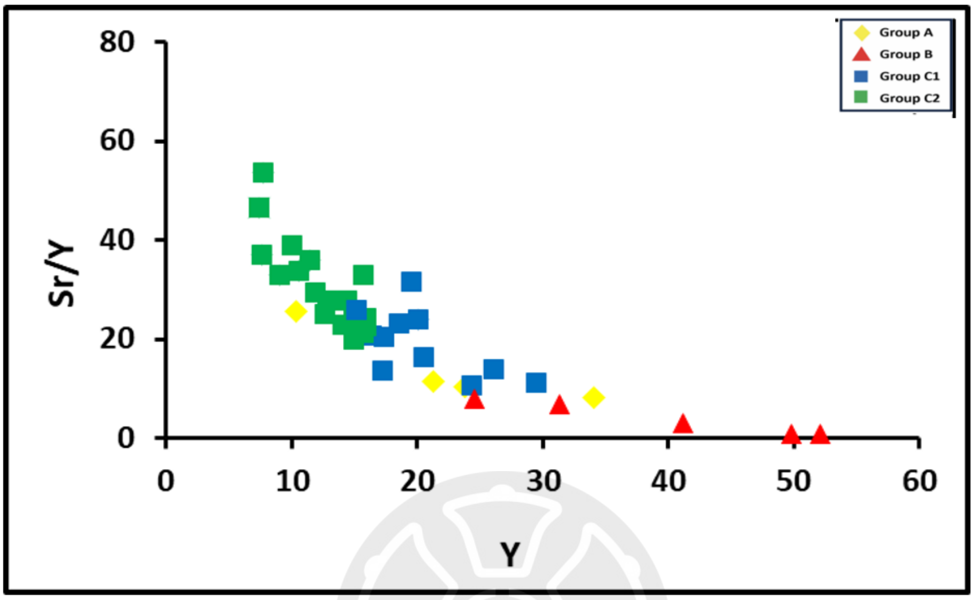

Fig. 5.4. Sr/Y versus Y diagram showing characteristic of adakite

5.3. Adakite in Pacitan

According to Defant and Drummond (1990), adakite is volcanic rock form slowly in the crusts, characterized by medium SiO_2 content, relatively high Al_2O_3, Sr/Y, and La/Yb ratios, and low Y and Yb concentrations **(Fig. 5.5)**. These rocks are originally formed from the melting of young and hot subducted oceanic crust, which explains the formation process of adakitic magmas (Defant and Kepezhinskas, 2019; Sun et al., 2020) **(Fig. 5.6)**. The formation of adakitic rocks can be attributed to the following processes:

a) Partial melting of subducted oceanic crust (Defant and Drummond, 1990; Martin, 1999; Castillo, 2012; Tang et al., 2014);
b) Partial melting of subducted continental crust (Wang et al., 2008);
c) Partial melting of the lower crust (thickened and/or delaminated basaltic lower crust) (Atherton and Petford, 1993; Rudnick, 1995; Chung et al., 2003; Wang et al., 2006; Karsli et al., 2010);
d) High-pressure crystallization (Macpherson et al., 2006); and
e) Assimilation and low-pressure fractional crystallization of the parent basaltic magma (Castillo et al., 1999; Li et al., 2009)

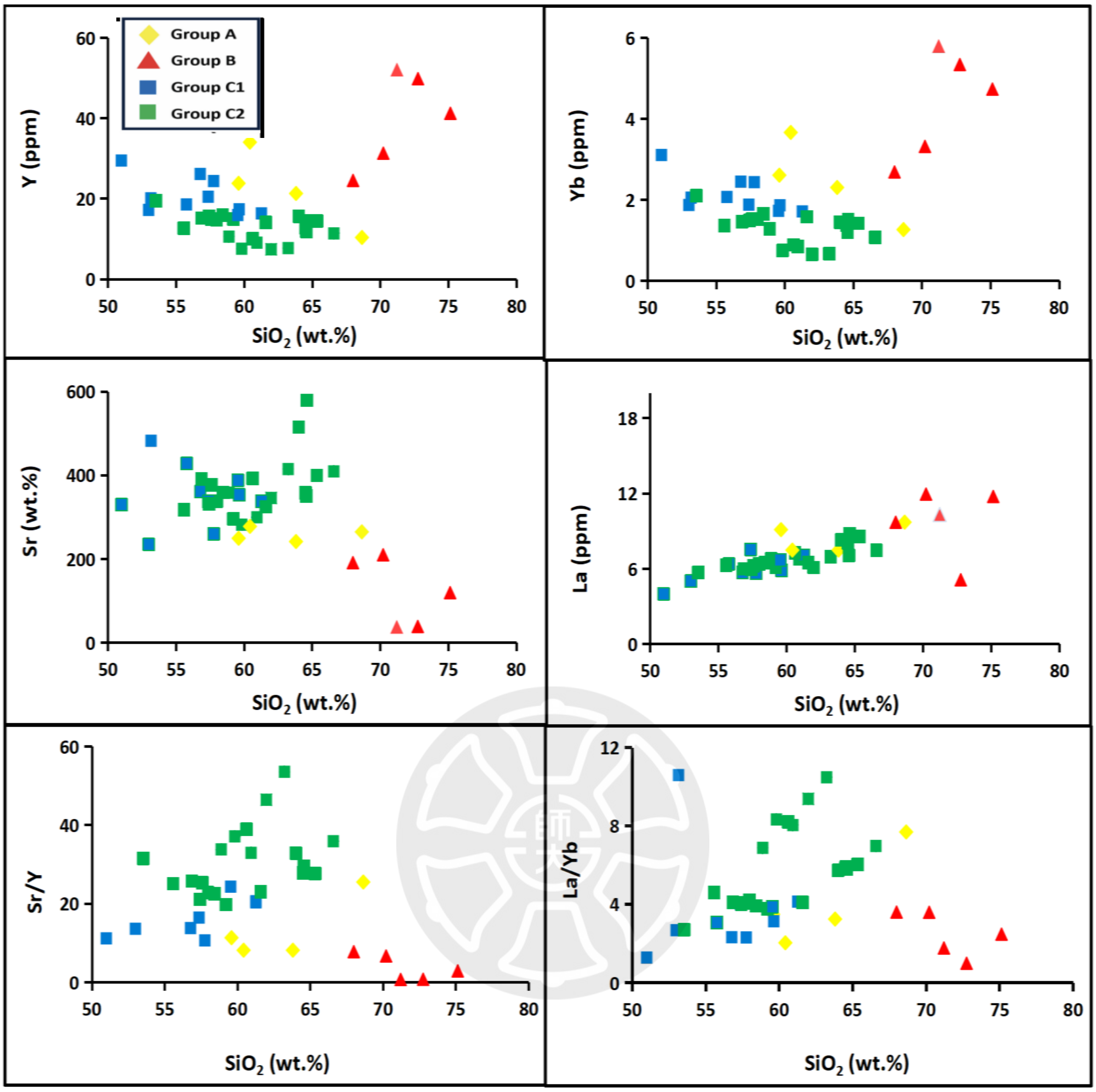

Fig. 5.5. Geochemical bivariate plot of the studied rocks

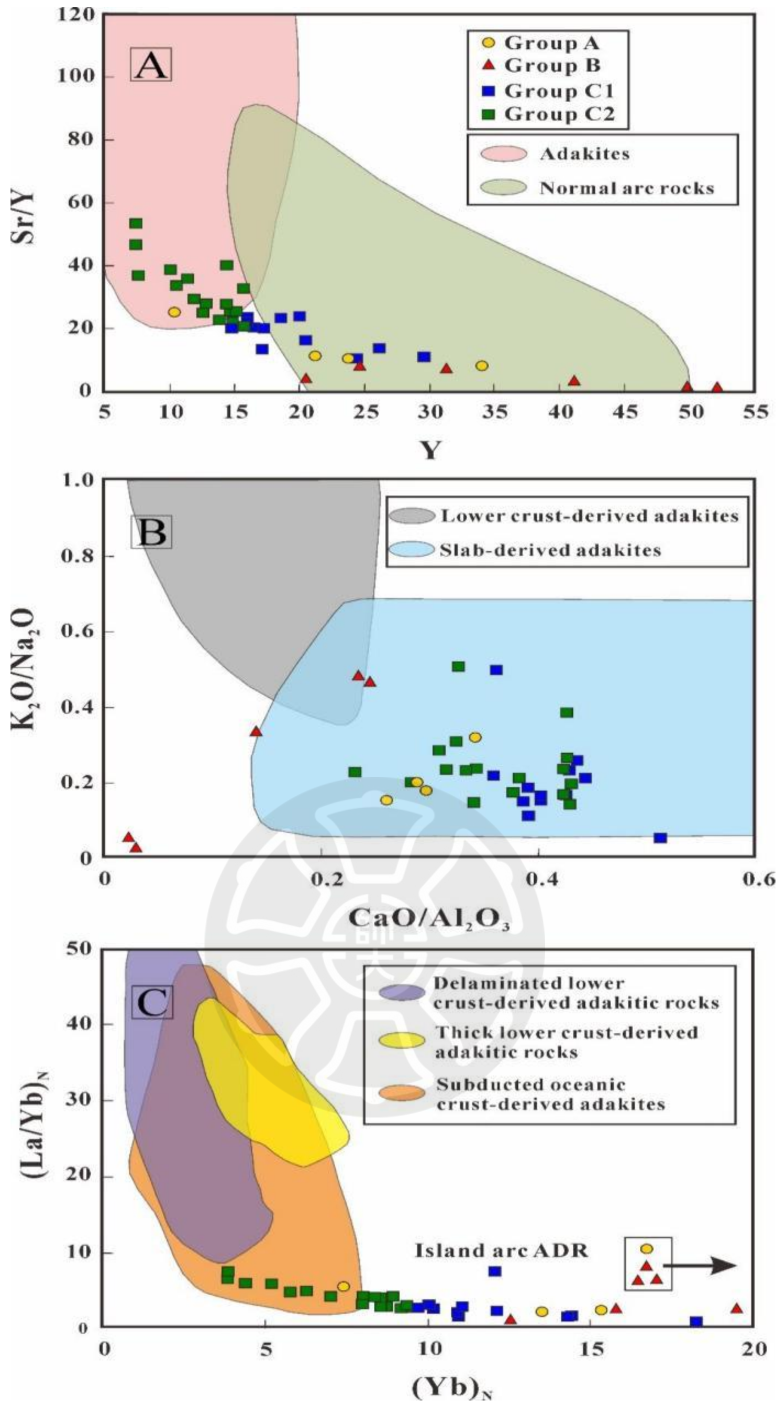

Fig. 5.6. Geochemical bivariate plot of the studied rocks. (A) Sr/Y versus Y diagram showing of adakite with characteristic of island arcs (Defant and Drummond, 1990). (B) K_2O/Na_2O versus CaO/Al_2O_3 diagram, showing the lower crust-derived adakites and slab-derived adakites (Li et al., 2016). (C) Diagram of $(La)_N/(Yb)_N$ versus $(Yb)_N$, showing for adakite derived from delaminated lower crust, adakite derived from thick lower crust, and adakite derived from subducted oceanic crust (Wang et al., 2006).

5.3.1 Partial melting of subducted oceanic crust

The process of adakite formation starts from partial melting of subducted oceanic crust. Such research has been published by Setijadji et al. (2006) in the Karangsambung area, Central Java, the Selogiri and Wediombo areas along the southern direction from Muria Volcano to the south coast, and the Tulungagung area east of Pacitan. The process is related to the northward subduction of mid-ocean ridge basalt (MORB) of the India-Australian Plate, which leads to melting. Another mechanism is related to the melting of the plate beneath another plate.

The chemical composition of adakite, according to Wang et al. (2006), Li and Zhu (2016), and Shao et al. (2020), is consistent with the chemical composition of regions derived from oceanic plates and is tectonically associated with oceanic plate subduction. According to several studies, there is evidence of subduction of oceanic ridges south of Java (Hall, 2012; Xia et al., 2022). Ridge subduction is a form of subduction that causes tearing of the subducting plate, allowing heat from the underlying asthenosphere to rise and cause melting of the subducted oceanic plate (Setijadji et al., 2006). Another study by Xia et al. (2023) states that, in the last 10 Ma, a ridge subduction process occurred in southern Java, which took place 3 Ma later than the adakite occurrence in the Pacitan area.

5.3.2 Partial melting of the lower crust

Adakitic magma processes originate from partial melting of the thickened lower crust (Rudnick, 1995; Chung et al., 2003; Karsli et al., 2010) or from delaminated lower crust processes (Wang et al., 2007; Karsli et al., 2010). Tectonic processes such as continental collision can cause thickening of the Earth's crust, increase the density of the lower crust and cause it to sink into the mantle lithosphere. As a result, the dense crust detaches, and the upper crust sinks into the mantle.

The composition of adakite derived from the thickened lower crust has relatively low values of Mg#, MgO, Cr, Ni, and Yb compared to the composition of Pacitan adakite. Adakite derived from thickened lower crust implies a process of partial melting within garnet-amphibolite to eclogite facies. According to Atherton and Petford (1993), partial melting that occurs in the thickened lower crust can reach high temperatures of about 1000°C at a depth of 50 km, producing residual garnet, hornblende, plagioclase, and clinopyroxene. Crustal thickness and residual mineralogy in Pacitan adakite are significant factors.

Partial melting in the delaminated lower crust occurs at a depth of more than 40 km (>1.2 GPa) (Rapp and Watson, 1995; Petford and Atherton, 1996). Several studies concluded that the thickness of the Earth's crust in East Java does not exceed 39 km, making delamination processes in East Java unlikely (Wolbern and Rümpker, 2016). Based on geochemical diagrams, the Pacitan area falls outside the range for sources originating from either thickened or delaminated lower crust. Therefore, the Pacitan adakite magma source is not related to partial melting of the lower crust.

5.3.3 Partial melting of subducted continental crust

The process of partial melting of subducted continental crust may explain the origin of adakite magmas. However, during Cenozoic magmatism in Java, no subduction of continental crust occurred. Based on rock geochemical data, the K_2O composition of adakite in Pacitan is below 3 wt.%, with ε_{Nd} values ranging from +4.2 to +5.3, which indicates that no continental collision occurred. (**Fig. 5.7**).

5.3.4 High-pressure crystallization

Adakitic magmas are formed from mantle melts that undergo high-pressure fractionation of garnet and amphibole. The basaltic melt process occurs due to hydrous melting in arc systems of mantle wedges, which then accumulate and are deposited in lower crustal magma chambers. Adakitic magmas usually produce geochemical trends with decreasing Al_2O_3 and La contents, while Dy/Yb and Sr/Y ratios, as well as SiO_2 content, increase (Prouteau et al., 2001; Macpherson et al., 2006). A different case occurs in the Pacitan area, where with increasing SiO_2 content, Al_2O_3 and La do not decrease, and Sr/Y and La/Yb ratios also do not increase. Therefore, the formation process of Pacitan adakite is not always associated with high-pressure crystallization (see **Fig. 5.8**).

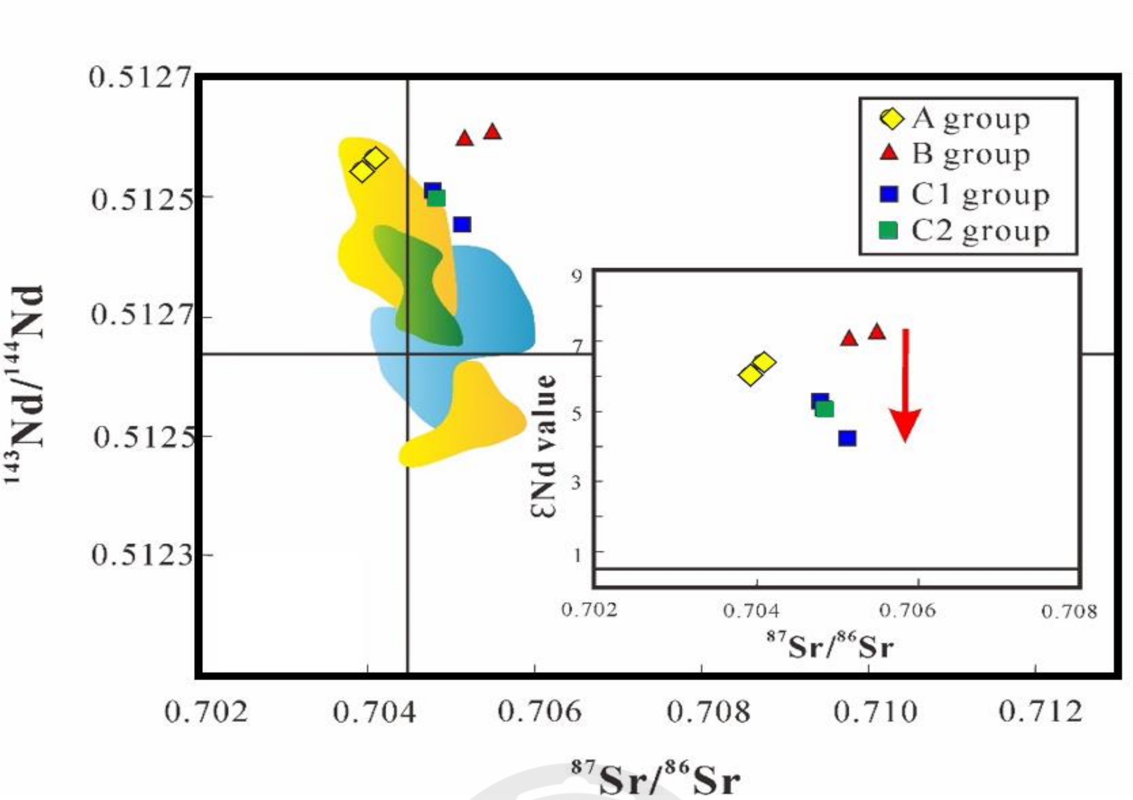

Fig. 5.7. The $^{143}Nd/^{144}Nd$ versus $^{87}Sr/^{86}Sr$ diagram. The yellow data range is sourced from West Java (Edwards et al., 1993; Gerbe et al., 1992; Sendjaja et al., 2009; Turner and Foden, 2001; White and Patchett, 1984), the blue data range is from Central Java (Edwards et al., 1991; Gertisser and Keller, 2003; Turner and Foden, 2001; White and Patchett, 1984; Whitford et al., 1981; Whitford and Jezek, 1979), and the green data range is from East Java (Edwards et al., 1994). In all figures, blue arrows indicate samples affected by fractional crystallization, while red arrows indicate crustal contamination**.**

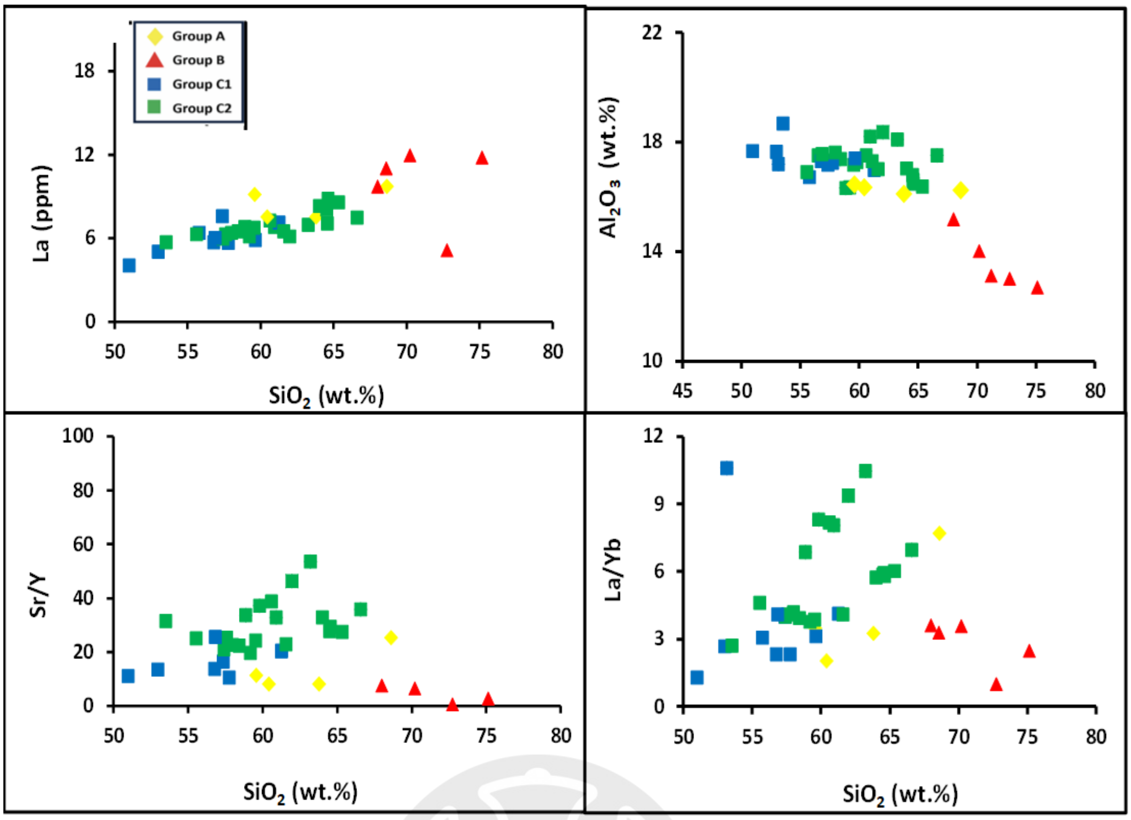

Fig. 5.8 Geochemical bivariate of studied La versus SiO_2 diagram, Sr/Y versus SiO_2 diagram, Al_2O_3 versus SiO_2 diagram, and La/Yb versus SiO_2 diagram.

5.3.5 Assimilation-low-pressure fractional crystallization from parent basaltic magmas

The final stage of adakitic magma formation is associated with assimilation and fractional crystallization processes, which originate from basaltic magma parents in the Earth's crust (Castillo et al., 1999; Bourdon et al., 2002; Grove et al., 2003; Gao et al., 2007). The process of assimilation and fractional crystallization occurs on a large scale, resulting in the composition of mafic to felsic rocks and the formation of cumulates. Adakite in the Pacitan area has a composition of $SiO_2 > 55$ wt.% with hornblende fractionation (see **Fig. 4.14, Fig. 4.17, Fig. 4.20, and Fig. 4.23)**, which occurs at low pressure but can still produce adakitic melts (Castillo et al., 1999). In addition, the Sr/Y composition does not show a significant decrease with increasing SiO_2 content (see **Fig. 5.8)**. In general, if olivine and pyroxene are fractionated from basaltic magma, it will cause a relative enrichment of HREE in the magma residue, but this is very different in the Pacitan area. The process of magma petrogenesis that occurs is not responsible for the formation of Pacitan adakite. The adakite formation mechanism in Pacitan was not caused by ridge subduction that occurred after the Late Miocene to Pliocene, as previously proposed in earlier studies, but rather is related to a formation mechanism that occurred earlier, before 13 Ma.

5.4 Tectonic and magmatic evolution

Based on the data obtained, Pacitan can be grouped into three stages (U-Pb age data), i.e., Group A (30–25 Ma), Group B (20 Ma), and Group C (15–10 Ma). From the age data, there is a magmatic gap between 25–15 Ma, with Group B only slightly representing the remaining magmatism that occurred before the eruption **(Fig. 5.9**). This is evident from the ε_{Hf}(t) and U-Pb dating diagram. In addition, comparisons were made with several previous studies related to the Sunda Arc, namely from Sumatra and West Java.

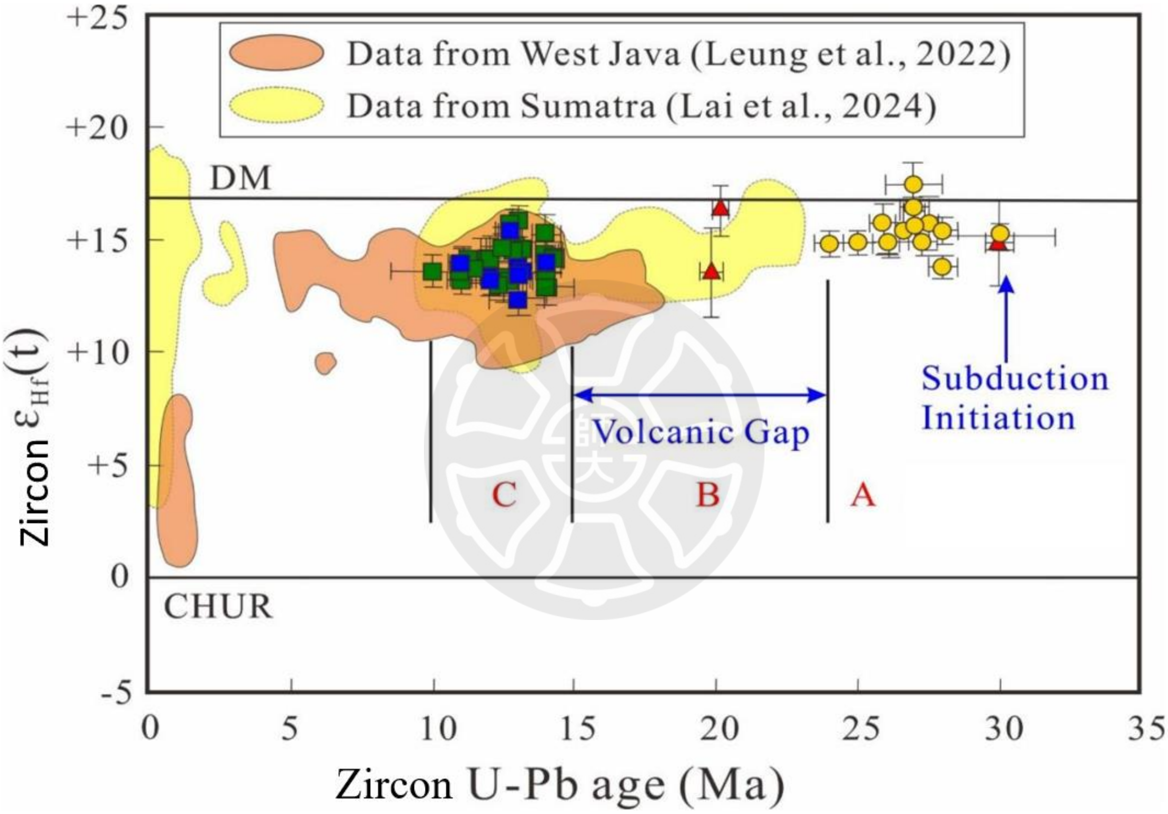

Fig. 5.9. Zircon ε_{Hf} versus zircon U–Pb age diagrams. Pacitan area (Yellow circles, red triangles, and blue). West Java (yellow color, Lai et al. (2022)), Sumatra (orange color, Lai et al. (2023)).

The evolution of tectonics and magmatism during the Tertiary period in the Pacitan area is divided into three stages of tectonic and magmatic evolution models:

- Stage 1 (30 Ma to 25 Ma):

In the Cenozoic, there was subduction of the India-Australian plate northward beneath Sundaland. At 30 Ma, magmatic activity occurred along the south coast of Java and produced Old Andesite **(Fig. 5.10)**. This interpretation contradicts previous research suggesting an earlier magmatism period (van Bemmellen, 1949). The magmatic process continued until 25 Ma. Based on ε_{Nd} values of +6.4 to +6.0 and ε_{Hf} values of +17.5 to +13.8, this indicates the initial composition of the Sunda Arc and underwent fractional crystallization before eruption

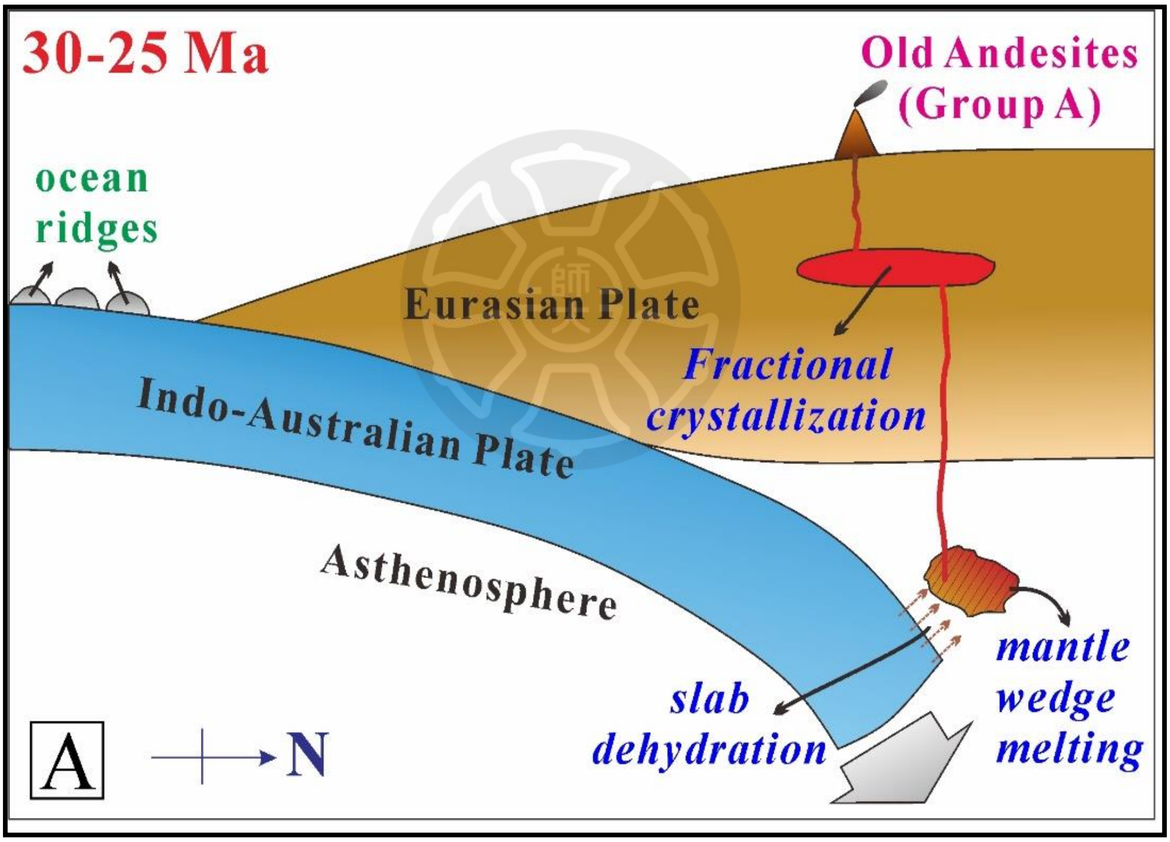

Fig. 5.10 Tectonic and magmatic evolution in Pacitan during 30- 25 Ma. (Lintjewas et al., 2025). Between 30 and 25 Ma, the subduction of the Indo-Australian plate led to the formation of the Old Andesite (Group A).

- Stage 2 (25 to 15 Ma):

The subduction of the ridge in southern East Java during the Miocene was influenced by the buoyancy effect derived from the subducting oceanic plate and the overlying ridge. This process caused a temporary cessation of subduction and magmatic activity, estimated to have started at 25 Ma. This cessation continued until 15 Ma as a result of the subducting ridge being trapped within the subduction zone. At 20 Ma, the eruptive process resumed briefly and deposited magma from Group B in the magma chamber **(Fig. 5.11).**

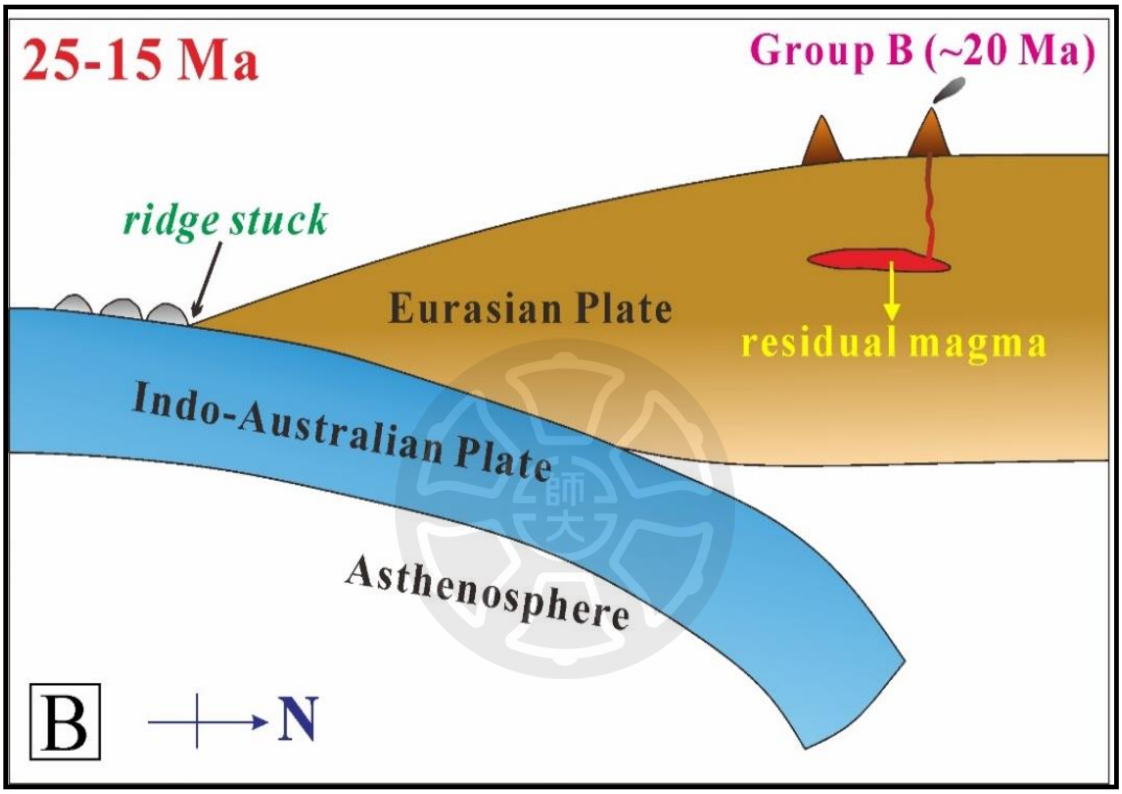

Fig. 5.11. Tectonic and magmatic evolution in Pacitan during 25-15 Ma (Lintjewas et al., 2025). From 25 to 15 Ma, ridge subduction caused the slab to become immobilized, resulting in a cessation of magmatic activity. Residual magma from Group A briefly erupted around 20 Ma (Group B).

- Stage 3 (15 to 10 Ma):

At this stage, plate tearing occurs due to the downward pull on the subducting slab. This causes heat from the asthenosphere to rise along the tear and enter the top of the subducting plate (Wu et al., 2022), further inducing partial melting of the subducting oceanic plate (Zhang et al., 2024; Shao et al., 2020), and forming adakitic magma. According to Lallemand et al. (1992) and Scholl et al. (2011), after the slab is torn, the angle of the subducting plate increases and then gradually rolls back. The overturning process occurs simultaneously and is induced by mantle circulation and heat, which causes partial melting of the mantle and produces ADR magma. After both magmas accumulate in the magma chamber, the two magmas undergo crustal contamination **(Fig. 5.12).**

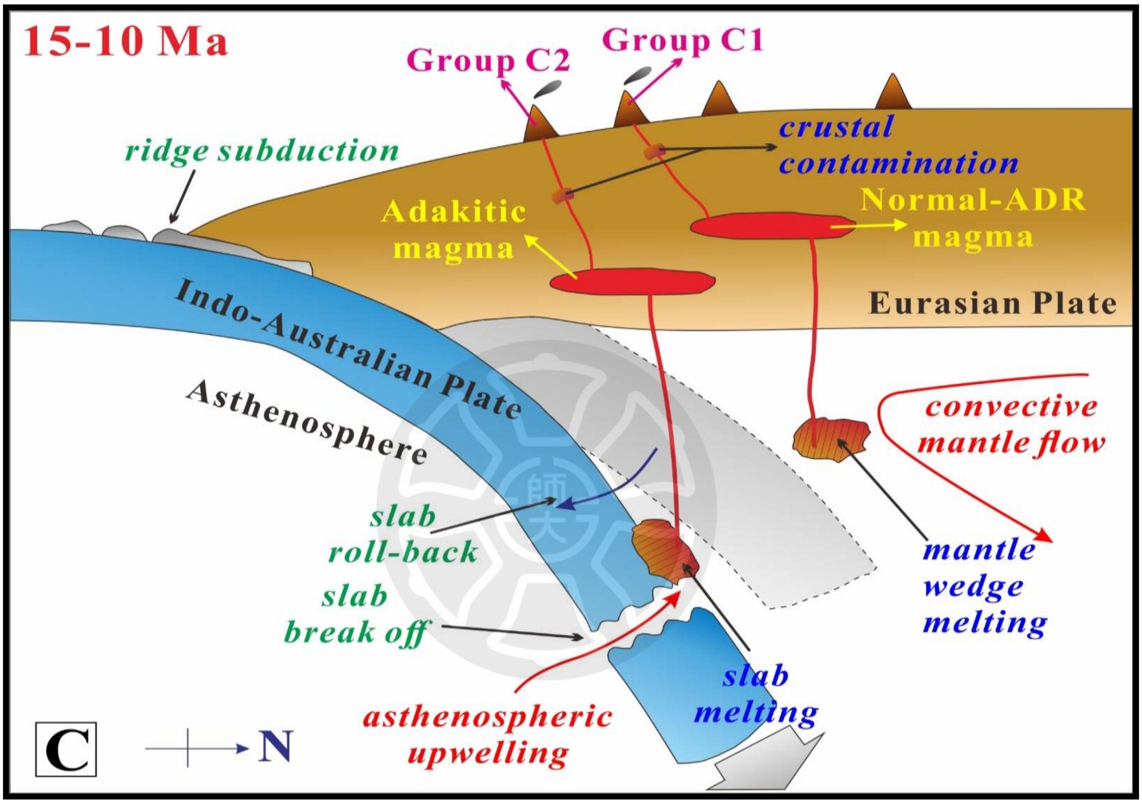

Fig. 5.12. Tectonic and magmatic evolution in Pacitan during 15-10 Ma (Lintjewas et al., 2025). The downward pull of the subducting slab caused tearing, while the upwelling asthenosphere facilitated partial melting of the subducted oceanic crust, resulting in the formation of adakitic magma (Group C2). Subsequently, subduction continued, characterized by slab rollback-induced mantle circulation and mantle wedge partial melting, which produced normal ADR magma (Group C1). Both magmas erupted simultaneously after undergoing slight crustal contamination between 15 and 10 Ma.

CHAPTER 6. CONCLUSIONS

The results of geochronological and geochemical studies conducted using new U-Pb zircon and whole-rock geochemical data shed light on the temporal-spatial distribution of Pacitan magmatism. The magmatism and tectonic evolution in Pacitan began in the Oligocene. The magmatic evolution in Pacitan has three periods: Late Oligocene from 26.7 to 26.0 Ma (Group A), Early Miocene around 19.9 Ma (Group B), and Middle Miocene from 13.4 to 11.8 Ma (Group C). The magmatic and tectonic evolution processes in Pacitan consist of 5 stages:

1. Group A is related to the Old Andesite in the southern Java mountains, characterized by volcanic activity that produces volcanic rocks with a composition ranging from andesite to dacite, with a silica range of 59-69 wt.%. Geochemical data shows that before magma eruptions occurred the magma underwent fractional crystallization. This data, combined with previous dating results, suggests that magmatic activity occurred between 25 and 30 Ma.
2. Between 25 and 20 Ma, the subduction process stopped because the ridge located in the southern part of Java reached a trough and became stuck, leading to a magmatic gap.
3. The process of asthenosphere upwelling in the mantle wedge occurs due to the tearing of subducted plates. This process causes partial melting of the lower crust to form magmatism with SiO_2 content > 67 wt.%, zircon $_{\varepsilon Hf}$ values of +13.6 to +16.3, and $_{\varepsilon Nd}$ values of +7.0 to +7.2, with low Pb, K, and P concentrations and high HREE content. This process occurred around 20 Ma.
4. The second magmatic gap occurred around 19 Ma, where the ridge subduction process caused the rollback of the subducted slab.
5. Around 15 Ma, a change in subduction angle occurred, where the subducted plate reached the depth of magma generation, resulting in the formation of arc-derived magmas (ADRs) related to the C1 group. C2 relates to adakitic magmas formed due to circulation induced by slab overthrow, leading to the partial subduction of oceanic crust. Between 15 and 11 Ma, crustal contamination occurred, showing zircon $_{\varepsilon Hf}$ values of +11.9 to +15.6 and whole-rock $_{\varepsilon Nd}$ values of +4.2 to +5.3.

References

Anderson, T., 2002. Correction of common lead in U-Pb analyses that do not report ^{204}pb: Chemical Geology 192, 59-79.

Alonso-Perez, R., Muntener, O. and Ulmer, P., 2009. Igneous garnet and amphibole fractionation in the roots of island arcs: experimental constraints on andesitic liquids. Contributions to Mineralogy and Petrology 157, 542-558.

Atherton, M.P., Petford, N., 1993. Generation of sodium-rich magmas from newly underplated basaltic crust. Nature 362, 144-146.

Bourdon, E., Eissen, J., Monzier, M., Robin, C., Martin, H., Cotten, J., Hall, M.L., 2002. Adakite-like Lavas from Antisana Volcano (Ecuador): evidence for slab melt metasomatism beneath Andean Northern Volcanic Zone. J. Petrol. 43 (2), 199-217.

Clements, B., Hall, R., Smyth, H.R., Cottam, M.H., 2009. Thrusting of a volcanic arc: a new structural model for Java. Petroleum Geosciences. 159-174.

Castillo, P. R., Janney, P. E. and Solidum, R. U. (1999). Petrology and geochemistry of Camiguin Island, southern Philippines: insights to the source of adakites and other lavas in a complex arc setting. Contributions to Mineralogy and Petrology. 134, 33-51.

Chiu, H.-Y., Chung, S.-L., Zarrinkoub, M.H., Mohammadi, S.S., Khatib, M.M., Iizuka, Y., 2013. Zircon U–Pb age constraints from Iran on the magmatic evolution related to Neotethyan subduction and Zagros orogeny. Lithos 162-163, 70-87.

Chung, S.-L., Liu, D.-Y., Ji, J.-Q., Chu, M.-F., Lee, H.-Y., Wen, D.-J., Lo, C.-H., Lee, T.-Y., Qian, Q., Zhang, Q., 2003. Adakites from continental collision zones: melting of thickened lower crust beneath southern Tibet. Geology 31, 1021-1024.

Claproth, R., 1989. Magmatic affinities of volcanic rocks from Unggaran, Central Java. Geol. Indonesia 12 (1), 511-562.

Davidson, J., Turner, S., Handley, H., Macpherson, C, and Dosseto, A., 2007. Amphibole 'sponge' in arc crust? Geology 35, 787-790.

Defant, M.J. and Kepezhinskas, P., 2001. Adakites: A review of slab melting over the past decade and the case for a slab-melt component in arcs. EOS Transactions American Geophysical Union 82, 68-69.

Dempsey, S.R., 2013. Geochemistry of volcanic rocks from the Sunda Arc, Durham theses, Durham University. 1-307.

Dominguez, S., Malavielle, J., Lallemand, S.E., 2000. Deformation of accretionary wedges in response to seamount subduction: insights from sandbox experiments. Tectonics 19, 182-196.

Edwards, C.M., Menzies, M.A., and Thirlwall, M.F., 1991. Evidence from Muria, Indonesia, for the Interplay of Supra-Subduction Zone Intraplate Processes in the Genesis of potassic Alkaline Magmas. Journal of Petrology 32(2), 556-590.

Edwards, C. M., Morris, J. D., 1993. Separating mantle from slab signatures in arc lavas using B/Be and radiogenic isotope systematics. Nature, 362, 530-533.

Edwards, C.M., Menzies, M.A., Thirlwall, M.F., Morris, J.D., Leeman, W.P., Harmon, R.S.,1994. The transition to potassic alkaline volcanism in island arcs: The ringgit–beser complex, East Java, Indonesia. Journal of Petrology 35, 1557-1595.

Elburg, M.A., Foden, J., van Bergen, M., and Zulkarnain., 2005. Australia and Indonesia in collision: geochemical source of magmatism. Journal of Volcanology and Geothermal Research 140, 25-47.

Gasparon, M., Hilton, D.R., and Varne, R., 1994. Crustal contamination processes traced by helium isotopes: Examples from the Sunda Arc, Indonesia. Earth and Planetary Science Letters 126, 15-22.

Gasparon, M., and Varne, R., 1998. Crustal assimilation versus subducted sediment input in west Sunda Volcanic arc: an evaluation. Mineralogy and Petrology 64, 89-117.

Genske, F.S., Turner, S.P., Beier, C., Schaefer, B.F., 2012. The petrology and geochemistry of lavas from the western Azores Islands of Flores and Corvo. Journal of Petrology 53, 1673-1708.

Gerbe, M.-C., Gourgaud, A., Sigmarsson, O., Harmon, R.S., Joron, J.-L., and Provost, A., 1992. Mineralogical and geochemical evolution of the 1982-1983 Galunggung eruption (Indonesia). Bulletin. Volcanology 54, 284-298.

Ghose, R., Yoshioka, S. and oike, K., 1990. Three-dimensional numerical simulation of the subduction dynamic in the Sunda Arc region, Southeast Asia. Tectonophysics 181, 223-255.

Gill, J.B., 1981. Orogenic Andesite and Plate Tectonics. Springer, Berlin (390 pp).

Green, T. H., 1980. Island arc and continent-building magmatism – A review of petrogenic models based on experimental petrology and geochemistry. Tectonophysics 63, 367-385.

Griffin, W., 2008. GLITTER: data reduction software for laser ablation ICP-MS: laser Ablation ICP-MS in the Earth Sciences: Current practices and outstanding issues, Mineralogical Association of Canada Short Course. 308-311.

Handley, H. K., Macpherson, C. G., Davidson, J. P., Berlo, K., and Lowry, D., 2007. Constraining Fuid and Sediment Contributions to Subduction-Related Magmatism in Indonesia: Ijen Volcanic Complex. Journal of Petrology (6), 1155-1183.

Hall, R., 1996. Reconstructing Cenozoic SE Asia, Tectonic Evolution of SE Asia: Geological Society London Special Publication 106, 153-184.

Hall, R., 2002. Cenozoic geological and plate tectonic evolution of SE Asia and the SW Pacific: Computer-based reconstructions, model and animations: Journal of Asian Earth Sciences 20, 353-434.

Hall, R., and Morley, C.K., 2004. Sundaland Basins, Continent–Ocean Interactions within the East Asian Marginal Seas: American Geophysical Union Geophysical Monograph 149, 55-85.

Hall, R., Clements, B., Smyth, H, R., Cottam, M, A. 2007. A new interpretation of Java's structure. Proceedings, Indonesia petroleum association.153-154.

Hall, R., Smyth, H.R., 2008. Cenozoic arc processes in Indonesia: Identified cation of the key influences on the stratigraphic record in active volcanic arcs. The Geological Society of America 436, 27-54.

Hall, R., 2009. The Eurasian SE Asian margin as a modern example of an accretionary orogen. In P. A. Cawood, and A. Kroner (Eds). London: Geological Society, Special Publications.351-372.

Hall, R. 2012. Late Jurassic–Cenozoic reconstructions of the Indonesia region and the Indian ocean. Tectonophysics. 353-431.

Hall, R., Sevastjanova, I. 2012. Australian crust in Indonesia. Australian Journal of Earth Sciences 59, 827-844.

Hall, R. and Breitfeld, H.T., 2017. The Demise of the Proto-South China Sea. Bulletin of the Geological Society of Malaysia

Hart, S.R., Reid, M.R., 1991. Rb/Cs fractionation: a link between granulite metamorphism and the S-process. Geochimica et Cosmochimica Acta 55, 2379-2383.

Hamilton, W.B., 1979. Tectonic of the Indonesia region. US Geological Survey Professional Paper 1078, 345.

Hilton, D. R., Hoogewerff, J. A., van Bergen, M. J., and Hammerschmidt, K., 1992. Mapping magma sources in the east Sunda-Banda arcs, Indonesia: Constraints from helium isotopes. Geochimica et Cosmochimica Acta, 56, 851-859.

Hofmann, A.W., Jochum, K.P., Seufert, M., and White, W.M., 1986. Nb and Pb in oceanic basalts: new constraints on mantle evolution. Earth and Planetary Science Letters 79, 33-45.

Humphreys, E.R., Niu, Y., 2009. On the composition of ocean island basalts (OIB): the effects of lithospheric thickness variation and mantle metasomatism. Lithos 112, 118-136.

Husein, S., Nuckman, M., 2015. Rekonstruksi tektonik mikrokontinen pegunungan selatan Jawa Timur: sebuah hipotesis berdasarkan analisis kemagnetan purba. Proceeding, seminar nasional kebumian 8.

Hutchison, C. S., 1982 Indonesia. In R. S. Thorpe (Ed.), Andesite: Orogenic Andesite and Related Rocks. 207-224. J. Wiley and Sons Ltd.

Hutchison, C.S., 1989. Geological Evolution of South-East Asia. Oxford Monographs on Geology and Geophysics no. 13, 368 pp.

Irvine, T.N., Baragar, W.R.A., 1971. A guide to the chemical classification of the common volcanic rocks. Canadian Journal of Earth Sciences 8, 448-523.

Jackson, S.E., Pearson, N.J., Griffin, W.L., Belousova, E.A., 2004. The application of laser ablation-inductively coupled plasma-mass spectrometry to *insitu* U-Pb zircon geochronology. Chemical Geology 211,47-69.

JICA-JOGMEC., 2004. Report on the Mineral Exploration in the East Java Area, the Republic of Indonesia – Consolidated Report. Japan International Cooperation Agency and the Japan Oil, Gas and Metals National Corporation Report, Tokyo.

Karsli, O., Dokuz, A., Uysal, I., Aydin, F., Kandemir, R., Wijbran. 2010. Generation of the Early Cenozoic adakitic volcanism by partial melting of mafic lower crust, Eastern Turkey: Implications for crustal thickening to delamination. Lithos 114, 109-120.

Katili, J.A., 1975. Volcanism and plate tectonics in the Indonesia island arcs. Tectonophysics, 26, 165-188.

Kersting, A.B., Arculus, R.J., 1995. Pb isotope composition of Klyuchevskoy volcano, Kamchatka and North Pacific sediments: implications for magma genesis and crustal recycling in the Kamchatkan arc. Earth and Planetary Science Letters 136, 133-148.

Lai, Y.-M., Leung, W.-K., Chung, S.-L., Setiawan, I., Lee, H.-Y., Lintjewas, L., Kautsar, A. A., Iizuka, Y., 2022. Early-Miocene to Pleistocene Magmatism in the Western Part of West Java, Indonesia. Goldschmidt Conference Abstract, Honolulu, Hawaii. Abstract No. 9631.

Lai, Y.-M., Liu, P.-P., Chung, S.-L., Ghani, A.A., Lee, H.-Y., Quek, L.-X., Li, S., Roselee, M. H., Murtadha, S., Lintjewas, L., 2023. Zircon U-Pb geochronology and Hf isotopic compositions of igneous rocks from Sumatra: implications for the Cenozoic magmatic evolution of the western Sunda Arc. Geol. Soc. Lond. Spec. Publ. 537, 455-478.

Lallemand, S.E., Malavieille, J., Calassou, S., 1992. Effects of oceanic ridge subduction on accretionary wedges: experimental modeling and marine observations. Tectonics 11, 1301-1321.

Le Bas, M.J., Le Maitre, R.W., Streckeisen, A., and Zanettin, B., 1986. A chemical classification of volcanic rocks based on the total alkali–silica diagram. Journal of Petrology 27, 745-750.

LeMaître, R.W., 2002. Igneous Rocks: A Classification and Glossary of Terms: Recommendations of International Union of Geological Sciences Subcommission on the Systematics of Igneous Rocks. Cambridge University Press, Cambridge (236 pp).

Lintjewas, L., Lai, Y.-M., Setiawan, I., Chung, S.-L., Alkautsar., Lee, H.-Y., Quek, L.-X., Iizuka, Y., 2025. New age and geochemical constraints on the “Old Andesite” and middle miocene adakites from Pacitan, East Java, Indianesia. Lithos 494-495, 107943.

Linnemann, U., Ouzegane, K., Drareni, A., Hofman, M., Becker, S., Gartner, S., Sagawe, A. 2011. Sands of West Gondwana: An archive of secular magmatism and plate interactions -A case study from the Cambro-Ordovician section of the Tassili Ouan Ahaggar (Algerian Sahara) using U–Pb–LA-ICP-MS detrital zircon ages. Lithos, 123, 188-203.

Ludwig, K., 2008. Isoplot version 4.15: a geochronological toolkit for Microsoft Excel: Berkeley Geochronology Center, special Publication, no. 4, 247-270.

Lung, C.K., and Kirckpatrick, R.J., 1982. Pre eruption history of pyric basalt from DSDP legs 46 and 46: evidence from morphology and zoning pattern in plagioclase. Contribution to mineralogy and petrology 79, 13-27.

Marcoux, E. and Milesi, J.P., 1994. Epithermal gold deposits in West Java, Indonesia: geology, age and crustal source. Journal of Geochemical Exploration 50, 393-408.

McCaffrey, R., 1996. Slip partitioning at convergent plate boundaries of SE Asia. In: Hall, R., Blundell, D. (Eds.), Tectonic Evolution of SE Asia 106, 3-18.

McBirney, A.R., 1979. Effect of assimilation in: Yoder H.S. ed. the evolution of igneous rocks, 307-388. Princeton University Press, Princeton, New Jersey.

McDonough, W.F., Sun, S.S., Ringwood, A.E., Jagoutz, E., Hofmann, A.W., 1992. Potassium, rubidium, and cesium in the Earth and Moon and the evolution of the mantle of the Earth. Geochimica et Cosmochimica Acta 56, 1001-1012.

Metcalfe, I., 2013. Gondwana dispersion and Asian accretion: tectonic and palaeo-geographic evolution of eastern Tethys. Journal of Asian Earth Sciences 66, 1-33.

Miller, D.M., Goldstein, S.L., Langmuir, C.H., 1994. Cerium/lead and lead isotope ratios in arc magmas and the enrichment of lead in the continents. Nature 368, 514-520.

Moore, G. and Carmichael, I.S E., 1998. The hydrous phase equilibria (to 3 k-bar) of an andesite and basaltic andesite from western Mexico: constraints on water content and conditions of phenocrysts growth. Contributions to Mineralogy and Petrology 130, 304-319.

Newhall, C.G., 1979. Temporal variation in the lavas of Mayon volcano, Philippines. Journal of volcanology and geothermal research 6, 61-83.

Nicholls, I.A., Whitford, D.J., Harris, K.L. and Taylor, S.R., 1980. Variation in the geochemistry of mantle sources for tholeiitic and calc-alkaline mafic magmas, Western Sunda volcanic arc, Indonesia. Chemical Geology, 30, 177-199.

Nicholls, I.A., and Whitford, D.J., 1976. Primary magmas associated with Quaternary volcanism in the western Sunda Arc, Indonesia. (R. W. Johnson, Ed.) Volcanism in Australasia, 77-89.

Novianty, S., Abdurrahman, M., 2018. Tertiary Magmatic Activity in Southern East Java: An approaching to Volcano stratigraphy and Petrogenesis Studies. GEOSEA.

Pearce, J.A., Cann, J.R., 1973. Tectonic setting of basic volcanic rocks determined using trace element analyses. Earth and Planetary Science Letters 19, 290-300.

Pearce, J.A., Norry, M.J., 1979. Petrogenetic implications of Ti, Zr, Y, and Nb variations in volcanic rocks. Contributions to Mineralogy and Petrology 69, 33-47.

Pearce, J.A., Peate, D.W., 1995. Tectonic implications of the composition of volcanic arc magmas. Annual Review of Earth and Planetary Sciences 23, 251-285.

Pearce, J.A., Stern, R.J., Bloomer, S.H., Fryer, P., 2005. Geochemical mapping of the Mariana arc-basin system: implications for the nature and distribution of subduction components. Geochemistry, Geophysics, Geosystems 6 (2004GC000895).

Peccerillo, A., Taylor, S.R., 1976. Geochemistry of Eocene calc-alkaline volcanic rocks from Kastamonu area, Northern Turkey. Contributions to Mineralogy and Petrology 58, 63-81.

Prasetyadi, C., Suparka, E.R., Harsolumakso, A. H., and Sapiie, B., 2005. Eastern Java basement rock study: preliminary results of recent field study in Karangsambung and Bayat areas. Procceding. 34th Convention. Indonesia Association Geology, 310-321.

Pertamina-ITB., 2002. Regional Tectonic Study of Java and Hydrocarbon Potential of Central Java and West Java Basins. Unpublished report.

Purwanto, H.S., Abdullah, C.I., Noeradi, D. (1997). Rekonstruksi tegasan purba berdasarkan data struktur mesoskopik, di daerah Pacitan dan sekitarnya, Jawa Timur, Prosiding PIT XXVI, Jakarta. 443-452.

Purnomo, H., Syahrulyati, T., and Solihin., 2017. Geologi dan petrogenesa batuan beku diorit daerah Tulakan dan sekitarnya kecamatan Tulakan kabupaten Pacitan provinsi Jawa Timur.

Puspito, N.T and Shimazaki, K., 1995. Mantle structure and seismotectonic of the Sunda and Banda Arc. Tectonophysics, 251. 215-228.

Rittmann, A., 1953. Magmatic character and tectonic position of the Indonesia volcanoes. Bulletin. Volcanology 14, 45-58.

Rubbato. 2002. Zircon trace element geochemistry: Partitioning with garnet and the link between U-Pb ages and metamorphism. Chemical Geology 184, 123-138.

Saefudin, I.., 1994. Pentarikhan jejak belah terhadap batuan terobosan dacite dan andesite daerah Pacitan, Jawa Timur. Jurnal Geologi dan Sumberdaya Mineral, 18–36 (in Indonesia).

Samodra, H., Gafoer, S., and Tjokrosaputro, S., 1992. Geological map of the Pacitan quadrangle, Java. Geological Research and Development Centre.

Sartika, D. N., I Wayan, W., Bakti, Harahap, B. H., and Widiasmoro., 2009. Late Oligocene tholeiitic lava from kenanga river, Tegalombo Pacitan, East Java. J. SE Asian Application. Geology 1, 1-8.

Setiadji, L.D., Kajino, S., Imai, A., and Watanabe, K., 2006. Cenozoic Island Arc Magmatism in Java (Sunda Arc, Indonesia): Clues on Relationships between Geodynamics of Volcanic Centers and Ore Mineralization. Resource Geology 56, 267-292.

Shinjo, R., Ginoza, Y., and Meshesha, D., 2010. Improved method for Hf separation from silicate rocks for isotopic analysis using Ln-spec resin column: Journal of Mineralogical and Petrological Sciences 105, 297-302.

Sláma, J., Košler, J., Condon, D. J., Crowley, J. L., Gerdes, A., Hanchar, J. M., Horstwood, M. S. A., Morris, G.A., Nasdala, L., Norbeg, N., Schaltegger, U., Schoene, B., Tubrett, M.N., Whitehouse, M.J., 2008. Plesovice zircon — a new natural reference material for U–Pb and Hf isotopic microanalysis. Chemical Geology 249, 1-35.

Smith, A.D., Huang, L.-Y., 1997. The use extraction chromatography material in procedures for the isotopic analysis e.g. neodymium and strontium in rocks by thermal ionizations mass spectrometry. J. Natl. Cheng Kung University.32, 1-10.

Smyth, H., 2005. Eocene to Miocene basin history and volcanic activity in East Java, Indonesia. Geological Society America, 476.

Smyth, H. R., Hall, R. & Nichols, G. J. 2008. Cenozoic volcanic arc history of East Java, Indonesia: the stratigraphic record of eruptions on a continental margin. Geological Society America Special Publication, 436,199-222.

Soeria-Atmadja, R., Maury, R.C., Bellon, H., Pringgoprawiro, H., Polve, M, and Priadi, B., 1994. The Tertiary Magmatic Belts in Java, Proc. Symp. On Dynamics of Subduction and its products, the silver Jubilec Indonesia. Institution Of Sci (LIPI), 98-121.

Soeria-Atmadja, R., and Noeradi., 2005. Distribution of Early Tertiary volcanic in south Sumatra and West Java., The island arc 14, 679-680.

Sun, S.-s., McDonough, W.F., 1989. Chemical and isotopic systematics of oceanic basalts: implications for mantle composition and processes. In: Saunders, A.D., Norry, M.J. (Eds.), Magmatism in the Ocean Basin. Geological Society, London, Special Publications 42, 313-345.

Sutanto., 2003. Batuan volkanik Tersier didaerah Pacitan dan sekitarnya. Majalah Geologi Indonesia 18, 159-167.

Syracuse, E.M., and Abers, G.A., 2006. Global compilation of variations in slab depth beneath arc volcanoes and implications. Geochem. Geophys. Geosyst 7.

Tatsumi, Y., and Eggins, S., 1995. Subduction Zone Magmatism. Blackwell Science Publication 211.

Ulmer, P. (1988). High-pressure phase equilibria of a calc-alkaline picro-basalt: implications for the genesis of calc-alkaline magmas. Carnegie Institution of Washington Geophysical Laboratory Annual Report 28-35.

van Bemmellen, R.W. 1949. The Geology of Indonesia. General Geology of Indonesia and Adjacent Archipelagoes, vol. 1A. Government Printing Office, The Hague.

Vroon, P. Z., van Bergen, M. J., White, W. M., and Varekamp, J. C., 1993. Sr-Nd-Pb Isotope Systematics of the Banda Arc, Indonesia: Combined Subduction and Assimilation of Continental Material. Journal of Geophysical Research 98(B12), 349-366.

Vroon, P. Z., Lowry, D., van Bergen, M. J., Boyce, A. J., and Mattey, D. P., 2001. Oxigen isotope systematic of the Banda Arc: Low delta ^{18}O despite involvement of subducted continental material in magma genesis. Geochimica et Cosmochimica Acta, 65(4), 589-609.

Wilkinson, C.M., Ganerød, M., Hendriks, B.W.H. and Eide, E.A. 2017. Compilation and appraisal of geochronological data from the North Atlantic Igneous Province (NAIP). Péron-Pinvidic, G., et al., The NE Atlantic Region: A Reappraisal of Crustal Structure, Tectonostratigraphic and Magmatic Evolution—An Introduction to the NAG-TEC Project. Geological Society of London Special Publications, 44**7**, 69-103.

Wheller, G. E., Varne, R., Foden, J. D., and Abbot, M. J., 1987. Geochemistry of Quaternary volcanism in the Sunda-Banda arc, Indonesia, and three-component genesis of island arc basaltic magmas. Journal of Volcanology and Geothermal Research 32, 137-160.

Whitford, D. J., Nicholls, I. A., and Taylor, S. R., 1979. Spatial variation in the geochemistry of Quaternary lava across the Sunda Arc in Java and Bali. Contrib. Mineral. Petrology 70, 341-356.

Whitford, D. J., 1975. Strontium isotopic studies of volcanic rocks of the Sunda Arc, Indonesia, and their petrogenetic implications. Geochimica et Cosmochimica Acta, 39.

Whitford, D. J., and Nicholls, I. A., 1976. Potassium variation in lavas across the Sunda Arc in Java and Bali. (R. W. Johnson, Ed.) Volcanism in Australasia, 63-75.

Widiyantoro, S and van der Hilst, R., 1996. Structure and evolution of lithosphere slab beneath the Sunda Arc, Indonesia Sciences 271, 1566-1570.

Widiyantoro, S and van der Hilst, R., 1997. Mantle structure beneath Indonesia inferred from high-resolution tomographic imaging. Geophysical Journal International 130,167-182.

Wiendenbeck, M., Allé, P., Corfu, F., Griffin, W.L., Meier, M., Oberli, F., Von Quadt, A., Roddick, J.C., Spiegel, W., 1995. Three natural zircon standards for U–Th–Pb, Lu–Hf, trace element and REE analyses. Geostandard. Newsletter 19, 1-23.

Wikarno, R., Hardjono, T. and Graha, D.S., 1993. Distribution of Radiometric Ages in Indonesia, Scale 1: 5.000.000. Geological Research and Development Centre, Bandung.

APPENDIX

A1. Table zircon U-Pb ages

Spot	U(ppm)	Th(ppm)	Th/U	U-Th-Pb ratios									Ages (Ma)								Inferred Age (Ma)	1σ
				$^{207}Pb/^{206}Pb$	1σ	$^{207}Pb/^{235}U$	1σ	$^{206}Pb/^{238}U$	1σ	$^{208}Pb/^{232}Th$	1σ	rr	$^{207}Pb/^{206}Pb$	1σ	$^{207}Pb/^{235}U$	1σ	$^{206}Pb/^{238}U$	1σ	$^{208}Pb/^{232}Th$	1σ		
JA18-02-01	174	82	0.47	0.05929	0.03116	0.01341	0.00799	0.00164	0.00013	0.00076	0.00014	0.9	578	957	14	8	10.6	0.8	15	3	10.6	0.8
JA18-02-02	111	56	0.50	0.06774	0.04325	0.01701	0.01235	0.00182	0.00018	0.00081	0.00020	0.9	861	1024	17	12	12	1	16	4	12	1
JA18-02-03	164	52	0.32	0.06046	0.03836	0.01455	0.01041	0.00175	0.00016	0.00094	0.00027	0.9	620	989	15	10	11	1	19	5	11	1
JA18-02-04	86	30	0.35	0.05511	0.06077	0.01477	0.01798	0.00194	0.00025	0.00572	0.00054	0.9	417	1441	15	18	12	2	115	11	12	2
JA18-02-05	103	39	0.38	0.06279	0.05841	0.01672	0.01755	0.00193	0.00026	0.00115	0.00039	0.9	701	1424	17	18	12	2	23	8	12	2
JA18-02-06	111	49	0.44	0.04073	0.04411	0.01046	0.01218	0.00186	0.00017	0.00095	0.00023	0.9	-248	1256	11	12	12	1	19	5	12	1
JA18-02-07	213	85	0.40	0.05458	0.03391	0.01287	0.00893	0.00171	0.00014	0.00072	0.00018	0.9	395	938	13	9	11	0.9	15	4	11	0.9
JA18-02-08	242	117	0.49	0.05018	0.01993	0.01283	0.00571	0.00185	0.00010	0.00061	0.00011	0.9	203	634	13	6	11.9	0.6	12	2	11.9	0.6
JA18-02-09	271	205	0.76	0.06524	0.01626	0.01659	0.00485	0.00184	0.00009	0.00070	0.00007	0.9	782	474	17	5	11.9	0.6	14	1	11.9	0.6
JA18-02-10	113	48	0.42	0.05051	0.03448	0.01539	0.01156	0.00221	0.00017	0.00032	0.00023	0.9	219	906	16	12	14	1	6	5	14	1
JA18-02-11	81	27	0.33	0.07014	0.06439	0.01788	0.01847	0.00185	0.00024	0.00155	0.00046	0.9	932	1507	18	18	12	2	31	9	12	2
JA18-02-12	150	53	0.35	0.07206	0.04288	0.01853	0.01269	0.00187	0.00019	0.00104	0.00032	0.9	988	1037	19	13	12	1	21	6	12	1
JA18-02-13	90	31	0.35	0.07805	0.05993	0.02175	0.01927	0.00202	0.00027	0.00059	0.00047	0.9	1148	1274	22	19	13	2	12	9	13	2
JA18-02-14	656	962	1.47	0.05374	0.01294	0.02315	0.00681	0.00312	0.00019	0.00091	0.00009	0.9	360	440	23	7	20	1	18	2	20	1
JA18-02-15	90	34	0.38	0.03403	0.06821	0.01012	0.02154	0.00216	0.00030	0.00044	0.00048	0.9	-113	1458	10	22	14	2	9	10	14	2
JA18-02-16	49	17	0.35	0.04999	0.11227	0.01432	0.03486	0.00208	0.00044	0.00194	0.00086	0.9	195	2519	14	35	13	3	39	17	13	3
JA18-02-17	52	16	0.32	0.05395	0.11065	0.01369	0.03066	0.00184	0.00039	0.00092	0.00080	0.9	369	2447	14	31	12	3	19	16	12	3
JA18-02-18	62	19	0.30	0.06930	0.07725	0.01931	0.02407	0.00202	0.00030	0.00112	0.00064	0.9	908	1652	19	24	13	2	23	13	13	2
JA18-02-19	125	36	0.29	0.08720	0.04519	0.02285	0.01396	0.00190	0.00020	0.00056	0.00041	0.9	1365	1064	23	14	12	1	11	8	12	1
JA18-02-20	132	54	0.41	0.06573	0.05923	0.01351	0.01378	0.00149	0.00020	0.00063	0.00028	0.9	798	1407	14	14	10	1	13	6	10	1

Continue A1-2

Spot	U(ppm)	Th(ppm)	Th/U	U-Th-Pb ratios									Ages (Ma)								Inferred Age (Ma)	1σ
				$^{207}Pb/^{206}Pb$	1σ	$^{207}Pb/^{235}U$	1σ	$^{206}Pb/^{238}U$	1σ	ρr	$^{208}Pb/^{232}Th$	1σ	$^{207}Pb/^{206}Pb$	1σ	$^{207}Pb/^{235}U$	1σ	$^{206}Pb/^{238}U$	1σ	$^{208}Pb/^{232}Th$	1σ		
JA18-03-01	182	109	0.60	0.05857	0.01156	0.01608	0.00388	0.00199	0.00010	0.9	0.00072	0.00007	551	406	16	4	12.8	0.6	15	1	12.8	0.6
JA18-03-02	114	45	0.40	0.05600	0.01827	0.01693	0.00641	0.00219	0.00013	0.9	0.00045	0.00012	452	630	17	6	14.1	0.8	9	2	14.1	0.8
JA18-03-03	99	43	0.44	0.05054	0.01926	0.01386	0.00596	0.00199	0.00011	0.9	0.00084	0.00011	220	653	14	6	12.8	0.7	17	2	12.8	0.7
JA18-03-04	142	66	0.47	0.05959	0.01421	0.01688	0.00475	0.00205	0.00010	0.9	0.00063	0.00009	589	477	17	5	13.2	0.6	13	2	13.2	0.6
JA18-03-06	74	27	0.37	0.09529	0.03038	0.02720	0.01096	0.00207	0.00020	0.9	0.00042	0.00022	1534	722	27	11	13	1	8	4	13	1
JA18-03-7B	118	78	0.66	0.04605	0.02004	0.01342	0.00663	0.00211	0.00014	0.9	0.00058	0.00009		705	14	7	13.6	0.9	12	2	13.6	0.9
JA18-03-08	38	14	0.35	0.08712	0.06069	0.02326	0.01916	0.00194	0.00028	0.9	0.00144	0.00042	1363	1247	23	19	12	2	29	8	12	2
JA18-03-09	92	53	0.57	0.04478	0.02794	0.01411	0.00995	0.00229	0.00021	0.9	0.00064	0.00016	-31	900	14	10	15	1	13	3	15	1
JA18-03-10	84	52	0.61	0.05079	0.02612	0.01435	0.00831	0.00205	0.00015	0.9	0.00091	0.00012	231	847	14	8	13.2	1	18	2	13.2	1
JA18-03-11	80	39	0.48	0.04617	0.02266	0.01463	0.00797	0.00230	0.00014	0.9	0.00400	0.00023	7	764	15	8	14.8	0.9	81	5	14.8	0.9
JA18-03-12	158	76	0.48	0.05930	0.01238	0.01653	0.00410	0.00202	0.00009	0.9	0.00094	0.00008	578	426	17	4	13	0.6	19	2	13	0.6
JA18-03-13	61	22	0.36	0.07185	0.04395	0.01948	0.01392	0.00197	0.00023	0.9	0.00077	0.00030	982	1146	20	14	13	1	16	6	13	1
JA18-03-14	161	73	0.45	0.05814	0.01374	0.01762	0.00494	0.00220	0.00011	0.9	0.00070	0.00009	535	472	18	5	14.2	0.7	14	2	14.2	0.7
JA18-03-15	153	114	0.74	0.06267	0.02056	0.01754	0.00682	0.00203	0.00014	0.9	0.00060	0.00008	697	672	18	7	13.1	0.9	12	2	13.1	0.9
JA18-03-16	154	92	0.60	0.07915	0.01215	0.02256	0.00441	0.00207	0.00010	0.9	0.00064	0.00007	1176	329	23	4	13.3	0.6	13	1	13.3	0.6
JA18-03-17	46	16	0.35	0.07859	0.04134	0.02388	0.01476	0.00220	0.00023	0.9	0.00085	0.00034	1162	1014	24	15	14	1	17	7	14	1
JA18-03-18	185	94	0.51	0.06016	0.01342	0.01798	0.00481	0.00217	0.00011	0.9	0.00074	0.00008	609	448	18	5	14	0.7	15	2	14	0.7
JA18-03-19	75	33	0.45	0.08266	0.03248	0.02234	0.01048	0.00196	0.00017	0.9	0.00072	0.00020	1261	830	22	10	13	1	15	4	13	1
JA18-03-20	122	56	0.46	0.06916	0.02159	0.01956	0.00728	0.00205	0.00014	0.9	0.00055	0.00012	904	653	20	7	13.2	0.9	11	2	13.2	0.9
JA18-03-21	98	43	0.44	0.06728	0.02128	0.01916	0.00712	0.00207	0.00013	0.9	0.00075	0.00014	846	662	19	7	13.3	0.8	15	3	13.3	0.8

Continue A1-3

Spot	U(ppm)	Th(ppm)	Th/U	U-Th-Pb ratios									Ages (Ma)								Inferred Age (Ma)	1σ
				$^{207}Pb/^{206}Pb$	1σ	$^{207}Pb/^{235}U$	1σ	$^{206}Pb/^{238}U$	1σ	$^{208}Pb/^{232}Th$	1σ	ρr	$^{207}Pb/^{206}Pb$	1σ	$^{207}Pb/^{235}U$	1σ	$^{206}Pb/^{238}U$	1σ	$^{208}Pb/^{232}Th$	1σ		
JA18-04-01	35	13	0.38	0.02938	0.06628	0.00891	0.02115	0.00220	0.00029	0.00139	0.00042	0.9	-311	1631	9	21	14	2	28	8	14	2
JA18-04-02	84	39	0.47	0.08328	0.02922	0.02225	0.00922	0.00194	0.00014	0.00078	0.00016	0.9	1276	719	22	9	12.5	0.9	16	3	12.5	0.9
JA18-04-03	67	25	0.38	0.07939	0.04034	0.02178	0.01309	0.00199	0.00021	0.00058	0.00027	0.9	1182	1056	22	13	13	1	12	5	13	1
JA18-04-04	120	64	0.54	0.09337	0.02724	0.02569	0.00940	0.00200	0.00017	0.00093	0.00015	0.9	1495	644	26	9	13	1	19	3	13	1
JA18-04-05	271	177	0.65	0.04993	0.01253	0.01288	0.00378	0.00187	0.00009	0.00060	0.00005	0.9	192	459	13	4	12	0.6	12	1	12	0.6
JA18-04-06	62	22	0.36	0.05576	0.04232	0.01616	0.01370	0.00210	0.00021	0.00080	0.00029	0.9	443	1086	16	14	14	1	16	6	14	1
JA18-04-07	76	33	0.43	0.06867	0.03114	0.01939	0.01013	0.00205	0.00016	0.00025	0.00019	0.9	889	868	19	10	13	1	5	4	13	1
JA18-04-08	85	45	0.53	0.05245	0.03362	0.01408	0.01005	0.00195	0.00016	0.00085	0.00015	0.9	305	1017	14	10	13	1	17	3	13	1
JA18-04-09	28	10	0.36	0.06011	0.11393	0.01687	0.03550	0.00204	0.00048	0.00164	0.00076	0.9	608	2288	17	35	13	3	33	15	13	3
JA18-04-10	56	22	0.40	0.10366	0.04368	0.02726	0.01411	0.00191	0.00021	0.00116	0.00029	0.9	1691	880	27	14	12	1	23	6	12	1
JA18-04-11	263	204	0.77	0.06414	0.01206	0.01692	0.00388	0.00191	0.00009	0.00076	0.00006	0.9	746	407	17	4	12.3	0.6	15	1	12.3	0.6
JA18-04-12	47	17	0.36	0.07923	0.06195	0.02142	0.01945	0.00196	0.00028	0.00148	0.00043	0.9	1178	1352	22	19	13	2	30	9	13	2
JA18-04-13	97	39	0.40	0.07756	0.02483	0.02181	0.00830	0.00204	0.00014	0.00087	0.00017	0.9	1136	687	22	8	13.1	0.9	18	3	13.1	0.9
JA18-04-14	189	114	0.61	0.05132	0.01629	0.01250	0.00453	0.00177	0.00010	0.00056	0.00009	0.83	255	538	13	5	11.4	0.6	11	2	11.4	0.6
JA18-04-15	106	53	0.50	0.03423	0.02647	0.00908	0.00757	0.00192	0.00013	0.00066	0.00013	0.9	-105	878	9	8	12.4	0.8	13	3	12.4	0.8
JA18-04-16	173	82	0.47	0.05013	0.01722	0.01362	0.00535	0.00197	0.00011	0.00073	0.00010	0.9	201	622	14	5	12.7	0.7	15	2	12.7	0.7
JA18-04-17	145	81	0.56	0.05838	0.01706	0.01779	0.00605	0.00221	0.00012	0.00090	0.00010	0.9	544	580	18	6	14.2	0.8	18	2	14.2	0.8
JA18-04-18	196	98	0.50	0.02064	0.02062	0.00529	0.00559	0.00186	0.00012	0.00057	0.00010	0.9	-728	808	5	6	12	0.8	12	2	12	0.8
JA18-04-19	171	75	0.44	0.08176	0.01851	0.02186	0.00613	0.00194	0.00012	0.00068	0.00012	0.9	1240	484	22	6	12.5	0.8	14	2	12.5	0.8
JA18-04-20	92	42	0.45	0.05166	0.04701	0.01259	0.01272	0.00177	0.00020	0.00062	0.00022	0.9	270	1256	13	13	11	1	13	4	11	1

Continue A1-4

Spot	U(ppm)	Th(ppm)	Th/U	U-Th-Pb ratios									Ages (Ma)								Inferred Age (Ma)	1σ
				$^{207}Pb/^{206}Pb$	1σ	$^{207}Pb/^{235}U$	1σ	$^{206}Pb/^{238}U$	1σ	$^{208}Pb/^{232}Th$	1σ	*rr*	$^{207}Pb/^{206}Pb$	1σ	$^{207}Pb/^{235}U$	1σ	$^{206}Pb/^{238}U$	1σ	$^{208}Pb/^{232}Th$	1σ		
JA18-05-01	178	68	0.38	0.05758	0.03284	0.01441	0.00927	0.00182	0.00015	0.00081	0.00023	0.9	514	890	15	9	11.7	1	16	5	11.7	1
JA18-05-02	36	9	0.25	0.04489	0.02162	0.01356	0.00730	0.00219	0.00014	0.00043	0.00025	0.9	-25	699	14	7	14.1	0.9	9	5	14.1	0.9
JA18-05-03	63	48	0.76	0.06172	0.01597	0.01581	0.00484	0.00186	0.00010	0.00054	0.00007	0.9	664	505	16	5	12	0.6	11	1	12	0.6
JA18-05-04	154	76	0.49	0.06235	0.02945	0.01701	0.00925	0.00198	0.00016	0.00066	0.00018	0.9	686	867	17	9	13	1	13	4	13	1
JA18-05-05	151	169	1.13	0.04329	0.00630	0.01184	0.00204	0.00198	0.00006	0.00066	0.00003	0.9	-108	235	12	2	12.8	0.4	13.3	0.6	12.8	0.4
JA18-05-06	174	238	1.36	0.06314	0.01028	0.02369	0.00477	0.00272	0.00012	0.00082	0.00005	0.9	713	334	24	5	17.5	0.8	17	1	17.5	0.8
JA18-05-07	53	20	0.38	0.05935	0.06856	0.01409	0.01831	0.00172	0.00028	0.00011	0.00045	0.9	580	1547	14	18	11	2	2	9	11	2
JA18-05-08	123	54	0.44	0.05127	0.03181	0.01265	0.00879	0.00179	0.00015	0.00100	0.00019	0.9	253	911	13	9	11.5	1	20	4	11.5	1
JA18-05-09	121	39	0.32	0.05024	0.01644	0.01390	0.00516	0.00201	0.00010	0.00067	0.00015	0.9	206	540	14	5	12.9	0.6	14	3	12.9	0.6
JA18-05-10	154	63	0.41	0.06148	0.02218	0.01860	0.00776	0.00219	0.00014	0.00078	0.00018	0.9	656	681	19	8	14.1	0.9	16	4	14.1	0.9
JA18-05-11	84	27	0.32	0.06672	0.04132	0.01667	0.01179	0.00181	0.00018	0.00068	0.00034	0.9	829	1024	17	12	12	1	14	7	12	1
JA18-05-12	49	27	0.56	0.04051	0.01785	0.01215	0.00590	0.00218	0.00011	0.00061	0.00010	0.9	-260	598	12	6	14	0.7	12	2	14	0.7
JA18-05-13	178	80	0.45	0.10038	0.01957	0.02654	0.00650	0.00192	0.00011	0.00336	0.00021	0.9	1631	375	27	6	12.4	0.7	68	4	12.4	0.7
JA18-05-14	36	15	0.41	0.09477	0.10798	0.02976	0.04000	0.00228	0.00053	0.00176	0.00090	0.9	1524	2271	30	39	15	3	36	18	15	3
JA18-05-15	63	34	0.54	0.05727	0.05130	0.01816	0.01795	0.00230	0.00024	0.00060	0.00031	0.9	502	1268	18	18	15	2	12	6	15	2
JA18-05-16	154	72	0.47	0.10601	0.02078	0.03006	0.00742	0.00206	0.00012	0.00060	0.00015	0.9	1732	372	30	7	13.3	0.8	12	3	13.3	0.8
JA18-05-17	151	65	0.43	0.11151	0.02562	0.02785	0.00801	0.00181	0.00012	0.00066	0.00017	0.9	1824	482	28	8	11.7	0.8	13	3	11.7	0.8
JA18-05-18	174	75	0.43	0.07162	0.02450	0.02021	0.00813	0.00205	0.00014	0.00063	0.00019	0.9	975	736	20	8	13.2	0.9	13	4	13.2	0.9
JA18-05-19	53	22	0.43	0.05615	0.09856	0.01418	0.02737	0.00183	0.00036	0.00062	0.00061	0.9	458	2416	14	27	12	2	13	12	12	2
JA18-05-20	123	63	0.51	0.07233	0.03737	0.01759	0.01050	0.00176	0.00016	0.00084	0.00020	0.9	995	1029	18	10	11	1	17	4	11	1
JA18-05-21	121	53	0.44	0.08593	0.03931	0.02094	0.01135	0.00177	0.00017	0.00071	0.00024	0.9	1337	995	21	11	11	1	14	5	11	1
JA18-05-22	154	63	0.41	0.08044	0.02596	0.02354	0.00906	0.00212	0.00015	0.00228	0.00026	0.9	1208	712	24	9	13.7	1	46	5	13.7	1

Continue A1-5

Spot	U(ppm)	Th(ppm)	Th/U	U-Th-Pb ratios									Ages (Ma)								Inferred Age (Ma)	1σ
				$^{207}Pb/^{206}Pb$	1σ	$^{207}Pb/^{235}U$	1σ	$^{206}Pb/^{238}U$	1σ	$^{208}Pb/^{232}Th$	1σ	ρr	$^{207}Pb/^{206}Pb$	1σ	$^{207}Pb/^{235}U$	1σ	$^{206}Pb/^{238}U$	1σ	$^{208}Pb/^{232}Th$	1σ		
JA19-01-01	59	25	0.43	0.06334	0.05343	0.01594	0.01522	0.00183	0.00023	0.00042	0.00026	0.9	720	1295	16	15	12	1	8	5	12	1
JA19-01-02	116	70	0.61	0.06557	0.02873	0.01654	0.00852	0.00183	0.00016	0.00061	0.00012	0.9	793	819	17	9	12	1	12	2	12	1
JA19-01-03	134	62	0.47	0.06022	0.02573	0.01425	0.00704	0.00172	0.00013	0.00027	0.00011	0.9	612	767	14	7	11.1	0.8	5	2	11.1	0.8
JA19-01-04	93	37	0.39	0.06934	0.04129	0.01666	0.01161	0.00174	0.00020	0.00059	0.00023	0.9	909	1089	17	12	11	1	12	5	11	1
JA19-01-05	332	268	0.81	0.05978	0.01121	0.01654	0.00389	0.00201	0.00011	0.00065	0.00006	0.9	596	398	17	4	12.9	0.7	13	1	12.9	0.7
JA19-01-06	152	68	0.45	0.05719	0.03074	0.01568	0.00975	0.00199	0.00019	0.00057	0.00017	0.9	499	963	16	10	13	1	12	3	13	1
JA19-01-07	37	13	0.35	0.07727	0.10349	0.01944	0.02998	0.00183	0.00042	0.00068	0.00071	0.9	1128	2170	20	30	12	3	14	14	12	3
JA19-01-08	130	34	0.26	0.06339	0.02302	0.01877	0.00797	0.00215	0.00015	0.00069	0.00024	0.9	721	701	19	8	13.8	1	14	5	13.8	1
JA19-01-09	83	33	0.39	0.05692	0.03120	0.01628	0.00997	0.00207	0.00015	0.00049	0.00019	0.9	488	948	16	10	13.3	1	10	4	13.3	1
JA19-01-10	101	40	0.39	0.06347	0.02492	0.01882	0.00855	0.00215	0.00015	0.00033	0.00017	0.9	724	764	19	9	13.8	1	7	3	13.8	1
JA19-01-11	65	22	0.33	0.06399	0.04981	0.01856	0.01648	0.00210	0.00026	0.00088	0.00039	0.9	741	1202	19	16	14	2	18	8	14	2
JA19-01-12	90	32	0.35	0.04610	0.03343	0.01344	0.01082	0.00211	0.00019	0.00016	0.00025	0.9	3	983	14	11	14	1	3	5	14	1
JA19-01-13	76	25	0.33	0.08613	0.03238	0.02448	0.01108	0.00206	0.00018	0.00151	0.00029	0.9	1341	789	25	11	13	1	30	6	13	1
JA19-01-14	144	97	0.68	0.09487	0.01686	0.02631	0.00604	0.00201	0.00012	0.00073	0.00008	0.9	1525	373	26	6	12.9	0.8	15	2	12.9	0.8
JA19-01-15	105	55	0.52	0.00301	0.03034	0.00076	0.00771	0.00183	0.00013	0.00068	0.00013	0.9	-1794	1308	1	8	11.8	0.8	14	3	11.8	0.8
JA19-01-16	109	57	0.52	0.03447	0.02598	0.00951	0.00772	0.00200	0.00013	0.00056	0.00012	0.9	-95	881	10	8	12.9	0.8	11	2	12.9	0.8
JA19-01-17	122	55	0.45	0.06131	0.02126	0.01719	0.00686	0.00203	0.00012	0.00094	0.00013	0.9	650	707	17	7	13.1	0.8	19	3	13.1	0.8
JA19-01-18	142	80	0.57	0.03416	0.02486	0.00929	0.00735	0.00197	0.00014	0.00084	0.00012	0.9	-108	865	9	7	12.7	0.9	17	2	12.7	0.9
JA19-01-19	40	16	0.39	0.05700	0.06858	0.01594	0.02127	0.00203	0.00030	0.00091	0.00043	0.9	492	1593	16	21	13	2	18	9	13	2
JA19-01-20	97	39	0.40	0.07343	0.04197	0.02111	0.01420	0.00209	0.00024	0.00106	0.00029	0.9	1026	1102	21	14	13	2	21	6	13	2
JA19-01-21	367	696	1.90	0.05981	0.00629	0.02306	0.00321	0.00280	0.00011	0.00088	0.00005	0.9	597	238	23	3	18	0.7	18	1	18	0.7
JA19-01-22	64	30	0.47	0.07273	0.04270	0.01930	0.01302	0.00192	0.00019	0.00071	0.00023	0.9	1006	1098	19	13	12	1	14	5	12	1

Continue A1-6

Spot	U(ppm)	Th(ppm)	Th/U	U-Th-Pb ratios									Ages (Ma)								Inferred Age (Ma)	1σ
				$^{207}Pb/^{206}Pb$	1σ	$^{207}Pb/^{235}U$	1σ	$^{206}Pb/^{238}U$	1σ	$^{208}Pb/^{232}Th$	1σ	ρr	$^{207}Pb/^{206}Pb$	1σ	$^{207}Pb/^{235}U$	1σ	$^{206}Pb/^{238}U$	1σ	$^{208}Pb/^{232}Th$	1σ		
JA19-02-01	156	112	0.72	0.08323	0.01657	0.02430	0.00594	0.00212	0.00011	0.00064	0.00007	0.9	1275	416	24	6	13.7	0.7	13	1	13.7	0.7
JA19-02-02	60	22	0.37	0.07726	0.05015	0.01936	0.01454	0.00182	0.00021	0.00146	0.00030	0.9	1128	1137	19	14	12	1	29	6	12	1
JA19-02-03	71	27	0.38	0.02832	0.04302	0.00803	0.01286	0.00206	0.00019	0.00038	0.00025	0.9	-359	1198	8	13	13	1	8	5	13	1
JA19-02-04	140	74	0.53	0.06417	0.02158	0.01669	0.00647	0.00189	0.00011	0.00067	0.00010	0.9	747	699	17	6	12.2	0.7	14	2	12.2	0.7
JA19-02-05	116	77	0.66	0.03313	0.02714	0.00863	0.00760	0.00189	0.00013	0.00064	0.00009	0.9	-150	891	9	8	12.2	0.8	13	2	12.2	0.8
JA19-02-06	72	34	0.47	0.03092	0.04370	0.00819	0.01226	0.00192	0.00018	0.00049	0.00020	0.9	-244	1208	8	12	12	1	10	4	12	1
JA19-02-07	132	61	0.46	0.06038	0.02167	0.01630	0.00666	0.00196	0.00011	0.00085	0.00012	0.9	617	680	16	7	12.6	0.7	17	2	12.6	0.7
JA19-02-08	174	73	0.42	0.02735	0.01660	0.00788	0.00512	0.00209	0.00010	0.00078	0.00010	0.9	-403	697	8	5	13.5	0.6	16	2	13.5	0.6
JA19-02-09	124	58	0.47	0.07330	0.02203	0.02148	0.00761	0.00213	0.00013	0.00074	0.00013	0.9	1022	635	22	8	13.7	0.8	15	3	13.7	0.8
JA19-02-10	109	55	0.50	0.17415	0.02340	0.04452	0.00864	0.00185	0.00013	0.00067	0.00012	0.9	2598	238	44	8	11.9	0.8	14	2	11.9	0.8
JA19-02-11	88	37	0.42	0.06092	0.03153	0.01750	0.01025	0.00208	0.00016	0.00059	0.00018	0.9	636	960	18	10	13	1	12	4	13	1
JA19-02-12	128	83	0.65	0.06460	0.02162	0.01816	0.00702	0.00204	0.00012	0.00066	0.00009	0.9	761	699	18	7	13.1	0.8	13	2	13.1	0.8
JA19-02A-13	115	52	0.45	0.02651	0.03601	0.00700	0.01003	0.00192	0.00016	0.00087	0.00017	0.9	-441	1114	7	10	12	1	18	3	12	1
JA19-02A-14	93	53	0.57	0.03147	0.03781	0.00969	0.01238	0.00223	0.00019	0.00074	0.00017	0.9	-220	1127	10	12	14	1	15	3	14	1
JA19-02A-15	96	42	0.44	0.05405	0.03768	0.01594	0.01237	0.00214	0.00019	0.00050	0.00022	0.9	373	1022	16	12	14	1	10	4	14	1
JA19-02A-16	86	48	0.56	0.07706	0.04035	0.02389	0.01457	0.00225	0.00022	0.00045	0.00020	0.9	1123	1000	24	14	14	1	9	4	14	1
JA19-02A-17	96	70	0.73	0.05062	0.04048	0.01380	0.01215	0.00198	0.00018	0.00088	0.00014	0.9	224	1088	14	12	13	1	18	3	13	1
JA19-02A-18	120	61	0.51	0.02147	0.03692	0.00547	0.00983	0.00185	0.00016	0.00071	0.00015	0.9	-686	1124	6	10	12	1	14	3	12	1
JA19-02A-19	134	81	0.60	0.00484	0.02728	0.00154	0.00877	0.00231	0.00015	0.00074	0.00012	0.9	-1666	1191	2	9	14.9	1	15	2	14.9	1
JA19-02A-20	66	27	0.40	0.01803	0.06501	0.00478	0.01777	0.00192	0.00024	0.00054	0.00033	0.9	-865	1703	5	18	12	2	11	7	12	2
JA19-02A-21	49	19	0.38	0.09677	0.06933	0.02790	0.02386	0.00209	0.00033	0.00036	0.00046	0.9	1563	1372	28	24	13	2	7	9	13	2

Continue A1-7

Spot	U(ppm)	Th(ppm)	Th/U	U-Th-Pb ratios									Ages (Ma)								Inferred Age (Ma)	1σ
				$^{207}Pb/^{206}Pb$	1σ	$^{207}Pb/^{235}U$	1σ	$^{206}Pb/^{238}U$	1σ	$^{208}Pb/^{232}Th$	1σ	ρr	$^{207}Pb/^{206}Pb$	1σ	$^{207}Pb/^{235}U$	1σ	$^{206}Pb/^{238}U$	1σ	$^{208}Pb/^{232}Th$	1σ		
JA20-01-01	159	68	0.43	0.05073	0.00747	0.02846	0.00505	0.00407	0.00014	0.00123	0.00011	0.9	229	299	28	5	26.2	0.9	25	2	26.2	0.9
JA20-01-02	148	82	0.56	0.03421	0.01167	0.02003	0.00775	0.00425	0.00022	0.00117	0.00014	0.9	-106	466	20	8	27	1	24	3	27	1
JA20-01-04	130	65	0.50	0.05400	0.01017	0.03152	0.00718	0.00423	0.00019	0.00142	0.00014	0.9	371	374	32	7	27	1	29	3	27	1
JA20-01-05	296	189	0.64	0.05194	0.00586	0.02975	0.00441	0.00415	0.00017	0.00137	0.00010	0.9	283	246	30	4	27	1	28	2	27	1
JA20-01-06	139	91	0.66	0.04743	0.01927	0.02693	0.01284	0.00412	0.00033	0.00202	0.00024	0.9	71	661	27	13	27	2	41	5	27	2
JA20-01-07	263	162	0.62	0.04109	0.00669	0.02344	0.00466	0.00414	0.00017	0.00129	0.00010	0.9	-228	268	24	5	27	1	26	2	27	1
JA20-01-08	478	326	0.68	0.05025	0.00291	0.02907	0.00239	0.00420	0.00012	0.00146	0.00007	0.9	207	134	29	2	27	0.8	29	1	27	0.8
JA20-01-09	100	38	0.38	0.04872	0.01572	0.02766	0.01035	0.00412	0.00024	0.00137	0.00024	0.9	134	574	28	10	27	2	28	5	27	2
JA20-01-10	215	122	0.57	0.03820	0.00914	0.02109	0.00593	0.00400	0.00019	0.00151	0.00014	0.9	-397	393	21	6	26	1	30	3	26	1
JA20-01-11	118	55	0.47	0.05468	0.01017	0.03226	0.00719	0.00428	0.00018	0.00126	0.00014	0.9	399	373	32	7	28	1	25	3	28	1
JA20-01-12	738	638	0.86	0.05111	0.00157	0.02871	0.00151	0.00407	0.00011	0.00135	0.00006	0.9	246	73	29	1	26.2	0.7	27	1	26.2	0.7
JA20-01-13	174	93	0.53	0.05064	0.00872	0.02857	0.00596	0.00409	0.00017	0.00137	0.00012	0.9	224	334	29	6	26	1	28	2	26	1
JA20-01-14	97	51	0.53	0.05627	0.01296	0.03149	0.00855	0.00406	0.00019	0.00134	0.00015	0.9	463	459	31	8	26	1	27	3	26	1
JA20-01-15	116	80	0.69	0.04142	0.01713	0.02236	0.01051	0.00392	0.00025	0.00164	0.00018	0.9	-209	627	22	10	25	2	33	4	25	2
JA20-01-16	257	160	0.62	0.04865	0.00509	0.02763	0.00365	0.00412	0.00013	0.00145	0.00008	0.9	131	226	28	4	26.5	0.8	29	2	26.5	0.8
JA20-01-17	229	136	0.59	0.04754	0.00557	0.02719	0.00393	0.00415	0.00013	0.00152	0.00008	0.9	76	241	27	4	26.7	0.8	31	2	26.7	0.8
JA20-01-18	208	82	0.39	0.05514	0.00807	0.03149	0.00580	0.00414	0.00018	0.00154	0.00015	0.9	418	319	31	6	27	1	31	3	27	1
JA20-01-19	107	51	0.48	0.05898	0.01401	0.03146	0.00890	0.00387	0.00020	0.00154	0.00018	0.9	566	475	31	9	25	1	31	4	25	1
JA20-01-20	158	130	0.82	0.03949	0.00861	0.02246	0.00562	0.00412	0.00015	0.00132	0.00009	0.9	-320	350	23	6	26.5	1	27	2	26.5	1
JA20-01-21	1064	2340	2.20	0.05489	0.00138	0.03242	0.00148	0.00428	0.00011	0.00141	0.00007	0.9	408	58	32	1	27.5	0.7	28	1	27.5	0.7
JA20-01-22	107	47	0.44	0.03982	0.01766	0.02216	0.01109	0.00404	0.00026	0.00168	0.00026	0.9	-300	667	22	11	26	2	34	5	26	2
JA20-01-23	542	905	1.67	0.05103	0.00325	0.02842	0.00253	0.00404	0.00012	0.00116	0.00007	0.9	242	147	28	2	26	0.8	23	1	26	0.8

Continue A1-8

Spot	U(ppm)	Th(ppm)	Th/U	U-Th-Pb ratios									Ages (Ma)								Inferred Age (Ma)	1σ
				$^{207}Pb/^{206}Pb$	1σ	$^{207}Pb/^{235}U$	1σ	$^{206}Pb/^{238}U$	1σ	$^{208}Pb/^{232}Th$	1σ	ρr	$^{207}Pb/^{206}Pb$	1σ	$^{207}Pb/^{235}U$	1σ	$^{206}Pb/^{238}U$	1σ	$^{208}Pb/^{232}Th$	1σ		
JA20-02A-01	730	456	0.62	0.04851	0.00247	0.02703	0.00195	0.00404	0.00010	0.00123	0.00005	0.9	124	118	27	2	26	0.6	25	1	26	0.6
JA20-02A-02	601	465	0.77	0.04298	0.00326	0.02368	0.00236	0.00400	0.00011	0.00129	0.00005	0.9	-124	150	24	2	25.7	0.7	26	1	25.7	0.7
JA20-02A-03	918	846	0.92	0.05206	0.00193	0.02870	0.00166	0.00400	0.00010	0.00123	0.00005	0.9	288	87	29	2	25.7	0.6	25	1	25.7	0.6
JA20-02A-04	647	482	0.74	0.05622	0.00745	0.03034	0.00489	0.00391	0.00014	0.00122	0.00003	0.85	461	284	30	5	25.2	0.9	24.6	0.7	25.2	0.9
JA20-02A-05	932	1100	1.18	0.04690	0.00199	0.02654	0.00167	0.00410	0.00010	0.00125	0.00005	0.9	44	95	27	2	26.4	0.6	25	1	26.4	0.6
JA20-02A-06	1221	1019	0.83	0.05333	0.00145	0.02985	0.00141	0.00406	0.00010	0.00124	0.00005	0.9	343	64	30	1	26.1	0.6	25	1	26.1	0.6
JA20-02A-07	878	720	0.82	0.04915	0.00203	0.02736	0.00170	0.00404	0.00010	0.00120	0.00005	0.9	155	97	27	2	26	0.6	24	1	26	0.6
JA20-02A-08	582	375	0.65	0.05277	0.00407	0.02899	0.00305	0.00398	0.00013	0.00127	0.00007	0.9	319	178	29	3	25.6	0.8	26	1	25.6	0.8
JA20-02A-09	1369	2598	1.90	0.04785	0.00156	0.02659	0.00141	0.00403	0.00010	0.00128	0.00006	0.9	92	75	27	1	25.9	0.6	26	1	25.9	0.6
JA20-02A-10	707	522	0.74	0.04733	0.00264	0.02652	0.00209	0.00406	0.00011	0.00123	0.00006	0.9	66	126	27	2	26.1	0.7	25	1	26.1	0.7
JA20-02A-11	870	610	0.70	0.05507	0.00195	0.03132	0.00180	0.00413	0.00011	0.00128	0.00006	0.9	415	82	31	2	26.6	0.7	26	1	26.6	0.7
JA20-02A-12	358	270	0.76	0.05406	0.00484	0.03292	0.00379	0.00442	0.00013	0.00139	0.00008	0.9	374	206	33	4	28.4	0.8	28	2	28.4	0.8
JA20-02A-13	721	550	0.76	0.06183	0.00257	0.03542	0.00226	0.00415	0.00011	0.00138	0.00006	0.9	668	92	35	2	26.7	0.7	28	1	26.7	0.7
JA20-02A-15	1395	2411	1.73	0.04909	0.00130	0.02813	0.00129	0.00416	0.00010	0.00127	0.00005	0.9	152	63	28	1	26.8	0.6	26	1	26.8	0.6
JA20-02A-16	784	566	0.72	0.06062	0.00216	0.03419	0.00198	0.00409	0.00011	0.00136	0.00006	0.9	626	80	34	2	26.3	0.7	27	1	26.3	0.7
JA20-02A-17	979	790	0.81	0.05794	0.00191	0.03242	0.00173	0.00406	0.00010	0.00135	0.00006	0.9	528	69	32	2	26.1	0.6	27	1	26.1	0.6
JA20-02A-18	807	542	0.67	0.04707	0.00218	0.02756	0.00188	0.00425	0.00011	0.00133	0.00007	0.9	53	93	28	2	27.3	0.7	27	1	27.3	0.7
JA20-02A-19	905	626	0.69	0.04808	0.00187	0.02824	0.00171	0.00426	0.00011	0.00134	0.00007	0.9	103	82	28	2	27.4	0.7	27	1	27.4	0.7

Continue A1-9

Spot	U(ppm)	Th(ppm)	Th/U	U-Th-Pb ratios									Ages (Ma)								Inferred Age (Ma)	1σ
				$^{207}Pb/^{206}Pb$	1σ	$^{207}Pb/^{235}U$	1σ	$^{206}Pb/^{238}U$	1σ	$^{208}Pb/^{232}Th$	1σ	ρr	$^{207}Pb/^{206}Pb$	1σ	$^{207}Pb/^{235}U$	1σ	$^{206}Pb/^{238}U$	1σ	$^{208}Pb/^{232}Th$	1σ		
JA20-03-01	1346	980	0.73	0.05313	0.00111	0.02953	0.00123	0.00403	0.00011	0.00135	0.00005	0.9	334	45	30	1	25.9	0.7	27	1	25.9	0.7
JA20-03-02	792	576	0.73	0.05147	0.00150	0.02791	0.00139	0.00393	0.00010	0.00131	0.00005	0.9	262	64	28	1	25.3	0.6	26	1	25.3	0.6
JA20-03-03D	101	36	0.36	0.05779	0.01037	0.02972	0.00645	0.00373	0.00016	0.00162	0.00016	0.9	522	380	30	6	24	1	33	3	24	1
JA20-03-04	888	710	0.80	0.04609	0.00129	0.02508	0.00113	0.00395	0.00010	0.00132	0.00004	0.82	2	48	25	1	25.4	0.7	26.7	0.9	25.4	0.7
JA20-03-05	327	172	0.53	0.05161	0.00331	0.03007	0.00272	0.00423	0.00013	0.00144	0.00008	0.9	268	140	30	3	27.2	0.8	29	2	27.2	0.8
JA20-03-06	535	355	0.66	0.04600	0.00217	0.02569	0.00185	0.00405	0.00012	0.00140	0.00006	0.9	-2	91	26	2	26.1	0.8	28	1	26.1	0.8
JA20-03-07	654	356	0.54	0.04908	0.00144	0.02683	0.00134	0.00397	0.00010	0.00130	0.00005	0.9	152	65	27	1	25.5	0.6	26	1	25.5	0.6
JA20-03-08	173	91	0.53	0.04391	0.00556	0.02456	0.00380	0.00406	0.00013	0.00141	0.00008	0.9	-75	201	25	4	26.1	0.8	28	2	26.1	0.8
JA20-03-09	790	642	0.81	0.04770	0.00140	0.02691	0.00133	0.00409	0.00010	0.00129	0.00005	0.9	84	62	27	1	26.3	0.6	26	1	26.3	0.6
JA20-03-10	454	293	0.65	0.05241	0.00201	0.02940	0.00179	0.00407	0.00011	0.00133	0.00006	0.9	303	84	29	2	26.2	0.7	27	1	26.2	0.7
JA20-03-11	153	90	0.59	0.06327	0.00830	0.03683	0.00634	0.00422	0.00020	0.00146	0.00014	0.9	717	281	37	6	27	1	29	3	27	1
JA20-03-12	943	443	0.47	0.04612	0.00239	0.02582	0.00189	0.00406	0.00013	0.00135	0.00007	0.78	4	97	26	2	26.1	0.9	27	1	26.1	0.9
JA20-03-13	405	190	0.47	0.04611	0.00267	0.02498	0.00197	0.00393	0.00012	0.00132	0.00008	0.79	3	109	25	2	25.3	0.8	27	2	25.3	0.8
JA20-03-14	509	298	0.59	0.04008	0.00212	0.02270	0.00172	0.00411	0.00011	0.00117	0.00005	0.9	-285	117	23	2	26.4	0.7	24	1	26.4	0.7
JA20-03-15	286	285	1.00	0.04807	0.00392	0.02686	0.00288	0.00405	0.00012	0.00133	0.00006	0.9	103	171	27	3	26.1	0.8	27	1	26.1	0.8
JA20-03-16	222	173	0.78	0.06346	0.00580	0.03524	0.00428	0.00403	0.00014	0.00129	0.00008	0.9	724	191	35	4	25.9	0.9	26	2	25.9	0.9
JA20-03-17	688	453	0.66	0.04688	0.00184	0.02623	0.00162	0.00406	0.00011	0.00140	0.00006	0.9	43	77	26	2	26.1	0.7	28	1	26.1	0.7
JA20-03-18	984	943	0.96	0.04614	0.00304	0.02596	0.00216	0.00408	0.00011	0.00132	0.00004	0.75	5	127	26	2	26.3	0.7	26.6	0.7	26.3	0.7
JA20-03-19	287	120	0.42	0.05707	0.00945	0.03212	0.00702	0.00408	0.00025	0.00197	0.00021	0.9	494	353	32	7	26	2	40	4	26	2
JA20-03-20	714	470	0.66	0.04769	0.00138	0.02743	0.00138	0.00417	0.00011	0.00146	0.00006	0.9	84	61	27	1	26.8	0.7	29	1	26.8	0.7
JA20-03-21	614	255	0.42	0.04607	0.00063	0.02492	0.00094	0.00392	0.00013	0.00149	0.00011	0.94	1	22	25	0.9	25.2	0.8	30	2	25.2	0.8
JA20-03-22	129	64	0.50	0.04622	0.00784	0.02700	0.00542	0.00424	0.00015	0.00152	0.00011	0.9	9	269	27	5	27.3	1	31	2	27.3	1
JA20-03-23	229	138	0.61	0.04704	0.00588	0.02566	0.00400	0.00396	0.00014	0.00137	0.00009	0.9	51	228	26	4	25.5	0.9	28	2	25.5	0.9

Continue A1-10

Spot	U(ppm)	Th(ppm)	Th/U	U-Th-Pb ratios									Ages (Ma)								Inferred	1σ
				$^{207}Pb/^{206}Pb$	1σ	$^{207}Pb/^{235}U$	1σ	$^{206}Pb/^{238}U$	1σ	$^{208}Pb/^{232}Th$	1σ	*ρr*	$^{207}Pb/^{206}Pb$	1σ	$^{207}Pb/^{235}U$	1σ	$^{206}Pb/^{238}U$	1σ	$^{208}Pb/^{232}Th$	1σ	Age (Ma)	
JA27-01-01	168.78	91.76	0.54	0.04990	0.01033	0.01293	0.00316	0.00188	0.00008	0.00053	0.00004	0.9	190	345	13	3	12.1	0.5	10.7	0.8	12.1	0.5
JA27-01-03	143.85	107.08	0.74	0.05889	0.01263	0.01436	0.00365	0.00177	0.00008	0.00062	0.00004	0.9	563	401	14	4	11.4	0.5	12.5	0.8	11.4	0.5
JA27-01-04	110.46	60.05	0.54	0.07137	0.01469	0.01739	0.00427	0.00177	0.00008	0.00070	0.00006	0.9	968	401	18	4	11.4	0.5	14	1	11.4	0.5
JA27-01-05	231.43	159.97	0.69	0.05716	0.00760	0.01365	0.00223	0.00173	0.00006	0.00053	0.00003	0.9	498	270	14	2	11.1	0.4	10.7	0.6	11.1	0.4
JA27-01-06	145.34	82.25	0.57	0.05708	0.01084	0.01440	0.00322	0.00183	0.00007	0.00072	0.00005	0.9	495	361	15	3	11.8	0.5	15	1	11.8	0.5
JA27-01-07	261.11	233.96	0.90	0.05747	0.01139	0.01355	0.00314	0.00171	0.00007	0.00053	0.00002	0.87	510	366	14	3	11	0.4	10.7	0.5	11	0.4
JA27-01-08	88.26	42.71	0.48	0.06576	0.01879	0.01649	0.00551	0.00182	0.00010	0.00065	0.00008	0.9	799	543	17	6	11.7	0.6	13	2	11.7	0.6
JA27-01-09	143.49	108.48	0.76	0.05894	0.01898	0.01542	0.00564	0.00190	0.00010	0.00059	0.00008	0.86	565	541	16	6	12.2	0.6	12	2	12.2	0.6
JA27-01-10	504.59	536.60	1.06	0.05321	0.00463	0.01290	0.00144	0.00176	0.00005	0.00052	0.00003	0.9	338	177	13	1	11.3	0.3	10.5	0.6	11.3	0.3
JA27-01-11	181.67	97.67	0.54	0.04648	0.00921	0.01095	0.00251	0.00171	0.00006	0.00069	0.00004	0.9	23	281	11	3	11	0.4	13.9	0.8	11	0.4
JA27-01-12	218.82	176.46	0.81	0.04339	0.00764	0.01041	0.00215	0.00174	0.00006	0.00052	0.00003	0.9	-102	228	11	2	11.2	0.4	10.5	0.6	11.2	0.4
JA27-01-13	166.00	112.33	0.68	0.05116	0.01275	0.01241	0.00359	0.00176	0.00008	0.00058	0.00005	0.9	248	392	13	4	11.3	0.5	12	1	11.3	0.5
JA27-01-14	190.78	138.81	0.73	0.04653	0.00921	0.01116	0.00255	0.00174	0.00006	0.00049	0.00003	0.9	25	281	11	3	11.2	0.4	9.9	0.6	11.2	0.4
JA27-01-16	162.64	95.39	0.59	0.05707	0.01002	0.01452	0.00310	0.00185	0.00008	0.00082	0.00005	0.9	494	331	15	3	11.9	0.5	17	1	11.9	0.5
JA27-01-17	178.91	70.96	0.40	0.06967	0.01116	0.01686	0.00337	0.00176	0.00008	0.00056	0.00005	0.9	919	303	17	3	11.3	0.5	11	1	11.3	0.5
JA27-01-18	144.83	87.05	0.60	0.05652	0.01115	0.01503	0.00358	0.00193	0.00009	0.00067	0.00005	0.9	473	368	15	4	12.4	0.6	14	1	12.4	0.6

Continue A1-11

Spot	U(ppm)	Th(ppm)	Th/U	U-Th-Pb ratios									Ages (Ma)								Inferred Age (Ma)	1σ
				$^{207}Pb/^{206}Pb$	1σ	$^{207}Pb/^{235}U$	1σ	$^{206}Pb/^{238}U$	1σ	$^{208}Pb/^{232}Th$	1σ	ρr	$^{207}Pb/^{206}Pb$	1σ	$^{207}Pb/^{235}U$	1σ	$^{206}Pb/^{238}U$	1σ	$^{208}Pb/^{232}Th$	1σ		
JA32-02-01	50.57	19.42	0.38	0.00072	0.02629	0.00019	0.00695	0.00197	0.00015	0.00026	0.00014	0.9	-1960	1317		7	12.7	1	5	3	12.7	1
JA32-02-02	80.33	33.36	0.42	0.05409	0.01207	0.01431	0.00391	0.00192	0.00011	0.00065	0.00009	0.9	375	450	14	4	12.4	0.7	13	2	12.4	0.7
JA32-02-03	111.65	56.27	0.50	0.04943	0.00988	0.01242	0.00302	0.00182	0.00009	0.00066	0.00006	0.9	168	380	13	3	11.7	0.6	13	1	11.7	0.6
JA32-02-04	72.76	32.30	0.44	0.03895	0.01549	0.01076	0.00485	0.002	0.00012	0.00064	0.0001	0.9	-352	577	11	5	12.9	0.8	13	2	12.9	0.8
JA32-02-05	37.01	12.70	0.34	0.07845	0.02777	0.02001	0.0086	0.00185	0.00016	0.00079	0.0002	0.9	1158	774	20	9	12	1	16	4	12	1
JA32-02-06	33.63	9.63	0.29	0.01778	0.03016	0.00523	0.00929	0.00213	0.00019	0.00017	0.00026	0.9	-879	1016	5	9	14	1	3	5	14	1
JA32-02-07	113.04	62.51	0.55	0.0569	0.01102	0.0136	0.00332	0.00173	0.0001	0.00067	0.00007	0.9	488	405	14	3	11.1	0.6	14	1	11.1	0.6
JA32-02-08	81.87	37.02	0.45	0.04006	0.01321	0.01117	0.00422	0.00202	0.00011	0.00066	0.00009	0.9	-286	500	11	4	13	0.7	13	2	13	0.7
JA32-02-09	64.63	29.09	0.45	0.04675	0.01999	0.01141	0.00562	0.00177	0.00013	0.00138	0.00014	0.9	36	703	12	6	11.4	0.8	28	3	11.4	0.8
JA32-02-10	104.27	50.96	0.49	0.07115	0.01283	0.0182	0.00438	0.00186	0.00013	0.00052	0.00008	0.9	962	409	18	4	12	0.8	11	2	12	0.8
JA32-02-12	61.72	27.65	0.45	0.06898	0.01418	0.01725	0.00446	0.00181	0.00011	0.00048	0.00009	0.9	898	443	17	4	11.7	0.7	10	2	11.7	0.7
JA32-02-13	47.25	24.99	0.53	0.05739	0.02234	0.01483	0.00682	0.00187	0.00015	0.00058	0.00011	0.9	507	733	15	7	12	1	12	2	12	1
JA32-02-14	76.86	36.11	0.47	0.05326	0.01323	0.01456	0.00439	0.00198	0.00012	0.00058	0.00008	0.9	340	489	15	4	12.8	0.8	12	2	12.8	0.8
JA32-02-15	58.14	22.42	0.39	0.04955	0.01864	0.01341	0.00589	0.00196	0.00014	0.00051	0.00013	0.9	174	638	14	6	12.6	0.9	10	3	12.6	0.9
JA32-02-16	45.28	26.72	0.59	0.04805	0.02292	0.01223	0.00671	0.00185	0.00015	0.00071	0.00012	0.9	102	759	12	7	11.9	1	14	2	11.9	1
JA32-02-17	72.18	33.10	0.46	0.02479	0.01433	0.00655	0.00409	0.00192	0.0001	0.00057	0.00008	0.9	-522	630	7	4	12.4	0.6	12	2	12.4	0.6
JA32-02-18	31.40	13.27	0.42	0.09452	0.02708	0.02429	0.00878	0.00186	0.00016	0.00091	0.00016	0.9	1519	664	24	9	12	1	18	3	12	1
JA32-02-19	69.84	31.29	0.45	0.07235	0.01296	0.01776	0.00405	0.00178	0.0001	0.0008	0.00009	0.9	996	405	18	4	11.5	0.6	16	2	11.5	0.6

Continue A1-12

Spot	U(ppm)	Th(ppm)	Th/U	U-Th-Pb ratios									Ages (Ma)								Inferred Age (Ma)	1σ
				$^{207}Pb/^{206}Pb$	1σ	$^{207}Pb/^{235}U$	1σ	$^{206}Pb/^{238}U$	1σ	$^{208}Pb/^{232}Th$	1σ	ρr	$^{207}Pb/^{206}Pb$	1σ	$^{207}Pb/^{235}U$	1σ	$^{206}Pb/^{238}U$	1σ	$^{208}Pb/^{232}Th$	1σ		
JA36-01-01	102	49	0.48	0.10563	0.02948	0.02654	0.00899	0.00182	0.00012	0.00053	0.00003	0.9	1725	585	27	9	11.7	0.8	10.7	0.6	11.7	0.8
JA36-01-02	78	38	0.49	0.04608	0.01071	0.01274	0.00338	0.00201	0.0001	0.00087	0.00026	0.7	2	334	13	3	12.9	0.6	18	5	12.9	0.6
JA36-01-04	83	40	0.48	0.06598	0.02076	0.01738	0.00643	0.00191	0.00012	0.00057	0.00008	0.9	806	608	17	6	12.3	0.8	12	2	12.3	0.8
JA36-01-05	78	36	0.46	0.06408	0.01786	0.01614	0.0052	0.00183	0.00009	0.0009	0.00008	0.9	744	552	16	5	11.8	0.6	18	2	11.8	0.6
JA36-01-06	124	70	0.56	0.06218	0.0121	0.01576	0.00367	0.00184	0.00008	0.00091	0.00006	0.9	680	400	16	4	11.9	0.5	18	1	11.9	0.5
JA36-01-07	487	620	1.27	0.0461	0.00033	0.01157	0.00025	0.00182	0.00004	0.00069	0.00003	0.9	3	15	11.7	0.3	11.7	0.2	13.9	0.7	11.7	0.2
JA36-01-08	241	136	0.57	0.05186	0.00612	0.01402	0.00203	0.00196	0.00006	0.00064	0.00003	0.9	279	252	14	2	12.6	0.4	12.9	0.6	12.6	0.4
JA36-01-09	41	14	0.36	0.05866	0.03611	0.01375	0.00925	0.0017	0.00012	0.00053	0.00038	0.9	555	945	14	9	11	0.7	11	8	11	0.7
JA36-01-10	150	67	0.45	0.04609	0.0063	0.01046	0.00166	0.00165	0.00006	0.00064	0.00014	0.7	2	237	11	2	10.6	0.4	13	3	10.6	0.4
JA36-01-11	313	226	0.72	0.0673	0.01013	0.01643	0.00312	0.00177	0.00008	0.00065	0.00004	0.9	847	317	17	3	11.4	0.5	13.1	0.8	11.4	0.5
JA36-01-12	273	245	0.90	0.05042	0.00748	0.01255	0.00223	0.0018	0.00006	0.00056	0.00003	0.9	214	299	13	2	11.6	0.4	11.3	0.6	11.6	0.4
JA36-01-13	114	45	0.39	0.03893	0.01504	0.00953	0.00411	0.00178	0.00009	0.00074	0.00007	0.9	-353	538	10	4	11.5	0.6	15	1	11.5	0.6
JA36-01-14	151	78	0.52	0.05801	0.01563	0.01446	0.0046	0.00181	0.0001	0.00066	0.00006	0.9	530	502	15	5	11.7	0.6	13	1	11.7	0.6
JA36-01-15	143	71	0.50	0.05315	0.01188	0.01274	0.0033	0.00174	0.00007	0.00057	0.00005	0.9	335	403	13	3	11.2	0.5	12	1	11.2	0.5
JA36-01-16	117	60	0.52	0.05265	0.01537	0.01265	0.00427	0.00174	0.00009	0.00066	0.00006	0.9	314	503	13	4	11.2	0.6	13	1	11.2	0.6
JA36-01-17	156	94	0.60	0.04617	0.00999	0.01135	0.00285	0.00178	0.00007	0.00054	0.00004	0.9	7	339	11	3	11.5	0.5	10.9	0.8	11.5	0.5
JA36-01-18	163	68	0.42	0.06952	0.01041	0.01909	0.00353	0.00199	0.00008	0.00076	0.00006	0.9	914	313	19	4	12.8	0.5	15	1	12.8	0.5
JA36-01-19	104	58	0.56	0.07411	0.01515	0.02046	0.00508	0.002	0.0001	0.00066	0.00006	0.9	1044	430	21	5	12.9	0.6	13	1	12.9	0.6
JA36-01-20	247	187	0.76	0.05246	0.00708	0.01369	0.00223	0.00189	0.00006	0.00062	0.00003	0.9	306	279	14	2	12.2	0.4	12.5	0.6	12.2	0.4

Continue A1-13

Spot	U(ppm)	Th(ppm)	Th/U	U-Th-Pb ratios									Ages (Ma)								Inferred Age (Ma)	1σ
				$^{207}Pb/^{206}Pb$	1σ	$^{207}Pb/^{235}U$	1σ	$^{206}Pb/^{238}U$	1σ	$^{208}Pb/^{232}Th$	1σ	*ρr*	$^{207}Pb/^{206}Pb$	1σ	$^{207}Pb/^{235}U$	1σ	$^{206}Pb/^{238}U$	1σ	$^{208}Pb/^{232}Th$	1σ		
JA45-01-05	215.23	181.11	0.84	0.05076	0.01522	0.02089	0.00694	0.00299	0.00013	0.00094	0.00011	0.8	230	454	21	7	19.2	0.8	19	2	19.2	0.8
JA45-01-06	266.12	250.03	0.94	0.07995	0.01772	0.03595	0.00919	0.00326	0.00013	0.00098	0.00003	0.9	1196	441	36	9	21	0.8	19.7	0.6	21	0.8
JA45-01-07	36.36	13.53	0.37	0.07657	0.03585	0.03822	0.02062	0.00362	0.00032	0.00109	0.00048	0.8	1110	883	38	20	23	2	22	10	23	2
JA45-01-08	111.21	56.05	0.50	0.06743	0.02655	0.03053	0.01349	0.00328	0.00019	0.001	0.00023	0.8	851	704	31	13	21	1	20	5	21	1
JA45-01-10	491.90	610.28	1.24	0.06293	0.01479	0.02813	0.00746	0.00324	0.00012	0.001	0.00003	0.9	706	449	28	7	20.9	0.8	20.1	0.7	20.9	0.8
JA45-01-11	60.03	25.48	0.42	0.06051	0.03897	0.0257	0.01795	0.00308	0.00021	0.00095	0.00058	0.8	622	943	26	18	20	1	19	12	20	1
JA45-01-13	370.21	431.64	1.17	0.07016	0.01417	0.031	0.00723	0.00321	0.00012	0.00097	0.00002	0.9	933	399	31	7	20.6	0.8	19.6	0.5	20.6	0.8
JA45-01-14	270.38	142.98	0.53	0.06308	0.01511	0.02594	0.00709	0.00298	0.00012	0.00092	0.00007	0.8	711	454	26	7	19.2	0.8	19	1	19.2	0.8
JA45-01-15	339.21	349.21	1.03	0.11114	0.02417	0.04798	0.01246	0.00313	0.00015	0.0009	0.00003	0.9	1818	408	48	12	20.2	1	18.3	0.7	20.2	1
JA45-01-17	180.97	124.20	0.69	0.15429	0.02948	0.06725	0.01617	0.00316	0.00018	0.00088	0.00006	0.9	2394	327	66	15	20	1	18	1	20	1
JA45-01-18	258.52	166.79	0.65	0.07478	0.01548	0.03158	0.00761	0.00306	0.00012	0.00092	0.00003	0.9	1063	414	32	7	19.7	0.8	18.6	0.6	19.7	0.8
JA45-01-20	189.76	136.02	0.72	0.08148	0.01531	0.03341	0.00737	0.00297	0.00011	0.00089	0.00002	0.9	1233	371	33	7	19.1	0.7	17.9	0.5	19.1	0.7
JA45-01-21	122.79	88.02	0.72	0.05161	0.01762	0.02184	0.00831	0.00307	0.00016	0.00096	0.00016	0.8	268	516	22	8	20	1	19	3	20	1
JA45-01-22	192.62	107.75	0.56	0.05051	0.00566	0.02186	0.003	0.00314	0.00009	0.00097	0.00005	0.9	219	224	22	3	20.2	0.6	20	1	20.2	0.6
JA45-01-23	228.57	170.15	0.74	0.13172	0.02107	0.0562	0.01104	0.00309	0.00013	0.00088	0.00005	0.9	2121	274	56	11	19.9	0.8	17.8	0.9	19.9	0.8
JA45-01-27	249.27	199.36	0.80	0.10407	0.01462	0.04361	0.00754	0.00304	0.00012	0.00088	0.00003	0.9	1698	251	43	7	19.6	0.7	17.9	0.6	19.6	0.7
JA45-01-28	200.17	112.62	0.56	0.09682	0.0114	0.04017	0.00599	0.00301	0.00011	0.00088	0.00002	0.9	1564	212	40	6	19.4	0.7	17.8	0.5	19.4	0.7
JA45-01-29	123.35	67.44	0.55	0.09953	0.02351	0.0413	0.01157	0.00301	0.00015	0.00088	0.00004	0.9	1615	467	41	11	19.4	1	17.8	0.9	19.4	1
JA45-01-30	258.88	243.23	0.94	0.06733	0.01895	0.02893	0.00924	0.00312	0.00014	0.00095	0.00005	0.9	848	524	29	9	20.1	0.9	19	1	20.1	0.9

Continue A1-14

Spot	U(ppm)	Th(ppm)	Th/U	U-Th-Pb ratios									Ages (Ma)								Inferred Age (Ma)	1σ
				$^{207}Pb/^{206}Pb$	1σ	$^{207}Pb/^{235}U$	1σ	$^{206}Pb/^{238}U$	1σ	$^{208}Pb/^{232}Th$	1σ	ρr	$^{207}Pb/^{206}Pb$	1σ	$^{207}Pb/^{235}U$	1σ	$^{206}Pb/^{238}U$	1σ	$^{208}Pb/^{232}Th$	1σ		
JA46-01-01	1100.48	1936.27	1.76	0.04703	0.00213	0.01253	0.00079	0.00193	0.00004	0.00064	0.00002	0.9	51	82	12.6	0.8	12.4	0.3	12.9	0.4	12.4	0.3
JA46-01-02	823.20	1188.99	1.44	0.05574	0.00390	0.01495	0.00144	0.00195	0.00006	0.00064	0.00003	0.9	442	136	15	1	12.6	0.4	12.9	0.6	12.6	0.4
JA46-01-03	684.68	1142.38	1.67	0.05597	0.00353	0.01392	0.00121	0.00180	0.00005	0.00056	0.00002	0.9	451	123	14	1	11.6	0.3	11.3	0.4	11.6	0.3
JA46-01-04	1206.62	1577.93	1.31	0.04633	0.00187	0.01271	0.00078	0.00199	0.00005	0.00062	0.00002	0.9	15	70	12.8	0.8	12.8	0.3	12.5	0.4	12.8	0.3
JA46-01-05	1839.01	3422.39	1.86	0.04980	0.00178	0.01310	0.00070	0.00191	0.00004	0.00060	0.00002	0.9	186	72	13.2	0.7	12.3	0.3	12.1	0.4	12.3	0.3
JA46-01-07	1265.54	1611.43	1.27	0.05635	0.00200	0.01491	0.00079	0.00192	0.00004	0.00062	0.00002	0.9	466	68	15	0.8	12.4	0.3	12.5	0.4	12.4	0.3
JA46-01-08	976.62	1629.48	1.67	0.05208	0.00237	0.01372	0.00087	0.00191	0.00004	0.00059	0.00002	0.9	289	90	13.8	0.9	12.3	0.3	11.9	0.4	12.3	0.3
JA46-01-09	1108.65	2189.51	1.97	0.08502	0.01044	0.02187	0.00322	0.00187	0.00005	0.00055	0.00001	0.91	1316	212	22	3	12	0.3	11.2	0.2	12	0.3
JA46-01-10	1179.07	2112.97	1.79	0.05963	0.00242	0.01593	0.00099	0.00194	0.00005	0.00062	0.00002	0.9	590	76	16	1	12.5	0.3	12.5	0.4	12.5	0.3
JA46-01-11	1243.44	1037.32	0.83	0.05352	0.00216	0.01313	0.00078	0.00178	0.00004	0.00049	0.00001	0.9	351	79	13.2	0.8	11.5	0.3	9.9	0.2	11.5	0.3
JA46-01-12	1116.81	1688.68	1.51	0.06876	0.00306	0.01698	0.00108	0.00179	0.00004	0.00053	0.00002	0.9	892	80	17	1	11.5	0.3	10.7	0.4	11.5	0.3
JA46-01-13	1028.07	1326.51	1.29	0.05298	0.00292	0.01320	0.00098	0.00181	0.00004	0.00051	0.00002	0.9	328	109	13.3	1	11.7	0.3	10.3	0.4	11.7	0.3
JA46-01-14	1202.63	1531.32	1.27	0.04899	0.00238	0.01231	0.00083	0.00182	0.00004	0.00050	0.00001	0.9	147	95	12.4	0.8	11.7	0.3	10.1	0.2	11.7	0.3
JA46-01-15	1190.40	2133.28	1.79	0.07038	0.00262	0.01779	0.00099	0.00183	0.00004	0.00050	0.00001	0.9	939	66	17.9	1	11.8	0.3	10.1	0.2	11.8	0.3
JA46-01-16	1192.02	1955.15	1.64	0.04748	0.00242	0.01189	0.00083	0.00182	0.00004	0.00047	0.00001	0.9	73	94	12	0.8	11.7	0.3	9.5	0.2	11.7	0.3
JA46-01-17	326.03	553.53	1.70	0.11921	0.00971	0.03254	0.00377	0.00198	0.00008	0.00054	0.00003	0.9	1944	128	33	4	12.8	0.5	10.9	0.6	12.8	0.5
JA46-01-18	1124.97	1649.48	1.47	0.07722	0.00311	0.01913	0.00113	0.00180	0.00004	0.00054	0.00002	0.9	1127	69	19	1	11.6	0.3	10.9	0.4	11.6	0.3
JA46-01-19	827.40	1569.98	1.90	0.04588	0.00293	0.01186	0.00103	0.00188	0.00005	0.00047	0.00002	0.9	-8	115	12	1	12.1	0.3	9.5	0.4	12.1	0.3

A2. Table Zircon Hf Isotope

Spot	Inferred age (Ma)	±2 s	Hf isotopes										
			$^{176}Hf/^{177}Hf$	±2 s	$^{176}Lu/^{177}Hf$	±2 s	176Yb/^{177}Hf	±2 s	$^{176}Hf/^{177}Hf(T)$	$^{176}Hf/^{177}Hf$ CHUR(T)	εHf(0)	εHf(T)	±2 s
19JA20-01A-01	28	1	0.283159	0.000014	0.001736	0.000019	0.062670	0.000740	0.283158	0.282767	13.2	13.8	0.5
19JA20-01A-02	27.5	0.7	0.283216	0.000034	0.005435	0.000094	0.218451	0.003800	0.283213	0.282768	15.2	15.7	1.2
19JA20-01A-03	25	1	0.283191	0.000015	0.001998	0.000026	0.069939	0.001060	0.283189	0.282769	14.4	14.9	0.5
19JA20-01A-04	27	1	0.283222	0.000016	0.002213	0.000015	0.080186	0.000440	0.283221	0.282768	15.4	16.0	0.6
19JA20-01A-05	26.7	0.8	0.283206	0.000016	0.002394	0.000024	0.087316	0.000680	0.283196	0.282768	14.9	15.4	0.6
19JA20-01A-06	26	1	0.283191	0.000015	0.002272	0.000005	0.079830	0.000138	0.283189	0.282769	14.4	14.9	0.5
19JA20-01A-07	27	2	0.283263	0.000028	0.002370	0.000084	0.078375	0.001540	0.283262	0.282768	16.9	17.5	1.0
19JA20-01A-08	27	1	0.283235	0.000018	0.002893	0.000032	0.104771	0.001000	0.283234	0.282768	15.9	16.5	0.6
19JA20-01A-09	30	4	0.283195	0.000017	0.001059	0.000046	0.036579	0.001500	0.283195	0.282766	14.5	15.2	0.6
Spot	Inferred age (Ma)	±2 s	Hf isotopes										
			$^{176}Hf/^{177}Hf$	±2 s	$^{176}Lu/^{177}Hf$	±2 s	$^{176}Yb/^{177}Hf$	±2 s	$^{176}Hf/^{177}Hf(T)$	$^{176}Hf/^{177}Hf$ CHUR(T)	εHf(0)	εHf(T)	±2 s
19JA20-03A-01	28	1	0.283205	0.000017	0.002217	0.000028	0.077267	0.000980	0.283211	0.282767	14.8	15.4	0.6
19JA20-03A-02	27.3	1	0.283191	0.000017	0.001846	0.000028	0.065498	0.000800	0.283191	0.282768	14.4	14.9	0.6
19JA20-03A-03	25.9	0.9	0.283215	0.000024	0.001703	0.000030	0.063015	0.001420	0.283214	0.282769	15.2	15.7	0.8
19JA20-03A-05	27	1	0.283210	0.000024	0.001860	0.000044	0.066861	0.001360	0.283209	0.282768	15.0	15.6	0.8
19JA20-03A-07	26.1	0.8	0.283191	0.000020	0.002231	0.000038	0.072689	0.000540	0.283191	0.282769	14.4	14.9	0.7
19JA20-03A-09	24	1	0.283190	0.000016	0.002282	0.000028	0.081252	0.000960	0.283189	0.282769	14.3	14.8	0.6
Spot	Inferred age (Ma)	±2 s	Hf isotopes										
			$^{176}Hf/^{177}Hf$	±2 s	$^{176}Lu/^{177}Hf$	±2 s	$^{176}Yb/^{177}Hf$	±2 s	$^{176}Hf/^{177}Hf(T)$	$^{176}Hf/^{177}Hf$ CHUR(T)	εHf(0)	εHf(T)	±2 s
19JA18-03A-01	12.5	0.7	0.283200	0.000019	0.001703	0.000034	0.057951	0.001120	0.283191	0.282777	14.7	14.9	0.7
19JA18-03A-02	13	1	0.283161	0.000019	0.001401	0.000030	0.048297	0.001040	0.283161	0.282777	13.3	13.6	0.7
19JA18-03A-03	13.2	0.9	0.283181	0.000019	0.001330	0.000022	0.045019	0.000720	0.283181	0.282777	14.0	14.3	0.7
19JA18-03A-04	13	1	0.283174	0.000020	0.001580	0.000011	0.051819	0.000460	0.283174	0.282777	13.8	14.0	0.7
19JA18-03A-05	14	0.7	0.283182	0.000015	0.001419	0.000010	0.048268	0.000440	0.283182	0.282776	14.1	14.4	0.5
19JA18-03A-06	14	1	0.283164	0.000017	0.001200	0.000004	0.040648	0.000182	0.283164	0.282776	13.4	13.7	0.6
19JA18-03A-07	13.3	0.6	0.283179	0.000022	0.000859	0.000019	0.027905	0.000520	0.283179	0.282777	13.9	14.2	0.8
19JA18-03A-08	14.2	0.7	0.283181	0.000017	0.001583	0.000022	0.055753	0.001040	0.283181	0.282776	14.0	14.3	0.6
19JA18-03A-09	13.1	0.9	0.283187	0.000016	0.001900	0.000024	0.064094	0.000700	0.283186	0.282777	14.2	14.5	0.6
Spot	Inferred age (Ma)	±2 s	Hf isotopes										
			$^{176}Hf/^{177}Hf$	±2 s	$^{176}Lu/^{177}Hf$	±2 s	$^{176}Yb/^{177}Hf$	±2 s	$^{176}Hf/^{177}Hf(T)$	$^{176}Hf/^{177}Hf$ CHUR(T)	εHf(0)	εHf(T)	±2 s
19JA19-01A-01	14	1	0.283173	0.000022	0.000675	0.000005	0.020899	0.000186	0.283173	0.282776	13.7	14.0	0.8
19JA19-01A-02	13.2	0.6	0.283163	0.000022	0.000458	0.000013	0.015414	0.000560	0.283162	0.282777	13.3	13.6	0.8
19JA19-01A-03	13	2	0.283127	0.000020	0.000946	0.000018	0.030855	0.000720	0.283126	0.282777	12.1	12.4	0.7
19JA19-01A-04	12.7	0.9	0.283214	0.000020	0.001859	0.000048	0.063091	0.001580	0.283213	0.282777	15.2	15.4	0.7
19JA19-01A-05	13	1	0.283166	0.000020	0.001186	0.000038	0.039275	0.001220	0.283166	0.282777	13.5	13.8	0.7
19JA19-01A-06	13	1	0.283161	0.000020	0.001376	0.000018	0.046727	0.000380	0.283161	0.282777	13.3	13.6	0.7
19JA19-01A-07	12	3	0.283151	0.000020	0.000763	0.000004	0.024536	0.000220	0.283151	0.282777	12.9	13.2	0.7
19JA19-01A-08	11	1	0.283174	0.000018	0.001528	0.000013	0.051428	0.000440	0.283174	0.282778	13.8	14.0	0.6
19JA19-01A-09	12	1	0.283156	0.000022	0.001064	0.000004	0.034349	0.000162	0.283155	0.282777	13.1	13.4	0.8
Spot	Inferred age (Ma)	±2 s	Hf isotopes										
			$^{176}Hf/^{177}Hf$	±2 s	$^{176}Lu/^{177}Hf$	±2 s	$^{176}Yb/^{177}Hf$	±2 s	$^{176}Hf/^{177}Hf(T)$	$^{176}Hf/^{177}Hf$ CHUR(T)	εHf(0)	εHf(T)	±2 s
19JA18-04A-01	14.2	0.9	0.283187	0.000020	0.002236	0.000034	0.073770	0.001280	0.283186	0.282776	14.2	0.7	93
19JA18-04A-02	10	3	0.283169	0.000020	0.001353	0.000022	0.043177	0.000760	0.283169	0.282779	13.6	0.7	117
19JA18-04A-03	11	1	0.283160	0.000020	0.000994	0.000013	0.032217	0.000440	0.283160	0.282778	13.3	0.7	128
19JA18-04A-04	12	0.8	0.283188	0.000026	0.001480	0.000022	0.049291	0.000900	0.283187	0.282777	14.2	0.9	90
19JA18-04A-05	12.5	0.8	0.283149	0.000018	0.001575	0.000015	0.052219	0.000420	0.283149	0.282777	12.9	0.6	147
19JA18-04A-06	13.1	0.9	0.283165	0.000017	0.001207	0.000004	0.039126	0.000154	0.283165	0.282777	13.4	0.6	122
19JA18-04A-07	11.4	0.6	0.283178	0.000018	0.001662	0.000007	0.054998	0.000320	0.283177	0.282778	13.9	0.6	106
19JA18-04A-08	13	1	0.283180	0.000019	0.001360	0.000024	0.044290	0.000740	0.283179	0.282777	14.0	0.7	101
19JA18-04A-09	14	2	0.283150	0.000022	0.000795	0.000014	0.025049	0.000360	0.283150	0.282776	12.9	0.8	142
Spot	Inferred age (Ma)	±2 s	Hf isotopes										
			$^{176}Hf/^{177}Hf$	±2 s	$^{176}Lu/^{177}Hf$	±2 s	$^{176}Yb/^{177}Hf$	±2 s	$^{176}Hf/^{177}Hf(T)$	$^{176}Hf/^{177}Hf$ CHUR(T)	εHf(0)	εHf(T)	±2 s
19JA32-02A-01	12.7	1	0.283152	0.000020	0.001500	0.000011	0.047857	0.000400	0.283151	0.282777	13.0	13.2	0.7
19JA32-02A-02	12.9	0.8	0.283192	0.000022	0.001936	0.000007	0.062978	0.000440	0.283191	0.282777	14.4	14.7	0.8
19JA32-02A-03	14	1	0.283209	0.000024	0.001381	0.000028	0.043213	0.000760	0.283208	0.282776	15.0	15.3	0.8
19JA32-02A-04	11.1	0.6	0.283167	0.000022	0.002494	0.000024	0.084172	0.000900	0.283166	0.282778	13.5	13.7	0.8
19JA32-02A-05	13	0.7	0.283224	0.000020	0.002508	0.000032	0.080193	0.000360	0.283223	0.282777	15.5	15.8	0.7
19JA32-02A-06	11.7	0.7	0.283176	0.000028	0.001516	0.000020	0.045797	0.000300	0.283176	0.282778	13.8	14.1	1.0
19JA32-02A-07	12.8	0.8	0.283219	0.000020	0.002254	0.000010	0.072351	0.000700	0.283219	0.282777	15.4	15.6	0.7
19JA32-02A-08	11.9	1	0.283178	0.000024	0.001994	0.000052	0.068484	0.001980	0.283178	0.282778	13.9	14.2	0.8
19JA32-02A-09	12	1	0.283170	0.000024	0.001674	0.000012	0.054561	0.000560	0.283169	0.282777	13.6	13.9	0.8
Spot	Inferred age (Ma)	±2 s	Hf isotopes										
			$^{176}Hf/^{177}Hf$	±2 s	$^{176}Lu/^{177}Hf$	±2 s	$^{176}Yb/^{177}Hf$	±2 s	$^{176}Hf/^{177}Hf(T)$	$^{176}Hf/^{177}Hf$ CHUR(T)	εHf(0)	εHf(T)	±2 s
19JA45-01-07	20.2	0.6	0.283234	0.000032	0.002056	0.000052	0.068283	0.000440	0.282772	0.283233	15.9	16.3	1.1
19JA45-01-09	30	1	0.283189	0.000054	0.004498	0.000100	0.142778	0.004200	0.282766	0.283187	14.3	14.9	1.9
19JA45-01-10	19.9	0.8	0.283158	0.000056	0.003462	0.000008	0.100921	0.000240	0.282773	0.283157	13.2	13.6	2.0

A.2 Figure Cl Image

19JA20-03A N=60

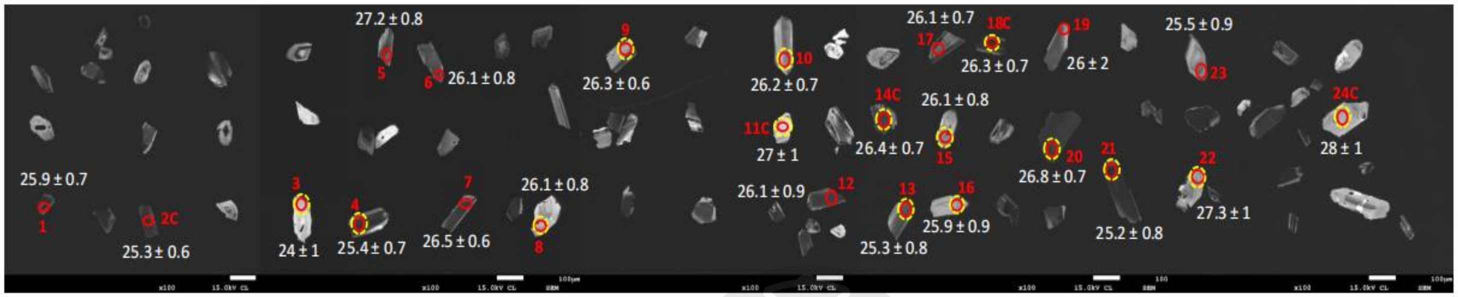

19JA20-01A N=60

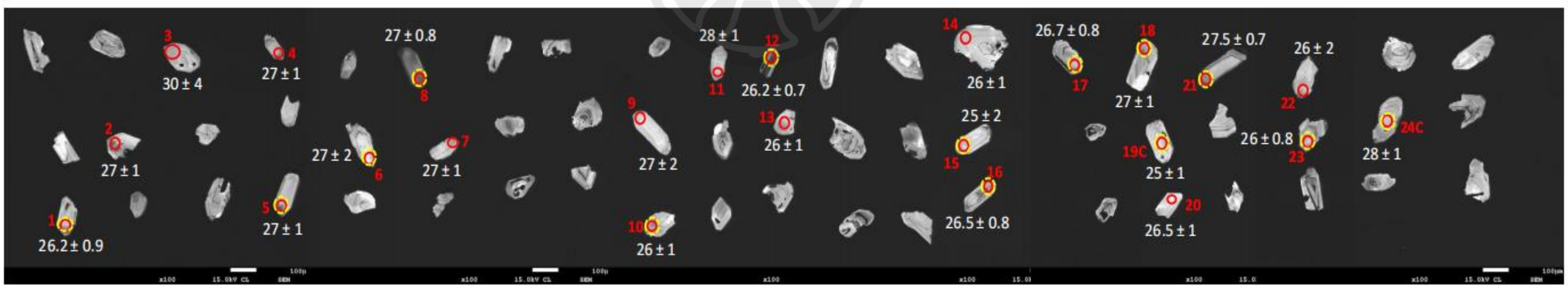

19JA18-05A N=60

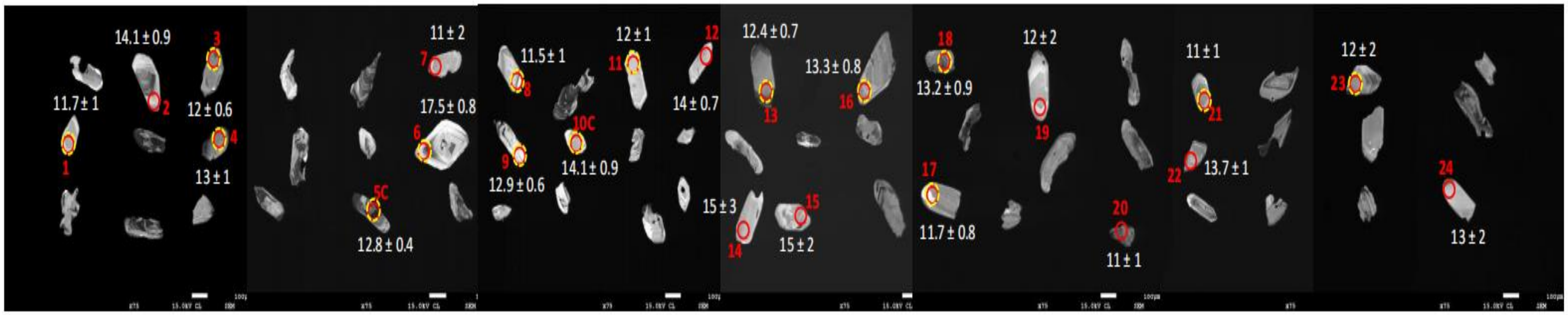

19JA18-02A N=60

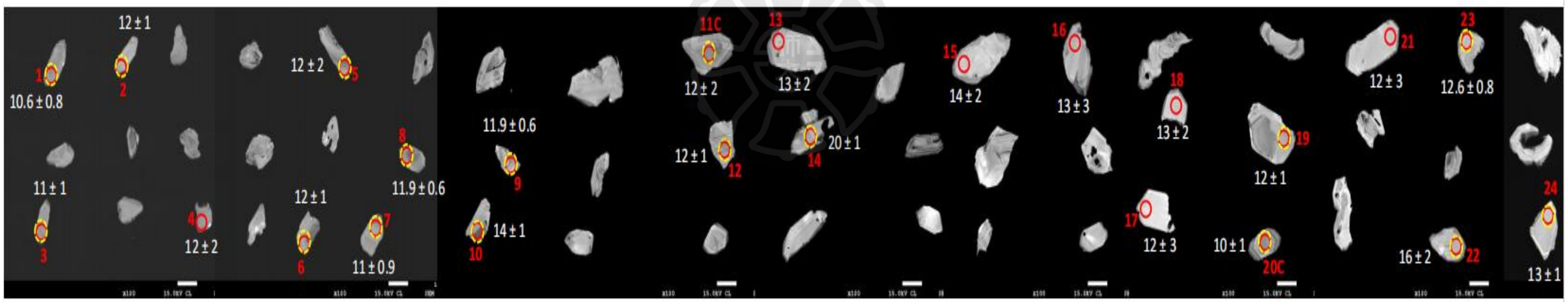

19JA19-02A N=60

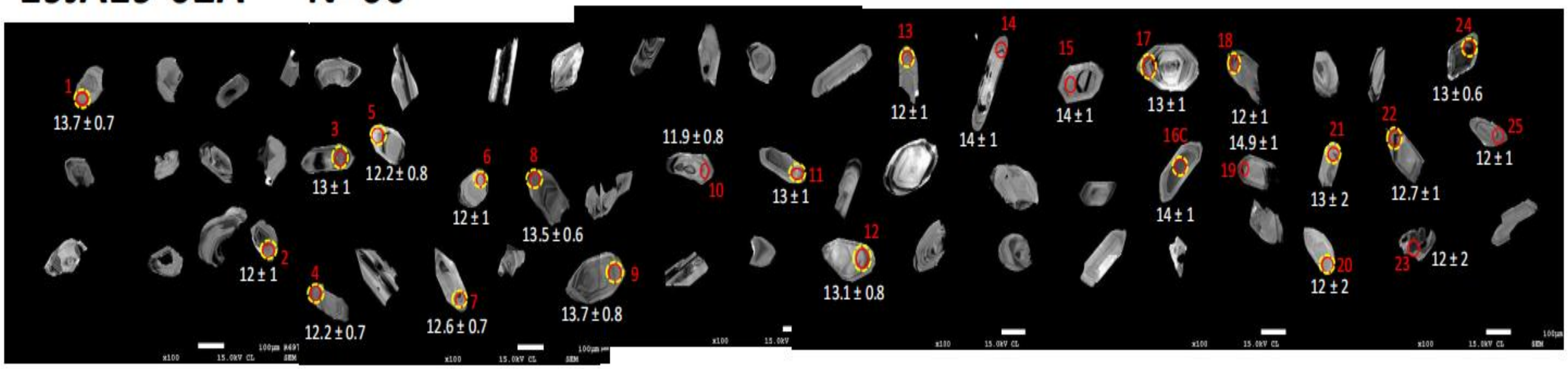

19JA20-02A N=60

19JA18-03A N=60

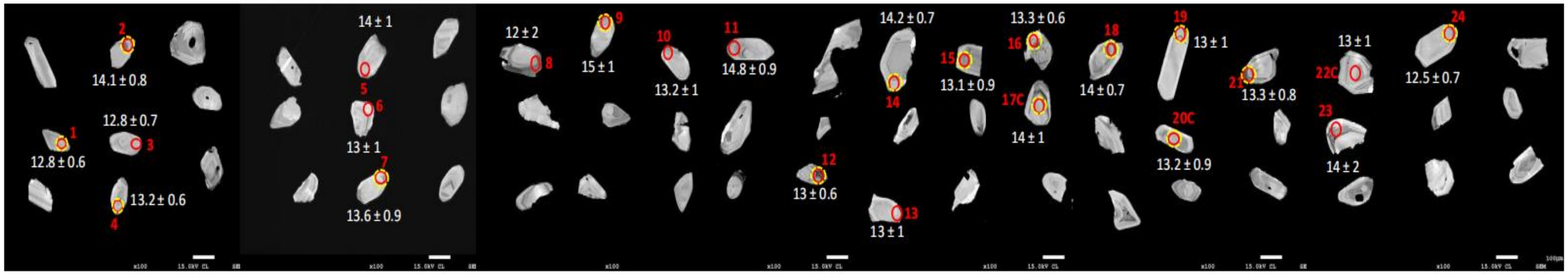

19JA19-01A N=60

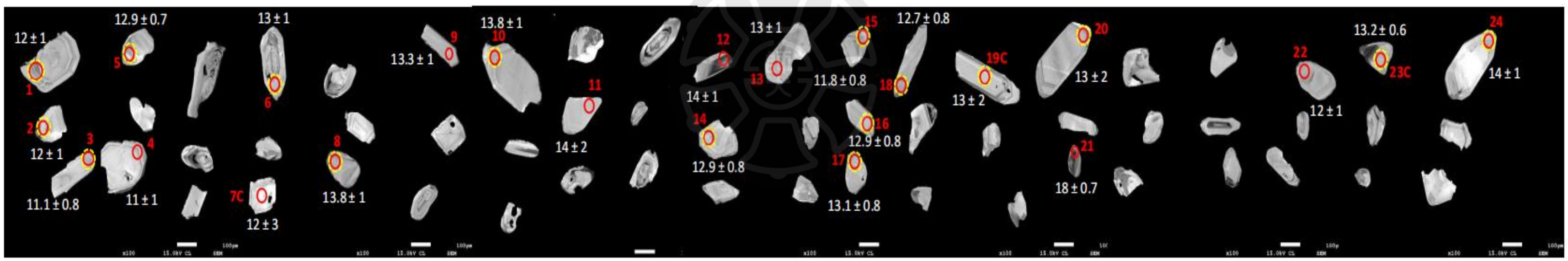

19JA18-04A N=60

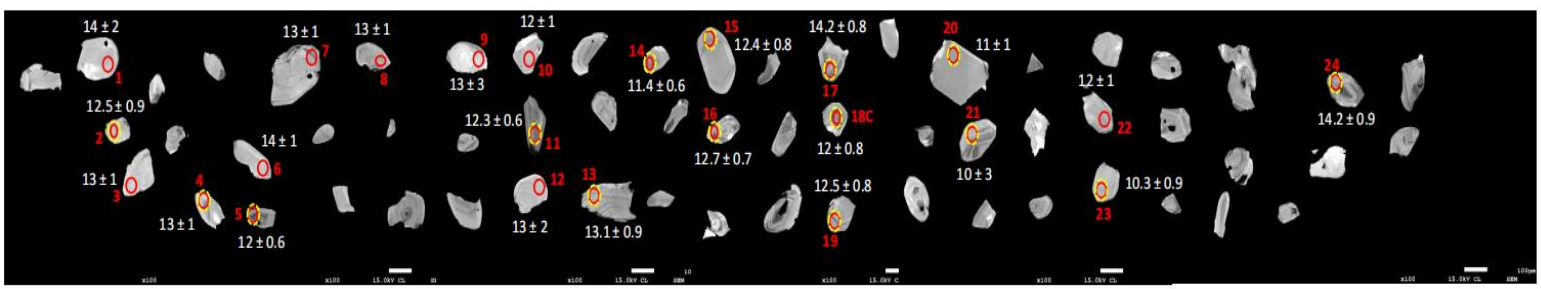

19JA19-03A N=60

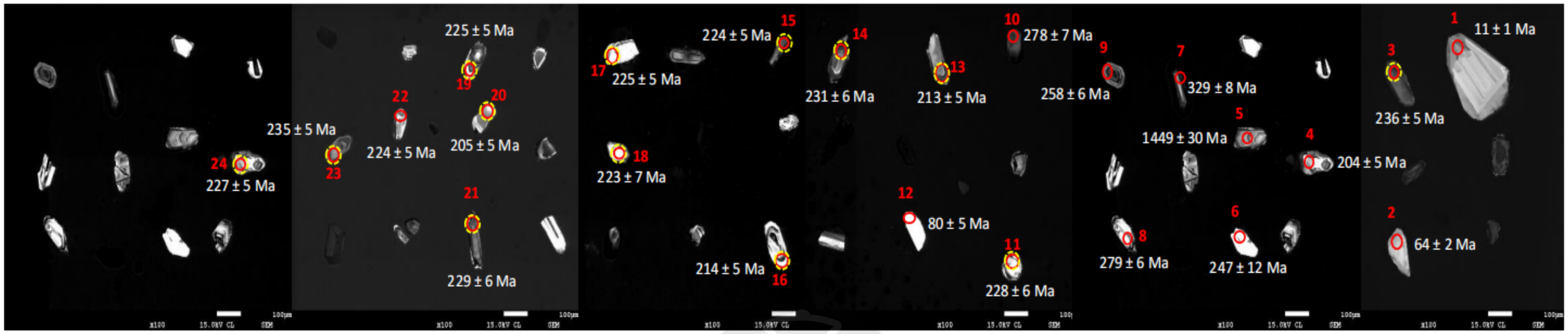

19JA17-01A N=60